UNIVERSITY OF BELGRADE
SCHOOL OF ELECTRICAL ENGINEERING

UNIVERSITY PARIS-EST CRÉTEIL
DOCTORAL SCHOOL MSTIC

Filip B. Bečanović

Uncovering optimal strategies in human motion through inverse optimal control

Doctoral Dissertation

Paris/Belgrade, 2023.

УНИВЕРЗИТЕТ У БЕОГРАДУ
ЕЛЕКТРОТЕХНИЧКИ ФАКУЛТЕТ

УНИВЕРЗИТЕТ ПАРИ-ЕСТ КРЕТЕЈ
ДОКТОРСКА ШКОЛА МСТИЦ

Филип Б. Бечановић

Откривање оптималних стратегија у људском кретању путем инверзног оптималног управљања

Докторска Дисертација

Париз/Београд, 2023.

UNIVERSITÉ DE BELGRADE
ÉCOLE D'INGÉNIERIE ÉLECTROTECHNIQUE

UNIVERSITÉ PARIS-EST CRÉTEIL
ÉCOLE DOCTORALE MSTIC

Filip B. Bečanović

Identification de stratégies optimales dans le mouvement humain via le contrôle optimal inverse

Doctoral Dissertation

Paris/Belgrade, 2023.

Supervisors

Dr. Samer Mohammed
Full Professor
Department of Science and Technology, University Paris-Est Créteil

Dr. Kosta Jovanović
Associate Professor
School of Electrical Engineering, University of Belgrade, Serbia

Thesis Committee

Dr. Francois Charpillet
Senior Research Director,
INRIA Nancy, France

Dr. Vincent Padois,
Senior Research Director,
INRIA Bordeaux, France

Dr. Željko Djurović
Full Professor
School of Electrical Engineering, University of Belgrade, Serbia

Dr. Milica Janković
Associate Professor
School of Electrical Engineering, University of Belgrade, Serbia

This Ph.D. thesis has been realized in accordance with the Agreement for the Joint Supervision of a Doctoral Thesis concluded between the University of Belgrade, the University of Paris Est-Créteil, and Filip Bečanović.

At the University of Paris Est-Créteil, Filip has enrolled in the Doctoral School MSTIC in the study program "Signal, Image, Automatique". At the University of Belgrade, Filip has enrolled in the Ph.D. program "Electrical and Computer Engineering" on the topic of Robotics and Biomechanics.

Acknowledgements

Ph.D. programs tend to last long, leaving a considerable mark on our lives. They are often grounds for meeting new people and shaping our life trajectory. As such, I dedicate this chapter to the numerous people who have shaped my life during my Ph.D. and I express my gratitude to:

My primary mentor, teacher, motivator, and gateway to my field of study, Prof. **Vincent Bonnet**, for shaping my scientific vision and providing the best opportunities and support I could ask for;

My mentor, Prof. **Kosta Jovanović**, for teaching me the importance of work ethic and perseverance and for guiding me and helping me with kind-hearted optimism even when success seemed far away;

My mentor, Prof. **Samer Mohammed**, for setting high standards, being a spokesperson for goal-oriented research, and helping me achieve those standards through rigorous feedback;

My colleagues, Dr. **Maja Trumić**, Dr. **Zaviša Gordić**, and Dr. **Branko Lukić**, for the occasional but timely helping hand;

My colleagues and office mates, **Nikola Knežević** and **Miloš Petrović**, for encouraging me the most, sometimes aggressively, and providing company in my coffee abuse;

My colleagues, Dr. **Randa Mallat**, **Huiseok Moon**, **Rami Jradi**, and **Oussama Bey** for their hospitality and their invaluable help in conducting experiments;

Prof. **Olivier Stasse**, for welcoming me as a two-time visitor to the Gepetto team in LAAS-CNRS in Toulouse;

My colleagues, **Alessandro Assirelli**, Dr. **Filippo Smaldone**, Dr. **Gianluigi Grandesso**, Dr. **Nahuel Villa**, **Quang Anh Le**, but also **Artur Haffemayer**, **Côme Perrot**, **Gabriele Fadini**, **Sonia-Laure Hadj Sassi**, **Virgile Batto**, and **Zoé Pomarat**, for their hospitality and for making the work environment the most enjoyable place;

My colleague, Dr. **Jared Miller**, for our delightful and fruitful collaboration during our stay at the LAAS-CNRS lab in Toulouse, for all the mathematics and travel tips he taught me, and for becoming a great friend;

My colleague, **Mohamed Ajdel**, who has shared the same hardships as me since we were Master's students, for his hospitality, generosity, and helpfulness, for being one of the most significant sources of humor for the last four years, and for becoming a lifelong friend;

My colleague, **Maxime Sabbah**, for his hospitality, moral support, exciting discussions, and all the good times we had together, and also for becoming a lifelong friend;

My parents, **Branislava** and **Miodrag**, and my grandmothers **Vojslava** and **Mileva**, for providing the initial conditions necessary for me even to start a Ph.D. and for cheering me on all the way;

My girlfriend, **Nika**, for being an inspiration since long before my Ph.D. started;

My friends, **Aleksandar**, **Borko**, **Fedja**, **Marko B.**, **Marko K.**, **Matija**, **Milutin**, and **Vuk**, as well as **Badr**, **Erwan**, **Maxime**, **Olivier**, **Raphaël**, and **Thibault**, who have been with me throughout the journey, have all my thanks. Special thanks to Erwan for lodging me in his home.

Belgrade, September 26, 2023.

Filip Bečanović

Dissertation title: Uncovering Optimal Control Strategies in Human Motion through Inverse Optimal Control

Abstract: This thesis navigates the interdisciplinary realm of human biomechanics and optimization-based motion modeling. It focuses on inverse optimal control and its application to resolve associated challenges in designing more accurate data-driven simulations of human muscle force sharing during gait and human box-lifting. A thorough survey of contemporary advancements in optimization-based approaches in human motion modeling and inverse optimal control, touching on connections to inverse reinforcement learning and bi-level optimization, lays the groundwork for the research. One theme of this research is formulating a novel method designed to ascertain lower bounds on the error of inverse optimal control processes for quadratic programming optimal control models, which possess practical potential. Though not directly applicable to the formulation of muscle force sharing and box-lifting, this method may be extended for this to be the case. The main themes of this research are the biomechanical simulations of box-lifting and the sharing of muscle force in the lower limbs during gait. Box-lifting and muscle-force-sharing simulation applications emphasize the critical potential of optimization-based simulation methods in biomechanics and the ongoing need for enhancements in existing models. The pertinence and potential of inverse optimal control approaches for augmenting accuracy in human motion simulation are demonstrated through these applications while taking a step back and exploring the difficulties in large-scale applications. The application to box-lifting required acquiring human motion data, utilizing advanced motion capture systems and a force plate. A detailed presentation of the collected data, its post-processing, and its use for the final model identification has been given. In contrast, the application to muscle-force sharing has been made on pre-processed open-sourced data. This dissertation consolidates and scrutinizes existing knowledge of inverse optimal control, proposing incremental advancements in human biomechanics and motion simulation through its use.

Keywords: biomechanics, human modeling, human motion simulation, inverse optimal control, human motion analysis, ergonomics, muscle force analysis, box lifting

Scientific field: Electrical and Computer Engineering

Scientific subfield: Inverse Optimal Control, Biomechanics

Наслов дисертације: Откривање Оптималних Стратегија у Људском Кретању Путем Инверзног Оптималног Управљања

Апстракт: Ова теза се бави интердисциплинарним подручјем људске биомеханике и моделирањем кретања заснованог на оптимизацији. Фокусира се на инверзно оптимално управљање и његову примену за решавање изазова у дизајнирању прецизнијих симулација заснованих на подацима расподеле људске мишићне силе током хода и људског подизања кутија. Темељно истраживање савременог напретка у оптимизационом моделирању људских покрета и инверзог оптималног управљања, дотичући се веза са инверзним учењем подстицањем и оптимизацијом на два нивоа, поставља основу за истраживање. Једна тема овог истраживања је формулисање новог метода за утврдјивање доње границе грешке инверзних процеса оптималног управљања за моделе оптималног управљања заснованих на квадратном програмирању, који поседују практичну примену. Иако метод није директно применљива на формулацију проблема расподеле мишићне силе и подизања кутија, овај метод се може проширити да би то био случај. Главне теме овог истраживања су биомеханичке симулације подизања кутија и расподеле мишићне силе у доњим удовима током хода. Примене симулације подизања кутија и расподелу мишићне силе наглашавају критични потенцијал симулационих метода заснованих на оптимизацији у биомеханици и сталну потребу за побољшањима у постојећим моделима. Прикладност и потенцијал инверзних оптималних приступа управљања за повећање прецизности у симулацији људског кретања демонстрирани су кроз ове примене док се потешкоће у применама великих размера стављају у перспективу. Примена на подизање кутија захтевала је прикупљање података о људском кретању, коришћењем система за хватање покрета и платформе за мерење силе. Дат је детаљан приказ прикупљених података, њихове накнадне обраде и употребе за коначну идентификацију модела. Насупрот томе, примена на расподелу мишићних сила је заснована на претходно обрађеним јавно доступним подацима. Ова дисертација консолидује и испитује постојеће знање о инверзном оптималном управљању, предлажући инкременталну напредак у људској биомеханици и симулацији кретања кроз њену употребу.

Кључне речи: биомеханика, људско моделирање, симулација људског покрета, инверзно оптимално управљање, анализа људског покрета, ергономија, анализа мишићне силе, дизање кутија

Научна област: Електротехника и рачунарство

Научна подобласт: Инверзно оптимално управљање, Биомеханика

Titre de la thèse: Découvertes de Stratégies de Contrôle Optimal dans le Mouvement Humain Grâce au Contrôle Optimal Inverse

Résumé: Cette thèse explore le domaine interdisciplinaire de la biomécanique humaine et de la modélisation du mouvement basée sur l'optimisation. Elle se concentre sur le contrôle optimal inverse et son application pour résoudre les défis associés à la conception de simulations plus précises basées sur des données de la répartition de la force musculaire humaine pendant la marche et le mouvement de levage de boîtes. Une étude approfondie des progrès contemporains dans les approches basées sur l'optimisation dans la modélisation du mouvement humain et le contrôle optimal inverse, abordant les liens avec l'apprentissage par renforcement inverse et l'optimisation à deux niveaux, jette les bases de la recherche. L'un des thèmes de cette recherche consiste à formuler une nouvelle méthode conçue pour déterminer les limites inférieures de l'erreur des processus de contrôle optimal inverse pour les modèles de contrôle optimal quadratiques, qui possèdent un potentiel pratique. Bien qu'elle ne soit pas directement applicable à la formulation de la répartition de la force musculaire et du levage de boîtes, cette méthode peut être étendue pour que ce soit le cas. Les thèmes principaux de cette recherche sont les simulations biomécaniques du levage de boîtes et la répartition de la force musculaire dans les membres inférieurs lors de la marche. Les applications de simulation de levage de boîtes et de répartition de force musculaire soulignent le potentiel critique des méthodes de simulation basées sur l'optimisation en biomécanique et le besoin continu d'améliorations des modèles existants. La pertinence et le potentiel des approches de contrôle optimal inverse pour augmenter la précision de la simulation du mouvement humain sont démontrés à travers ces applications tout en prenant du recul et en explorant les difficultés des applications à grande échelle. L'application au levage de caisses nécessitait l'acquisition de données sur les mouvements humains, à l'aide de systèmes de capture de mouvements et d'une plaque de force. Une présentation détaillée des données collectées, de leur traitement et de leur utilisation pour l'identification finale du modèle a été donnée. En revanche, l'application à la répartition de la force musculaire a été réalisée sur des données open source prétraitées. Cette thèse consolide et examine les connaissances existantes sur le contrôle optimal inverse, proposant des avancées progressives dans la biomécanique humaine et la simulation du mouvement grâce à son utilisation.

Mots clés: biomécanique, modélisation humaine, simulation du mouvement humain, contrôle optimal inverse, analyse du mouvement humain, ergonomie, analyse de la force musculaire, levage de boîtes

Domaine scientifique: Génie électrique et informatique

Sous-domaine scientifique: Contrôle optimal inverse, biomécanique

Contents

Chapter 1

Introduction

1.1 Subject, Aim, and Significance of the Research

In the ergonomics, biomechanics, and robotics research, understanding human motor control has significant implications – from advancing technologies in the healthcare and rehabilitation sector to designing more efficient robotic assistance [141]. Even though automation has been widely implemented in many industries, tasks cannot be fully automated because of their flexible requirements, necessitating human-level perception, decision-making, and operation [119]. Many of these tasks involve heavy physical work, excessive repetition, awkward postures, and heavy lifting, often identified as the leading causes of Musculoskeletal Disorders (MDs) [67]. MDs are prevalent among industrial workers, accounting for 80% of industrial diseases with an annual increase of 3% over the past decade. MDs can lead to early retirement and significant difficulties in accomplishing basic everyday tasks for affected people, thus presenting significant economic and societal challenges from the point of view of both companies and governments [116]. Human-robot collaboration and exoskeletons are promising solutions for reducing MDs by combining the human's superior perception and decision-making with the robot's physical power generation [119]. Additionally, they have the potential to improve the future of assistive technology in rehabilitation centers [94]. However, a limited understanding of human motion and the inability of robots to algorithmically anticipate it during collaborative or assistive tasks hinder their safe coexistence with humans and successful task performance [59].

To overcome this challenge, a promising solution is to use data-driven Inverse Optimal Control (IOC) to learn human-like motions from demonstrations of a human supervisor [129, 138]. IOC has yielded encouraging results in various biomechanical and robotic applications, including torque-controlled locomotion [108], muscle-force sharing during locomotion [149], grasping [72], and industrial screwing [97], and has the potential to become essential in designing seamless and natural robotic assistance [112]. Furthermore, IOC can be used to determine changes in motion control objectives and segment human motion into phases [111, 135], leading to more informative feedback in the ergonomic evaluation of task difficulty for human workers [97, 111]. This can also lead to more accurate human simulations and, in turn, facilitate the design of ergonomic workspaces that will reduce the risks of MDs [37]. IOC and similar techniques have been applied in numerous fields, including but not limited to control theory, artificial intelligence, robotics, health systems, energy systems, and marketing [120, 129, 138]. Despite efforts to survey and classify the numerous approaches [129, 138], there seems to be no consensus on terminology, assumptions, and solution methods. Regarding IOC, there remain questions pertaining to its resilience to noise [120, 148] or to the type of learning loss function to be used [120, 138, 147, 148].

The research will focus on the study of human motor control via the use of data-driven IOC

on experimentally acquired data. The expected use cases and applications of the results are in ergonomics, biomechanics, and robotics, with the potential for improving and advancing assistive technologies in industry, healthcare, and rehabilitation. Moreover, the research will partially focus on methods for data-driven IOC in and of itself, with the outputs of the research targeting impact in related fields of control theory and artificial intelligence.

1.2 Research Hypotheses

The research will be based on the following hypotheses that are ingrained in the existing literature:

- For a given motor task, there are invariant aspects in the motion produced by the human motor control system, which can be measured and quantified, whether the motion is analyzed in joint space or muscle space [72, 97, 108, 111, 112, 120, 135, 147, 148, 149],
- The invariant aspects of the motion produced by the motor control system can be modeled as an optimization process: a process of selection among infinite possibilities of the most appropriate motion. The invariant aspects can be identified using measured data of human motion with IOC. Once the constant elements of the movement are identified, they can be used in the future for predicting human motion, generating human-like trajectories, and analysis of the motion objectives [72, 97, 108, 111, 112, 120, 135, 147, 148, 149].

These hypotheses will be explored in Chapter 4, which deals with the distribution of muscle forces during gait, and in Chapter 5, which deals with the box-lifting motion of humans.

1.3 Research Outline

The dissertation begins by reviewing optimal control and the optimal control-based modeling of the human motor control system. Chapter 2 blend the state-of-the-art theory and applications of data-driven IOC [129, 138], with a focus on its applications in human motion [72, 97, 108, 111, 112, 120, 135, 147, 148, 149]. Chapter 2 and Chapter 3 will also briefly explore the connections between IOC and theories of multi-objective optimization [26] and bi-level optimization [99]. To illustrate the methods of IOC, the research will provide simple computational examples and accompanying graphical illustrations. Chapter 3 will delve into the issue of "basis function selection" in the context of IOC, with a particular emphasis on convex quadratic basis functions [147]. Based on techniques from the field of polynomial optimization [100], the research will present a procedure for finding lower bounds on the error of an IOC approach for a given data set and basis functions [147]. Motivated by the potential applications of IOC in designing rehabilitation technology, especially walking exoskeletons, Chapter 4 will investigate how the human motor control system distributes muscle forces in the lower limbs during gait. The study will use IOC to analyze hemiparetic patient walking data, collected using Electromyography (EMG), motion capture, force-plates, and a treadmill and open-sourced alongside a calibrated geometric model of the lower body and extracted reference muscle forces in the lower limbs [144]. The calibrated geometric model and the reference muscle forces will serve as a baseline, and an IOC procedure will be applied to infer which biomechanical objectives from the literature best explain the obtained data [149]. The study will analyze and compare the simulation results with the learned objectives against literature baselines. Chapter 5 will include experiments on healthy human

participants performing a box-lifting task, chosen due to an estimated 52% of work-related MDs being caused by overloading during lifting tasks [126]. The chapter's goal will be to investigate the biomechanics of the specific box-lifting motor task and how one can represent a human's unconscious decision-making and control process using optimal control theory. The study will use an Optitrack motion capture system, an AMTI Force Plate, the box to be lifted during the experiments, and a table to place the box upon lifting. The obtained experimental data will be input into the IOC framework to analyze the control objectives of human subjects during a box-lifting task. The study will explore variations in retrieved control objectives across subjects and trials. The learned control objectives will be used for simulation and compared to state-of-the-art approaches from the literature [104, 134].

1.4 Research Timeline

The research was conducted to apply IOC to actual human data with different models and tasks to learn human motion objectives. Moreover, it comprises an inquiry into IOC methods and algorithms and their applicability to simple mathematical models in order to grasp the intricacies of application to complex models of human motion. The objective will be to give a biomechanical analysis of the results of the application of IOC to human motion, as well as to design more realistic simulations of human motion and shed light on the applicability of various IOC methods and algorithms to human motion models.

1. First phase – Familiarization The study started with analyzing the structure of the IOC problem through a literature review of related fields. In parallel, a survey on the modeling of human motion was performed. Popular IOC methods were tested on simple numerical examples, and the results were reported. The advantages of different approaches and their applicability to human motion models were evaluated and compared. Particular problems of IOC were studied, like the selection of basis functions, and contributions were published.

2. Second phase – First study – Muscle force sharing in lower limbs during gait The task of muscle-force sharing in lower limbs during gait was chosen as a first study on the basis of the availability of open-source clinical research data [144] and because of its the possibility of using relatively simple mathematical models.

3. Third phase – Second study – Data collection – Box-lifting The task of box-lifting was chosen as a second study on the basis of its essential correlation with work-related MDs and due to its moderately complex modeling. An experiment was designed to investigate the motor control objectives of humans when performing the box-lifting task. The data were collected using an Optitrack motion capture and AMTI force plate, were processed, and will be made publicly available upon publication of results. Known IOC techniques, as well as heuristic adaptations, were applied to the data in order to analyze it within this framework. The intricacies of the application of IOC to more complex models were discussed.

The studies are accompanied by detailed descriptions of the mathematical models and available datasets. The numerical methods were explained, and numerical results were comprehensively presented in tabular and figure forms. Biomechanical interpretation of the results alongside their implication for the design of better rehabilitation assistance and human-robot collaboration were discussed and cross-referenced with literature.

1.5 Biomechanics and Motor Control

The biomechanics of human movement is the study of the structure and function of human movement as viewed from the perspective of mechanics. This includes applying principles from physics to understand how the body moves (kinematics) and the forces that cause this movement (kinetics) [65]. Biomechanics often refers to the study of how the skeletal and muscular systems work under different conditions, such as walking, running, jumping, or lifting. It provides crucial insights into human performance and injury prevention [34, 101]. On the other hand, Motor Control is a sub-discipline of neuroscience and physiology that aims to understand how the nervous system interacts with the environment to produce purposeful, coordinated, or involuntary movements. It investigates how the central nervous system integrates information from the sensory systems (like vision and proprioception) with information about the desired action to produce motor commands [101]. Motor control theories often categorize movements into reflex-driven or planned actions and consider the role of feedback and feedforward control mechanisms [34]. Also, they study how motor skills are learned and retained, known as motor learning [38, 44]. Biomechanics and Motor Control intersect when we try to understand how the mechanical properties of the body (muscle properties, bone structures, etc.) interact with the control signals sent from the nervous system to produce motion. The field of Computational Neuroscience has produced models of motor control that try to capture these complex interactions. These models can help design better prosthetic limbs, improve outcomes in physical rehabilitation, or develop more realistic animations in computer graphics [34].

A pioneering study by Hogan [3] argues that the tendency of the motor behavior of primates to select a particular motor behavior during arm reaching motion is a product of an optimization process. The straight hand paths and bell-shaped velocity profiles observed during the reaching motion have been attributed to the minimization of elbow joint jerks with linear dynamics. Motion was simulated by optimizing the mentioned cost function.

The minimization of jerk has been re-used as a principle for studying human motion in [4] where the authors present a mathematical model of human arm movement coordination, utilizing dynamic optimization theory to optimize for smoothness by minimizing jerk of a 2 Degree of Freedom (DoF) model actuated at the shoulder and the elbow, with experimental confirmation that the model accurately predicts observed features, including straight point-to-point motions, bell-shaped velocity profiles, and variations in curvature along trajectories. Also considering a model actuated at the shoulder and the elbow, [22] introduce a model that accurately predicts complex arm movement speed profiles by maximizing smoothness along a predefined path, replacing the 2/3 power law with a jerk minimization constraint and demonstrates that this new model outperforms existing versions of the 2/3 power law, suggesting that the correlation between speed and curvature in arm movements may be a result of a motor strategy for producing smoother motions.

Another pioneering study by Nelson [2] explores various optimization objectives for motion, such as movement time, distance, peak velocity, energy, peak acceleration, and jerk, for a 1 DoF system ultimately revealing performance trade-offs in skilled movements and demonstrating how considerations of physical economy influence movements during activities like violin bowing.

A procedure that accounts for the formation of hand trajectories using the square of the rate of change of torque of a 2 DoF shoulder-elbow joint model integrated over the entire movement as an objective function has been presented in [6]. Experimental results support that human hand trajectories are planned and controlled according to the minimum torque change criterion.

Again using a two-link model for arm reaching (upper arm and forearm), [27] examines

internal representations for arm trajectory planning, comparing four computational models minimum hand-jerk model, minimum joint-jerk model, minimum joint torque change model, and the minimum commanded torque model (internal representation of changes in muscle tension), and finds that the minimum commanded torque change model in an "intrinsic-dynamic-neural" space reproduces actual trajectories best, with a key result being that longer movement durations lead to larger trajectory curvatures and the importance of initial and final positions in trajectory curvatures. A study [15] by the same group used a 17-muscle, 2-joint DoF model to model the arm motions of monkeys using a minimum muscle-tension change model.

Using a 4 DoF model of the arm (3 DoF in the shoulder and one in the elbow), Soechting et al. [14] found that it was impossible to predict the pointing motion of a human arm across a wide range of positions and orientations by using only kinematic quantities. They found that the minimum effort/work model, equal to the integral of joint power, produced the best predictions across the experimental data.

An optimal control model has been proposed in [13] to simulate the non-ballistic movement of rising from a chair, highlighting the importance of a performance criterion based on the time derivative of muscle force to minimize peak forces developed by muscles during the movement, ultimately showing that multi-joint coordination is influenced by both the chosen performance criterion and motion constraints.

A theory of eye and arm movements that explains the observed smooth and stereotyped trajectories based on the assumption that neural control signals are affected by signal-dependent noise has been developed in [21], with the key result being that minimizing the variance of the final eye or arm position accurately predicts these trajectories and the speed-accuracy trade-off, providing a unified perspective for both eye and arm movement control. Through the study of numerous human movements, [38] develops a theory of motor coordination called stochastic optimal feedback control, which reconciles the reliability of achieving behavioral goals with the richness of motor variability by allowing variability in redundant dimensions and intelligently using feedback to correct deviations interfering with task goals, providing a framework for understanding task-constrained variability, goal-directed corrections, motor synergies, and other aspects of motor control. Kuo [12] introduced an optimal control model for analyzing human postural balance, which incorporates linearized equations, state estimation, and gain-scheduling to study various control objectives, and finds that an objective function weighting center of mass excursion and deviations from an upright stable position, while considering system inertial parameters and musculoskeletal geometry, produces controls that reasonably match experimental data, shedding light on how humans select control strategies for maintaining balance.

More information can also be found in Chapter 4, which provides a review of optimal control-based approaches for predicting the distribution of muscle forces in the lower limbs during gait. Meanwhile, Chapter 5 provides a comprehensive and detailed review of the optimization-based approaches for the prediction of box-lifting motion.

Optimal Control Problems (OCPs) are a ubiquitous way to model a large number of natural phenomena related to biomechanics and motor control. A biological system chooses to distribute its motor commands in a way that minimizes an intrinsic cost function, usually representing a measure of smoothness of effort. The motor commands are often subjected to physical constraints while the invariant components of the motion are encoded within an objective function that the biological system has the task of minimizing.

A huge body of literature blending the theory of optimal control with the field of biomechanics and motor control has focused on finding a unifying principle for particular classes of human motion like pointing, grasping, walking, rising from a chair, balancing, and box-lifting. Almost as large is the set of unifying principles that have been proposed in these studies,

although much of them are focused on expressing the tendency for biological motion to be smooth or energy efficient.

Outside observers who wish to study or simulate the biological system's behavior may have direct or indirect access to measurements of the system's motor commands, but the biomechanical motor command objective function which is crucial for the simulation and prediction of motion is certainly not available to the observers. From the perspective of a simulation designer, the objective function design can sometimes prove to be very difficult. Data-driven modeling is supposed to alleviate this problem and uses observations and measurements of the biological system's motor commands which may be readily available to enhance the simulation models.

This dissertation will focus on IOC, which is a data-driven technique that imputes the objective function of a dynamical system given observation of its trajectories. IOC is, like much of the aforementioned literature, preconceived on the assumption that the observations are optimal with respect to some objective function that it attempts to uncover.

1.6 Thesis Contributions and Related Publications

The expected scientific contributions of the thesis are:

- The systematic overview of the literature and methods in optimization-based human motion modeling and IOC. A partial summary of the connections to related fields of inverse reinforcement learning, multi-objective optimization, and bi-level optimization is provided.
- Analysis and interpretation of the properties of current IOC methods, with remarks about practical implementations and performance.
- Design of a procedure for finding lower bounds on the error of an IOC approach for a given data set and basis functions in the context of convex quadratic basis functions.
- Application of IOC to two actual use cases related to industrial and rehabilitation applications. One use case is box-lifting, and another is muscle-force sharing in lower limbs during gait.
- Experimental human box-lifting data collection using a motion capture system and a force plate.
- Analysis of the variations in retrieved control objectives across subjects and trials for the box-lifting task.
- Application of IOC to infer the biomechanical objectives that best explain the obtained data on muscle force distribution in the lower limbs during gait, using data collected from hemiparetic patient walking and a calibrated geometric model of the lower body and comparing the results against literature baselines.
- Validation of the learned control objectives from the above two use cases through simulation and comparison with state-of-the-art approaches from the literature.

The scientific contributions that have been achieved throughout the thesis have been compiled and published in the following articles:

- Filip Bečanović et al. "Assessing the Quality of a Set of Basis Functions for Inverse Optimal Control via Projection onto Global Minimizers". In: *2022 IEEE 61st Conference on Decision and Control (CDC)*. IEEE. 2022, pp. 7598–7605,

- Filip Becanovic et al. “Force Sharing Problem During Gait Using Inverse Optimal Control”. In: *IEEE Robotics and Automation Letters* 8.2 (2023), pp–872,
- Marija Radmilović et al. *Influence of muscle co-contraction indicators for different task conditions.* 2021,
- Filip Bečanović et al. *Pronalazak Optimizacione Funkcije Kretanja iz Simulirane Demonstracije Pokreta Čučnja.* 2021.

Chapter 2

Inverse Optimal Control

There is a consensus in the literature on biomechanics, human motor control, and robotics that a broad spectrum of human motions can be modeled and predicted using optimal control approaches. This is especially the case for repetitive motions or tasks that are subject to strict biomechanical constraints such as walking, jumping, or lifting. Though trends do exist, there is no consensus on the objective function used for any particular class of human motion. The use of IOC methods has been proposed and extensively studied to use human motion data to infer the biomechanical objective function underlying some classes of human motion.

The field of IOC is still young, and "IOC" seems to be an umbrella term for a variety of related, although formally different, problems. Initially, in this chapter, a very general formulation of the IOC problem will be presented, which will attempt to consolidate as many of the different problems under the IOC umbrella as was necessary for the author to understand them. This unifying presentation is a byproduct of the numerous difficulties I have experienced when researching this subject, requiring a breadth of knowledge far beyond my initial expectations. It is an attempt to grasp the issue comprehensively.

Towards the end of the chapter, the exposition shifts towards a more narrow view of IOC, which has been the predominant perspective in the IOC literature embedded in the biomechanics, motor control, and robotics communities. This perspective will be adopted throughout the rest of the manuscript and thus will be referred to generically as IOC. In contrast, the aforementioned broader approach to IOC will be referred to as the General Inverse Problem.

The application of IOC requires at least one observation, which is assumed to be optimal or at least nearly optimal, and knowledge of the constraints related to the task's biomechanics and the human body that define the set of feasible motions. A necessary and crucial component of IOC is a finite-cardinality set of basis objective functions, which is inextricably linked to the variety of human motions our model will be able to produce. These basis objective functions are combined into a single compound objective function in a convex combination of the basis functions. The human motion produced by the model is then shaped by varying the weights of different basis functions in the compound function. Finally, the goal of IOC is to identify the optimal weights of this combination such that the observation output by the model is as close as possible to the training data.

The two measures of closeness that have shaped the literature amalgamating IOC with biomechanics, motor control, and robotics are presented in Section 2.6.

2.1 Introduction

Though [48] preceded it, the pioneering study that introduced IOC to the field of biomechanics and robotics and sparked an interest in the community was the study by Mombaur,

Truong, and Laumond [69], which introduced the idea of using IOC to transfer biological motions to robots, by demonstrating how this approach could be employed to understand and identify the optimization criteria underlying human locomotion. The study employed temporal, kinematic, and geometric objective basis functions. It used a bilevel approach that combines efficient direct multiple shooting and derivative-free trust region optimization techniques to identify the weighting coefficients of the basis functions. The study focused on transferring the natural locomotion paths to humanoid robots through a fully holonomic model of humanoid locomotion.

Multiple studies emerged thereafter, using IOC to analyze different human motions. Berret et al. [72] address the question of what cost function the brain optimizes for coordinating arm movements by employing a bilevel IOC method in an experimental setting involving arm reaching with target redundancy, revealing that subjects' arm trajectories best fit a combination of two cost functions: the absolute work of torques and the integrated squared joint acceleration, supporting the hypothesis that composite cost functions underlie natural movements. Arm motion was modeled in the sagittal plane with 2 DoF, one for the shoulder and one for the elbow, and the IOC problem was solved using a pseudospectral method for solving the direct problem combined with a derivative-free approach for the inverse problem. Albrecht, Leibold, and Ulbrich [77] also employ a bilevel IOC approach to explore how humans plan and execute their arm movements, except they analyze a 2 DoF model of the arm in the transversal plane, considering minimum jerk and minimum torque change models and their combinations. Sylla et al. [97] study an industrial screwing task, combining multiple criteria such as energy expenditure and trajectory smoothness, and demonstrating through bilevel IOC that the resulting cost function mainly consists of energy expenditure and geodesic criteria, highlighting the relevance of using composite cost functions in human motion planning for improving ergonomics in industrial tasks with collaborative robots. Clever and Mombaur [108] investigate human walking, successfully using IOC to identify weights for seven elementary criteria across different walking motions from various subjects and observing a correlation in the optimality across subjects, despite variations in walking styles.

Branching in the literature occurred with the publication of a methodology paper by Keshavarz, Wang, and Boyd [74] in which a method is presented for estimating the unknown objective function in direct optimization models by solving a convex optimization problem. In other words, it appeared they had found a way to represent the IOC problem as a convex optimization problem, making it many times more efficient to solve. This stimulated many publications based on this attractive and computationally efficient method. For example, authors of [84] model human locomotion trajectories, as in [69], but solve the IOC problem by using the method of Keshavarz, Wang, and Boyd [74] which minimizes the extent to which observed decisions violate first-order necessary conditions for optimality. This IOC method has been adapted to hybrid dynamical systems with impacts [76]. It has been applied to a dynamic bipedal climbing robot in simulation, successfully recovering cost functions from observed trajectories consistent with different modes of locomotion. The method has also been adapted to continuous time optimal control problems [88] by use of Pontryagin Maximum Principle (PMP). In [91], the IOC approach was adapted to differentially flat systems and formulated as a finite-dimensional linear least-squares minimization. It was used to model human locomotion during stair ascent, successfully predicting joint angle trajectories for novel stair heights and providing a basis for tuning controller parameters for lower-limb prosthetic devices.

Panchea and Ramdani [102] were one of the first groups to wonder about the robustness of this newfound IOC method in the presence of noise. In [102], they studied this IOC method with a focus on scenarios where both systems and observations are imperfect and uncertain,

introducing a framework for solving these IOC problems with bounded but unknown uncertainties and disturbances, providing a set membership algorithm based on interval analysis to compute the smallest set containing the true values of the objective function weights. In their subsequent paper, Panchea and Ramdani [118] generalize their interval method and apply it to a discrete unicycle robot model and a planar elastica model. The studies of [102, 118] are the first to refer to the method of Keshavarz, Wang, and Boyd [74] as "Inverse Karush-Kuhn-Tucker (IKKT)". Englert, Vien, and Toussaint [115] introduce the name "IKKT" in the title of their paper, thus paving the way for that name to stick. They emphasize that the method assumes demonstrations satisfy the Karush-Kuhn-Tucker (KKT) conditions of an unknown constrained optimization problem. They successfully apply the approach to a robot drawer and door opening task by considering various task-space-related objective functions for IOC. Panchea et al. [122] demonstrate the application of IKKT to 3D arm motion by recovering weight values for a basis of eight biomechanical objective functions and later extending this basis to 28 objective functions. Westermann, Lin, and Kulić Westermann, Lin, and Kulić focus on distance jumping where the time-varying cost function is retrieved using IKKT and analyze how different control objectives influence task success and how the control strategy changes during the motor learning process

A method for segmenting human movement based on detecting changes in the optimization criterion retrieved by IOC has been proposed in [111], where it is hypothesized that human motor control relies on weighted combinations of basis cost functions that adapt with changes in motion objectives, and the proposed algorithm successfully segments movements with an accuracy of 84%, demonstrating its effectiveness in identifying human motion patterns in a human squatting task. An extension of this is proposed in [127], where the authors recover the cost weights of each phase and estimate the phase transition points in a dynamical system with a multiphase cost function. The technique is applied to a simulated robot arm and human participants performing squatting tasks by reliably retrieving the cost function of each phase and achieving a segmentation accuracy above 90%. Within [143], the authors develop an online incremental IOC algorithm that requires a minimal number of observations. They introduce the concept of a recovery matrix to establish the relationship between currently available samples and weight recoverability.

In a more recent context, Colombel, Daney, and Charpillet [148] have questioned the reliability of IKKT methods for human motion analysis, proposing an approach based on Singular Value Decomposition of the recovery matrix to assess reliability. It provides a methodology to make IOC results more reliable by analyzing properties of matrices under various conditions and noise levels, emphasizing the importance of ensuring the trustworthiness of IOC outcomes. One key finding is the low noise threshold for which IKKT becomes unreliable. In their following paper, Colombel, Daney, and Charpillet [150] have come to the same conclusion as we will in our study detailed in Chapter 3. They refer to their framework as Projected Inverse Optimal Control, in which IOC is viewed as a projection of trajectories in the solution space of Direct Optimal Control (DOC) problems.

Amidst this abundance of new ideas about uses of IOC brought by the appearance of a computationally more efficient method, the bilevel approach has been abandoned in the literature on biomechanics and robotics due mostly to its long execution time. However, the bilevel approach has been known to have the merit of dealing with relatively noisy input data. Aswani, Shen, and Siddiq [120] had been applying IOC in the field of healthcare systems. They emerged with an Operations Research paper, which provided a grounded mathematical analysis of both the bilevel and the IKKT method. Through the lens of probability and statistics, the IOC algorithms were regarded as estimators of unknown underlying cost function weights. The key takeaway from the paper is that the bilevel IOC algorithm is a consistent estimator while the IKKT algorithm is an inconsistent estimator. This means

that, as more data is input into the algorithms for weight estimation, the bilevel IOC will converge to the true values of the underlying weights while the IKKT is not guaranteed to converge. This conclusion raised suspicion about the reliability of the IKKT method, which led to the development of reasonably trivial numerical examples in Bečanović et al. [147] and Becanovic et al. [149] where the IKKT method severely underperforms. Details about those examples are given in Chapter 3 and Chapter 4.

Finally, Chan, Mahmood, and Zhu [138] provide a comprehensive review of IOC approaches that have been in use far beyond the domains of biomechanics and robotics.

The aforementioned IOC literature focuses primarily on inverting DOC models, which are expressed and formulated as trajectory optimization problems. A prosperous decade older literature on Inverse Reinforcement Learning [33, 40] develops inverse conditions for optimal control problems formulated using Dynamic Programming (DP). Ng, Russell, et al. [33] focus on the problem of Inverse Reinforcement Learning in Markov decision processes, where the objective is to extract a reward function from observed optimal behavior to understand the reward function of natural systems. The paper presents three algorithms for IRL, addressing scenarios with known policies and observed trajectories, and proposes heuristics to address degeneracy issues. Abbeel and Ng [40] treat the problem of IRL where an expert's optimal behavior is observed and used to learn a reward function expressible as a linear combination of known features. The key result is the development of an algorithm that successfully learns the demonstrated task, even without explicitly recovering the expert's reward function, and yields a policy achieving performance close to that of the expert, as measured with respect to the expert's unknown reward function.

2.2 General Direct Problem

Many processes in physics, engineering, and biology, whether natural or artificial, are easily modeled as optimization problems [41]. Optimal control problems can also be expressed as optimization problems, and they represent straightforward models for many problems. The standard notation for a constrained optimization problem is given in equation (2.1).

$$\min_{\boldsymbol{x}\in\mathbb{R}^n} \quad f(\boldsymbol{x}) \tag{2.1a}$$

$$\text{subject to} \quad \boldsymbol{g}(\boldsymbol{x}) \leq 0 \tag{2.1b}$$

$$\boldsymbol{h}(\boldsymbol{x}) = 0 \tag{2.1c}$$

where $\boldsymbol{x} \in \mathbb{R}^n$ is the vector decision variable, $f : \mathbb{R}^n \mapsto \mathbb{R}$ is the scalar-valued objective function, $\boldsymbol{g} : \mathbb{R}^n \mapsto \mathbb{R}^q$ is the vector-valued inequality-constraint function, and $\boldsymbol{h} : \mathbb{R}^n \mapsto \mathbb{R}^r$ is the vector-valued equality-constraint function.

The semantics of an optimization problem is that one desires to find a value $\boldsymbol{x}^*$ for the decision variable $\boldsymbol{x}$ such that the objective function evaluated at that value $f(\boldsymbol{x}^*)$ attains its minimum p^* on the set described by a finite number of inequality and equality constraints, $\boldsymbol{g}(\boldsymbol{x}) \leq 0$ and $\boldsymbol{h}(\boldsymbol{x}) = 0$ respectively.

If we interpret the equation (2.1) as a direct formulation of an OCP then $\boldsymbol{x}$ is a vector describing the state and control trajectories, $f(\boldsymbol{x})$ is an approximation of the cost functional of the OCP, $\boldsymbol{g}(\boldsymbol{x})$ is an approximation of the control limits and algebraic path-constraints, and $\boldsymbol{h}(\boldsymbol{x})$ is an approximation of the boundary conditions and dynamics equation.

Parametric Optimization: Depending on the circumstances, the particular instance of the problem to solve may vary. For example, one may want to solve the same trajectory optimization problem but with different initial conditions. In another scenario, one may want

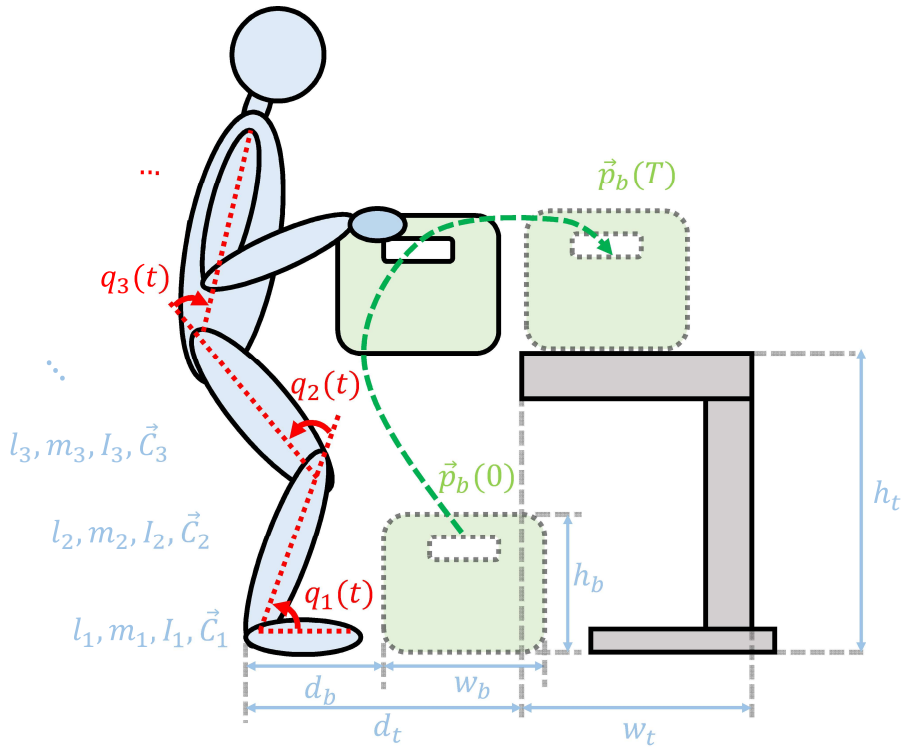

Figure 2.1: Diagram of a human box-lifting motion. The illustration contains a planar model of a human performing the motion, annotating the ankle, knee, and hip joint angles. The geometric parameters of the environment are also annotated and described in Example 2.2.1, as are the geometric and inertial parameters of the human model.

to solve the same trajectory optimization problem but with a different obstacle disposition. In general motion-generation problems, the value of the cost functional and the values of the constraints will be influenced by the state of the environment. The essential aspects of the environment can be described by a vector $\boldsymbol{\theta}$.

Treating the environment variables $\boldsymbol{\theta}$ as static, and separately from the trajectory variables $\boldsymbol{x}$, can ease the computational burden of the trajectory optimization and is essentially justified the environment variables are not expected to change under the influence of the agent acting out the optimized trajectory. In such cases, we can describe the cost functional $f(\boldsymbol{x};\boldsymbol{\theta})$ and the constraints $\boldsymbol{g}(\boldsymbol{x};\boldsymbol{\theta})$ and $\boldsymbol{h}(\boldsymbol{x};\boldsymbol{\theta})$ as being functions of the environment variables $\boldsymbol{\theta}$. The optimization model from equation (2.1) becomes a parametric optimization problem, with parameter $\boldsymbol{\theta}$.

Example 2.2.1. ***Human Box-Lifting Motion***

Consider Figure 2.1 for this example. The trajectory variables $\boldsymbol{x}$ describe the joint-angle trajectories $(q_1(t), q_2(t), q_3(t), \ldots)$ of the human model performing the box-lifting motion. The static environment variables $\boldsymbol{\theta}$ describe the aspects of the task that need not be treated as variables as they are not expected to change throughout the task. Such are the table width w_t, the table height h_t, the box width w_b, the box height h_b, the distance of the table from the human's feet d_t, and the initial distance of the box from the human's feet d_b. These parameters may change between different task instances but never during the task itself. In a similar vein, the person performing the task can change. As such, the geometrical and inertial parameters of the human model fulfilling the task need to be adjusted accordingly. Change occurs for parameters of link i of the model, namely, its length l_i, its mass m_i, its inertia I_i, and the position of its center of mass in the segment proximal reference frame $\vec{C}_i$. Thus, the generated motion depends not only on the disposition of the objects in the environment but

also on the geometry and inertia of the person performing the motion. In essence, knowing the mapping between the environment state $\boldsymbol{\theta}$ and the produced human trajectory $\boldsymbol{y}$ would allow prediction of the box-lifting motion under varying circumstances in terms of geometric disposition of the environment, but also in terms of the inertial parameters of the person performing the motion. This example has been picked as a case study for this thesis and is described in extensive detail in Chapter 5.

In general IOC [138], the idea is to represent the mapping between the external/environment parameters $\boldsymbol{\theta}$ and the expert behavior $\boldsymbol{y}$, through the means of an optimization problem. As mentioned in the introduction of this chapter, it has been demonstrated that human motion is well-modeled as an optimization problem. Thus, it is believed in the literature that it is possible to learn the mapping between the environmental parameters and human behavior through IOC. Therefore, the direct problem is often represented as a parametric optimization problem described in (2.2),

$$\hat{\boldsymbol{y}}(\boldsymbol{\theta}) = \underset{\boldsymbol{x}\in\mathbb{R}^n}{\operatorname{argmin}} \quad f(\boldsymbol{x};\boldsymbol{\theta}) \tag{2.2a}$$

$$\text{subject to} \quad \boldsymbol{g}(\boldsymbol{x};\boldsymbol{\theta}) \leq 0 \tag{2.2b}$$

$$\boldsymbol{h}(\boldsymbol{x};\boldsymbol{\theta}) = 0 \tag{2.2c}$$

with $\hat{\boldsymbol{y}}(\boldsymbol{\theta})$ being the prediction given by the direct model for the static task environment parameter $\boldsymbol{\theta}$. More precisely, we can define the direct optimization map.

Definition 2.2.1. *The **feasible region map** X is a set-valued map, from the space of static task environment parameters Θ to the task decision space $\mathbb{R}^n$,*

$$X : \Omega \rightrightarrows \mathbb{R}^n$$

*and is defined by the vector of parametric inequality constraints $\boldsymbol{g}(\boldsymbol{x};\boldsymbol{\theta})$, $\boldsymbol{g} : \mathbb{R}^n \times \Theta \mapsto \mathbb{R}^r$ and the vector of parametric equality constraints $\boldsymbol{h}(\boldsymbol{x};\boldsymbol{\theta})$, $\boldsymbol{h} : \mathbb{R}^n \times \Theta \mapsto \mathbb{R}^q$. This mapping maps the static task environment parameter vector $\boldsymbol{\theta}$ to the **feasible region** $X(\boldsymbol{\theta})$ of the input space $\mathbb{R}^n$, where the constraints are satisfied.*

$$X(\boldsymbol{\theta}) = \{\boldsymbol{x} \in \mathbb{R}^n \mid \boldsymbol{h}(\boldsymbol{x};\boldsymbol{\theta}) = 0,\, \boldsymbol{g}(\boldsymbol{x};\boldsymbol{\theta}) \leq 0\}, \qquad \boldsymbol{\theta} \in \Theta,$$

Definition 2.2.2. *The **direct model map** $\mathcal{D}$ is a set-valued map, from the space of static task environment parameters Θ to the task decision space $\mathbb{R}^n$,*

$$\mathcal{D} : \Theta \rightrightarrows \mathbb{R}^n$$

and is defined by the parametric objective function $f(\boldsymbol{x};\boldsymbol{\theta})$, $f : \mathbb{R}^n \times \Theta \mapsto \mathbb{R}$, the vector of parametric inequality constraints $\boldsymbol{g}(\boldsymbol{x};\boldsymbol{\theta})$, $\boldsymbol{g} : \mathbb{R}^n \times \Theta \mapsto \mathbb{R}^r$ and the vector of parametric equality constraints $\boldsymbol{h}(\boldsymbol{x};\boldsymbol{\theta})$, $\boldsymbol{h} : \mathbb{R}^n \times \Theta \mapsto \mathbb{R}^q$. This mapping maps a static task environment parameter vector $\boldsymbol{\theta}$ to the set of the inequality and equality-constrained local minima of the function $f(\boldsymbol{x};\boldsymbol{\theta})$.

$$\mathcal{D}(\boldsymbol{\theta}) = \underset{\boldsymbol{x}\in X(\boldsymbol{\theta})}{\operatorname{argmin}} \quad f(\boldsymbol{x};\boldsymbol{\theta})$$

To achieve the goal of IOC, of learning the mapping $\mathcal{D}$ between $\boldsymbol{\theta}$ and $\boldsymbol{y}$ through an OCP (2.2), it is supposed that there are available measurements of pairs $(\boldsymbol{\theta}, \boldsymbol{y})$. The mapping is then indirectly inferred by learning the cost and/or constraint functions. The types of the

cost and constraint functions are described within equation (2.3).

$$f : \mathbb{R}^n \times \mathbb{R}^p \mapsto \mathbb{R} \tag{2.3a}$$
$$\boldsymbol{g} : \mathbb{R}^n \times \mathbb{R}^p \mapsto \mathbb{R}^q \tag{2.3b}$$
$$\boldsymbol{h} : \mathbb{R}^n \times \mathbb{R}^p \mapsto \mathbb{R}^r \tag{2.3c}$$

The set of all continuous cost and constraint functions is infinite-dimensional. As a consequence, one must usually opt for a parametric representation and introduce a vector of parameters $\boldsymbol{\omega}$ to represent a class of cost and constraint functions. The optimal control model is then parametrized by the parameter $\boldsymbol{\omega}$, as is the mapping between the static task external/environment parameters $\boldsymbol{\theta}$ and the decisions $\boldsymbol{y}$, which is shown in equation (2.4).

$$\hat{\boldsymbol{y}}(\boldsymbol{\theta}, \boldsymbol{\omega}) = \underset{\boldsymbol{x} \in X(\boldsymbol{\theta}, \boldsymbol{\omega})}{\operatorname{argmin}} \quad f(\boldsymbol{x}; \boldsymbol{\theta}, \boldsymbol{\omega}) \tag{2.4a}$$
$$\text{subject to} \quad \boldsymbol{g}(\boldsymbol{x}; \boldsymbol{\theta}, \boldsymbol{\omega}) \leq 0 \tag{2.4b}$$
$$\boldsymbol{h}(\boldsymbol{x}; \boldsymbol{\theta}, \boldsymbol{\omega}) = 0 \tag{2.4c}$$

From here on, $\boldsymbol{\omega}$ will be referred to as the task model parameters, $\boldsymbol{\theta}$ as the static task environment parameters, and $\boldsymbol{y}$ as the task output.

The introduction of task model parameters $\boldsymbol{\omega}$ as parameters in the constraint functions of the optimal control model implies that the feasible region of the OCP will depend on it.

Definition 2.2.3. *The **parameteric feasible region map** is a set-valued map $X_{\boldsymbol{\omega}}$, from the space of static task environment parameters Θ to the task decision space $\mathbb{R}^n$, parametrized by the task model parameters $\boldsymbol{\omega} \in \Omega$,*

$$X_{\boldsymbol{\omega}} : \Theta \rightrightarrows \mathbb{R}^n$$

*and is defined by the vector of parametric inequality constraints $\boldsymbol{g}(\boldsymbol{x}; \boldsymbol{\theta}, \boldsymbol{\omega})$, $\boldsymbol{g} : \mathbb{R}^n \times \Theta \times \Omega \mapsto \mathbb{R}^r$ and the vector of parametric equality constraints $\boldsymbol{h}(\boldsymbol{x}; \boldsymbol{\theta}, \boldsymbol{\omega})$, $\boldsymbol{h} : \mathbb{R}^n \times \Theta \times \Omega \mapsto \mathbb{R}^q$. For a given value $\boldsymbol{\omega}$ of the task model parameter vector, this mapping maps static task environment parameters $\boldsymbol{\theta}$ to the subset $X_{\boldsymbol{\omega}}(\boldsymbol{\theta})$ of the input space $\mathbb{R}^n$, called the **parametric feasible region**, where the constraints are satisfied.*

$$X_{\boldsymbol{\omega}}(\boldsymbol{\theta}) = \{\boldsymbol{x} \in \mathbb{R}^n \mid \boldsymbol{h}(\boldsymbol{x}; \boldsymbol{\theta}, \boldsymbol{\omega}) = 0,\, \boldsymbol{g}(\boldsymbol{x}; \boldsymbol{\theta}, \boldsymbol{\omega}) \leq 0\}, \qquad \boldsymbol{\theta} \in \Theta, \quad \boldsymbol{\omega} \in \Omega,$$

Moreover, the direct optimization model map also becomes dependent on the task model parameters. By adjusting task model parameters, we will thus be able to modify the predicted trajectories across all values of the static task environment parameters $\boldsymbol{\theta}$.

Definition 2.2.4. *The **parametric direct optimization model map** $\mathcal{D}_{\boldsymbol{\omega}}$ is a set-valued map, from the space of static task environment parameters Θ to the task decision space $\mathbb{R}^n$, parametrized by the task model parameters $\boldsymbol{\omega} \in \Omega$,*

$$\mathcal{D}_{\boldsymbol{\omega}} : \Theta \rightrightarrows \mathbb{R}^n$$

and is defined by the parametric objective function $f(\boldsymbol{x}; \boldsymbol{\theta}, \boldsymbol{\omega})$, $f : \mathbb{R}^n \times \Theta \times \Omega \mapsto \mathbb{R}$, the vector of parametric inequality constraints $\boldsymbol{g}(\boldsymbol{x}; \boldsymbol{\theta}, \boldsymbol{\omega})$, $\boldsymbol{g} : \mathbb{R}^n \times \Theta \times \Omega \mapsto \mathbb{R}^r$ and the vector of parametric equality constraints $\boldsymbol{h}(\boldsymbol{x}; \boldsymbol{\theta}, \boldsymbol{\omega})$, $\boldsymbol{h} : \mathbb{R}^n \times \Theta \times \Omega \mapsto \mathbb{R}^q$. For a given value $\boldsymbol{\omega}$ of the task model parameter vector, this mapping maps static task environment parameters $\boldsymbol{\theta}$ to the set of the inequality and equality-constrained local minima of the parametrized function

$f(\boldsymbol{x};\boldsymbol{\theta},\boldsymbol{\omega})$, *called the* ***constrained direct optimal decisions****.*

$$\mathcal{D}_{\boldsymbol{\omega}}(\boldsymbol{\theta}) = \underset{\boldsymbol{x}\in X_{\boldsymbol{\omega}}(\boldsymbol{\theta})}{\operatorname{argmin}} \quad f(\boldsymbol{x};\boldsymbol{\theta},\boldsymbol{\omega})$$

2.3 General Inverse Problem

Mathematically, the task model parameters $\boldsymbol{\omega} \in \Omega \subseteq \mathbb{R}^m$ belong to a set $\Omega \subseteq \mathbb{R}^m$ which can be described by a finite number m of scalar quantities. The static task environment parameters $\boldsymbol{\theta} \in \Theta \subseteq \mathbb{R}^p$ belong to a set $\Theta \subseteq \mathbb{R}^p$ which can be described by a finite number p of scalar quantities, while the task output $\boldsymbol{y} \in X(\boldsymbol{\theta},\boldsymbol{\omega}) \subseteq \mathbb{R}^n$ belongs to a set $X(\boldsymbol{\theta},\boldsymbol{\omega}) \subseteq \mathbb{R}^n$ that is dependent on the task model parameters $\boldsymbol{\omega}$ and the static task environment parameters $\boldsymbol{\theta}$ and that can be described by a finite amount n of scalar variables.

With the previously mentioned context, we hope to learn or extract the objective function of the task decision-maker from measurements of its behavior, whether its behavior is truly, or nearly, optimal. At our disposal are measured instances of the task

$$(\boldsymbol{\theta}^{(1)},\boldsymbol{y}^{(1)}),\ldots,(\boldsymbol{\theta}^{(D)},\boldsymbol{y}^{(D)}) \tag{2.5}$$

with varying static task environment parameters and task outputs. Early research in IOC often considered the case when only a single data point was available ($D = 1$) but the class of cost functions considered was fixed (*e.g.* linear, quadratic, ...).

Briefly, the task of IOC is to extract plausible cost and/or constraint functions

$$f(\boldsymbol{x};\boldsymbol{\theta},\boldsymbol{\omega}) : X(\boldsymbol{\theta},\boldsymbol{\omega}) \times \Theta \times \Omega \mapsto \mathbb{R} \tag{2.6a}$$
$$\boldsymbol{g}(\boldsymbol{x};\boldsymbol{\theta},\boldsymbol{\omega}) : X(\boldsymbol{\theta},\boldsymbol{\omega}) \times \Theta \times \Omega \mapsto \mathbb{R}^q \tag{2.6b}$$
$$\boldsymbol{h}(\boldsymbol{x};\boldsymbol{\theta},\boldsymbol{\omega}) : X(\boldsymbol{\theta},\boldsymbol{\omega}) \times \Theta \times \Omega \mapsto \mathbb{R}^r \tag{2.6c}$$

which could have generated an available data set of points (2.5). The parametric representations of the cost and constraint functions reduce the problem of extracting a plausible value for the task model parameters $\boldsymbol{\omega}$, which could have generated the available data set.

Naturally, the concept of **consistency** emerges. One can define the notion of consistency of an optimization problem model for a test point and for a data set (2.5).

Definition 2.3.1. *We say that an optimization problem, defined by its cost function $f(\boldsymbol{x};\boldsymbol{\theta},\boldsymbol{\omega})$, and vector-function constraints $\boldsymbol{g}(\boldsymbol{x};\boldsymbol{\theta},\boldsymbol{\omega})$ and $\boldsymbol{h}(\boldsymbol{x};\boldsymbol{\theta},\boldsymbol{\omega})$ defining the feasible set $X(\boldsymbol{\theta},\boldsymbol{\omega})$, is* ***consistent with a test point*** *$(\boldsymbol{\theta},\boldsymbol{y})$ if*

$$\boldsymbol{y} = \underset{\boldsymbol{x}\in X(\boldsymbol{\theta},\boldsymbol{\omega})}{\operatorname{argmin}} f(\boldsymbol{x};\boldsymbol{\theta},\boldsymbol{\omega}) \tag{2.7}$$

We also say that a value of the task model parameter $\boldsymbol{\omega}$ is ***consistent with the test point*** *$(\boldsymbol{\theta},\boldsymbol{y})$ if the previous affirmation holds.*

Definition 2.3.2. *We say that an optimization problem, defined by its cost function $f(\boldsymbol{x};\boldsymbol{\theta},\boldsymbol{\omega})$, and vector-function constraints $\boldsymbol{g}(\boldsymbol{x};\boldsymbol{\theta},\boldsymbol{\omega})$ and $\boldsymbol{h}(\boldsymbol{x};\boldsymbol{\theta},\boldsymbol{\omega})$ defining the collection of feasible sets $X(\boldsymbol{\theta}^{(1)},\boldsymbol{\omega}),\ldots,X(\boldsymbol{\theta}^{(D)},\boldsymbol{\omega})$, is* ***consistent with the data-set*** *$(\boldsymbol{\theta}^{(1)},\boldsymbol{y}^{(1)}),\ldots,(\boldsymbol{\theta}^{(D)},\boldsymbol{y}^{(D)})$ if*

$$\boldsymbol{y}^{(d)} = \underset{\boldsymbol{x}\in X(\boldsymbol{\theta}^{(d)},\boldsymbol{\omega})}{\operatorname{argmin}} f(\boldsymbol{x};\boldsymbol{\theta}^{(d)},\boldsymbol{\omega}), \quad d = 1,\ldots,D \tag{2.8}$$

We also say that a value of the task model parameter $\boldsymbol{\omega}$ *is* ***consistent with the data-set*** $(\boldsymbol{\theta}^{(1)}, \boldsymbol{y}^{(1)}), \ldots, (\boldsymbol{\theta}^{(D)}, \boldsymbol{y}^{(D)})$ *if the previous affirmation holds.*

Section 2.5 will be dedicated to verifying consistency.

Often, we cannot find a value for the parameter $\boldsymbol{\omega}$ that is consistent with our data set (2.5). The reason why is well formulated by Aswani, Shen, and Siddiq (2018) [120]. Real-world data is noisy because

1. the data collection introduces measurement noise,
2. the decision-maker deviates from optimal decisions,
3. there is a mismatch between the parametric form of the model and the true underlying decision-making process.

IOC with actual data is therefore done by minimizing a cumulated loss function $\sum_{d=1}^{D} \ell(\boldsymbol{\omega}, \boldsymbol{y}^{(d)}, \hat{\boldsymbol{y}}^{(d)})$ over the data-set, and represents a sort of regression. The general formulation of an IOC problem is given in equation (2.9).

$$\hat{\boldsymbol{\omega}} = \underset{\boldsymbol{\omega} \in \Omega}{\operatorname{argmin}} \quad \sum_{d=1}^{D} \ell(\boldsymbol{\omega}, \boldsymbol{y}^{(d)}, \hat{\boldsymbol{y}}^{(d)}) \tag{2.9a}$$

$$\text{subject to} \quad \hat{\boldsymbol{y}}^{(d)} = \underset{\boldsymbol{x} \in \mathbb{R}^n}{\operatorname{argmin}} \quad f(\boldsymbol{x}; \boldsymbol{\theta}^{(d)}, \boldsymbol{\omega}), \qquad d = 1, \ldots, D \tag{2.9b}$$

$$\text{subject to} \quad \boldsymbol{g}(\boldsymbol{x}; \boldsymbol{\theta}, \boldsymbol{\omega}) \leq 0 \tag{2.9c}$$

$$\boldsymbol{h}(\boldsymbol{x}; \boldsymbol{\theta}, \boldsymbol{\omega}) = 0 \tag{2.9d}$$

A graphical description of the IOC process with loss function is given in Figure 2.2.

Definition 2.3.3. *The* ***inverse optimization map*** $\mathcal{I}[(\boldsymbol{\theta}^{(1)}, \boldsymbol{y}^{(1)}), \ldots, (\boldsymbol{\theta}^{(D)}, \boldsymbol{y}^{(D)})]$ *is a set-valued map, from the space of the data set* $\underbrace{(\Theta \times \mathbb{R}^n) \times \ldots \times (\Theta \times \mathbb{R}^n)}_{D}$ *to the space of task model parameters* Ω,

$$\mathcal{I} : \underbrace{(\Theta \times \mathbb{R}^n) \times \ldots \times (\Theta \times \mathbb{R}^n)}_{D} \rightrightarrows \Omega$$

and is defined by the direct parametric optimization problem (2.4) through its objective function $f(\boldsymbol{x}; \boldsymbol{\theta}, \boldsymbol{\omega})$, $f : \mathbb{R}^n \times \Theta \times \Omega \mapsto \mathbb{R}$, *its vector of parametric inequality constraints* $\boldsymbol{g}(\boldsymbol{x}; \boldsymbol{\theta}, \boldsymbol{\omega})$, $\boldsymbol{g} : \mathbb{R}^n \times \Theta \times \Omega \mapsto \mathbb{R}^r$ *and its vector of parametric equality constraints* $\boldsymbol{h}(\boldsymbol{x}; \boldsymbol{\theta}, \boldsymbol{\omega})$, $\boldsymbol{h} : \mathbb{R}^n \times \Theta \times \Omega \mapsto \mathbb{R}^q$. *It is also defined by the inverse optimization loss function* $\ell(\boldsymbol{\omega}, \boldsymbol{y}^{(d)}, \hat{\boldsymbol{y}}^{(d)})$. *This mapping maps the measured data set* $(\boldsymbol{\theta}^{(1)}, \boldsymbol{y}^{(1)}), \ldots (\boldsymbol{\theta}^{(D)}, \boldsymbol{y}^{(D)})$ *to the task model parameters* $\boldsymbol{\omega}$ *producing the least cumulative loss across the data set.*

$$\mathcal{I}[(\boldsymbol{\theta}^{(1)}, \boldsymbol{y}^{(1)}), \ldots, (\boldsymbol{\theta}^{(D)}, \boldsymbol{y}^{(D)})] = \left\{ \boldsymbol{\omega} \in \Omega \;\middle|\; \boldsymbol{\omega} \text{ solves (2.9)} \right\} \tag{2.10}$$

Section 2.4 will treat the most common direct optimization model structure treated in the literature. The general form is given by equation (2.4). Section 2.5 will explain how one can verify the consistency of the direct optimization models described in Section 2.4. Section 2.6 will explain two different choices for the loss function $\ell(\boldsymbol{\omega}, \boldsymbol{y}^{(d)}, \hat{\boldsymbol{y}}^{(d)})$, the properties of the solutions of the problem with those loss functions, and the solution methods.

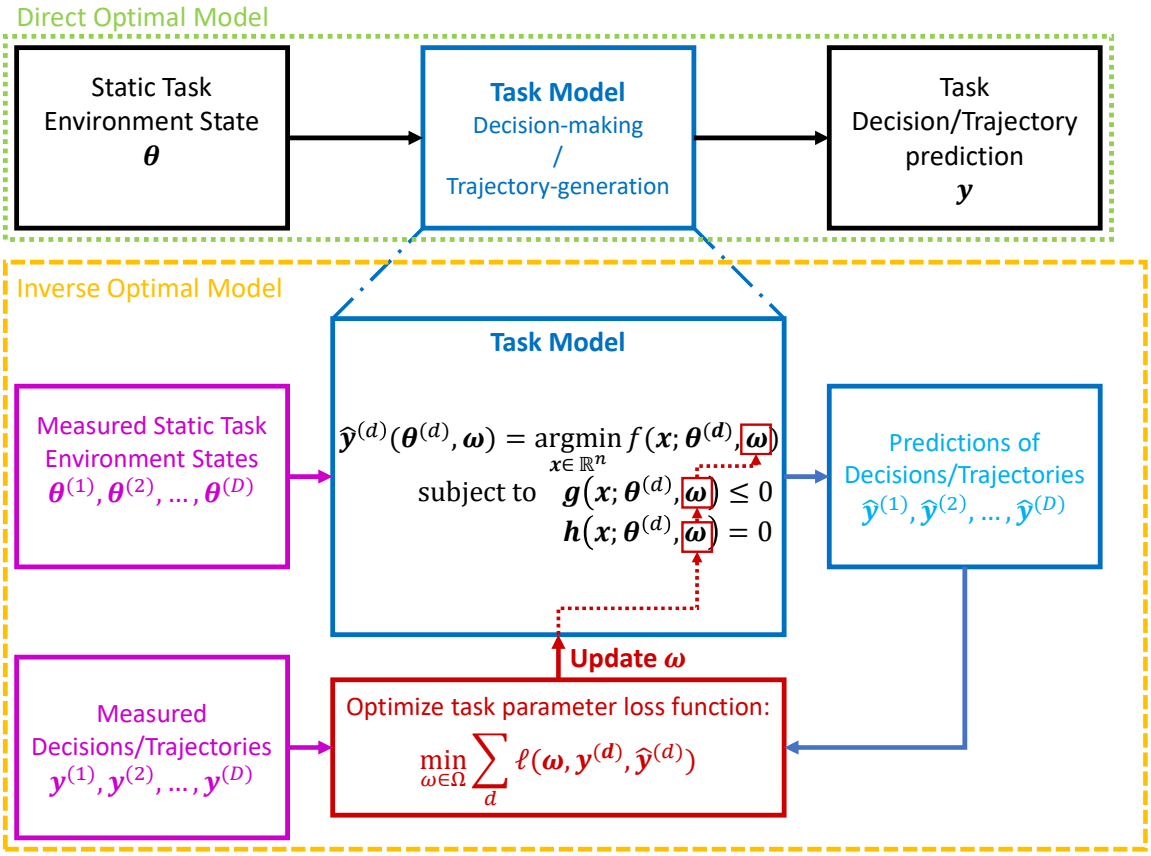

Figure 2.2: Simple schematic of the optimization-based trajectory prediction process and the inverse optimization-based identification.

2.4 Direct and Inverse Optimal Control

The most common parametrization found in the literature for inverse optimization, particularly in motion-generation tasks [69, 72, 77, 78, 84, 102, 108, 111, 115, 118, 122, 127, 132, 135, 143], will be presented in this section. This parametrization assumes that constraints represent some known physical limitations of the task and are thus known in advance. This implies that the number of constraint functions q and r, as well as the constraint functions themselves, $\boldsymbol{h}$ and $\boldsymbol{g}$ do not depend on the parameter $\boldsymbol{\omega}$, as is shown below.

$$\begin{aligned} \boldsymbol{g}(\boldsymbol{x}; \boldsymbol{\theta}, \boldsymbol{\omega}) &= \boldsymbol{g}(\boldsymbol{x}; \boldsymbol{\theta}) \in \mathbb{R}^q & \qquad q(\boldsymbol{\omega}) &= q \\ \boldsymbol{h}(\boldsymbol{x}; \boldsymbol{\theta}, \boldsymbol{\omega}) &= \boldsymbol{h}(\boldsymbol{x}; \boldsymbol{\theta}) \in \mathbb{R}^r & \qquad r(\boldsymbol{\omega}) &= r \end{aligned}$$

The goal will be to find the objective function $f(\boldsymbol{x}; \boldsymbol{\theta})$. If the objective function is considered in its non-parametric form, the set of conceivable functions $f(\boldsymbol{x}; \boldsymbol{\theta}) : X(\boldsymbol{\theta}) \times \boldsymbol{\theta} \mapsto \mathbb{R}$ is an infinite-dimensional vector space, and is increasingly difficult to represent as the dimensions of $\boldsymbol{x}$ and $\boldsymbol{\theta}$ increase. Because this set is so large, many trivial solutions exist, and finding a proper solution is complex and redundant as infinitely many consistent solutions can be constructed from a single one. These two problems can be identified:

1. **Curse of dimensionality** The simplest way to represent a general function $f(\boldsymbol{x}; \boldsymbol{\theta})$ in a non-parametric way is to grid the input space $(\boldsymbol{x}, \boldsymbol{\theta})$ and assign a value for each grid point. This way of non-parametric function representation is subject to the curse of dimensionality, meaning that the complexity of this representation increases exponentially with the number of dimensions of the input space.

2. **Existence of trivial solutions** The problem is ill-posed in the general sense, as there are infinitely many (trivial) solutions to this problem. Namely, as long as a data point $\boldsymbol{x}$ is feasible with respect to its constraints $\boldsymbol{g}$ and $\boldsymbol{h}$, it is optimal with respect to a constant cost function $f = c$.

3. **Redundancy of non-trivial solutions** Moreover, even when a non-constant cost function f is identified, for which a given $\boldsymbol{y}$ is optimal, $\boldsymbol{y}$ will also be optimal with respect to the composition $\gamma \circ f$ of that function with any convex non-decreasing function $\gamma : \mathbb{R} \mapsto \mathbb{R}$, of which there are infinitely many.

To solve the curse of dimensionality problem, it is customary to adopt a parametric representation for the function $f(\boldsymbol{x}; \boldsymbol{\theta}) = f(\boldsymbol{x}; \boldsymbol{\theta}, \boldsymbol{\omega})$. The most common is the weighted basis function parametrization, given in equation (2.12). A key role in IOC is played by the basis function vector $\boldsymbol{\phi} = (\phi_1, \ldots, \phi_m)$, and choosing the best basis function vector, or even a sufficiently good basis function vector, is an unsolved problem in the field. A study on quantifying the quality of a chosen vector of basis functions will be discussed in Chapter 3. Once a basis function vector $\boldsymbol{\phi}$ is chosen, the objective function is treated as a linear combination of the basis function vector components. This is equivalent to applying the scalarization technique [26, 68] to a multi-objective optimization problem with the vector objective equal to $\boldsymbol{\phi}$, which is why this is sometimes referred to as Inverse Multiobjective Optimization [140].

$$f = \sum_{i=1}^{m} \omega_i \phi_i = \boldsymbol{\omega}^T \boldsymbol{\phi} \tag{2.12}$$

In this nonconstrained state, where $\omega_i \in \mathbb{R},\ i = 1, \ldots, m$, this parametrization still suffers from the existence of trivial solutions and the redundancy of non-trivial solutions.

1. **Existence of trivial solutions** The weighted sum of basis functions still contains a trivial solution. Namely, as long as a data point $\boldsymbol{x}$ is feasible with respect to its constraints $\boldsymbol{g}$ and $\boldsymbol{h}$, it is optimal with respect to the parametrization $\boldsymbol{\omega} = \boldsymbol{0}$.

   The basis may also contain two basis functions ϕ_i and ϕ_j $(i \neq j)$ which are affinely related $\phi_i = c\phi_j + d$. A trivial non-zero solution may then be to set $\boldsymbol{\omega}$ according to the relation

$$\omega_k = \begin{cases} 0, & k \neq i, j \\ -c, & k = i \\ 1, & k = j \end{cases}$$

2. **Redundancy of non-trivial solutions** Moreover, even when a parameter $\boldsymbol{\omega}$ describing cost function f for which a given $\boldsymbol{y}$ is optimal is identified, $\boldsymbol{y}$ will also be optimal with respect to $f' = c \cdot f$ corresponding to parameter $\boldsymbol{\omega}' = c \cdot \boldsymbol{\omega},\ c \geq 0$.

Assuming that the basis functions are chosen such that no two basis functions ϕ_i and ϕ_j $(i \neq j)$ are affinely related $\phi_i = c\phi_j + d$ we can resolve both the trivial solution problem and redundancy problem by fixing the L_1 or the L_2 norm of the parameter vector to 1 [74, 102],

$$\sum_{i=1}^{m} |\omega_i| = 1, \qquad \sum_{i=1}^{m} |\omega_i|^2 = 1,$$

or to fix a particular basis function ϕ_i weight $\omega_i = 1$ to one. To preserve the local convexity of the basis functions, the parameters are frequently constrained to be non-negative $\omega_i \geq 0,\ i = 1..m$. In this thesis, the consideration will be narrowed to the parameter non-negativity

condition and the L_1-norm condition. Together, these two conditions yield the **probability-simplex** condition described in equation (2.13).

$$\boldsymbol{\omega} \in \Delta^m \iff \omega_i \geq 0,\ i = 1, \ldots, m \qquad \text{and} \qquad \sum_{i=1}^{m} \omega_i = 1 \tag{2.13}$$

The goal of the inverse optimization problem then becomes identifying the parameter $\omega \in \Delta^m$ corresponding to a given vector $\boldsymbol{\phi}$ of basis functions $\phi_i,\ i = 1..m$, which is consistent with a particular test point, or with a data-set (2.5). The inverse problem is sometimes referred to as inverse multi-objective optimization [140].

The rest of this text will focus on this parametric manner of treating inverse optimization, referred to as IOC.

Given a vector of basis objective functions $\boldsymbol{\phi} = (\phi_1, \ldots, \phi_m)$, a vector of fixed inequality constraint functions $\boldsymbol{g} = (g_1, \ldots, g_r)$ and a vector of fixed equality constraints $\boldsymbol{h} = (h_1, \ldots, h_q)$ we can formally define a **direct optimization** model and an **inverse optimization** model. Consider all mentioned functions to be maps of type $\mathbb{R}^n \times \Theta \mapsto \mathbb{R}$ that are continuous and twice continuously differentiable.

Considering the discussion in the previous section, we can formulate the direct optimization model in Equation (2.14).

$$\hat{\boldsymbol{y}}(\boldsymbol{\omega}, \boldsymbol{\theta}) = \underset{\boldsymbol{x} \in \mathbb{R}^n}{\operatorname{argmin}} \quad f(\boldsymbol{x}; \boldsymbol{\theta}, \boldsymbol{\omega}) = \sum_{i=1}^{m} \omega_i \phi_i(\boldsymbol{x}; \boldsymbol{\theta}) \tag{2.14a}$$

$$\text{subject to} \quad \boldsymbol{g}(\boldsymbol{x}; \boldsymbol{\theta}) \leq 0 \tag{2.14b}$$

$$\boldsymbol{h}(\boldsymbol{x}; \boldsymbol{\theta}) = 0 \tag{2.14c}$$

All these concepts are defined with respect to a particular vector of basis functions $\boldsymbol{\phi}$, and particular vectors of inequality and equality constraint functions $\boldsymbol{g}$ and $\boldsymbol{h}$.

2.5 Verifying Inverse Optimality

Verifying if a data-point $(\boldsymbol{\theta}, \boldsymbol{y})$ is consistent with our direct optimization model (2.14) can be simple in the convex unconstrained case but more complicated in the non-convex constrained case. We will define the concept of **exact inverse optimality**, which is complementary to the idea of consistency defined in definitions 2.3.1 and 2.3.2. This section will present formulations for the problem of finding a consistent parameter $\boldsymbol{\omega}$ for the direct optimization model (2.14), for both convex and non-convex, and both constrained and unconstrained formulations of the direct optimization problem. In the convex case, both constrained and unconstrained, the verification/feasibility of exact inverse optimization can be expressed as a Linear Programming (LP). For the non-convex case, the verification/feasibility of exact inverse optimization can be expressed as a Conic Program.

Given a vector of basis functions $\boldsymbol{\phi} = (\phi_1, \ldots, \phi_m)$, an inequality constraint function vector $\boldsymbol{g} = (g_1, \ldots, g_r)$, and arbitrary equality constraint functions $\boldsymbol{h} = (h_1, \ldots, h_q)$, we can conceive a direct optimization model $\mathcal{D}_{\boldsymbol{\omega}} : \Theta \rightrightarrows \mathbb{R}^n$ by referring to equation (2.14) and definition 2.2.2.

Definition 2.5.1. *A measurement $(\boldsymbol{\theta}, \boldsymbol{y}) \in \Theta \times \mathbb{R}^n$ is said to be exactly inversely optimal with respect to a direct optimization model (2.14) if there exists a parameter $\boldsymbol{\omega} \in \Delta^m$ that is consistent with it.*

2.5.1 Convex Unconstrained Case

Let the vector of basis functions be $\boldsymbol{\phi} = (\phi_1, \ldots, \phi_m)$, and let every member ϕ_i be convex. Moreover, let there be no inequality and equality constraints *i.e.* $\boldsymbol{g} = \emptyset$ and $\boldsymbol{h} = \emptyset$. Checking whether a given pair $(\boldsymbol{\theta}, \boldsymbol{y}) \in \Theta \times \mathbb{R}^n$ is exactly inversely optimal for the direct optimization model defined by $\boldsymbol{\phi}$, means checking if there exists an $\boldsymbol{\omega} \in \Delta^m$ such that $\boldsymbol{y} = \operatorname{argmin}_{\boldsymbol{x} \in \mathbb{R}^n} f(\boldsymbol{x}; \boldsymbol{\theta}, \boldsymbol{\omega})$, where $f(\boldsymbol{x}; \boldsymbol{\theta}, \boldsymbol{\omega}) = \sum_{i=1}^m \omega_i \phi_i(\boldsymbol{x}; \boldsymbol{\theta})$. As $\nabla_{\boldsymbol{x}} f(\boldsymbol{x}; \boldsymbol{\theta}, \boldsymbol{\omega}) = \mathbf{0}$ is a necessary and sufficient condition for global (thus local) optimality, it is only necessary to solve the following query problem

$$\operatorname*{find}_{\omega \in \Delta^m} \text{ s.t. } \nabla_{\boldsymbol{x}} f(\boldsymbol{x}; \boldsymbol{\theta}, \boldsymbol{\omega}) = \mathbf{0}. \tag{2.15}$$

Because of the linearity of the gradient, due to the affine parameterization (2.14),

$$\nabla_{\boldsymbol{x}} f(\boldsymbol{y}; \boldsymbol{\theta}, \boldsymbol{\omega}) = \sum_{i=1}^m \omega_i \nabla_{\boldsymbol{x}} \phi_i(\boldsymbol{y}; \boldsymbol{\theta}) = \begin{bmatrix} \nabla_{\boldsymbol{x}} \phi_1(\boldsymbol{y}; \boldsymbol{\theta}) & \ldots & \nabla_{\boldsymbol{x}} \phi_m(\boldsymbol{y}; \boldsymbol{\theta}) \end{bmatrix} \boldsymbol{\omega} = \nabla_{\boldsymbol{x}} \boldsymbol{\phi}(\boldsymbol{y}; \boldsymbol{\theta}) \boldsymbol{\omega} \tag{2.16}$$

the query problem in (2.15) reduces to a LP.

$$\begin{aligned} \min_{\boldsymbol{\omega} \in \Delta^m} \quad & 0 \\ \text{subject to} \quad & \nabla_{\boldsymbol{x}} \boldsymbol{\phi}(\boldsymbol{y}; \boldsymbol{\theta}) \boldsymbol{\omega} = 0 \end{aligned} \tag{2.17}$$

2.5.2 Convex Constrained Case

Let the vector of basis functions be $\boldsymbol{\phi} = (\phi_1, \ldots, \phi_m)$, and let every member ϕ_i be convex. Let the vector of inequality constraint functions be $\boldsymbol{g} = (g_1, \ldots, g_r)$, and let every member g_j be convex. Let the vector of equality constraint functions be $\boldsymbol{h} = (h_1, \ldots, h_q)$, and let every member h_k be affine. Checking whether a given pair $(\boldsymbol{\theta}, \boldsymbol{y}) \in \Theta \times \mathbb{R}^n$ is exactly inversely optimal for the direct optimization model defined by $\boldsymbol{\phi}$, $\boldsymbol{g}$, and $\boldsymbol{h}$ means checking if there exists an $\boldsymbol{\omega} \in \Delta^m$ such that $\boldsymbol{y} = \operatorname{argmin}_{\boldsymbol{x} \in X(\boldsymbol{\theta})} f(\boldsymbol{x}; \boldsymbol{\theta}, \boldsymbol{\omega})$, where $f(\boldsymbol{x}; \boldsymbol{\theta}, \boldsymbol{\omega}) = \sum_{i=1}^m \omega_i \phi_i(\boldsymbol{x}; \boldsymbol{\theta})$ and $X(\boldsymbol{\theta})$ is the feasible set defined by $\boldsymbol{g}$ and $\boldsymbol{h}$. Here, too, it becomes only necessary to solve a query problem, but the query problem is harder to formulate and requires stating the KKT conditions. The first-order KKT conditions are given in equation (2.18),

$$\exists \boldsymbol{\lambda} \in \mathbb{R}^q, \ \boldsymbol{\mu} \in \mathbb{R}^r \tag{2.18a}$$
$$\nabla_{\boldsymbol{x}} \mathcal{L}_(\boldsymbol{y}, \boldsymbol{\lambda}, \boldsymbol{\mu}; \boldsymbol{\theta}, \boldsymbol{\omega}) = \mathbf{0} \tag{2.18b}$$
$$\boldsymbol{h}(\boldsymbol{y}; \boldsymbol{\theta}) = 0 \tag{2.18c}$$
$$\boldsymbol{\mu} \odot \boldsymbol{g}(\boldsymbol{x}) = 0 \tag{2.18d}$$
$$\boldsymbol{g}(\boldsymbol{y}; \boldsymbol{\theta}) \leq 0, \tag{2.18e}$$
$$\boldsymbol{\mu} \geq 0, \tag{2.18f}$$

while the Linear Independence Constraint Qualification (LICQ) is formulated in equation (2.19),

$$\operatorname{rank}([\nabla_{\boldsymbol{x}} \boldsymbol{h}(\boldsymbol{y}; \boldsymbol{\theta}) \ \nabla_{\boldsymbol{x}} \boldsymbol{g}_A(\boldsymbol{y}; \boldsymbol{\theta})]) = q + r_A, \ r_A = |I_A(\boldsymbol{y})|, \tag{2.19}$$

where $I_A(\boldsymbol{y}) = \{j \mid g_j(\boldsymbol{y}; \boldsymbol{\theta}) = 0\}$ is the index-set of active inequality constraints, and $\boldsymbol{g}_A(\boldsymbol{y}; \boldsymbol{\theta}) = \{g_j(\boldsymbol{y}; \boldsymbol{\theta}) \mid j \in I_A(\boldsymbol{y})\}$ is the set of active inequality constraints for a particular

feasible point $\boldsymbol{y}$.

Because of the convexity of members of $\boldsymbol{\phi}$ and $\boldsymbol{g}$, and affinity of members of $\boldsymbol{h}$, the KKT conditions along with the LICQ are necessary and sufficient conditions for global (thus local) optimality, therefore it is only necessary to solve the following query problem for $\boldsymbol{\omega}$, $\boldsymbol{\lambda}$ and $\boldsymbol{\mu}$, with $\mathcal{W} = \Delta^m \times \mathbb{R}^q \times \mathbb{R}^r_+$,

$$\begin{aligned} \underset{(\boldsymbol{\omega},\boldsymbol{\lambda},\boldsymbol{\mu})\in\mathcal{W}}{\text{find}} \quad \text{s.t.} \quad & \nabla_{\boldsymbol{x}}\mathcal{L}(\boldsymbol{y},\boldsymbol{\lambda},\boldsymbol{\mu};\boldsymbol{\theta},\boldsymbol{\omega}) = 0 \\ & \boldsymbol{\mu} \odot \boldsymbol{g}(\boldsymbol{y};\boldsymbol{\theta}) = 0 \end{aligned} \tag{2.20}$$

assuming that the rest of the KKT conditions and the LICQ are satisfied for $(\boldsymbol{\theta},\boldsymbol{y}) \in \Theta \times \mathbb{R}^n$:

$$\begin{aligned} & \boldsymbol{h}(\boldsymbol{y};\boldsymbol{\theta}) = 0 \\ & \boldsymbol{g}(\boldsymbol{y};\boldsymbol{\theta}) \leq 0 \\ & \text{rank}([\nabla_{\boldsymbol{x}}\boldsymbol{h}(\boldsymbol{y};\boldsymbol{\theta})\ \nabla_{\boldsymbol{x}}\boldsymbol{g}_A(\boldsymbol{y};\boldsymbol{\theta})]) = q + r_A,\ r_A = |I_A(\boldsymbol{y})| \end{aligned} \tag{2.21}$$

.

Because of the linearity of the gradient due to the affine parameterization (2.14),

$$\begin{aligned} \nabla_{\boldsymbol{x}}\mathcal{L}(\boldsymbol{y},\boldsymbol{\lambda},\boldsymbol{\mu};\boldsymbol{\theta},\boldsymbol{\omega}) &= \sum_{i=1}^{m}\omega_i\nabla_{\boldsymbol{x}}\phi_i(\boldsymbol{y};\boldsymbol{\theta}) + \sum_{j=1}^{q}\lambda_j\nabla_{\boldsymbol{x}}h_j(\boldsymbol{y};\boldsymbol{\theta}) + \sum_{k=1}^{r}\mu_k\nabla_{\boldsymbol{x}}g_k(\boldsymbol{y};\boldsymbol{\theta}) \\ &= [\nabla_{\boldsymbol{x}}\boldsymbol{\phi}(\boldsymbol{y};\boldsymbol{\theta})\ \nabla_{\boldsymbol{x}}\boldsymbol{h}(\boldsymbol{y};\boldsymbol{\theta})\ \nabla_{\boldsymbol{x}}\boldsymbol{g}(\boldsymbol{y};\boldsymbol{\theta})] \begin{bmatrix}\boldsymbol{\omega}\\ \boldsymbol{\lambda}\\ \boldsymbol{\mu}\end{bmatrix} \end{aligned} \tag{2.22}$$

and the independence of $\boldsymbol{g}(\boldsymbol{y};\boldsymbol{\theta})$ with respect to the parameters $\boldsymbol{\omega}$, $\boldsymbol{\lambda}$, and $\boldsymbol{\mu}$,

$$\boldsymbol{\mu} \odot \boldsymbol{g}(\boldsymbol{y};\boldsymbol{\theta}) = \text{diag}(\boldsymbol{g}(\boldsymbol{y};\boldsymbol{\theta}))\boldsymbol{\mu} = [0\ 0\ \text{diag}(\boldsymbol{g}(\boldsymbol{y};\boldsymbol{\theta}))] \begin{bmatrix}\boldsymbol{\omega}\\ \boldsymbol{\lambda}\\ \boldsymbol{\mu}\end{bmatrix} \tag{2.23}$$

the query problem in (2.20) reduces to a LP.

$$\begin{aligned} \min_{(\boldsymbol{\omega},\boldsymbol{\lambda},\boldsymbol{\mu})\in\mathcal{W}} \quad & 0 \\ \text{subject to} \quad & [\nabla_{\boldsymbol{x}}\boldsymbol{\phi}(\boldsymbol{y};\boldsymbol{\theta})\ \nabla_{\boldsymbol{x}}\boldsymbol{h}(\boldsymbol{y};\boldsymbol{\theta})\ \nabla_{\boldsymbol{x}}\boldsymbol{g}(\boldsymbol{y};\boldsymbol{\theta})] \begin{bmatrix}\boldsymbol{\omega}\\ \boldsymbol{\lambda}\\ \boldsymbol{\mu}\end{bmatrix} = 0 \\ & [0\ 0\ \text{diag}(\boldsymbol{g}(\boldsymbol{y};\boldsymbol{\theta}))] \begin{bmatrix}\boldsymbol{\omega}\\ \boldsymbol{\lambda}\\ \boldsymbol{\mu}\end{bmatrix} = 0 \end{aligned} \tag{2.24}$$

2.5.3 Non-Convex Unconstrained Case

Let the vector of basis functions be $\boldsymbol{\phi} = (\phi_1, \ldots, \phi_m)$, and let at least one member ϕ_i be non-convex. Moreover, let there be no inequality and equality constraints *i.e.* $\boldsymbol{g} = \emptyset$ and $\boldsymbol{h} = \emptyset$. Checking whether a given pair $(\boldsymbol{\theta},\boldsymbol{y}) \in \Theta \times \mathbb{R}^n$ is exactly inversely optimal for the direct optimization model defined by $\boldsymbol{\phi}$, means checking if there exists an $\boldsymbol{\omega} \in \Delta^m$ such that $\boldsymbol{y} = \text{argmin}_{\boldsymbol{x}\in\mathbb{R}^n} f(\boldsymbol{x};\boldsymbol{\theta},\boldsymbol{\omega})$, where $f(\boldsymbol{x};\boldsymbol{\theta},\boldsymbol{\omega}) = \sum_{i=1}^{m}\omega_i\phi_i(\boldsymbol{x};\boldsymbol{\theta})$. As $\nabla_{\boldsymbol{x}}f(\boldsymbol{x};\boldsymbol{\theta},\boldsymbol{\omega}) = 0$ and $\nabla^2_{xx}f(\boldsymbol{x};\boldsymbol{\theta},\boldsymbol{\omega}) > 0$ ($\Leftrightarrow \exists\delta > 0 : \nabla^2_{xx}f(\boldsymbol{x};\boldsymbol{\theta},\boldsymbol{\omega}) - \delta I \geq 0$) are sufficient conditions for local optimality, it is also sufficient to solve the following query problem for $\boldsymbol{\omega}$ and δ

$$\begin{aligned} \underset{(\boldsymbol{\omega},\delta)\in\Delta^m\times R_{++}}{\text{find}} \quad \text{s.t.} \quad & \nabla_{\boldsymbol{x}} f(\boldsymbol{y};\boldsymbol{\theta},\boldsymbol{\omega}) = 0 \\ & \nabla^2_{xx} f(\boldsymbol{y};\boldsymbol{\theta},\boldsymbol{\omega}) - \delta I \geq 0 \end{aligned} \tag{2.25}$$

Because of the linearity of the gradient and the hessian, due to the affine parameterization (2.14),

$$\nabla_{\boldsymbol{x}} f(\boldsymbol{y};\boldsymbol{\theta},\boldsymbol{\omega}) = \sum_{i=1}^{m} \omega_i \nabla_{\boldsymbol{x}} \phi_i(\boldsymbol{y};\boldsymbol{\theta}) \tag{2.26a}$$

$$\nabla^2_{xx} f(\boldsymbol{y};\boldsymbol{\theta},\boldsymbol{\omega}) = \sum_{i=1}^{m} \omega_i \nabla^2_{xx} \phi_i(\boldsymbol{y};\boldsymbol{\theta}) \tag{2.26b}$$

the query in (2.25) reduces to a conic programming problem (with the introduction of $\boldsymbol{Q}$ as a matrix variable from the space of symmetric $n \times n$ matrices $\mathbb{S}^n$).

$$\begin{aligned} \underset{(\boldsymbol{Q},\boldsymbol{\omega},\delta)\ \in\ \mathbb{S}^n\times\Delta^m\times\mathbb{R}_{++}}{\min} \quad & 0 \\ \text{subject to} \quad & [\nabla_{\boldsymbol{x}} \boldsymbol{\phi}(\boldsymbol{y};\boldsymbol{\theta})]\,\boldsymbol{\omega} = 0 \\ & \boldsymbol{Q} = \sum_{i=1}^{m} \omega_i \nabla^2_{xx} \phi_i(\boldsymbol{y};\boldsymbol{\theta}) \\ & \boldsymbol{Q} - \delta I \geq 0 \end{aligned} \tag{2.27}$$

2.5.4 Non-Convex Constrained Case

Let the vector of basis functions be $\boldsymbol{\phi} = (\phi_1, \ldots, \phi_m)$. Let the vector of inequality constraint functions be $\boldsymbol{g} = (g_1, \ldots, g_r)$. Let the vector of equality constraint functions be $\boldsymbol{h} = (h_1, \ldots, h_q)$. Let at least one of the following be true (i) at least one ϕ_i is non-convex (ii) at least one g_j is non-convex (iii) at least one h_k is non-affine. Checking whether a given pair $(\boldsymbol{\theta}, \boldsymbol{y}) \in \Theta \times \mathbb{R}^n$ is exactly inversely optimal for the direct optimization model defined by $\boldsymbol{\phi}$, $\boldsymbol{g}$, and $\boldsymbol{h}$ means checking if there exists an $\boldsymbol{\omega} \in \Delta^m$ such that $y = \operatorname{argmin}_{\boldsymbol{x}\in X(\boldsymbol{\theta})} f(\boldsymbol{x};\boldsymbol{\theta},\boldsymbol{\omega})$, where $f(\boldsymbol{x};\boldsymbol{\theta},\boldsymbol{\omega}) = \sum_{i=1}^{m} \omega_i \phi_i(\boldsymbol{x})$ and $X(\boldsymbol{\theta})$ is the feasible set defined by $\boldsymbol{g}$ and $\boldsymbol{h}$. The first-order KKT conditions along with the LICQ are given in (2.18) and (2.19).

The second order KKT condition is

$$\forall \boldsymbol{d} \in \mathcal{N}([\nabla_{\boldsymbol{x}} \boldsymbol{h}(\boldsymbol{y};\boldsymbol{\theta})\ \nabla_{\boldsymbol{x}} \boldsymbol{g}_A(\boldsymbol{y};\boldsymbol{\theta})]^T) \qquad \boldsymbol{d}^T \nabla^2_{xx} \mathcal{L}(\boldsymbol{x},\boldsymbol{\lambda},\boldsymbol{\mu};\boldsymbol{\theta},\boldsymbol{\omega})\boldsymbol{d} > 0. \tag{2.28}$$

which we can substitute with the stronger condition

$$\nabla^2_{xx} \mathcal{L}(\boldsymbol{x},\boldsymbol{\lambda},\boldsymbol{\mu};\boldsymbol{\theta},\boldsymbol{\omega}) > 0 \quad \Leftrightarrow \quad \exists \delta > 0 : \nabla^2_{xx} \mathcal{L}(\boldsymbol{x},\boldsymbol{\lambda},\boldsymbol{\mu};\boldsymbol{\theta},\boldsymbol{\omega}) - \delta I \geq 0. \tag{2.29}$$

As the first-order KKT conditions along with the LICQ and the second-order KKT condition are necessary and sufficient condition for local optimality, it is only necessary to solve the following query problem for $\boldsymbol{\omega}$, $\boldsymbol{\lambda}$, $\boldsymbol{\mu}$, and δ with $\mathcal{W}^c = \Delta^m \times \mathbb{R}^q \times \mathbb{R}^r_+ \times R_{++}$,

$$\begin{aligned} \underset{(\boldsymbol{\omega},\boldsymbol{\lambda},\boldsymbol{\mu},\delta)\in\mathcal{W}^c}{\text{find}} \quad \text{s.t.} \quad & \nabla_{\boldsymbol{x}} \mathcal{L}(\boldsymbol{y},\boldsymbol{\lambda},\boldsymbol{\mu};\boldsymbol{\theta},\boldsymbol{\omega}) = 0 \\ & \boldsymbol{\mu} \odot \boldsymbol{g}(\boldsymbol{y};\boldsymbol{\theta}) = 0 \\ & \nabla^2_{xx} \mathcal{L}(\boldsymbol{x},\boldsymbol{\lambda},\boldsymbol{\mu};\boldsymbol{\theta},\boldsymbol{\omega}) - \delta I \geq 0 \end{aligned} \tag{2.30}$$

assuming that the rest of the KKT conditions and the LICQ are satisfied at $y \in \mathbb{R}^n$, as in

(2.21).

Because of the linearity of the gradient and of the hessian, due to the affine parameterization (2.14),

$$\nabla_{\boldsymbol{x}} \mathcal{L}(\boldsymbol{y}, \boldsymbol{\lambda}, \boldsymbol{\mu}; \boldsymbol{\theta}, \boldsymbol{\omega}) = \sum_{i=1}^{m} \omega_i \nabla_{\boldsymbol{x}} \phi_i(\boldsymbol{y}; \boldsymbol{\theta}) + \sum_{j=1}^{q} \lambda_j \nabla_{\boldsymbol{x}} h_j(\boldsymbol{y}; \boldsymbol{\theta}) + \sum_{k=1}^{r} \mu_k \nabla_{\boldsymbol{x}} g_k(\boldsymbol{y}; \boldsymbol{\theta}) \tag{2.31a}$$

$$\nabla^2_{xx} \mathcal{L}(\boldsymbol{y}, \boldsymbol{\lambda}, \boldsymbol{\mu}; \boldsymbol{\theta}, \boldsymbol{\omega}) = \sum_{i=1}^{m} \omega_i \nabla^2_{xx} \phi_i(\boldsymbol{y}; \boldsymbol{\theta}) + \sum_{j=1}^{q} \lambda_j \nabla^2_{xx} h_j(\boldsymbol{y}; \boldsymbol{\theta}) + \sum_{k=1}^{r} \mu_k \nabla^2_{xx} g_k(\boldsymbol{y}; \boldsymbol{\theta}) \tag{2.31b}$$

and the independence of $\boldsymbol{g}(\boldsymbol{y}; \boldsymbol{\theta})$ with respect to the parameters $\boldsymbol{\omega}$, $\boldsymbol{\lambda}$, and $\boldsymbol{\mu}$, (2.23), the query in (2.30) reduces to a conic programming problem, with $\mathcal{W}^c_Q = \mathbb{S}^n \times \Delta^m \times \mathbb{R}^q \times \mathbb{R}^r_+ \times \mathbb{R}_{++}$

$$\begin{aligned}
\min_{(\boldsymbol{Q}, \boldsymbol{\omega}, \boldsymbol{\lambda}, \boldsymbol{\mu}, \delta) \in \mathcal{W}^c_Q} \quad & 0 \\
\text{subject to} \quad & [\nabla_{\boldsymbol{x}} \boldsymbol{\phi}(\boldsymbol{y}; \boldsymbol{\theta}) \ \nabla_{\boldsymbol{x}} \boldsymbol{h}(\boldsymbol{y}; \boldsymbol{\theta}) \ \nabla_{\boldsymbol{x}} \boldsymbol{g}(\boldsymbol{y}; \boldsymbol{\theta})] \begin{bmatrix} \boldsymbol{\omega} \\ \boldsymbol{\lambda} \\ \boldsymbol{\mu} \end{bmatrix} = 0 \\
& [0 \ 0 \ \operatorname{diag}(\boldsymbol{g}(\boldsymbol{y}; \boldsymbol{\theta}))] \begin{bmatrix} \boldsymbol{\omega} \\ \boldsymbol{\lambda} \\ \boldsymbol{\mu} \end{bmatrix} = 0 \\
& \boldsymbol{Q} = \sum_{i=1}^{m} \omega_i \nabla^2_{xx} \phi_i(\boldsymbol{y}; \boldsymbol{\theta}) + \sum_{j=1}^{q} \lambda_j \nabla^2_{xx} h_j(\boldsymbol{y}; \boldsymbol{\theta}) + \sum_{k=1}^{r} \mu_k \nabla^2_{xx} g_k(\boldsymbol{y}; \boldsymbol{\theta}) \\
& \boldsymbol{Q} - \delta I \geq 0
\end{aligned} \tag{2.32}$$

2.6 Approximate Optimality

Most commonly, it is not known if a given observation $(\boldsymbol{\theta}, \boldsymbol{y}) \in \Theta \times \mathbb{R}^n$ or a given data-set

$$(\boldsymbol{\theta}, \boldsymbol{y}^{(1)}), \ldots, (\boldsymbol{\theta}, \boldsymbol{y}^{(D)}) \in \underbrace{(\Theta \times \mathbb{R}^n) \times \ldots \times (\Theta \times \mathbb{R}^n)}_{D}$$

was generated by an optimization process, and even if it were, we don't know if the measurement noise during the measurement process or inaccuracies during the modeling process render the data suboptimal.

In Section 2.4, the most common parametrization of the direct optimization model was presented: the weighted multiobjective parametrization. As shown in Section 2.5, one can verify whether a given data set is inversely optimal with respect to a given weighted multiobjective direct optimization model through Linear Programming and Conic Programming. Exact inverse optimality is tightly related to the cost function basis $\boldsymbol{\phi}$, so we can practically say that a data set is exactly inversely optimal with respect to an objective function basis $\boldsymbol{\phi}$.

When the data is not exactly inversely optimal with respect to a proposed objective function basis $\boldsymbol{\phi}$, or when we know it isn't, we can formulate approaches to inverse optimization that are based on minimizing some loss function $\ell(\boldsymbol{\omega}, \hat{\boldsymbol{y}}, \boldsymbol{y})$ across the data set. As this is almost always the case, most inverse optimization research is focused on it.

2.6.1 Minimum Euclidian Distance Loss

We can formulate the inverse optimization as a minimum-distance projection problem onto the local/global optima set. This function was first proposed in [69] and was used in many studies like [72, 77, 97, 108]. The loss function is the Euclidian distance between the measured behavior $\boldsymbol{y}^{(d)}$ and the model output behavior $\hat{\boldsymbol{y}}^{(d)}$. This loss function gives rise to the most commonly encountered bilevel IOC in the literature.

$$\ell(\boldsymbol{\omega}, \boldsymbol{y}^{(d)}, \hat{\boldsymbol{y}}^{(d)}) = \|\hat{\boldsymbol{y}}^{(d)} - \boldsymbol{y}^{(d)}\|_2^2$$

Given a collection of test points $(\boldsymbol{\theta}, \boldsymbol{y}^{(1)}), \ldots, (\boldsymbol{\theta}, \boldsymbol{y}^{(D)})$, one needs to find the parametrization $\boldsymbol{\omega} \in \mathbb{R}^m$ and a collection of predictions $\hat{\boldsymbol{y}}^{(1)}, \ldots, \hat{\boldsymbol{y}}^{(D)}$ by the DOC model such that sum of distances between pairs of predictions $\hat{\boldsymbol{y}}^{(1)}, \ldots, \hat{\boldsymbol{y}}^{(D)}$ and data $\boldsymbol{y}^{(1)}, \ldots, \boldsymbol{y}^{(D)}$ be the smallest possible in terms of Euclidian distance.

$$\begin{aligned}
\min_{\boldsymbol{\omega}\in\Delta^m,\ \boldsymbol{x}\in\mathbb{R}^n} \quad & \sum_{d=1}^{D} \|\boldsymbol{y}^{(d)} - \hat{\boldsymbol{y}}^{(d)}\|_2^2 \\
\text{subject to} \quad & \hat{\boldsymbol{y}}^{(d)} = \underset{\boldsymbol{x}\in\mathbb{R}^n}{\operatorname{argmin}} \quad \sum_{i=1}^{m} \omega_i \phi_i(\boldsymbol{x}; \boldsymbol{\theta}^{(d)}) \qquad d = 1, \ldots, D \\
& \qquad\qquad \text{subject to} \quad h_j(\boldsymbol{x}; \boldsymbol{\theta}^{(d)}) = 0,\ j = 1..q \\
& \qquad\qquad\qquad\quad\ \ g_k(\boldsymbol{x}; \boldsymbol{\theta}^{(d)}) \leq 0,\ k = 1..r
\end{aligned} \tag{2.33}$$

We can reformulate bi-level formulation from equation (2.33) into a single-level problem using the KKT conditions of the inner optimization. This is a standard procedure in bilevel optimization [99] and has been applied by [77]. However, the dimensionality of the problem becomes enormous for a large data set. Moreover, regularity problems arise with the constraint qualifications of the single-level problem (2.34) [99].

$$\begin{aligned}
\min_{(\boldsymbol{\omega}, \hat{\boldsymbol{y}}^{(1)}, \ldots, \hat{\boldsymbol{y}}^{(D)}, \boldsymbol{\lambda}^{(1)}, \ldots, \boldsymbol{\lambda}^{(D)}, \boldsymbol{\mu}^{(1)}, \ldots, \boldsymbol{\mu}^{(D)})} \quad & \sum_{d=1}^{D} \|\boldsymbol{y}^{(d)} - \hat{\boldsymbol{y}}^{(d)}\|_2^2 \\
\text{subject to} \quad & \nabla_{\boldsymbol{x}} \mathcal{L}(\hat{\boldsymbol{y}}^{(d)}, \boldsymbol{\lambda}^{(d)}, \boldsymbol{\mu}^{(d)}; \boldsymbol{\theta}^{(d)}, \boldsymbol{\omega}) = 0, \quad d = 1, \ldots, D \\
& \boldsymbol{h}(\hat{\boldsymbol{y}}^{(d)}; \boldsymbol{\theta}^{(d)}) = 0, \qquad\qquad d = 1, \ldots, D \\
& \boldsymbol{\mu}^{(d)} \odot \boldsymbol{g}(\hat{\boldsymbol{y}}^{(d)}; \boldsymbol{\theta}^{(d)}) = 0, \qquad d = 1, \ldots, D \\
& \boldsymbol{\mu}^{(d)} \geq 0, \qquad\qquad d = 1, \ldots, D \\
& \boldsymbol{g}(\hat{\boldsymbol{y}}^{(d)}; \boldsymbol{\theta}^{(d)}) \leq 0, \qquad d = 1, \ldots, D \\
& \boldsymbol{\omega} \in \Delta^m
\end{aligned} \tag{2.34}$$

According to [120], this loss function provides a statistically consistent parameter estimation.

2.6.2 Minimum Optimality Condition Violation Loss - IKKT method

This loss function was first proposed in [74], and was subsequently extensively used throughout the literature [76, 84, 88, 91, 102, 111, 115, 118, 122, 127, 135, 143]. As it was formulated in [74], the loss function could have been any norm of the residuals of the KKT conditions. However, as it was appropriated in the biomechanics and robotics literature,

the customary loss function became the L_2 norm of the residual of the KKT stationarity condition (2.22) summed with the L_2 norm of the KKT complementary slackness condition (2.18d) which yields the expression in equation (2.35).

$$\ell(\boldsymbol{\omega}, \boldsymbol{y}^{(d)}, \hat{\boldsymbol{y}}^{(d)}) = \|\nabla_{\boldsymbol{x}} \mathcal{L}(\boldsymbol{y}^{(d)}, \boldsymbol{\lambda}^{(d)}, \boldsymbol{\mu}^{(d)}; \boldsymbol{\theta}^{(d)}, \boldsymbol{\omega})\|_2^2 + \|\boldsymbol{\mu}^{(d)} \odot \boldsymbol{g}(\boldsymbol{y}^{(d)}; \boldsymbol{\theta}^{(d)})\|_2^2 \tag{2.35}$$

Solving the IOC problem with the IKKT algorithm then corresponds to solving the optimization problem from equation (2.36), where the KKT stationarity (2.18b) and complementary slackness (2.18d) residual norms are minimized, where the KKT dual feasibility (2.18f) is enforced as a constraint, and where the primal feasibility equality (2.18c) and inequality (2.18e) are assumed to be satisfied at each data-point.

$$\begin{aligned} \min_{(\boldsymbol{\omega}, \boldsymbol{\lambda}^{(1)}, \boldsymbol{\mu}^{(1)}, \ldots, \boldsymbol{\lambda}^{(D)}, \boldsymbol{\mu}^{(D)})} \quad & \sum_{d=1}^{D} \|\nabla_{\boldsymbol{x}} \mathcal{L}(\boldsymbol{y}^{(d)}, \boldsymbol{\lambda}^{(d)}, \boldsymbol{\mu}^{(d)}; \boldsymbol{\theta}^{(d)}, \boldsymbol{\omega})\|_2^2 \\ & + \|\boldsymbol{\mu}^{(d)} \odot \boldsymbol{g}(\boldsymbol{y}^{(d)}; \boldsymbol{\theta}^{(d)})\|_2^2 \\ \text{subject to} \quad & \boldsymbol{\omega} \in \Delta^m \\ & \boldsymbol{\mu}^{(d)} \geq 0, \ d = 1, \ldots, D \end{aligned} \tag{2.36}$$

By exploiting the linearity of the Lagrangian (2.22) and of the complementary slackness constraints with respect to the objective function weights and the dual variables, as well as the fact that the L_2 norm of the residuals is minimized, one can reformulate the IKKT problem as a constrained least squares problem, a subclass of Quadratic Programmings (QPs). This reformulation is presented in some existing papers [91, 102, 118, 122]. It is similar to the QP reformulation by [115], which goes one step further by pre-computing the dual variables.

$$\begin{aligned} \min_{(\boldsymbol{\omega}, \boldsymbol{\lambda}^{(1)}, \boldsymbol{\mu}^{(1)}, \ldots, \boldsymbol{\lambda}^{(D)}, \boldsymbol{\mu}^{(D)})} \quad & \sum_{d=1}^{D} \|R(\boldsymbol{y}^{(d)}; \boldsymbol{\theta}^{(d)}) \begin{bmatrix} \boldsymbol{\omega} \\ \boldsymbol{\lambda}^{(d)} \\ \boldsymbol{\mu}^{(d)} \end{bmatrix} \|_2^2 \\ \text{subject to} \quad & \boldsymbol{\omega} \in \Delta^m \\ & \boldsymbol{\mu}^{(d)} \geq 0, \ d = 1, \ldots, D \end{aligned}$$

The matrix $R(\boldsymbol{y}^{(d)}; \boldsymbol{\theta}^{(d)})$ that appears in the constrained least-squares reformulation of IKKT will be referred to as the recovery matrix. Though related to the concept of recovery matrices in [127, 135, 143], it is not the same and should not be confused.

$$R(\boldsymbol{y}^{(d)}; \boldsymbol{\theta}^{(d)}) = \begin{bmatrix} \nabla_{\boldsymbol{x}} f(\boldsymbol{y}^{(d)}; \boldsymbol{\theta}^{(d)}) & \nabla_{\boldsymbol{x}} \boldsymbol{h}(\boldsymbol{y}^{(d)}; \boldsymbol{\theta}^{(d)}) & \nabla_{\boldsymbol{x}} \boldsymbol{g}(\boldsymbol{y}^{(d)}; \boldsymbol{\theta}^{(d)}) \\ 0 & 0 & \operatorname{diag}(\boldsymbol{g}(\boldsymbol{y}^{(d)}; \boldsymbol{\theta}^{(d)})) \end{bmatrix}$$

According to [120], this loss function does not estimate a statistically consistent parameter.

2.6.3 Other Loss Functions

Other loss functions can be found in Chan, Mahmood, and Zhu [138], where a comprehensive summary of the existing IOC methods is given. Apart from those listed here, they include the absolute sub-optimality, the relative sub-optimality, and the variational inequality loss functions.

2.7 Conclusion

This chapter provided a broad and comprehensive overview of the literature in IOC that is in relation to human biomechanics and robotics, with related fields having been touched on.

A very broad and general formulation of the direct and the inverse problems was given in Section 2.2 and in Section 2.3, and was accompanied by a discussion of the involvement of parametric optimization and parametric mappings.

An introduction to the more common notions of DOC and IOC was given in Section 2.4. A comprehensive overview of what it implies for a data point to be exactly inversely optimal was given in Section 2.5. The overview is divided into cases according to whether the DOC model is convex or non-convex, and constrained or unconstrained, as the verification of optimality becomes vastly different. Finally, the most common loss functions for IOC are introduced in 2.6 *i.e.* the bilevel minimum distance loss and the IKKT loss functions. This chapter has thoroughly described the different aspects of IOC.

Chapter 3

Bounding Errors via Polynomial Optimization

In studies combining IOC with human motion analysis, a recurring theme is the choice of basis functions and how excluding or including a particular basis function affects the end-model quality [118, 135, 139]. When applying IOC to a specific task of human motion, the basis functions are taken from previous optimal-control-based studies of that task [122, 135]. On the one hand, it is advantageous to include all possible basis functions in the IOC formulation as it will increase the number of parameters and the expressive power of the DOC model and will allow one to achieve better fitting [139]. On the other hand, because of the considerable computational requirements of bilevel optimization, it is desirable to have as few parameters to identify as possible in order to render the identification procedure computationally tractable.

Moreover, the objective function seems task-dependent and may vary between individuals with different skill levels in performing the task [135]. For some tasks where this is particularly pronounced, one may have to retrieve separate objective functions for each subject, which will require computing many solutions to different bilevel optimization problems. The quality of the retrieved objective function lies in the accuracy with which it predicts human-like motion and is inextricably linked to the choice of the included basis functions [97, 111, 118, 122, 139]. This chapter will focus on calculating upper and notably lower bounds on the accuracy with which the input human motion data can be learned and predicted. Knowing the bounds on accuracy allows for discarding bases that are guaranteed not to be good enough. The advantage of this approach is the bounds can be computed much more efficiently than the original problem can be solved.

As a step towards tackling the aforementioned conflict, this chapter will introduce a computationally tractable procedure for quickly testing the quality of a collection of quadratic basis functions within QP direct models. The main idea will be to relax the bilevel IOC problem and use the minimal value of the loss function of the relaxation as a measure of the quality of the basis. This would allow one interested in applying IOC to learn a particular task objective to quickly test multiple collections of basis functions and discard ones whose 'quality' is judged poor. Once the poor bases are discarded, there are fewer bases for which the inverse optimal problem must be solved. The procedure relies on Semidefinite Programming (SDP) [41], which is commonly used to relax Quadratically Constrained Quadratic Programs (QCQPs) [71], as will be the case here.

A central concept of this chapter will be that of a set of global minimizers for a convex DOC model, which is the set of all possible trajectories the DOC model can produce as we vary the objective function parameters. The chapter will also inquire into the analytic properties of this set. Multiple properties that can be analytically shown to hold for QP

models are of interest in the general nonlinear case and thus represent a stepping stone towards tackling the general nonlinear case.

3.1 Introduction

This section starts by re-introducing the IOC problem alongside the problem of finding bounds on the IOC problem's solution. It subsequently introduces the concept of the set of global minimizers in the context of IOC with convex direct models. The set of global minimizers is a concept analogous to the Pareto optimal set [26] in multiobjective optimization or to the set of parametric minimizers [123] in parametric optimization. It represents the set of all trajectories one can obtain by solving the DOC problem while varying the model parameters.

Once the set of global minimizers is conceptualized, the IOC is reformulated as a projection problem onto that set. Namely, if the measured trajectories lie outside the set, solving the IOC problem corresponds to finding the closest point from the set and the matching parametrization for which it is optimal.

3.1.1 Projection onto the Set of Global Minimizers

Recall the concept of basis functions $\boldsymbol{\phi} = (\phi_1, \ldots, \phi_m)$ from Chapter 2, and how they are used to parametrically represent the DOC objective function $f = \sum_{i=1}^{m} \omega_i \phi_i$ as a convex combination of basis functions, like in equation (2.12), where the parameters $\boldsymbol{\omega}$ belong to Δ^m, the m-dimensional probability simplex $\Delta^m = \{\boldsymbol{\omega} \in \mathbb{R}^m \mid \boldsymbol{\omega} \geq 0, \sum_i \omega_i = 1\}$. Moreover, recall the concept of a feasible set for the DOC, let it be denoted with X, and let it be a subset of a finite-dimensional vector space $X \subseteq \mathbb{R}^n$. The analysis that permeates through the chapter will be based on the following assumption pertaining to the basis functions and the feasible set (the same setting as used in [74]),

Assumption 1 (Convexity)**.** *Each ϕ_i is a C^1 convex function, and X is a convex set.*

Under this assumption, we can justify the word "global" when defining the set of global minimizers within Definition 3.1.1. Informally, one can tell the set of global minimizers is the set of all possible minimizers one can obtain by solving an optimization problem with an objective function being a convex combination of the basis functions.

Definition 3.1.1 (Set of Global Minimizers)**.** *Given a vector of basis functions $\boldsymbol{\phi}$ and a feasible set X, and under assumption 1, one can define the set of global minimizers of the vector of basis functions $\boldsymbol{\phi}$ as in equation (3.1) below.*

$$\mathcal{G} = \left\{ \boldsymbol{x} \;\middle|\; \exists \boldsymbol{\omega} \in \Delta^m \;:\; \boldsymbol{x} \in \underset{\boldsymbol{x} \in X}{\operatorname{argmin}} \sum_{i=1}^{m} \omega_i \phi_i \right\} \tag{3.1}$$

The set of global minimizers from Definition 3.1.1 can be characterized by the first-order optimality conditions [41] for convex optimization problems, which will be explored in Section 3.1.2 for the case of unconstrained optimization and in Section 3.1.3 for the case of constrained optimization. Section 3.2 will characterize sets of global minimizers in the case of quadratic programming direct models, will dive into some of its analytical properties, and will provide numerical examples.

This whole chapter is primarily concerned with Problems 1, 2, and 3 listed below.

Problem 1 (Feasibility). *Does there exist an* $\boldsymbol{\omega} \in \Delta^m$ *such that* $\boldsymbol{y}$ *is a global optimum?*

$$\underset{\boldsymbol{\omega} \in \Delta^m}{\text{find}} \ \boldsymbol{y} \in \operatorname{argmin}_{\boldsymbol{x} \in X} \sum_{i=1}^{m} \omega_i \phi_i(\boldsymbol{x}) \tag{3.2}$$

Problem 1 is essentially asking whether a given basis $\boldsymbol{\phi} = (\phi_1, \ldots, \phi_m)$ can represent a measurement $\boldsymbol{y}$. In other words, is it possible to obtain $\boldsymbol{y}$ as the solution to an optimization problem where the objective function is a convex combination of the basis functions? Within the context of multiobjective optimization [26], one could re-frame this question as whether $\boldsymbol{y}$ belongs to the Pareto optimal set of the multiobjective optimization problem with vector objective $\boldsymbol{\phi}$. From the point of view of Parametric Optimization [123], one could ask whether $\boldsymbol{y}$ belongs to the set of parametric minimizers of the optimization problem with the parametric objective function $f = \sum_{i=1}^{m} \omega_i \phi_i(\boldsymbol{x})$ with parameter vector $\boldsymbol{\omega} \in \Delta^m$.

The answer to the question asked by Problem 1 is either 'yes' or 'no.' If the answer is 'yes,' the parameter vector $\boldsymbol{\omega}$, which solves the problem is provided alongside the answer. Once the parameter vector of parameters is known, one can solve the DOC problem to obtain the corresponding DOC solution $\boldsymbol{x}$. If it has been established that the answer is 'no,' then Problem 2 becomes of interest.

Problem 2 (Projection onto Global Minimizers (PGM)). *What is the distance from* $\boldsymbol{y}$ *to the set of global optima?*

$$p^* = \min_{\boldsymbol{x} \in X} \|\boldsymbol{y} - \boldsymbol{x}\|_2^2 \tag{3.3a}$$

$$\exists \boldsymbol{\omega} \in \Delta^m \mid \boldsymbol{x} \in \operatorname{argmin}_{\boldsymbol{x}' \in X} \sum_{i=1}^{m} \omega_i \phi_i(\boldsymbol{x}') \tag{3.3b}$$

Problem 2 is essentially asking what is the error (*i.e.* L_2 distance) with which a given basis $\boldsymbol{\phi} = (\phi_1, \ldots, \phi_m)$ can represent a measurement $\boldsymbol{y}$. In other words, what is the smallest error (*i.e.* L_2 distance) to $\boldsymbol{y}$ one can obtain from the solution of an optimization problem where the objective function is a convex combination of the basis functions? Within the context of multiobjective optimization [26], one could re-frame this question as what is the L_2 distance from $\boldsymbol{y}$ to the Pareto optimal set of the multiobjective optimization problem with vector objective $\boldsymbol{\phi}$. From the point of view of Parametric Optimization [123], one could ask what the L_2 distance of $\boldsymbol{y}$ to the set of parametric minimizers of the optimization problem with the parametric objective function $f = \sum_{i=1}^{m} \omega_i \phi_i(\boldsymbol{x})$ with parameter vector $\boldsymbol{\omega} \in \Delta^m$ is.

The answer to the question asked by Problem 2 is a positive real number p^* representing the aforementioned minimum L_2 distance, with the parameter vector $\boldsymbol{\omega}$ and the closest element $\boldsymbol{x}$ which solve the problem provided as well. However, solving this problem requires solving a bilevel optimization problem that may be computationally intensive. An alternative but relevant question is raised within Problem 3.

Problem 3 (Lower Bound on Projection Distance). *Is it possible to find a positive real number* p^- *that is inferior to the distance of* $\boldsymbol{y}$ *to the set of global optima?*

$$\underset{p^- \in \mathbb{R}_+}{\text{find}} \quad p^- \leq p^* \tag{3.4a}$$

$$\text{where} \quad p^* = \min_{\boldsymbol{x} \in X} \|\boldsymbol{y} - \boldsymbol{x}\|_2^2 \tag{3.4b}$$

$$\exists \boldsymbol{\omega} \in \Delta^m \mid \boldsymbol{x} \in \operatorname*{argmin}_{\boldsymbol{x}' \in X} \sum_{i=1}^{m} \omega_i \phi_i(\boldsymbol{x}') \tag{3.4c}$$

Problem 3 is essentially asking for any positive real number p^- which is inferior to the error with which a given basis $\boldsymbol{\phi} = (\phi_1, \ldots, \phi_m)$ can represent a measurement $\boldsymbol{y}$. In other words, provide a lower bound on the distance to $\boldsymbol{y}$ one can obtain from the solution of

an optimization problem where the objective function is a convex combination of the basis functions.

The answer to Problem 3 is a positive real number p^- representing a lower bound on the aforementioned distance, and may be accompanied by $\hat{\boldsymbol{\omega}}$ and $\hat{\boldsymbol{x}}$ which represent guesses for the parameter vector $\boldsymbol{\omega}$ and the closest element $\boldsymbol{x}$ which solve the Problem 2.

Problem 1 under Assumption 1 may be decided by analyzing the feasibility of a simple n-dimensional LP in $\boldsymbol{\omega}$. Problem 2 is a bilevel optimization problem that assesses the quality of the basis $\boldsymbol{\phi}$ from (2.12) in characterizing $\boldsymbol{y}$ as an optimal point. A large distance p^* from Program (3.3) indicates that the basis $\boldsymbol{\phi}$ does not accurately describe $\boldsymbol{y}$ as a global minimum and therefore $\boldsymbol{\phi}$ should be redesigned. Problem 2 is a generically nonconvex and nontrivial problem even under Assumption 1. Local search and trust-region methods may be used to find upper bounds for p^*, but the exact computation of p^* is typically intractable. Problem 3 may be solved for instance by relaxing the bilevel optimization Problem 2. Within this chapter, the problem will be relaxed to an Linear Matrix Inequality (LMI) in order to obtain lower bounds for p^*, and this LMI relaxation is tight to p^* if the Positive Semidefinite (PSD) matrix solution is rank-1.

There also exists a hierarchy among the problems. If $\boldsymbol{\omega}$ solves the feasibility program from Problem 1, then the objective from Problem 2 will necessarily be $p^* = 0$ with $\boldsymbol{x} = \boldsymbol{y}$ and there will be no need to solve Problem 2 nor Problem 3. If $\boldsymbol{\omega}$ and $\boldsymbol{x}$ solve the PGM Problem 2 with objective $p^* > 0$, then Problem 1 will be unfeasible and the strictest possible answer to Problem 3 will be p^*, so there will be no need to solve it. If $p^- > 0$ is the solution to Problem 3, then Problem 1 will be unfeasible so there will be no need to solve it. The answer to Problem 2 will be $p^* \geq p^-$. So if p^- is greater than a desired value for p^*, one does not need to solve Problem 2 but instead needs to redesign the basis functions $\boldsymbol{\phi}$. The existence of the hierarchy implies the following Algorithm 1 when dealing with IOC problems.

Algorithm 1: IOC procedure

Input: $\boldsymbol{y}, \boldsymbol{\phi}, p^*_{\text{des}}$
Output: p, $\boldsymbol{\omega}$, $\boldsymbol{x}$, Flag

```
(∃ω), ω, x ← Solve Problem 1
if (∃ω) then
    p* ← 0
    return p*, ω, x, "Solved"
p⁻, ω̂, x̂ ← Solve Problem 3
if p⁻ > p*_des then
    return p⁻, ω̂, x̂, "Desired bounds cannot be met"
p*, ω, x ← Solve Problem 2 approximately using local search
if p* > p*_des then
    return p*, ω, x, "Approximately solved, bounds unmet"
return p*, ω, x, "Approximately solved, bounds met"
```

We conclude that by using this framework for IOC, four outcomes are possible:

(a) Problem 1 is exactly solved, in which case there is nothing more to do,

(b) the solution to Problem 3 guarantees that the desired bounds cannot be met, in which case we need to change the model,

(c) Problem 2 is approximately solved via local search, but the bounds are unmet, in which case we may need to change the model or approximately solver Problem 2 multiple times from different starting points hoping to get better bounds,

(d) Problem 2 is approximately solved using local search, and the desired bounds is met and there is nothing more to do.

3.1.2 Unconstrained Global Minimizers Characterization

This subsection uses the first-order optimality conditions to characterize the set of global optima when the feasible set X is the whole space $\mathbb{R}^n$ *i.e.* when the optimal control model is unconstrained. Due to repeated usage throughout this section, the symbol $\mathcal{W}$ will denote $\mathbb{R}^n \times \Delta^m$, which is the Cartesian product of the feasible trajectory set $X = \mathbb{R}^n$ with the set of feasible parameters Δ^m. Denoted as "the extended set of global optima and weights", $\hat{\mathcal{G}}$ is associated with a basis $\boldsymbol{\phi}$ and set mixed cost functions $f_{\boldsymbol{\omega}} = \sum_{i=1}^m \omega_i \phi_i$ as in (2.12), and given Assumption 1 it can be characterized as

$$\hat{\mathcal{G}} = \{(\boldsymbol{x}, \boldsymbol{\omega}) \in \mathcal{W} \mid \nabla_{\boldsymbol{x}} f_{\boldsymbol{\omega}}(\boldsymbol{x}) = 0\}. \tag{3.5}$$

The convexity of $f_{\boldsymbol{\omega}}$ implies that every local minimizer $\boldsymbol{x}$ satisfying the first-order optimality condition $\nabla_{\boldsymbol{x}} f_{\boldsymbol{\omega}}(\boldsymbol{x}) = 0$ [17, 29, 41] is also a global minimizer. Therefore, if the measured trajectory $\boldsymbol{y}$ is optimal, it must satisfy $\nabla_{\boldsymbol{x}} f_{\boldsymbol{\omega}}(\boldsymbol{y}) = 0$. This condition can be simplified as in equation (3.6).

$$\begin{aligned}
\nabla_{\boldsymbol{x}} f_{\boldsymbol{\omega}}(\boldsymbol{y}) &= 0 \\
\nabla_{\boldsymbol{x}} \left(\sum_{i=1}^m \omega_i \phi_i(\boldsymbol{y}) \right) &= 0 \\
\sum_{i=1}^m \omega_i \nabla_{\boldsymbol{x}} \phi_i(\boldsymbol{y}) &= 0 \\
\begin{bmatrix} \nabla_{\boldsymbol{x}} \phi_1(\boldsymbol{y}) & \nabla_{\boldsymbol{x}} \phi_2(\boldsymbol{y}) & \dots & \nabla_{\boldsymbol{x}} \phi_m(\boldsymbol{y}) \end{bmatrix} \boldsymbol{\omega} &= 0 \\
\left(\frac{\partial}{\partial \boldsymbol{x}} \boldsymbol{\phi}(\boldsymbol{y}) \right)^T \boldsymbol{\omega} &= 0
\end{aligned} \tag{3.6}$$

As the optimality condition is linear in $\boldsymbol{\omega}$, as well as the $\boldsymbol{\omega} \in \Delta^m$ condition defined in (2.13), the feasibility Problem 1 given $\boldsymbol{y} \in \mathbb{R}^n$ may be posed as an LP in $\boldsymbol{\omega}$, as proposed in Problem 4.

Problem 4 (Unconstrained Feasibility)**.** *There exists an $\boldsymbol{\omega} \in \Delta^m$ such that $\boldsymbol{y}$ is a global optimum if and only if there exists an $\boldsymbol{\omega} \in \Delta^m$ which is solution to the LP in equation (3.7).*

$$\underset{\boldsymbol{\omega} \in \Delta^m}{\text{find}} \ (\boldsymbol{y}, \boldsymbol{\omega}) \in \hat{\mathcal{G}} \quad \Longleftrightarrow \quad \begin{aligned} &\min_{\boldsymbol{\omega} \in \Delta^m} \quad 0 \\ &\text{subject to} \quad \left(\frac{\partial}{\partial \boldsymbol{x}} \boldsymbol{\phi}(\boldsymbol{y}) \right)^T \boldsymbol{\omega} = 0 \end{aligned} \tag{3.7}$$

The unconstrained PGM problem for the same $\boldsymbol{y}$ is,

Problem 5 (Unconstrained PGM)**.**

$$p^* = \min_{(\boldsymbol{x}, \boldsymbol{\omega}) \in \hat{\mathcal{G}}} \|\boldsymbol{y} - \boldsymbol{x}\|_2^2 \quad \Longleftrightarrow \quad \begin{aligned} &\min_{\boldsymbol{x} \in \mathbb{R}^n, \ \boldsymbol{\omega} \in \Delta^m} \quad \|\boldsymbol{y} - \boldsymbol{x}\|_2^2 \\ &\text{subject to} \quad \left(\frac{\partial}{\partial \boldsymbol{x}} \boldsymbol{\phi}(\boldsymbol{x}) \right)^T \boldsymbol{\omega} = 0 \end{aligned} \tag{3.8}$$

3.1.3 Constrained Global Minimizers Characterization

This section will extend 3.1.2 to consider the case when the feasible set X is a constrained convex subset of the whole space $\mathbb{R}^n$.

The following assumption and representation are required,

Assumption 2. *There exists matrices* $A_{eq} \in \mathbb{R}^{q\times n}$, $b_{eq} \in \mathbb{R}^q$ *and* C^1 *convex functions* $\{g_k(\boldsymbol{x})\}_{k=1}^r$ *such that,*

$$X = \{\boldsymbol{x} \in \mathbb{R}^n \mid A_{eq}\boldsymbol{x} = b_{eq},\ g_k(\boldsymbol{x}) \leq 0\ \forall k = 1..r\}. \tag{3.9}$$

Assumption 3 (Slater's Condition)**.** *There exists a point* $\boldsymbol{x}' \in \mathbb{R}^n$ *such that* $A_{eq}\boldsymbol{x}' = b$ *and* $g_k(\boldsymbol{x}') < 0\ \forall k = 1..n$*, meaning* X *is non-empty.*

Define $\boldsymbol{\mu} \in \mathbb{R}^r_+$ and $\boldsymbol{\lambda} \in \mathbb{R}^q$ as dual variables against the inequality and equality constraints describing X, respectively. The KKT necessary conditions are sufficient to classify all optimal (minimizer) points of $f_{\boldsymbol{\omega}}(\boldsymbol{x})$ given a weighting $\boldsymbol{\omega} \in \Delta^n$ and Assumptions 1, 2, 3 [41]:

$$\nabla_{\boldsymbol{x}} f_{\boldsymbol{\omega}}(\boldsymbol{x}) + A_{eq}^T\boldsymbol{\lambda} + \sum_{k=1}^{r} \mu_k \nabla_{\boldsymbol{x}} g_k(\boldsymbol{x}) = 0 \tag{3.10a}$$

$$A_{eq}\boldsymbol{x} = b \tag{3.10b}$$

$$g_k(\boldsymbol{x}) \leq 0,\ \mu_k \geq 0 \qquad \forall k = 1..n \tag{3.10c}$$

$$\sum_k \mu_k g_k(\boldsymbol{x}) = 0. \tag{3.10d}$$

Define the symbol $\mathcal{W}^c = \mathbb{R}^n \times \Delta^n \times \mathbb{R}^r_+ \times \mathbb{R}^q$ as the resident set containing $(\boldsymbol{x}, \boldsymbol{\omega}, \boldsymbol{\mu}, \boldsymbol{\lambda})$. The optima-weight set in the constrained case is,

$$\hat{\mathcal{G}}^c = \{(\boldsymbol{x}, \boldsymbol{\omega}, \boldsymbol{\mu}, \boldsymbol{\lambda}) \in \hat{\mathcal{W}} \mid \text{KKT conditions (3.10) hold}\} \tag{3.11}$$

$$\mathcal{G}^c = \pi^{\boldsymbol{x}}\hat{\mathcal{G}}^c. \tag{3.12}$$

The feasibility LP to check if a $\boldsymbol{y} \in \mathbb{R}^n$ is constrained-optimal (similar to (3.7) for the unconstrained case) is,

Problem 6 (Constrained Feasibility)**.**

$$\text{find}_{\boldsymbol{\omega}\in\Delta^m,\ \boldsymbol{\mu}\in\mathbb{R}^r_+,\ \boldsymbol{\lambda}\in\mathbb{R}^q}\ (\boldsymbol{y}, \boldsymbol{\omega}, \boldsymbol{\mu}, \boldsymbol{\lambda}) \in \hat{\mathcal{G}}^c, \tag{3.13}$$

with a constrained PGM program,

Problem 7 (Constrained PGM)**.**

$$p^* = \min_{(\boldsymbol{x},\boldsymbol{\omega},\boldsymbol{\mu},\boldsymbol{\lambda})\in\hat{\mathcal{G}}^c} \|\boldsymbol{y} - \boldsymbol{x}\|_2^2. \tag{3.14}$$

The structure of the feasibility problem remains the same in both the unconstrained and the constrained cases: it is a LP. The structure of the PGM remains in both cases a bilevel optimization problem, but in the constrained case contains as many more variables as there are constraints in the direct model. Constrained models are much more difficult to treat because of this.

In the next subsection, the special case of QP direct models will be considered. Because of their special structure and additional assumptions one is able to say something about their sets of global minimizers.

3.2 Inverse Quadratic Programming

A QP is an optimization problem with a quadratic objective function and linear constraints. Although important in its own right, QP arises as a subproblem in a variety of numerical methods for general constrained optimization like Sequential Quadratic Programming or Augmented Lagrangian Methods [29] and is crucial in a variety of applications, such as finance, engineering, machine learning, operations research, and statistics. The versatility and efficiency of QP, along with its tractability, have made it a fundamental tool in these and many other disciplines.

In this section, we will characterize unconstrained and constrained sets of global minima for QP models of DOC. A standard form convex QP is given in equation (3.15),

$$\begin{aligned} \min_{\boldsymbol{x}\in\mathbb{R}^n} \quad & \frac{1}{2}\boldsymbol{x}^T\boldsymbol{Q}\boldsymbol{x} + \boldsymbol{\varphi}^T\boldsymbol{x} && \text{(3.15a)} \\ \text{subject to} \quad & \boldsymbol{A}_{eq}\boldsymbol{x} = \boldsymbol{b}_{eq} && \text{(3.15b)} \\ & \boldsymbol{A}\boldsymbol{x} \leq \boldsymbol{b} && \text{(3.15c)} \end{aligned}$$

for matrices $\boldsymbol{Q} \in \mathbb{S}^n_+$, $\boldsymbol{\varphi} \in \mathbb{R}^n$, $\boldsymbol{A}_{eq} \in \mathbb{R}^{q\times n}$, $\boldsymbol{b}_{eq} \in \mathbb{R}^q$, $\boldsymbol{A} \in \mathbb{R}^{r\times n}$, and $b \in \mathbb{R}^r$ such that Assumption 3 (Slater) holds. Under this assumption, the standard form QP always has at least one solution but can have infinitely many under certain conditions related to the relationship of the different matrices that are present in the QP.

3.2.1 Unconstrained Quadratic Programming

Further analysis in this section will require the following assumption,

Assumption 4 (Strictly Convex Quadratics)**.** *Functions in $\boldsymbol{\phi}$ are strictly convex quadratics with,*

$$\begin{aligned} \phi_i(\boldsymbol{x}) &= (\boldsymbol{x} - \boldsymbol{x}_i^\phi)^T\boldsymbol{Q}_i(\boldsymbol{x} - \boldsymbol{x}_i^\phi)/2 && \forall i = 1..m && \text{(3.16a)} \\ \nabla_x\phi_i(\boldsymbol{x}) &= \boldsymbol{Q}_i(\boldsymbol{x} - \boldsymbol{x}_i^\phi) && \forall i = 1..m. && \text{(3.16b)} \end{aligned}$$

where all elements in $(\boldsymbol{Q}_i, \boldsymbol{x}_i^\phi)$ are bounded and $\boldsymbol{Q}_i \in \mathbb{S}^n_{++}$ for all $i = 1..m$.

Following from the first-order sufficient and necessary condition for the characterization of a minimum of a convex function presented in equation (3.5) the optima-weight sets $\hat{\mathcal{G}}(\boldsymbol{x}, \boldsymbol{\omega})$ and $\mathcal{G}(\boldsymbol{x})$ under Assumption 4 is,

$$\hat{\mathcal{G}} = \{(\boldsymbol{x}, \boldsymbol{\omega}) \in \mathcal{W} \mid (\textstyle\sum_i \omega_i\boldsymbol{Q}_i)\,\boldsymbol{x} = \sum_i \omega_i\boldsymbol{Q}_i\boldsymbol{x}_i^\phi\} \quad \text{(3.17)}$$

$$\mathcal{G} = \pi^{\boldsymbol{x}}\hat{\mathcal{G}}. \quad \text{(3.18)}$$

Remark 1. *Letting $\{\boldsymbol{e}_j\}_{j=1}^m$ be the standard basis vectors in $\mathbb{R}^m$, the points $\{(\boldsymbol{x}_i^\phi, \boldsymbol{e}_j)\}_{j=1}^m$ are all members of $\hat{\mathcal{G}}$.*

Remark 2. *All descriptor constraints in $\hat{\mathcal{G}}$ from (3.17) have polynomial degree at most two, and there is a bilinearity between $(\boldsymbol{\omega}, \boldsymbol{x})$.*

The mapping $\kappa : \Delta^m \to \mathcal{G}$ with $\kappa(\boldsymbol{\omega}) = \boldsymbol{x}^*_{\boldsymbol{\omega}}$ in terms of finding an optimal $\boldsymbol{x}$ minimizing $f_{\boldsymbol{\omega}}$ is single-valued, and has an expression,

$$\kappa(\boldsymbol{\omega}) = \boldsymbol{x}^*_{\boldsymbol{\omega}} = (\textstyle\sum_i \omega_i\boldsymbol{Q}_i)^{-1}\left(\sum_i \omega_i\boldsymbol{Q}_i\boldsymbol{x}_i^\phi\right). \quad \text{(3.19)}$$

Remark 3. *Conversely, the mapping $\kappa^{-1} : \mathcal{G} \rightrightarrows \Delta^m$ is set-valued. Its values are the compact polytopic sets containing feasible points of the program (3.7).*

Theorem 3.2.1. *The map $\kappa(\boldsymbol{\omega})$ from (3.19) is a continuous surjection from Δ^m onto $\mathcal{G}$ under Assumption 4.*

Proof. Surjection holds by definition of $\hat{\mathcal{G}}$ in (3.17): $\boldsymbol{x}$ is only a member of $\hat{\mathcal{G}}$ if there exists an $\boldsymbol{\omega}' \in \Delta^m$ such that $\boldsymbol{x} = \boldsymbol{x}^*_{\boldsymbol{\omega}'}$. Continuity of $\boldsymbol{x}^*_{\boldsymbol{\omega}}$ is based on continuity of the matrix inverse $\boldsymbol{A}^{-1}$ for all nonsingular matrices $\boldsymbol{A} \in \mathbb{R}^{n\times n}$. □

Definition 3.2.1 (Compact)**.** *A set $X \in \mathbb{R}^n$ is compact if it is closed and bounded (Heine-Borel). A consequence is that X is compact if there exists a finite $R > 0$ such that X is a subset of the ball with radius R : $\{\boldsymbol{x} \mid \|\boldsymbol{x}\|_2 < R\}$ [32].*

Theorem 3.2.2. *Under Assumption 4, the set $\hat{\mathcal{G}}$ is compact.*

Proof. There exists a finite quantity $R > 0$ that satisfies $\max_j \|\boldsymbol{x}_i^\phi\|_2 < R$ due to boundedness of $\boldsymbol{x}^\phi$. It is implied that $\max_{\boldsymbol{\omega}\in\Delta^m} \|\sum_{j=1}^m \omega_i \boldsymbol{x}_i^\phi\|_2 < R$ by convexity of the norm $\|\cdot\|_2$. Let Λ be the solution to,

$$\Lambda = \min_{\boldsymbol{\omega}\in\Delta^m} \lambda_{min}\left(\textstyle\sum_i \omega_i \boldsymbol{Q}_i\right). \tag{3.20}$$

It holds that $\Lambda > 0$ because Positive Definite (PD) matrices form a convex (non-pointed) cone. The maximum norm of any global-optimal point in $\mathcal{G}$ is bounded above by,

$$\|\kappa(\boldsymbol{\omega})\|_2 = \|(\textstyle\sum_i \omega_i \boldsymbol{Q}_i)^{-1}\left(\sum_i \omega_i \boldsymbol{Q}_i \boldsymbol{x}_i^\phi\right)\|_2 \tag{3.21a}$$

$$\leq (1/\Lambda)\|\left(\textstyle\sum_i \omega_i \boldsymbol{Q}_i \boldsymbol{x}_i^\phi\right)\|_2 \leq R/\Lambda < \infty. \tag{3.21b}$$

The compact set $\{(\boldsymbol{x}, \boldsymbol{\omega}) \in \mathcal{W} \mid \|\boldsymbol{x}\|_2 \leq R/\Lambda\}$ is a superset of $\hat{\mathcal{G}}$ from (3.17), which proves that $\hat{\mathcal{G}}$ is compact. □

Definition 3.2.2 (Path-Connected)**.** *A set X is path-connected if for every two points $\boldsymbol{x}^0, \boldsymbol{x}^1 \in X$ there exists a continuous path (curve) $\omega : [0,1] \to X$ with $\omega(0) = \boldsymbol{x}^0$, $\omega(1) = \boldsymbol{x}^1$ such that $\omega(t) \in X$ $\forall t \in [0,1]$ [32].*

Theorem 3.2.3. *Under Assumption 4, the set $\mathcal{G}$ is path-connected.*

Proof. Let $\boldsymbol{x}^0, \boldsymbol{x}^1$ be a pair of distinct points in $\mathcal{G}$. Choose $\boldsymbol{\omega}^0 \in \kappa^{-1}(\boldsymbol{x}^0)$ and $\boldsymbol{\omega}^1 \in \kappa^{-1}(\boldsymbol{x}^1)$ as weights generating the optimal points $\boldsymbol{x}^0, \boldsymbol{x}^1$. A path $\omega : [0,1] \to \Delta^m$ may be drawn between the points by $\omega(t) : \boldsymbol{\omega}^0 t + \boldsymbol{\omega}^1(1-t)$. The path $(\omega(t), \kappa(\omega(t)))$ remains inside $\hat{\mathcal{G}}$ for all $t \in [0,1]$ by continuity of κ from Theorem 3.2.1. This containment holds for all pairs $(\boldsymbol{x}^0, \boldsymbol{x}^1)$, so $\mathcal{G}$ is path-connected. □

Remark 4. *No conclusions can be drawn in this manner about path-connectedness of $\hat{\mathcal{G}}$.*

Figure 3.1 depicts the set of unconstrained global minima $\mathcal{G}$ for $\boldsymbol{x} \in \mathbb{R}^3$, generated by 5 different basis functions, thus $\boldsymbol{\omega} \in \Delta^5$. Optimal points of the individual basis functions, as well as the 1-level-sets of the quadratics, are plotted, in order to give a sense of pairs $(\boldsymbol{Q}_i, \boldsymbol{x}_i^\phi)_{j=1}^5$ involved. The black edges connecting pairs of $\boldsymbol{x}_i^\phi$ correspond to edges of the geometric shape, but also to sets of global minima of pairwise function combinations. Compactness and path-connectedness are visually obvious in this example. The numerical values of $\boldsymbol{Q}_{1:5}$ and $\boldsymbol{x}_{1:5}^\phi$ used to generate these meshes are given within equation (3.22) below.

$$\boldsymbol{Q}_1 = \begin{bmatrix} 2.175 & -0.037 & -0.251 \\ -0.037 & 0.836 & 0.117 \\ -0.251 & 0.117 & 0.795 \end{bmatrix} \qquad \boldsymbol{x}_1^{\phi} = \begin{bmatrix} -1.521 \\ -2.342 \\ -3.135 \end{bmatrix} \tag{3.22a}$$

$$\boldsymbol{Q}_2 = \begin{bmatrix} 1.627 & -0.178 & 0.439 \\ -0.178 & 1.782 & -0.160 \\ 0.439 & -0.160 & 1.727 \end{bmatrix} \qquad \boldsymbol{x}_2^{\phi} = \begin{bmatrix} 3.754 \\ -0.449 \\ -1.387 \end{bmatrix} \tag{3.22b}$$

$$\boldsymbol{Q}_3 = \begin{bmatrix} 1.883 & 0.425 & -0.482 \\ 0.425 & 0.750 & -0.176 \\ -0.482 & -0.176 & 1.642 \end{bmatrix} \qquad \boldsymbol{x}_3^{\phi} = \begin{bmatrix} -1.363 \\ -2.765 \\ 1.823 \end{bmatrix} \tag{3.22c}$$

$$\boldsymbol{Q}_4 = \begin{bmatrix} 1.656 & 0.068 & 0.012 \\ 0.068 & 2.016 & 0.271 \\ 0.012 & 0.271 & 1.818 \end{bmatrix} \qquad \boldsymbol{x}_4^{\phi} = \begin{bmatrix} 1.125 \\ -1.152 \\ 3.332 \end{bmatrix} \tag{3.22d}$$

$$\boldsymbol{Q}_5 = \begin{bmatrix} 1.272 & -0.484 & 0.223 \\ -0.484 & 1.508 & -0.051 \\ 0.223 & -0.051 & 1.366 \end{bmatrix} \qquad \boldsymbol{x}_5^{\phi} = \begin{bmatrix} 3.380 \\ 1.614 \\ -1.831 \end{bmatrix} \tag{3.22e}$$

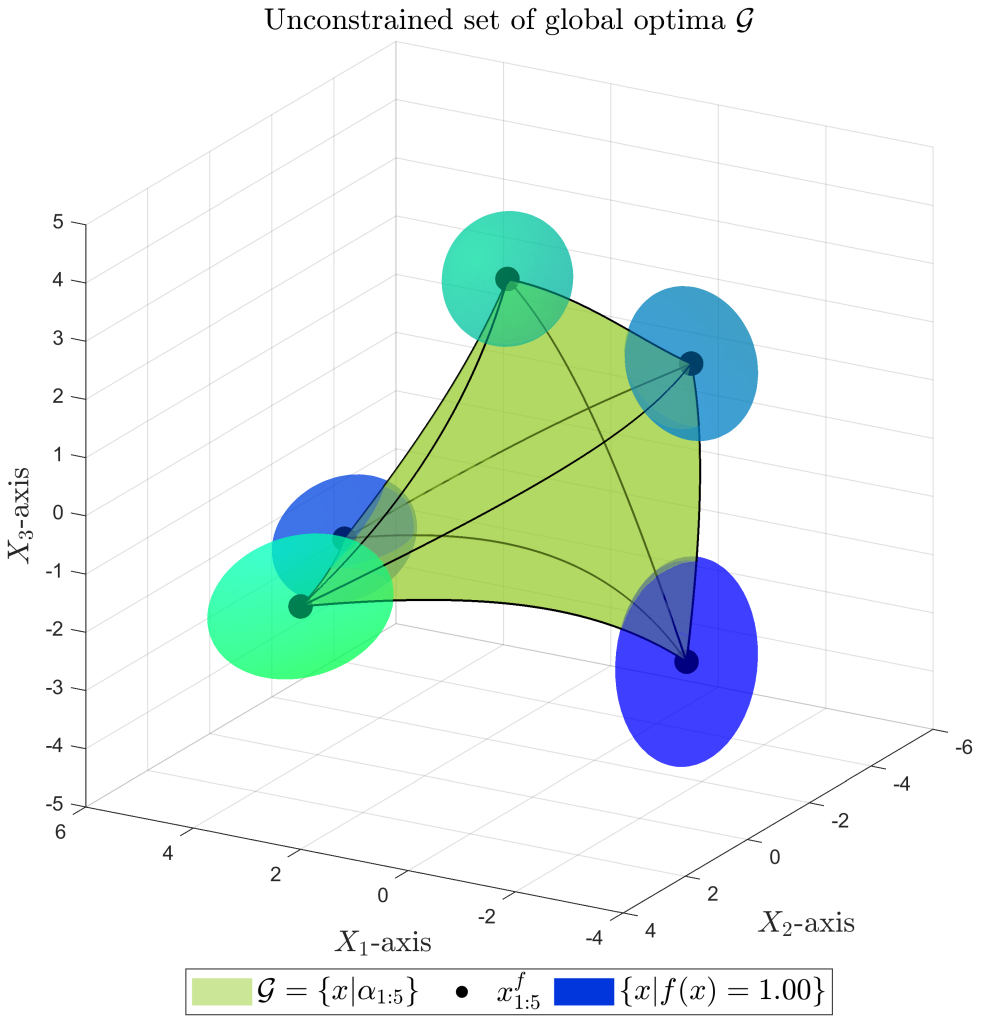

Figure 3.1: A set of unconstrained global optima in 3D

3.2.2 Constrained Quadratic Programming

We note that the special case of QP involves candidate functions and a constraint set,

$$\phi_i = \boldsymbol{x}^T \boldsymbol{Q}_i \boldsymbol{x}/2 + \boldsymbol{\varphi}_i{}^T \boldsymbol{x}, \ \forall i = 1..m \tag{3.23a}$$

$$X = \{\boldsymbol{x} \in \mathbb{R}^n \mid \boldsymbol{A}_{eq}\boldsymbol{x} = \boldsymbol{b}_{eq}, \ \boldsymbol{A}\boldsymbol{x} \leq b\}, \tag{3.23b}$$

for matrices $\{\boldsymbol{Q}_i \in \mathbb{S}^n_+, \ \boldsymbol{\varphi}_i \in \mathbb{R}^n\}_{i=1..m}$ and $\boldsymbol{A}_{eq} \in \mathbb{R}^{q\times n}$, $\boldsymbol{b}_{eq} \in \mathbb{R}^q$, $\boldsymbol{A} \in \mathbb{R}^{r\times n}$, $b \in \mathbb{R}^r$ such that Assumption 3 (Slater) holds.

The constrained-optimal solution map given $\boldsymbol{\omega}$ and the parameters in (3.23) is,

$$\kappa^c(\boldsymbol{\omega}) = \text{argmin}_{\boldsymbol{x}\in X} \textstyle\sum_{j=1}^m \omega_i \phi_i(\boldsymbol{x}). \tag{3.24}$$

Remark 5. *Due to possible weak convexity of some cost functions in $\boldsymbol{\phi}$, there may exist points $\boldsymbol{\omega} \in \Delta^m$ such that $\kappa^c(\boldsymbol{\omega})$ is set-valued rather than single-valued. This will occur when $Q_{\boldsymbol{\omega}} = (\sum_{j=1}^m \omega_i \boldsymbol{Q}_i)$ is rank-deficient and $(\sum_{j=1}^m \omega_i \boldsymbol{\varphi}_i)$ is orthogonal to $Q_{\boldsymbol{\omega}}$'s nullspace.*

In this case, the possibly discontinuous selection (translation of the minimum map),

$$s(\kappa^c(\boldsymbol{\omega})) = \underset{\boldsymbol{x}\in\kappa^c(\boldsymbol{\omega})}{\text{argmin}} \|\boldsymbol{y} - \boldsymbol{x}\|_2^2, \tag{3.25}$$

will denote a constrained-optimal point in $\kappa^c(\boldsymbol{\omega})$ that is closest to $\boldsymbol{y}$. Finding a selection $s(\kappa^c(\boldsymbol{\omega}))$ requires solving a second QP over the X-intersected subspace of solutions of (3.24). This two-step approach involving a minimal selection was also performed in [57].

Figure 3.2 depicts constrained global optima $\mathcal{G}^c$, and its unconstrained version $\mathcal{G}$ generated from the same basis function set $\boldsymbol{\phi}$. Here 2 variables, 3 cost functions, and 4 inequality constraints with $(\boldsymbol{x}, \boldsymbol{\omega}, \mu) \in \mathbb{R}^2 \times \Delta^3 \times \mathbb{R}^4_+$ are considered. Unconstrained and constrained optimal points of the individual basis functions, $\boldsymbol{x}^{\phi}_{1:5}$ and $\boldsymbol{x}^{f,c}_{1:5}$, are shown as colored dots. The black square denotes the feasible region. The blue ellipses are the level sets of the quadratic cost functions, chosen to highlight the spots where they are tangential to the constrained set boundary (implying the position of their constrained minima). The red box highlights the spot where the intersection of $\mathcal{G}^c$ and the complement of $\mathcal{G}$ is non-empty.

The numerical values of $\boldsymbol{Q}_{1:3}$, $\boldsymbol{\varphi}_{1:3}$ and $\boldsymbol{x}^{\phi}_{1:3}$ used to generate these meshes are given within equation (3.26) below.

$$\boldsymbol{Q}_1 = \begin{bmatrix} 1.284 & -0.348 \\ -0.348 & 0.858 \end{bmatrix} \quad \boldsymbol{\varphi}_1 = \begin{bmatrix} 1.346 \\ -0.883 \end{bmatrix} \quad \boldsymbol{x}^{\phi}_1 = \begin{bmatrix} -0.864 \\ 0.679 \end{bmatrix} \tag{3.26a}$$

$$\boldsymbol{Q}_2 = \begin{bmatrix} 0.593 & -0.001 \\ -0.001 & 0.553 \end{bmatrix} \quad \boldsymbol{\varphi}_2 = \begin{bmatrix} 0.292 \\ -0.505 \end{bmatrix} \quad \boldsymbol{x}^{\phi}_2 = \begin{bmatrix} -0.491 \\ 0.911 \end{bmatrix} \tag{3.26b}$$

$$\boldsymbol{Q}_3 = \begin{bmatrix} 1.056 & -0.033 \\ -0.033 & 1.056 \end{bmatrix} \quad \boldsymbol{\varphi}_3 = \begin{bmatrix} -0.874 \\ 0.753 \end{bmatrix} \quad \boldsymbol{x}^{\phi}_3 = \begin{bmatrix} 0.807 \\ -0.689 \end{bmatrix} \tag{3.26c}$$

The 4 inequality constraints are described by the matrices $\boldsymbol{A}$ and $\boldsymbol{b}$ given in equation (3.27) below.

$$\boldsymbol{A} = \begin{bmatrix} 1 & 1 \\ -1 & 1 \\ 1 & -1 \\ -1 & -1 \end{bmatrix} \quad \boldsymbol{b} = \begin{bmatrix} 1 \\ 1 \\ 1 \\ 1 \end{bmatrix} \tag{3.27}$$

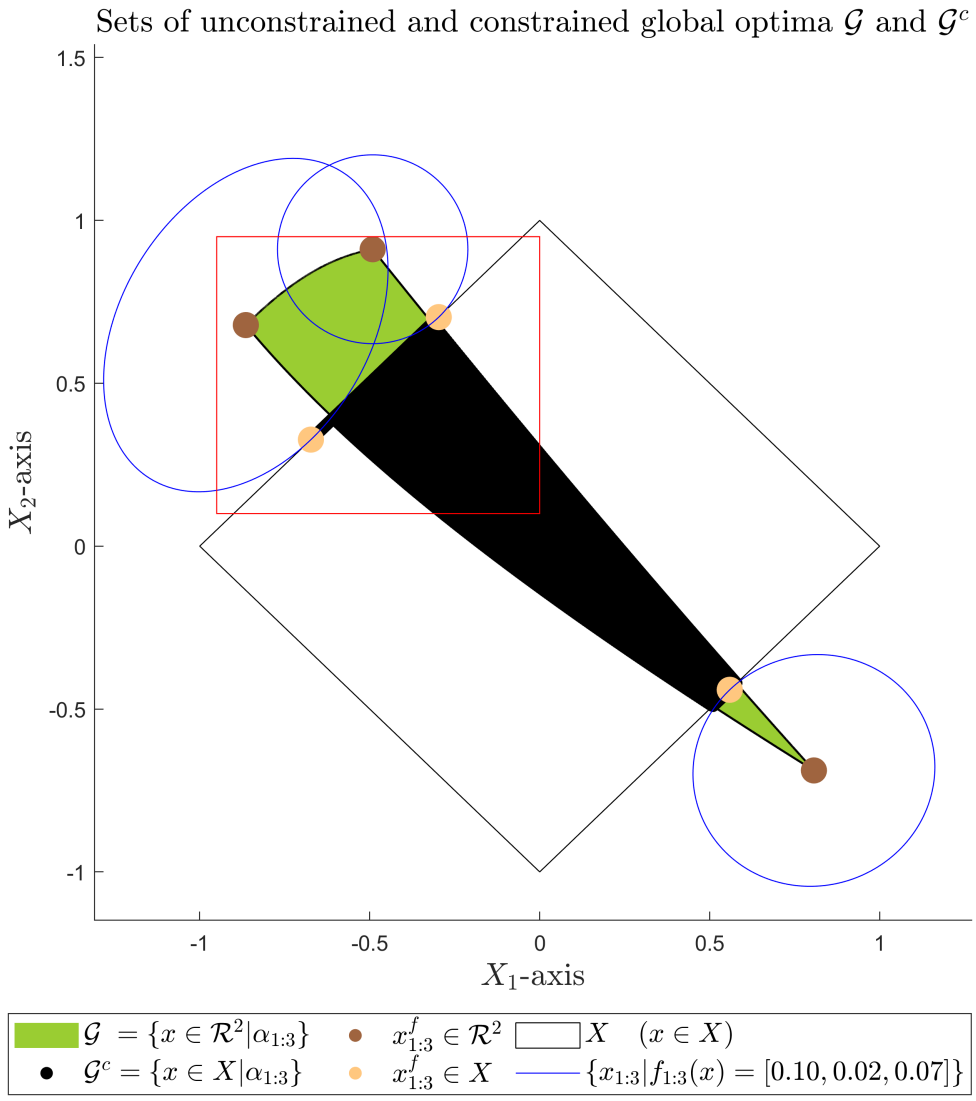

Figure 3.2: The set $\mathcal{G}^c$ is not necessarily a subset of $\mathcal{G}$

3.3 Numerical Methods

This section will present numerical approaches to find upper and lower bounds for the unconstrained PGM 5 and constrained PGM 7.

3.3.1 Upper Bounds

Upper bounds of p^* may be computed through sampling and local search optimization. The PGM problems may be formulated solely in terms of $\boldsymbol{\omega}$ through the use of the optimization maps $\kappa(\boldsymbol{\omega})$ and $\kappa^c(\boldsymbol{\omega})$ for $\boldsymbol{\omega} \in \Delta^*$ (bi-level optimization).

The objective in 5 and its gradient with respect to $\boldsymbol{\omega}$ is,

$$F(\boldsymbol{\omega}) = \|\kappa(\boldsymbol{\omega}) - \boldsymbol{y}\|_2^2 \tag{3.28}$$

$$\nabla_{\boldsymbol{\omega}} F(\boldsymbol{\omega})_j = 2(\kappa(\boldsymbol{\omega}) - \boldsymbol{y})^T \left(\textstyle\sum_i \omega_i \boldsymbol{Q}_i\right)^{-1} \boldsymbol{Q}_j (\boldsymbol{x}_j^{\phi} - \kappa(\boldsymbol{\omega})). \tag{3.29}$$

A Hessian for F may be similarly derived in closed form (omitted due to space constraints).

Local solvers such as `fmincon` in MATLAB or Manopt[1] [93] may be given this value and derivative information to perform optimization over $\boldsymbol{\omega} \in \Delta^m$ (e.g. L-BFGS, trust-region).

$$\begin{aligned}
&\nabla_{\boldsymbol{\omega}\boldsymbol{\omega}} F(\boldsymbol{\omega})_{jk} = \\
&2(\kappa(\boldsymbol{\omega}) - \boldsymbol{y})^T \left(\textstyle\sum_i \omega_i \boldsymbol{Q}_i\right)^{-1} \left[\boldsymbol{Q}_j \left(\textstyle\sum_i \omega_i \boldsymbol{Q}_i\right)^{-1} \boldsymbol{Q}_k (\boldsymbol{x}_k^\phi - \kappa(\boldsymbol{\omega})) + \boldsymbol{Q}_k \left(\textstyle\sum_i \omega_i \boldsymbol{Q}_i\right)^{-1} \boldsymbol{Q}_j (\boldsymbol{x}_j^\phi - \kappa(\boldsymbol{\omega}))\right] \\
&2(\boldsymbol{x}_k^\phi - \kappa(\boldsymbol{\omega}))^T \boldsymbol{Q}_k \left(\textstyle\sum_i \omega_i \boldsymbol{Q}_i\right)^{-2} \boldsymbol{Q}_j (\boldsymbol{x}_j^\phi - \kappa(\boldsymbol{\omega}))
\end{aligned} \tag{3.30}$$

The constrained objective in 7 may be expressed as,

$$F^c(\boldsymbol{\omega}) = \|s(\kappa^c(\boldsymbol{\omega})) - \boldsymbol{y}\|_2^2. \tag{3.31}$$

The constrained objective (3.31) is not generally differentiable with only the weak convexity assumption. Two possible options to minimize $F^c(\boldsymbol{\omega})$ include gridding Δ^m, and using `fmincon` in terms of $(\boldsymbol{x}, \boldsymbol{\omega}, \boldsymbol{\mu}, \boldsymbol{\lambda}) \in \hat{\mathcal{G}}^c$ directly on the constrained optimization Problem 7.

3.3.2 Lower Bounds

Lower bounds $p_{low} \leq p^*$ to Problems 5 and 7 in the quadratic case may be acquired through SDP. The presented method in this subsection is a QCQP that is equivalent to the degree-1 moment-Sum of squares (SOS) hierarchy LMI enriched by additional constraints.

Unconstrained Lower Bound

Every point $(\boldsymbol{x}, \boldsymbol{\omega}) \in \mathcal{W}$ defines a rank-1 PSD matrix $\boldsymbol{M} = [1 \ \boldsymbol{x} \ \boldsymbol{\omega}][1 \ \boldsymbol{x} \ \boldsymbol{\omega}]^T$. Setting $\boldsymbol{M} \in \mathbb{S}_+^{1+n+m}$ indexed by $(1, \boldsymbol{x}, \boldsymbol{\omega})$ as a matrix variable,

$$\boldsymbol{M} = \begin{bmatrix} M_{11} & M_{1\boldsymbol{x}} & M_{1\boldsymbol{\omega}} \\ M_{\boldsymbol{x}1} & M_{\boldsymbol{x}\boldsymbol{x}} & M_{\boldsymbol{x}\boldsymbol{\omega}} \\ M_{\boldsymbol{\omega}1} & M_{\boldsymbol{\omega}\boldsymbol{x}} & M_{\boldsymbol{\omega}\boldsymbol{\omega}} \end{bmatrix}, \tag{3.32}$$

the objective $\|\boldsymbol{y} - \boldsymbol{x}\|_2^2$ may be converted into an affine expression,

$$\textstyle\sum_{i=1}^n (M_{\boldsymbol{x}_i\boldsymbol{x}_i} - 2\boldsymbol{y}_i M_{1\boldsymbol{x}_i}) + \|\boldsymbol{y}\|_2^2 \tag{3.33}$$

Containment in $\hat{\mathcal{G}}$ from (3.17) may be expressed as,

$$\textstyle\sum_{j=1}^m M_{\omega_j 1} = 1 \tag{3.34a}$$

$$M_{\omega_j 1} \geq 0 \qquad \forall j = 1..m \tag{3.34b}$$

$$\textstyle\sum_{j=1}^m \boldsymbol{Q}_j M_{\boldsymbol{x}\omega_j} - (\boldsymbol{Q}_j \boldsymbol{x}_j^\phi) M_{1\omega_j} = 0. \tag{3.34c}$$

Valid constraints are a set of relations that are always satisfied by an $\boldsymbol{M}$ generated by the

[1] As Δ^m is not a manifold, the Hadamard parameterization $\Delta^m = \{z \odot z \mid \|z\|_2^2 = 1\}$ may be employed [145].

optimal point $(\boldsymbol{x}^*, \boldsymbol{\omega}^*)$ solving Problem 5. These valid constraints include,

$$M_{\omega_i 1} = \sum_{j=1}^m M_{\omega_i \omega_j} \qquad \forall i \neq j \tag{3.35a}$$
$$M_{\omega_i \omega_j} \geq 0 \qquad \forall i \neq j \tag{3.35b}$$
$$M_{\omega_i \omega_j} \leq \omega_i, \;\; M_{\omega_i \omega_j} \leq \omega_j \qquad \forall i \neq j \tag{3.35c}$$
$$M_{\omega_i \omega_i} \leq M_{1 \omega_i} \qquad \forall i = 1..m \tag{3.35d}$$
$$M_{\omega_i \omega_j} \leq 1/4 \qquad \forall i \neq j. \tag{3.35e}$$

Constraints (3.35a)-(3.35b) arise from multiplying together defining constraints for the simplex. The diagonal entry $M_{\omega_i \omega_i}$ will automatically be positive by $\boldsymbol{M} \in \mathbb{S}_+^{1+n+m}$. Constraints (3.35c)-(3.35e) originate from observations about the simplex Δ^m. Because $\boldsymbol{\omega} \in \Delta^m \subsetneq [0,1]^m$, coordinate-wise multiplication will satisfy $\omega_i \omega_j \leq \omega_i$ for all $i, j \in 1..n$.

Constraint (3.35e) results from the fact that elementary symmetric polynomials on the probability simplex Δ^σ are maximized at the vector $\mathbf{1}/\sigma$. The elementary symmetric polynomial applied to $\boldsymbol{\omega}' \in \Delta^\sigma$ is $e_2^\sigma(\boldsymbol{\omega}') = \sum_{1 \leq i < j \leq n} \omega_i' \omega_j'$, and admits the maximum value of $\max e_2^\sigma = \binom{\sigma}{2} \frac{1}{\sigma^2}$. The valid inequality derived from $\sigma = 2$ with $\max e_2^\sigma = \frac{1}{4}$ is written in (3.35e). Valid inequalities with higher σ may be written at the cost of including a combinatorially increasing number of constraints.

Algorithm 2: Unconstrained LMI

Input: $\boldsymbol{y}$, $\boldsymbol{Q}$, $\boldsymbol{x}_f$
Output: p^*_{low}, $\boldsymbol{M}$ (or Infeasibility)

1 Solve (or find infeasibility certificate):

$$p^*_{low} = \min_{\boldsymbol{M}} \quad \text{Objective (3.33)} \tag{3.36a}$$
$$\text{Optimality (3.34), Valid (3.35)} \tag{3.36b}$$
$$M_{11} = 1, \;\; \boldsymbol{M} \in \mathbb{S}_+^{1+n+m}. \tag{3.36c}$$

A rank-1 matrix solution $\boldsymbol{M}$ of Algorithm 2 certifies that $p^*_{low} = p^*$. The optimal entries $(\boldsymbol{x}, \boldsymbol{\omega})$ can then be read from the solution's entries $(M_{1\boldsymbol{x}}, M_{1\boldsymbol{\omega}})$. Adding valid inequalities (3.35) can encourage rank-1 solutions of LMI lower bound problem, refer to [136] for further examples of this phenomenon.

Constrained Lower Bounds

The lower bound SDP for the QP setting in Section 3.2.2 requires a matrix $\boldsymbol{M} \in \mathbb{S}_+^{1+n+m+r}$ and a vector $\boldsymbol{\lambda} \in \mathbb{R}^q$ such that the entries of $\boldsymbol{M}$ are indexed by $[1, \boldsymbol{x}, \boldsymbol{\omega}, \boldsymbol{\mu}]$. The equality multipliers $\boldsymbol{\lambda}$ may be ommited from $\boldsymbol{M}$ because there is no multiplication in (3.10) between terms that contain $\boldsymbol{x}$ and $\boldsymbol{\lambda}$. The affine constraint interpretation of the KKT conditions in (3.10) is,

$$\sum_{j=1}^m (\boldsymbol{Q}_j M_{\boldsymbol{x}\omega_j} + \varphi_j M_{\omega_j 1}) + \boldsymbol{A}_{eq}^T \boldsymbol{\lambda} + \boldsymbol{A}^T M_{\boldsymbol{\mu} 1} = 0 \tag{3.37a}$$
$$\boldsymbol{A}_{eq} M_{\boldsymbol{x}1} = \boldsymbol{b}_{eq} \tag{3.37b}$$
$$\boldsymbol{A} M_{\boldsymbol{x}1} \leq \boldsymbol{b} \quad M_{\boldsymbol{\mu}1} \geq 0 \tag{3.37c}$$
$$-\boldsymbol{b}^T M_{\boldsymbol{\mu}1} + \sum_{k=1}^r A_k M_{\boldsymbol{x}\mu_k} = 0. \tag{3.37d}$$

The notation A_k in the complementary slackness constraint (3.37d) indicates row k of the matrix $\boldsymbol{A}$. Valid inequalities for the constrained QP case include (with inequality constraint

indices (k, ℓ)),

$$M_{\mu_k \mu_\ell} \geq 0 \qquad \forall k \neq \ell \tag{3.38a}$$
$$M_{\mu_k \omega_i} \geq 0 \qquad \forall k = 1..r,\ i = 1..m. \tag{3.38b}$$
$$M_{\mu_k \omega_i} \leq M_{\mu_k 1} \qquad \forall k = 1..r,\ i = 1..m. \tag{3.38c}$$

Both $\boldsymbol{\omega} \in \Delta^m$ and $\boldsymbol{\mu} \in \mathbb{R}^r_+$ are nonnegative, so their multiplications should also be nonnegative. The QP-lower-bounding LMI is,

Algorithm 3: Constrained LMI

Input: $\boldsymbol{y}$, $\boldsymbol{Q}$, $\boldsymbol{\varphi}$, $\boldsymbol{A}$, $\boldsymbol{b}$, $\boldsymbol{A}_{eq}$, $\boldsymbol{b}_{eq}$
Output: p^*_{low}, $\boldsymbol{M}$ (or Infeasibility)
1 Solve (or find infeasibility certificate):

$$p^*_{low} = \min_{\boldsymbol{\lambda} \in \mathbb{R}^q,\ \boldsymbol{M}} \quad \text{Objective (3.33)} \tag{3.39a}$$
$$\text{Simplex (3.34a)-(3.34b), KKT (3.37)} \tag{3.39b}$$
$$\text{Valid (3.35), (3.38)} \tag{3.39c}$$
$$M_{11} = 1,\ \boldsymbol{M} \in \mathbb{S}^{1+n+m+r}_+ \tag{3.39d}$$

The accuracy of $p^*_{low} \leq p^*$ from Algorithm 3 may be improved if an upper bound for μ_k^2 $(M_{\mu_k \mu_k})$ was known for each k. Bisection-based approaches with convex cost heuristics may also be applied to the presented LMIs [83].

3.4 Numerical Examples

This section contains small-scale toy examples with visuals, to develop intuition. The examples will showcase flaws in the approximate projection method [74] when an inconsistent basis is supposed, and the robustness of the bi-level method. The proposed distance-bounding methods will also be displayed. Future works will showcase the method for larger-scale examples and will be applied to real data.

Assume that an observed human decision (or trajectory) can be represented by a vector $y \in \mathbb{R}^2$, or by a vector $y^c \in X \subset R^3$ and that it is generated via an unknown process (as is actually the case in real-world applications). Assume bases $\boldsymbol{\phi}$ and $\boldsymbol{\phi}^c$ contain 5 and 3 quadratic cost functions respectively, believed to be underlying the decision-making (or trajectory-generation). Figure 3.3 depicts the 2-dimensional test point $y \in \mathbb{R}^2$, and the set of unconstrained global optima $\mathcal{G}$ which is generated using $\boldsymbol{\phi}$. Figure 3.4 depicts the 3-dimensional test point $y^c \in \mathbb{R}^3$, the feasible set X, and the set of constrained global optima $\mathcal{G}^c$ generated by using $\boldsymbol{\phi}^c$.

For the example shown in Figure 3.3, the numerical values of the matrices of the examples are given in equation (3.41) below. The test point and the numerical values of the retrieved points are given in equation (3.40) below.

$$\boldsymbol{y} = \begin{bmatrix} 6 \\ 2 \end{bmatrix} \quad \boldsymbol{x}_{\text{Proj}_{\mathcal{G}}(\boldsymbol{y})} = \begin{bmatrix} 2.205 \\ 0.662 \end{bmatrix} \quad \boldsymbol{x}_{\text{ProjGM}} = \begin{bmatrix} 2.216 \\ 0.631 \end{bmatrix} \quad \boldsymbol{x}_{\text{Keshavaraz}} = \begin{bmatrix} -0.750 \\ 1.287 \end{bmatrix} \quad \boldsymbol{x}_{\text{LMI}} = \begin{bmatrix} 2.845 \\ 0.727 \end{bmatrix} \tag{3.40}$$

$$\boldsymbol{Q}_1 = \begin{bmatrix} 0.615 & 0.033 \\ 0.033 & 1.400 \end{bmatrix} \qquad \boldsymbol{x}_1^f = \begin{bmatrix} -2.559 \\ 2.245 \end{bmatrix} \tag{3.41a}$$

$$\boldsymbol{Q}_2 = \begin{bmatrix} 2.102 & 1.035 \\ 1.035 & 1.426 \end{bmatrix} \qquad \boldsymbol{x}_2^f = \begin{bmatrix} 0.541 \\ 3.946 \end{bmatrix} \tag{3.41b}$$

$$\boldsymbol{Q}_3 = \begin{bmatrix} 1.124 & 0.019 \\ 0.019 & 0.898 \end{bmatrix} \qquad \boldsymbol{x}_3^f = \begin{bmatrix} 2.378 \\ -3.303 \end{bmatrix} \tag{3.41c}$$

$$\boldsymbol{Q}_4 = \begin{bmatrix} 1.205 & 0.262 \\ 0.262 & 1.450 \end{bmatrix} \qquad \boldsymbol{x}_4^f = \begin{bmatrix} 1.551 \\ -2.319 \end{bmatrix} \tag{3.41d}$$

$$\boldsymbol{Q}_5 = \begin{bmatrix} 1.527 & -0.192 \\ -0.192 & 1.440 \end{bmatrix} \qquad \boldsymbol{x}_5^f = \begin{bmatrix} 1.909 \\ -0.705 \end{bmatrix} \tag{3.41e}$$

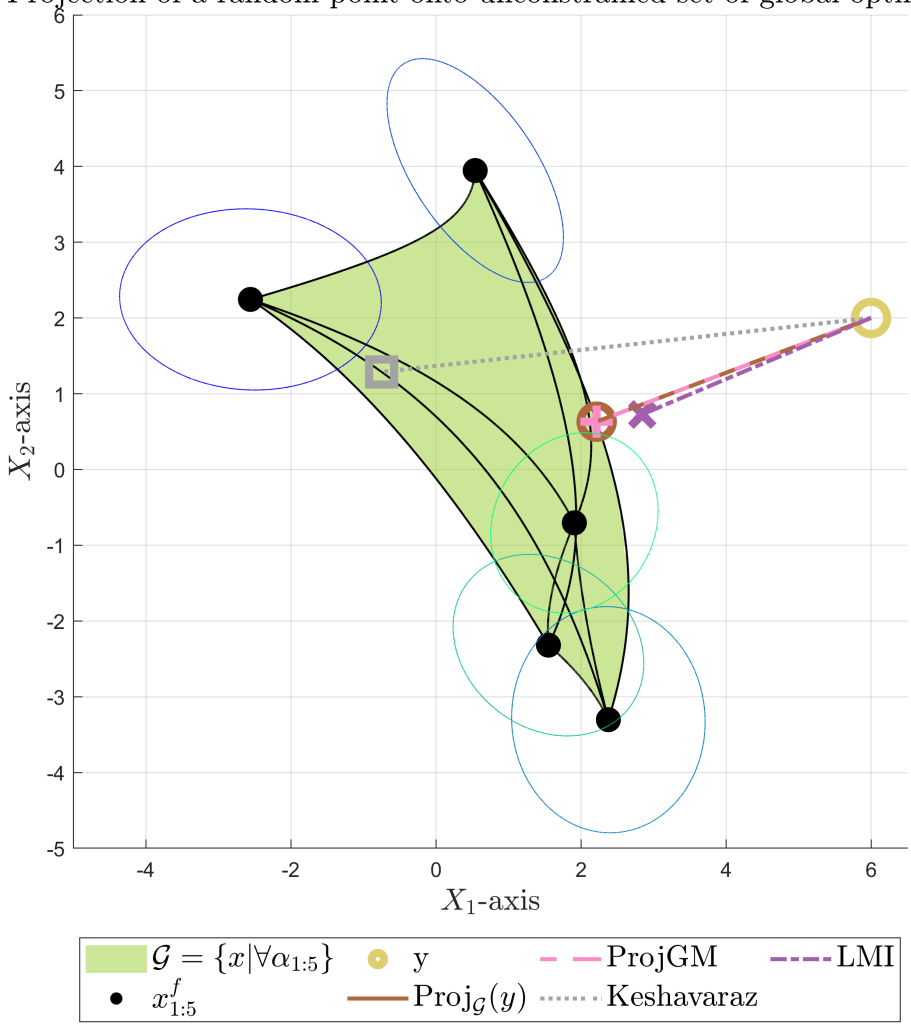

Figure 3.3: Comparison of the projection onto an unconstrained set of optima $\mathcal{G}$.

Both in Figure 3.3 and 3.4 the actual minimum distance projection $\text{Proj}_{\mathcal{G}}(y)$ is shown as reference and is computed by a combined brute-force grid search and local bi-level search on the cost function parametrization $\boldsymbol{\omega} \in \Delta^5$ and $\boldsymbol{\omega} \in \Delta^3$ respectively. The minimum distance local bi-level formulation result, initialized with $\omega_i = 0.2$, is annotated as ProjGM and shown, alongside the Keshavaraz minimum KKT-constraint violation formulation [74]. The M_{x1} entry of the PSD matrix output by Algorithm 2 is also shown.

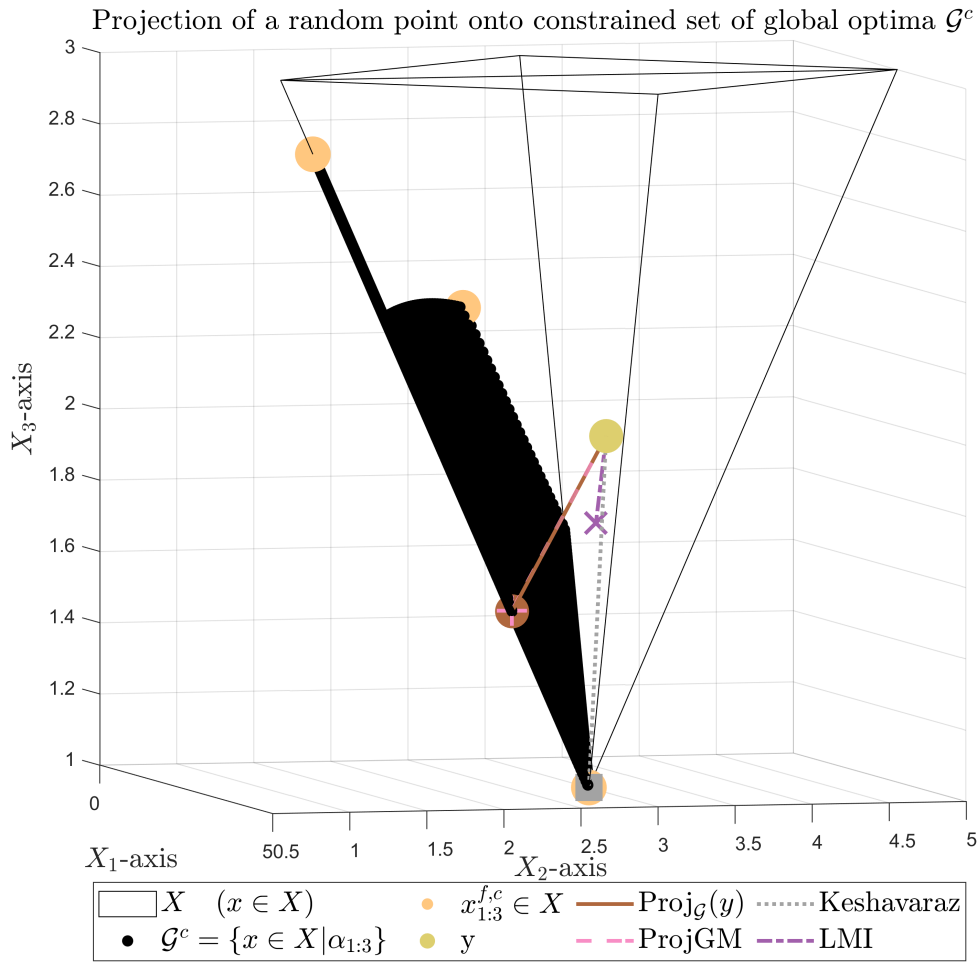

Figure 3.4: Comparison of the projection onto a constrained set of optima $\mathcal{G}^c$.

From Figures 3.3 and 3.4 it is possible to see that the approximate Keshavaraz method can impute a strongly inconsistent objective if the test point is outside the set of global optima $\mathcal{G}$.

The numerical values used in the example from Figure 3.4 are given in equation (3.42) below.

$$\boldsymbol{Q}_1 = \begin{bmatrix} 1 & 0 & 0 \\ 0 & 1 & 0 \\ 0 & 0 & 1 \end{bmatrix} \quad \boldsymbol{\varphi}_1 = \begin{bmatrix} 0 \\ 0 \\ 0 \end{bmatrix} \quad \boldsymbol{x}_1^f = \begin{bmatrix} 0 \\ 0 \\ 0 \end{bmatrix} \quad \boldsymbol{x}_1^{f,c} = \begin{bmatrix} 2.333 \\ 2.333 \\ 2.333 \end{bmatrix} \tag{3.42a}$$

$$\boldsymbol{Q}_2 = \begin{bmatrix} 1 & 0 & 0 \\ 0 & 3 & 0 \\ 0 & 0 & 1.300 \end{bmatrix} \quad \boldsymbol{\varphi}_2 = \begin{bmatrix} -2 \\ 0 \\ 0 \end{bmatrix} \quad \boldsymbol{x}_2^f = \begin{bmatrix} 2 \\ 0 \\ 0 \end{bmatrix} \quad \boldsymbol{x}_2^{f,c} = \begin{bmatrix} 3 \\ 1.209 \\ 2.791 \end{bmatrix} \tag{3.42b}$$

$$\boldsymbol{Q}_3 = \begin{bmatrix} 0.500 & 0 & 0 \\ 0 & 1.600 & 0 \\ 0 & 0 & 2 \end{bmatrix} \quad \boldsymbol{\varphi}_3 = \begin{bmatrix} 0 \\ -6.400 \\ 0 \end{bmatrix} \quad \boldsymbol{x}_3^f = \begin{bmatrix} 0 \\ 4 \\ 0 \end{bmatrix} \quad \boldsymbol{x}_3^{f,c} = \begin{bmatrix} 3 \\ 3 \\ 1 \end{bmatrix} \tag{3.42c}$$

The inequality constraint matrices from the example from Figure 3.4 are given in equation (3.43) below.

$$\boldsymbol{A} = \begin{bmatrix} 1 & 1 & -1 \\ 1 & -1 & -1 \\ -1 & 1 & -1 \\ -1 & -1 & -1 \end{bmatrix} \qquad \boldsymbol{b} = \begin{bmatrix} 5 \\ -1 \\ -1 \\ -7 \end{bmatrix} \tag{3.43a}$$

The LMI Algorithms 2 and 3, are designed to invalidate a proposed set of basis functions with respect to a data set. In other words, the algorithm is able to say whether IOC with proposed basis functions can be successfully applied to a given data set.

Given a data set of 100 points $y \in \mathbb{R}^2$ generated by adding Gaussian noise to the shown test point in Figure 3.3, the distance of each of them to the set of global optima is calculated via different methods. The mean distance to the set of global optima for different methods is, in ascending order, $d_{\text{LMI}} = 3.78$, $d_{\text{ProjGM}} = 4.09$ and $d_{\text{Keshavaraz}} = 6.98$, the true value being $d_{Proj_{\mathcal{G}}(y)} = 4.09$.

In practice, for higher-dimensional data, running the bi-level method may be expensive. If the Keshavaraz method does not produce a zero or extremely close-to-zero error, it is useful to be able to run the LMI algorithm to check the lower bound of the distance from the set of global optima. If the lower bound is higher than the desired error in data replication, we can conclude that the proposed set of basis functions $\boldsymbol{\phi}$ is not good enough to represent the data.

MATLAB (2021b) code to replicate figures and experiments is publicly available at `https://github.com/jarmill/inverse-optimal`. Dependencies include Mosek [130] and YALMIP [42].

3.5 Extensions

This section will detail extensions of the current work and some discussion of future research directions.

3.5.1 Piecewise Functions and Convex Lifts

The method of convex lifts [7, 87] may be applied to solve the PGM problem over some classes of piecewise-defined costs ϕ_j. Assume there exists a set of C^1 functions $\{\xi_{j\ell}(\boldsymbol{x})\}_{\ell=1}^{L_j}$ with L_j finite such that the convex ϕ_j satisfies,

$$\phi_j(\boldsymbol{x}) = \max_{\ell \in 1..L_j} \xi_{j\ell}(\boldsymbol{x}). \tag{3.44}$$

Remark 6. *Convexity is preserved under the pointwise maximum operation (though not under the pointwise minimum).*

Remark 7. *The class of convex piecewise affine functions with* $\xi_{j\ell}(\boldsymbol{x}) = \beta j\ell^T \boldsymbol{x} - \gamma_{j\ell}$ *for* $\beta j\ell \in \mathbb{R}^{n\times 1}, \gamma_{j\ell} \in \mathbb{R}$ *may be expressed as an instance of* (3.44).

New variables τ_j may be added for every max-representable function $\phi_j(\boldsymbol{x})$, forming the equivalent optimization problems with equal objectives:

$$f^* = \min_{\boldsymbol{x}\in\boldsymbol{x}} \sum_{j=1}^m \phi_j(\boldsymbol{x}) \tag{3.45a}$$

$$\iff$$

$$\begin{aligned} f^* = \min_{\boldsymbol{x}\in\boldsymbol{x},\ \tau\in\mathbb{R}^m} \quad & \sum_{j=1}^m \tau_j \\ \text{subject to} \quad & \alpha_j \xi_{j\ell}(\boldsymbol{x}) \leq \tau_j, \qquad \forall \ell = 1..L_j,\ j = 1..m. \end{aligned} \tag{3.45b}$$

The formerly non-differentiable objectives $\phi_j(\boldsymbol{x})$ from Equation (3.45a) are lifted into the constrained problem from Equation (3.45b) where each $\xi_{j\ell}(\boldsymbol{x})$ is differentiable for all $\boldsymbol{x} \in \boldsymbol{x}$. KKT equations may then be written for (3.45b) and then utilized in (3.11) to describe the cone $\hat{\mathcal{G}}^c(\boldsymbol{x}, \tau, \boldsymbol{\omega}, \boldsymbol{\mu}, \boldsymbol{\lambda})$ for use in the constrained PGM Problem 7.

Remark 8. *Minimization of the L_1 norm $\|\boldsymbol{x}\|_1$ may be expressed as $\min \sum_{i=1}^n t_i : \ -t_i \leq x_i \leq t_i$ in $2n$ inequality constraints by adding n new variables $\{t_i\}_{i=1}^n$ for use in constrained PGM. L_p norms with rational $p \in [1, \infty)$ admit second-order-cone representations [39] through lifting, and can therefore be members of the dictionary $\boldsymbol{\phi}$.*

A rank-1 solution M of (3.36) certifies that $p^*_{low} = p^*$ from (3.8), and the optimal $(\boldsymbol{x}, \boldsymbol{\omega})$ may be read from $M_{\boldsymbol{x}1}$ and $M_{\boldsymbol{\omega}1}$

3.5.2 Projection onto Local Minimizers

This paper was restricted to convex cost functions in $\boldsymbol{\phi}$ and convex sets $\boldsymbol{x}$, with an additional polynomial requirement for PGM. Problem 2 may be extended to finding the minimum distance p^* between y and some local minimizer of $f_{\boldsymbol{\omega}}(\boldsymbol{x})$. Theorem 12.6 (Eq. (12.65)) of [28] outlines second-order necessary conditions for a point $\boldsymbol{x}^*$ to be a local minimizer. In the unconstrained case, the Hessian matrix $\nabla_x^2 f_{\boldsymbol{\omega}}(\boldsymbol{x})$ must be PD in addition to $(\boldsymbol{x}, \boldsymbol{\omega})$ satisfying the first-order condition $\nabla_x f_{\boldsymbol{\omega}}(\boldsymbol{x}) = 0$. The constrained case with non-convex functions requires more delicacy, as the quadratic form $w \to w^T \nabla_x^2 f_{\boldsymbol{\omega}} q(\boldsymbol{x}) w$ must be positive for all $w \neq 0$ vectors inside the Critical Cone (Eq. (12.53) of [28]) formed by $(\boldsymbol{x}, \boldsymbol{\lambda}, \boldsymbol{\mu})$.

3.5.3 Polynomial Optimization

The PGM programs 5 and 7 are instances of Polynomial Optimization Problems when $\phi_j(\boldsymbol{x}), g_k(\boldsymbol{x})$ are all convex polynomial functions of $\boldsymbol{x}$. The sets $\hat{\mathcal{G}}(\boldsymbol{x}, \boldsymbol{\omega}), \hat{\mathcal{G}}^c(\boldsymbol{x}, \boldsymbol{\omega}, \boldsymbol{\mu}, \boldsymbol{\lambda})$ are basic semialgebraic sets, and their projections $\mathcal{G}(\boldsymbol{x}), \mathcal{G}^c(\boldsymbol{x})$ are in turn semialgebraic sets. The projections $\mathcal{G}(\boldsymbol{x}), \mathcal{G}^c(\boldsymbol{x})$ may be analyzed by quantifier elimination algorithms such as the Cylindrical Algebraic Decomposition [79]. The moment-SOS hierarchy is a method that yields a rising sequence of lower bounds to the distances p^* by solving a sequence of LMIs in combinatorially increasing size [63]. Theorem 3.2.2 assures (under mild conditions) that the moment-SOS relaxations of the unconstrained Problem 5 will converge at a finite degree. Convergence of the moment-SOS hierarchy for bilevel Polynomial Optimization Problems is established in [110]. The LMI presented in Section 3.3.2 is an instance of the degree-1 moment-SOS hierarchy as enriched with valid constraints.

Given arbitrary convex polynomials $\phi_j(\boldsymbol{x}), g_k(\boldsymbol{x})$, all constraints in $\hat{\mathcal{G}}(\boldsymbol{x}, \boldsymbol{\omega})$ are affine w.r.t. $\boldsymbol{\omega}$. Likewise, the describing constraints of $\hat{\mathcal{G}}^c(\boldsymbol{x}, \boldsymbol{\omega}, \boldsymbol{\mu}, \boldsymbol{\lambda})$ are affine in $(\boldsymbol{\omega}, \boldsymbol{\mu}, \boldsymbol{\lambda})$ all together. A theorem of alternatives may be used to eliminate the affine-dependent groups $(\boldsymbol{\omega})$ or $(\boldsymbol{\omega}, \boldsymbol{\mu}, \boldsymbol{\lambda})$, yielding a set of linked LMI constraints of smaller size that solely depend on $\boldsymbol{x}$ [98]. This reduction in the number of variables decreases the computational burden of solving LMIs as the degree increases. A full presentation and application of polynomial optimization for PGM will take place in sequel work.

3.6 Conclusion

This chapter proposed to use the solution of IOC to express how well a basis of cost functions $\boldsymbol{\phi}$ of an optimization-based model can represent a given measurement $\boldsymbol{y}$. To make this concept intuitive, the concept of the set of global minimizers $\mathcal{G}^c$ $(\mathcal{G})$ has been introduced. Evaluating a basis of cost functions $\boldsymbol{\phi}$ has been formulated as the minimum-distance projection from the observation $\boldsymbol{y}$ to the set of global minima $\mathcal{G}^c$ $(\mathcal{G})$ generated by $\boldsymbol{\phi}$, which is equivalent to finding the global minima of the general non-convex bi-level IOC problem with no reliable way of finding global solutions. Under the assumption that the optimization-based model is a QP, which is satisfied for many practical models, one can derive a lower bound on this distance by using Algorithm 3, through the use of LMI. Medium-sized LMIs are readily solved, which makes this approach applicable to problems of moderate sizes. As the distance between any point from $\mathcal{G}^c$ to $\boldsymbol{y}$ yields an upper bound on the minimum distance, one should strive to make the bound tighter by picking at least a local minimum of the bi-level problem. Important considerations for the implementation of the local search for the bi-level problem were presented in Section 3.3.1.

A basis function set invalidation interpretation of the PGM problem was introduced within Algorithm 1 and further explained through numerical examples in Section 3.4. The geometry of the set of global minimizers $\mathcal{G}^c$ $(\mathcal{G})$ was explored in the constrained and unconstrained cases of convex QP direct models in Section 3.2. Numerical algorithms were implemented to compute the upper and lower bounds on the PGM optima in Section 3.3, and they have been applied to numerical examples, the results of which have been presented and explained in detail in Sections 3.4.

The restriction of the consideration to QP direct models has been discussed. Moreover, three possible extensions to this framework have been proposed *i.e.* allowing for max-representable functions to the basis, allowing for polynomial objective functions in the basis, and finally relaxing the convexity requirements on the basis functions which would make the analytical characterization of global minimizers impossible. This last extension would lead to an interpretation of IOC as a projection onto the set of local minimizers. Apart from the first, for which the introductory work has already been laid out in Section 3.5, the extensions are highly non-trivial and would require a very thorough familiarization with the theory of polynomial optimization [100] and with the theory of nonlinear programming [17].

The application even to simple biomechanical models where constraints are convex would require the polynomial extension mentioned above, but for more complex mechanical systems the full extension of this framework is necessary. Therefore, the proposed method should be applied to convex polynomial IOC problems.

On the theoretical side, apart from tackling the aforementioned extensions, sensitivity methods from the set-valued mathematical analysis could be applied to determine which properties of $\mathcal{G}$ and $\hat{\mathcal{G}}$ are preserved when assumptions are lifted (e.g. does Theorem 3.2.3 hold when all ϕ_j are strongly convex rather than strongly convex quadratic?). The continuity properties of the solution map (3.24) and its selection (3.25) should also be explored for broader classes of direct models [30, 62].

An interesting future application could include performing cost-function discovery in order to generate candidate functions $\phi_j(\boldsymbol{x})$ that would reduce the distance p^* from (3.3) when added to the set of cost functions $\boldsymbol{\phi}$.

Chapter 4

Force Sharing During Gait

This chapter addresses the problem of muscle force sharing in the lower limbs during human gait. Muscle force patterns of human gait have been extensively researched from both medical and engineering viewpoints to comprehend and rectify pathologies. Nonetheless, answering the question of muscle-force sharing remains necessary due to the complex nature of acquiring precise measurements of individual muscle forces, often necessitating the use of intrusive devices. A substantial body of literature, employing diverse objective functions, has postulated that muscle-force sharing might be a consequence of an optimization process. This chapter advocates the utilization of optimal control to determine muscle force sharing.

IOC is used to determine an objective function. The bilevel and the IKKT methods, two prevalent methods of IOC, were examined. The identified objective functions were subsequently applied to predict muscle forces during gait, and their precision was compared with a comprehensive array of biological cost functions found in the existing literature. The best prediction was attained by the objective function retrieved by the bilevel IOC method, registering a Root Mean-Squared Error (RMSE) of 176N (162N) and a correlation coefficient of 0.76 (0.68) during the stance (swing) phase of the gait cycle. Following this, these predictions of muscle force were leveraged to calculate Joint Stiffness (JS), exhibiting an average RMSE of 42 Nm.rad^{-1} and a correlation coefficient of 0.90 in contrast to the reference.

The bilevel method prevailed over its counterpart, the IKKT method, which notably underperformed on this task. An elaboration on this issue has been provided through a reduced and simplified numerical example.

4.1 Introduction

Addressing mobility impairments in individuals afflicted by neuromuscular disorders constitutes a challenge, necessitating comprehensive rehabilitation strategies to facilitate gait restoration [125]. To this end, a variety of assistive robots have been innovated to support individuals with impediments in walking [82, 125]. In the context of controlling a robot while interacting closely with a human, a crucial challenge is developing a robust controller capable of realizing adaptive impedance behavior: recognizing and responding to impedance requirements effectively. A critical aspect of human-robot interaction is the formulation of a sturdy controller, able to modulate JS [125]. This chapter is concerned with the prediction of the distribution of muscle forces as a mechanism for interpreting JS, acting as a fixed component of mechanical impedance [5]. Co-contraction, or the concurrent activation of muscles within antagonistic settings relative to a joint, alters the level of JS. It is a pivotal mechanism employed by the central nervous system to control movement precision, stability, speed, and energy utilization. Since the muscle groups operating a joint outnumber the degrees

of freedom implicated in a motion, co-contraction presents a mathematically indeterminate problem [8]. This study will leverage constrained optimization methodologies, a conventional approach to addressing indeterminate problems [20].

Measurements of muscle forces can be conducted employing invasive electromyographic sensors, coupled with sophisticated identification methodologies necessitating individual-specific calibration [103]. The complexities in estimation have motivated the application of optimization techniques [56] to solve the muscle force sharing problem. In light of the emergence of approaches that are based on model predictive control [142], possessing an optimization-centric model for the distribution of muscle force represents a substantial advantage [125].

The literature proposes several optimization objectives related to muscle endurance and energy [80]. They can be classified into minimizing muscle activations [66], muscle forces [109], and muscle stresses [81] with different physiological scaling factors. The muscle force norms, from L_1 to L_5, are the most commonly used minimization objectives, as experimental studies showed that muscle endurance is inversely related to these objectives [128]. The muscle stress criterion accounts for the capacity of muscles to produce different amounts of force by normalizing the muscles' forces by their physiological cross-sectional area. Some objective functions also account for the fact that maximal muscle force is variable at each time sample depending on the muscle's length and velocity.

However, even if these objectives were widely compared with actual human data, they were evaluated separately using various metrics, usually considering muscles actuating a single joint and over the whole gait cycle. As of today, there is no consensus on which objective function best predicts muscle force sharing during gait. This study shows that a hybrid objective function would be more suitable for predicting human muscle force sharing. This is supported by the literature on human motor control and robotics which has shown that repetitive and constrained human motions such as gait could be modeled and predicted using an optimal control process with a hybrid objective function [69, 77, 108, 111]. However, this has never been done for the muscle force-sharing problem.

The use of IOC methods has been extensively studied to determine the objective function used by humans to generate motion. IOC methods rely on parametric representations of the objective function, most often as affine combinations of interpretable basis functions. Studies usually refer to the parameters of this affine combination as basis or objective function weights and attempt to identify them from data [69, 77, 111, 122]. Because of its structure, one standard IOC method is referred to as the bilevel [99] approach. This approach consists of two nested optimization processes and it aims to identify the basis function weights that minimize the RMSE between observed motions and motions predicted by the DOC process with the given basis function weights. This approach suffers from its long execution time [69, 77].

A second, approximate solution method for the IOC problem was proposed based on a relaxation of the KKT optimality conditions [74, 88], reducing IOC to a convex minimization over the basis function weights [122]. Studies have referred to this method as the IKKT [115, 139]. These studies argue that the KKT residual presents a reasonable heuristic to minimize, boasting its fast execution time [74, 88, 122, 140]. Aswani et al. [120] were probably the only ones that severely questioned this approach and showed that, contrary to the bilevel approach, the IKKT approach does not yield a statistically consistent estimation of the objective function in the presence of noisy data. Furthermore, Colombel et al. [139] recently demonstrated that a small value of the KKT residual does not imply a consistent objective function identification. As such, it does not represent a good metric to assess the quality of the identified objective function. In this context, this study will show that IKKT was not applicable to the muscle-force sharing problem with the underlying model and data.

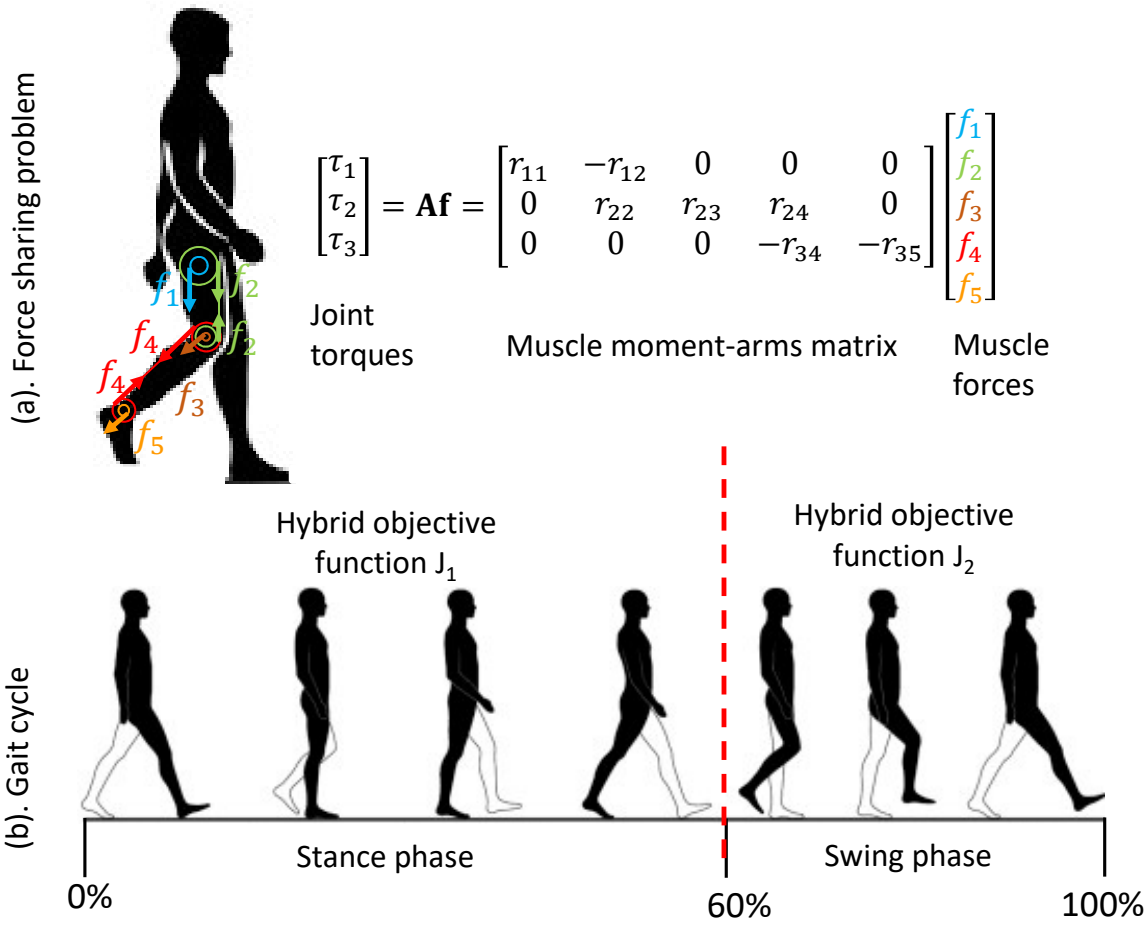

Figure 4.1: (a) Force sharing problem. (b) Gait cycle definition.

Moreover, a counterexample to the IKKT procedure was designed to show that identifying a DOC model using IKKT may result in the largest distance between model predictions and data.

This chapter proposes to evaluate how well a basis of objective functions proposed in the literature on biomechanics predicts muscle forces during gait. The muscle forces can then be used to assess JS. The main contributions of this work can be summarized as follows:

- Solving the muscle force sharing problem using different competing objective functions,
- using IOC to identify a hybrid objective function based on human data,
- comparing bilevel and IKKT approaches in Section 4.3.1,
- counterexample to the IKKT approach in Section 4.3.2.

4.2 Methods

4.2.1 Muscle-force Sharing Problem

As represented in Figure 4.1.a, for a musculoskeletal model with n_j joints and n_m muscles, the force sharing problem consists in finding the vector of instantaneous muscle forces $\boldsymbol{f}_t \in \mathbb{R}^{n_m}_+$ that is generated to produce a vector of instantaneous joint torques $\boldsymbol{\tau}_t \in \mathbb{R}^{n_j}$. At a particular instant in time t, muscle forces and joint torques can be related by the following

linear relation:

$$\boldsymbol{A}_t \boldsymbol{f}_t = \boldsymbol{\tau}_t \tag{4.1}$$

where $\boldsymbol{A}_t \in \mathbb{R}^{n_j \times n_m}$ is the matrix of instantaneous muscle moment-arms about the joints' rotation axes. As represented in Fig 4.1.a a muscle can articulate multiple joints thus the columns of matrix $\boldsymbol{A}_t$ may have multiple non-zero elements.

Given torque and moment-arms, $\boldsymbol{\tau}_t$ and $\boldsymbol{A}_t$, there are an infinite number of force-vectors $\boldsymbol{f}_t$ that could produce the torque $\boldsymbol{\tau}_t$, as this is a redundant problem with $n_m > n_j$.

4.2.2 Objective Functions Basis

The literature provides many biologically plausible criteria to predict muscle forces during gait. Table. 4.1 presents the 15 retained objective functions $\phi_1, \ldots, \phi_{15}$ [20, 36, 51]. All of these objective functions are convex functions of the muscle force vector.

The time-dependent parameters of the objective functions in Table 4.1 are: $\boldsymbol{f}_{\min t}$ minimal muscle forces (equal to the passive forces); $\boldsymbol{f}_{\max t}$ maximal muscle forces; $\mathbf{vmt}_t$ muscle tendon velocities; $\boldsymbol{\tau}_{\max t}$[1] maximal muscle torques (with all muscle forces set to 0 except one set to its maximum $\boldsymbol{f}_{\max t}$). The time-constant parameters of the objective functions in Table 4.1 are: $\boldsymbol{f}_0$ maximal muscle isometric force; $\mathbf{pcsa}$ muscle physiological cross-sectional areas; $\mathbf{m}$ muscle masses. All musculoskeletal parameters involved in the computation of the objective functions, and later on, the JS, were obtained from the study of Li et al. [144] and correspond to calibrated values.

The basis objective functions corresponding to indices $i = 1, 2, 3, 4$ are norms of the unscaled muscle force amplitude vector and are guided by the assumption that the central nervous system (CNS) attempts to minimize load in muscles during motion [11, 20, 36]. These objective functions were previously linked to energy minimization [20]. Stronger muscles will tend to be more affected by these objective functions, in particular as we consider higher-order norms of the muscle amplitudes vector. In principle, when minimizing ϕ_1 all muscle amplitudes will be equally minimized, but minimizing ϕ_3 implies prioritizing minimization of the muscle amplitudes of the few strongest muscles while minimizing ϕ_4 prioritizes only the strongest muscle. As such ϕ_1 will stimulate behavior where all unscaled muscle force amplitudes are kept as low as possible. In contrast, ϕ_4 will stimulate behavior where the strongest muscles' force amplitudes will be controlled, but the weaker muscles will have the freedom to adjust.

Guided by similar assumptions of the CNS tending towards minimal load, basis objective functions with indices $i = 5, 6, 7, 8$ correspond to norms of the muscle activation vector [20, 36]. These objective functions consider scaled muscle force amplitudes. The scale factors render the minimization independent of the muscles' relative strength, minimizing only how much a muscle is pulling compared to the maximum it can do. Moreover, the dependence of the maximum muscle force upon the current muscle state (*i.e.* current muscle length lmt_i, current muscle velocity vmt_i, ...) rendering these objectives more physiologically realistic [20]. Minimizing ϕ_5 favors activating as few muscles as possible and allows for high activations in individual muscles while minimizing ϕ_8 favors low activations for individual muscles and allows for the activation of many muscles.

Indexed by $i = 9, 10, 11, 12$ are the norms of the muscle stress vector [11, 20, 36, 51]. Muscle stresses have been linked to muscle endurance, and minimizing muscle stresses is therefore correlated to conserving endurance [20]. These objective functions represent the norms of the scaled muscle force amplitude vector, where each muscle force is scaled according to the inverse of its size (*i.e.* cross-sectional area). Thus the minimization of these functions pre-

[1] $\boldsymbol{\tau}_{\max ti} = \boldsymbol{A}_t \begin{bmatrix} 0 & \ldots & f_{\max i} & \ldots & 0 \end{bmatrix}^T$

vents muscles from producing forces disproportionately large compared to their size. Similar to previous analyses, ϕ_9 favors few muscles pulling with disproportionate strength but allows for large disproportionality, while ϕ_{12} favors small disproportionalities but allows for many muscles to pull with disproportionate strength.

The objective function ϕ_{13} minimizes the L_2 norm of instantaneous muscle powers [11], and relates to total work done by the muscles, promoting energy efficiency. The objective function ϕ_{14} minimizes the L_2 norm of the vector containing muscle forces scaled by the maximal muscle moments [20]. The maximal muscle moment is the sum of absolute values of the moments in all joints that the muscle could produce at maximum contraction. This objective function is informed by the state of the muscle, as the maximal muscle moments depend on muscle length and velocity. Moreover, the body state is also taken into account as maximal muscle moments take into account the instantaneous geometry of the musculoskeletal system. Finally, the objective function ϕ_{15} expresses an approximation of the total energy consumption of the muscle obtained by considering muscle metabolism [51, 106]. It is composed of two terms corresponding to two major energy-consuming processes in the muscle. One component is related to the attachment and detachment of cross-bridges between myosin and actin during muscle contraction. The number of bridges is proportional to the muscle force, and inversely to physiological cross-sectional area. The other component approximates the energy consumed during the re-uptake of calcium in the sarcoplasmic reticulum, which can be related to the ratio of muscle force to maximal isometric muscle force.

All of the objective functions that contain radical expressions (*i.e.* n-th roots) are usually presented without the radical within the literature. The radicals have been introduced to make the sensitivity of the minima of the affine combination of these functions (*i.e.* $\sum_{i=1}^{m} \omega_i \phi_i$) more uniform. This implies that no matter the current value of parameters $\boldsymbol{\omega}$, similar changes in the parameters of the affine combination $\|\Delta\boldsymbol{\omega}\|$ produce a similar change in the solution to the optimization problem $\|\Delta \boldsymbol{f}^*\|$. The introduction of radicals does not modify the minima of the individual radicand expressions. Furthermore, introducing radicals does not affect the convexity of the radicand expressions, as all the radicand expressions are positive definite and their polynomial degree is equal to that of the radical. Effectively, all of the radical expressions scale linearly with muscle force vector amplitude.

Therefore, introducing radicals did not fundamentally modify what the radicand expressions mean, nor did they modify their mathematical properties. Radicals simply reduce the need for a fine-grain grid search when performing IOC.

4.2.3 Direct Optimal Control

Supposing that at a particular time t the joint torques $\boldsymbol{\tau}_t$ and the matrix of instantaneous moment arms $\boldsymbol{A}_t$ are known, along with a vector of other parameters $\boldsymbol{\theta}_t \in \Theta$ (like instantaneous muscle velocity vmt_t or the physiological muscle cross-sectional area pcsa), the prediction of the muscle forces can be obtained by solving the following optimization problem:

$$\begin{aligned} \min_{\boldsymbol{f}_t} \quad & J(\boldsymbol{\theta}_t, \boldsymbol{f}_t) \\ \text{subject to} \quad & \boldsymbol{A}_t \boldsymbol{f}_t = \boldsymbol{\tau}_t \\ & \boldsymbol{f}_{\max t} \geq \boldsymbol{f}_t \geq \boldsymbol{f}_{\min t} \end{aligned} \tag{4.2}$$

Solving this DOC requires determining muscle forces $\boldsymbol{f}_t$, that minimize a certain parametric criterion $J(\boldsymbol{\theta}_t, \boldsymbol{f}_t) : \Theta \times \mathbb{R}^{n_m} \mapsto \mathbb{R}$, that can produce desired joint torques $\boldsymbol{\tau}_t$ with physical limitations such as that a muscle can only pull and have a stiffness ($\boldsymbol{f}_t \geq \boldsymbol{f}_{\min t}$) and that a maximal potential force exists ($\boldsymbol{f}_{\max t} \geq \boldsymbol{f}_t$). Parameters $\boldsymbol{f}_{\min t}$ and $\boldsymbol{f}_{\max t}$ correspond

Table 4.1: Investigated 15 most common objective functions from the biomechanics literature [20, 36, 51].

Name	Symbol	Formula
Sum of muscle forces	ϕ_1	$\frac{1}{n}\sum_{i=1}^{n} f_{ti}$
Sum of squares of muscle forces	ϕ_2	$\left(\frac{1}{n}\sum_{i=1}^{n} f_{ti}^2\right)^{\frac{1}{2}}$
Sum of cubes of muscle forces	ϕ_3	$\left(\frac{1}{n}\sum_{i=1}^{n} f_{ti}^3\right)^{\frac{1}{3}}$
Maximum muscle forces	ϕ_4	$\max_{i=1,\dots,n} f_{ti}$
Sum of muscle activations	ϕ_5	$\frac{1}{n}\sum_{i=1}^{n} \frac{f_{ti}-f_{\min ti}}{f_{\max ti}-f_{\min ti}}$
Sum of squares of muscle activations	ϕ_6	$\left(\frac{1}{n}\sum_{i=1}^{n} \left(\frac{f_{ti}-f_{\min ti}}{f_{\max ti}-f_{\min ti}}\right)^2\right)^{\frac{1}{2}}$
Sum of cubes of muscle activations	ϕ_7	$\left(\frac{1}{n}\sum_{i=1}^{n} \left(\frac{f_{ti}-f_{\min ti}}{f_{\max ti}-f_{\min ti}}\right)^3\right)^{\frac{1}{3}}$
Maximum muscle activations	ϕ_8	$\max_{i=1,\dots,n} \frac{f_{ti}-f_{\min ti}}{f_{\max ti}-f_{\min ti}}$
Sum of muscle stresses	ϕ_9	$\frac{1}{n}\sum_{i=1}^{n} \frac{f_{ti}}{\mathrm{pcsa}_i}$
Sum of squares of muscle stresses	ϕ_{10}	$\left(\frac{1}{n}\sum_{i=1}^{n} \left(\frac{f_{ti}}{\mathrm{pcsa}_i}\right)^2\right)^{\frac{1}{2}}$
Sum of cubes of muscle stresses	ϕ_{11}	$\left(\frac{1}{n}\sum_{i=1}^{n} \left(\frac{f_{ti}}{\mathrm{pcsa}_i}\right)^3\right)^{\frac{1}{3}}$
Maximum of muscle stresses	ϕ_{12}	$\max_{i=1,\dots,n} \frac{f_{ti}}{\mathrm{pcsa}_i}$
Sum of squares of muscle powers	ϕ_{13}	$\left(\frac{1}{n}\sum_{i=1}^{n} (f_{ti}\mathrm{vmt}_{ti})^2\right)^{\frac{1}{2}}$
Sum of squares of musculo-tendon forces scaled by maximal muscle moments	ϕ_{14}	$\left(\frac{1}{n}\sum_{i=1}^{n} \left(\frac{f_{ti}}{\lVert \boldsymbol{\tau}_{\max ti} \rVert_1}\right)^2\right)^{\frac{1}{2}}$
Metabolic energy-related function	ϕ_{15}	$\left(\frac{1}{n}\sum_{i=1}^{n} \frac{\mathrm{m}_i}{2}\left(\frac{f_{ti}-f_{\min ti}}{f_{0i}} + \left(\frac{f_{ti}-f_{\min ti}}{\mathrm{pcsa}_i}\right)^2\right)\right)^{\frac{1}{2}}$

to activation 0 and 1 and depend on the contraction dynamics parameters (i.e., Hill-type model) at each instant of time: $\boldsymbol{f}_{\min t}$ (at activation 0) is the muscle passive force, therefore $\boldsymbol{f}_t - \boldsymbol{f}_{\min t}$ is the muscle active force and $\frac{\boldsymbol{f}_t - \boldsymbol{f}_{\min t}}{\boldsymbol{f}_{\max t} - \boldsymbol{f}_{\min t}}$ stands for the instantaneous activation (between 0 and 1). Due to the contraction dynamics, instantaneous $f_{\max ti}$ can be superior to the constant maximal isometric force f_{0i} of the i-th muscle.

In Section 4.2.4, it will be supposed that $J(\boldsymbol{\theta}_t, \boldsymbol{f}_t)$ is the objective at the origin of the

collected human force data. A hybrid objective function form [69, 74, 120] is assumed which takes the shape of a non-zero conic combination of known features $\phi_i(\boldsymbol{\theta}_t, \boldsymbol{f}_t)$ with a weight vector $\boldsymbol{\omega} \in \mathbb{R}_+^{n_\phi} \backslash \{0\}$.

$$J(\boldsymbol{\theta}_t, \boldsymbol{f}_t) = J(\boldsymbol{\omega}, \boldsymbol{\theta}_t, \boldsymbol{f}_t) = \sum_{i=1}^{n_\phi} \omega_i \phi_i(\boldsymbol{\theta}_t, \boldsymbol{f}_t) \tag{4.3}$$

One can suppose that a particular value of $\boldsymbol{\omega} \in \mathbb{R}_+^{n_\phi} \backslash \{0\}$ exists which generated the measured data. Thus, it is assumed that the data is, at each time t, a solution of the parametric optimization problem from Equation (4.2) with the objective function $J(\boldsymbol{\theta}_t, \boldsymbol{f}_t) = J(\boldsymbol{\omega}, \boldsymbol{\theta}_t, \boldsymbol{f}_t)$ for fixed $\boldsymbol{\omega}$. Minimizing $J(\boldsymbol{\omega}, \boldsymbol{\theta}_t, \boldsymbol{f}_t)$ can be interpreted as a scalarization of the multi-objective optimization problem, the objectives being the features ϕ_i, $i = 1, \ldots, n_\phi$. As such, the minimum of such a scalarized problem depends only on the ratios $\frac{\omega_i}{\omega_j}$, $i \neq j$ and not on their absolute values ([41] Ch. 4.7.5). As such, it is sufficient to restrict the consideration of the weight vector $\boldsymbol{\omega}$ to the n_ϕ-dimensional simplex $\Delta^{n_\phi} = \left\{\boldsymbol{\omega} \in \mathbb{R}^{n_\phi} \mid \boldsymbol{\omega} \geq 0,\ \mathbf{1}^T \boldsymbol{\omega} = 1\right\}$. All cost functions, constraints, their gradients, and their hessians have been computed using automatic differentiation through the use of CasADi [124], and all DOC instances throughout the study have been solved using the CasADi interface for the IPOPT [53] solver.

As it will be important in the Subsection 4.2.4, please note that program (4.2) is a nonlinear programming problem, and its solution $\boldsymbol{f}_t^*$ must satisfy the first-order necessary conditions of optimality, under certain constraint qualifications ([41] Ch. 5.2.3). The conditions for problem (4.2) given in (4.4a)-(4.4f) are that for an optimal solution $\boldsymbol{f}_t^*$ there must exist lagrangian multipliers $\boldsymbol{\lambda}_t^*$, where $\boldsymbol{\lambda}_t^* \in \mathbb{R}^{n_j}$, and $\boldsymbol{\mu}_t^*, \boldsymbol{\nu}_t^*$, where $\boldsymbol{\mu}_t^*, \boldsymbol{\nu}_t^* \in \mathbb{R}^{n_m}$, such that

$$\nabla_{\boldsymbol{f}_t} \Phi(\boldsymbol{\theta}_t, \boldsymbol{f}_t^*)\boldsymbol{\omega} + \boldsymbol{A}_t^T \boldsymbol{\lambda}_t^* - \boldsymbol{\mu}_t^* + \boldsymbol{\nu}_t^* = 0 \tag{4.4a}$$
$$\boldsymbol{A}_t \boldsymbol{f}_t^* = \boldsymbol{\tau}_t \tag{4.4b}$$
$$\boldsymbol{f}_{\max t} \geq \boldsymbol{f}_t^* \geq \boldsymbol{f}_{\min t} \tag{4.4c}$$
$$\boldsymbol{\mu}_t^* \geq 0,\ \boldsymbol{\nu}_t^* \geq 0 \tag{4.4d}$$
$$(\boldsymbol{\mu}_t^*)_i(-\boldsymbol{f}_t^* + \boldsymbol{f}_{\min t})_i = 0 \quad i = 1, \ldots, n_m \tag{4.4e}$$
$$(\boldsymbol{\nu}_t^*)_i(\boldsymbol{f}_t^* - \boldsymbol{f}_{\max t})_i = 0 \quad i = 1, \ldots, n_m \tag{4.4f}$$

where $\nabla_{\boldsymbol{f}_t} \Phi(\boldsymbol{\theta}_t, \boldsymbol{f}_t) = \left[\nabla_{\boldsymbol{f}_t} \phi_1(\boldsymbol{\theta}_t, \boldsymbol{f}_t)\ , \ldots, \nabla_{\boldsymbol{f}_t} \phi_{n_\phi}(\boldsymbol{\theta}_t, \boldsymbol{f}_t)\right]$ is the matrix whose columns are gradients of the features, thus $\nabla_{\boldsymbol{f}_t} \Phi(\boldsymbol{\theta}_t, \boldsymbol{f}_t)\boldsymbol{\omega}$ corresponds to the gradient of the objective function $\nabla_{\boldsymbol{f}_t} J(\boldsymbol{\theta}_t, \boldsymbol{f}_t)$.

4.2.4 Inverse Optimal Control

The goal of the IOC process will be to identify the value of the objective function weights $\boldsymbol{\omega}$ that can reproduce the measured data $\boldsymbol{f}_t^{(d)}$ with $t = 0, \ldots, T$ being the time index and $d = 1, \ldots, D$ being the index of reference data sample (*i.e.* gait cycle). These weights may not exist, meaning that no combination of weights $\boldsymbol{\omega}$ will produce the data as the exact solution to the optimization problem (4.2). Multiple effects are then in play [120]:

1. Measurement noise in our data may drive the data away from optimal points of our features.

2. Modeling errors in our features may render them incapable of representing human objectives well enough.

3. Bounded rationality in humans suggests that the data may be sub-optimal for a given model, even should measurements be accurate.

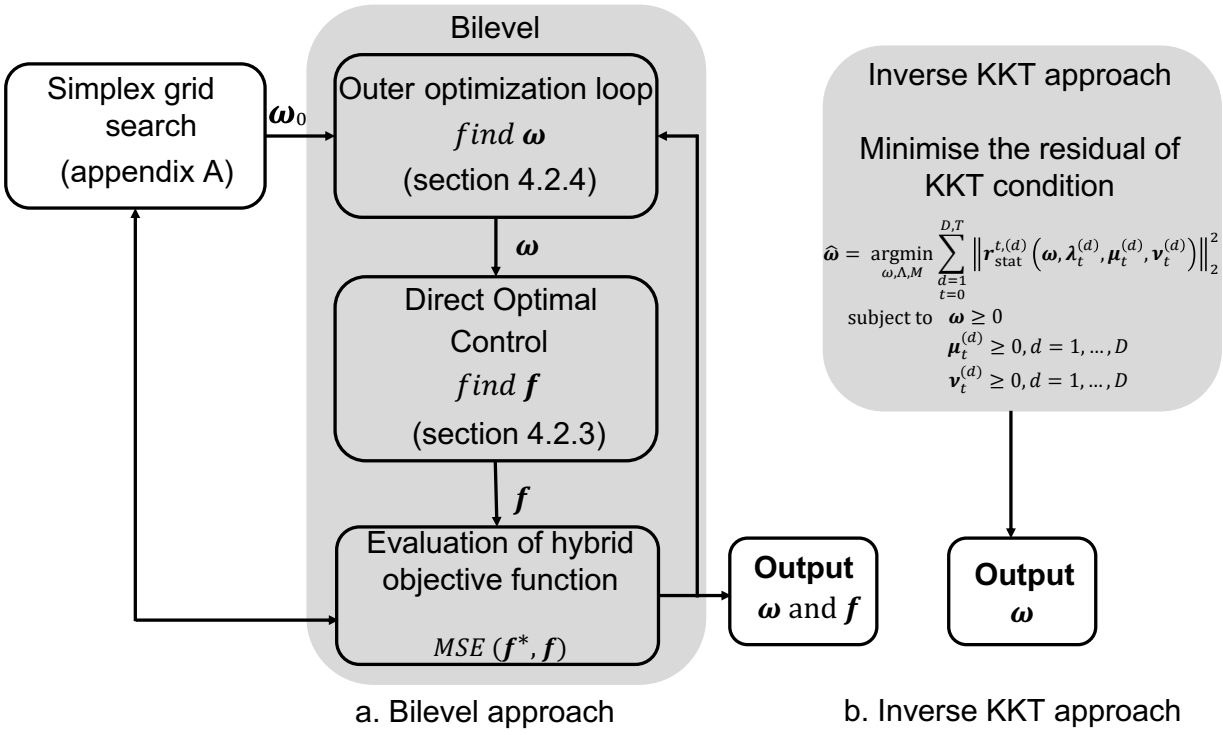

Figure 4.2: Two investigated approaches for solving the IOC problem.

As represented in Figure 4.2, two standard IOC techniques will be compared to investigate how they cope with these effects.

Bilevel IOC

The first is a bilevel formulation [69, 77, 97, 120] that minimizes the sum of squares of L_2-norms between model predictions and the data in an outer loop, subject to the constraint that model predictions are solutions of an inner optimization problem. The identified $\hat{\boldsymbol{\omega}}$ are then the weights producing the least squared error:

$$\begin{aligned} \hat{\boldsymbol{\omega}} = \underset{\boldsymbol{\omega}}{\operatorname{argmin}} \quad & \sum_{\substack{d=1 \\ t=0}}^{D,T} \| \boldsymbol{f}_t^{(d)} - \boldsymbol{f}_t^{*,(d)} \|_2^2 \\ \text{subject to} \quad & \boldsymbol{f}_t^{*,(d)} = \underset{\boldsymbol{f}_t}{\operatorname{argmin}} \quad \sum_{i=1}^{n_\phi} \omega_i \phi_i(\boldsymbol{\theta}_t^{(d)}, \boldsymbol{f}_t) \\ & \qquad\qquad \text{subject to} \quad \boldsymbol{A}_t^{(d)} \boldsymbol{f}_t = \boldsymbol{\tau}_t^{(d)} \\ & \qquad\qquad\qquad\quad \boldsymbol{f}_{\max t} \geq \boldsymbol{f}_t \geq \boldsymbol{f}_{\min t} \end{aligned} \tag{4.5}$$

To solve the bilevel programming problem, a global optimization approach in the outer loop is used. By constructing a grid over the probability-simplex Δ^{n_ϕ}, assigning to $\boldsymbol{\omega}$ the values of the grid points, then calculating the outer-loop objective function, a rough global search is performed [92]. A local gradient-based search is then initiated N times from the N best points $\boldsymbol{\omega}_0$ obtained in the grid search. The justification for the gradient-based search is that the set of optimal solutions of the inner-loop, parametrized by $\boldsymbol{\omega}$ is connected and continuous if the inner-loop objective function features are convex [120].The grid-search has been implemented using a self-implemented simplex grid-point generating function. The local search has been implemented using MATLAB's constrained optimization software *fmincon*

[31].

Inverse KKT IOC

The second technique is a recently widespread method based on a least-squares formulation [74, 88, 111, 139] that minimizes the violation of the satisfaction of the KKT stationarity constraint (4.4a). For simplicity, let us define the stationarity residual of the d-th observation at time t as the left-hand side of Equation (4.4a), where ${\boldsymbol{\mu}_t^{(d)}}_{\mathcal{A}_{\min}}$ and ${\boldsymbol{\nu}_t^{(d)}}_{\mathcal{A}_{\max}}$ represent Lagrangian multiplier vectors whose elements corresponding to inactive constraints have been hard-set to 0.

$$\begin{aligned} r_{\text{stat}}^{t,(d)}(\boldsymbol{\omega}, \boldsymbol{\lambda}_t^{(d)}, \boldsymbol{\mu}_t^{(d)}, \boldsymbol{\nu}_t^{(d)}) = \nabla_{\boldsymbol{f}_t}\Phi(\boldsymbol{\theta}_t^{(d)}, \boldsymbol{f}_t^{(d)})\boldsymbol{\omega} + \boldsymbol{A}_t^T\boldsymbol{\lambda}_t^{(d)} \\ - {\boldsymbol{\mu}_t^{(d)}}_{\mathcal{A}_{\min}} + {\boldsymbol{\nu}_t^{(d)}}_{\mathcal{A}_{\max}} \end{aligned} \tag{4.6}$$

The least squares-squares formulation then stems from the minimization of squares of L_2-norm of the stationarity residuals as follows:

$$\begin{aligned} \hat{\boldsymbol{\omega}} = \underset{\boldsymbol{\omega},\boldsymbol{\Lambda},\boldsymbol{M},\boldsymbol{N}}{\text{argmin}} \quad & \sum_{\substack{d=1 \\ t=0}}^{D,T} \| r_{\text{stat}}^{t,(d)}(\boldsymbol{\omega}, \boldsymbol{\lambda}_t^{(d)}, \boldsymbol{\mu}_t^{(d)}, \boldsymbol{\nu}_t^{(d)}) \|_2^2 \\ \text{subject to} \quad & \boldsymbol{\omega} \geq 0 \\ & \boldsymbol{\mu}_t^{(d)} \geq 0, \ d = 1, \ldots, D \\ & \boldsymbol{\nu}_t^{(d)} \geq 0, \ d = 1, \ldots, D \end{aligned} \tag{4.7}$$

As the residual is a linear function of the basis function weights $\boldsymbol{\omega}$ and stacked equality and inequality lagrangian multipliers, $\boldsymbol{\Lambda}$, $\boldsymbol{M}$, and $\boldsymbol{N}$, the constrained minimization of the sum of squares of residual norms can be reformulated as a constrained least-squares regression to a vector of zeros [115, 122, 139]. All instances of the IKKT have been solved using lsqlin, MATLAB's constrained least-squares solver [31].

4.2.5 Human Observations

Previously published human reference data was used in this study [117, 144]. To our knowledge, it is the only available source providing a reference estimate of muscle forces during gait. A total of 10 gait cycles were collected on a treadmill at a self-selected speed of 0.5m/s.

Joint torques were computed with data from a motion capture system and force-plates [117, 144]. Measurements also included EMG of 16 muscles in each leg using a combination of surface and fine-wire electrodes. The reference muscle forces were obtained after calibrating a state-of-the-art EMG-driven model using the aforementioned data [117]. The calibrated model parameters included those defining the conversion of raw EMG into muscle excitation, muscle excitation into muscle activation via activation dynamics, muscle activation into muscle force via contraction dynamics using a Hill-type muscle-tendon model with rigid tendon, and conversion of muscle force into joint torque via muscle moment-arms [117, 144]. Note that these estimated muscle forces are computed without any objective function for the muscle force-sharing problem.

Gait cycles were segmented automatically and two different phases of the gait cycle were considered as described in Figure 4.1.b: the stance phase from 0 to 60% and the swing phase from 61 to 100% of the gait cycle. Overall the variability of the muscle forces was relatively low, with an average standard deviation of 29.98N across all 35 muscles, all gait cycles, and

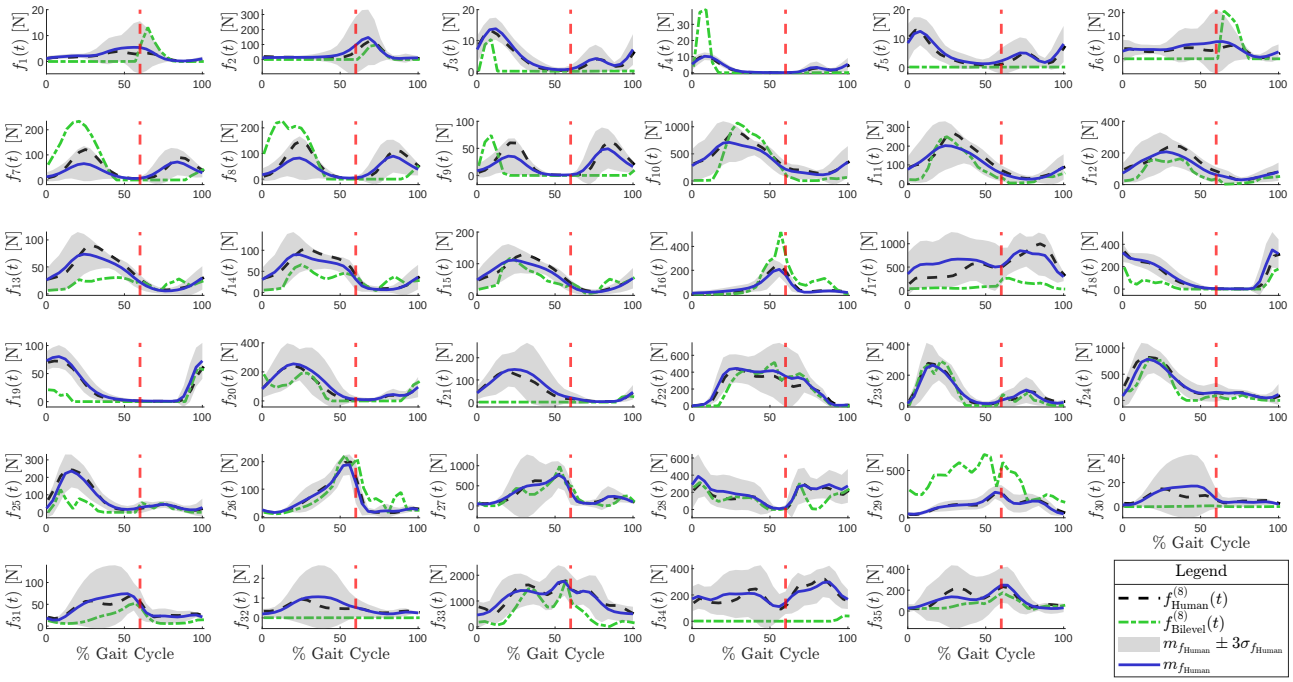

Figure 4.3: Mean (blue lines) and standard deviation (gray areas) of the muscle forces estimated during 10 gait cycles for the 35 investigated muscles [117], with gait-cycle separation (dashed red lines). Estimated muscle forces (dashed black lines) of the 8$^{\text{th}}$ gait cycle [117] and the proposed prediction-by-optimization (dashed green lines). Muscles are: $i = 1$ add. brevis; $i = 2$ add. longus; $i = 3$ add. magnus distal; $i = 4$ add. magnus ischial; $i = 5$ add. magnus middle; $i = 6$ add. magnus proximal; $i = 7$ gluteus max. superior; $i = 8$ gluteus max. middle; $i = 9$ gluteus max. inferior; $i = 10$ gluteus medius ant.; $i = 11$ gluteus medius middle; $i = 12$ gluteus medius post.; $i = 13$ gluteus min. ant.; $i = 14$ gluteus min. middle; $i = 15$ gluteus min. post.; $i = 16$ iliacus; $i = 17$ psoas; $i = 18$ semimembranosus; $i = 19$ semitendinosus; $i = 20$ biceps femoris long; $i = 21$ biceps femoris short; $i = 22$ rectus femoris; $i = 23$ vastus medialis; $i = 24$ vastus intermedius; $i = 25$ vastus lateralis; $i = 26$ lateral gastronemius; $i = 27$ medial gastronemius; $i = 28$ tibialis ant.; $i = 29$ tibialis post.; $i = 30$ peroneus brevis; $i = 31$ peroneus longus; $i = 32$ peroneus tertius; $i = 33$ soleus; $i = 34$ extensor digitorum longus; $i = 35$ flexor digitorum longus.

all time samples. This is a strong point to validate the hypothesis stating that muscle force sharing during gait is the result of an optimal process.

4.3 Results

4.3.1 Muscle-Forces Sharing Estimation

Table 4.2 shows the comparison of the average RMSE and Pearson CC across the 35 muscles and 10 gait cycles, between the reference muscle forces and their predictions obtained when solving the DOC with individual objective functions extracted from the literature (see Table 4.1), and with the hybrid objective functions identified by the bilevel approach and the IKKT approach. Additionally, Table 4.2 also contains the standard deviation of the RMSE and CC over the 10 gait cycles, averaged over the 35 muscles.

The best results for both gait phases were obtained from the bilevel approach with an RMSE 16% lower than the one obtained from the IKKT approach. Interestingly, some individual objective functions, such as the sum of squares of muscle activations (ϕ_6) or the sum of squares of muscle stresses (ϕ_{10}), provide a smaller RMSE than the IKKT approach, which supports the claim that the KKT residual is not a good metric to minimize in cost function retrieval [139].

Figure 4.3 shows the mean and standard deviation of muscle forces produced by the subject across 10 gait cycles, together with a typical comparison between the reference muscle

Table 4.2: Results of the average RMSE and Correlation Coefficient (CC) calculated between the reference muscle forces and the predicted ones when using the DOC and different objective functions.

Number	Stance phase		Swing phase	
-	RMSE [N]	CC	RMSE [N]	CC
J_{IKKT}	210 ± 23	.61 ± .16	218 ± 14	.58 ± .22
J_{Bilevel}	176 ± 25	.76 ± .15	162 ± 19	.68 ± .22
ϕ_1	258 ± 38	.46 ± .20	200 ± 24	.43 ± .23
ϕ_2	223 ± 23	.54 ± .17	196 ± 18	.42 ± .22
ϕ_3	223 ± 24	.53 ± .17	194 ± 19	.42 ± .21
ϕ_4	224 ± 25	.51 ± .17	194 ± 19	.41 ± .20
ϕ_5	228 ± 29	.66 ± .18	177 ± 19	.60 ± .19
ϕ_6	184 ± 23	.73 ± .14	164 ± 14	.67 ± .22
ϕ_7	187 ± 22	.71 ± .13	164 ± 14	.67 ± .22
ϕ_8	201 ± 29	.70 ± .16	172 ± 17	.63 ± .20
ϕ_9	252 ± 28	.56 ± .19	200 ± 24	.44 ± .21
ϕ_{10}	202 ± 22	.66 ± .15	192 ± 17	.46 ± .23
ϕ_{11}	196 ± 22	.68 ± .15	188 ± 17	.49 ± .23
ϕ_{12}	192 ± 21	.69 ± .16	183 ± 18	.52 ± .23
ϕ_{13}	301 ± 37	.32 ± .17	222 ± 30	.29 ± .21
ϕ_{14}	212 ± 24	.63 ± .16	173 ± 17	.61 ± .22
ϕ_{15}	236 ± 21	.49 ± .16	203 ± 17	.36 ± .21

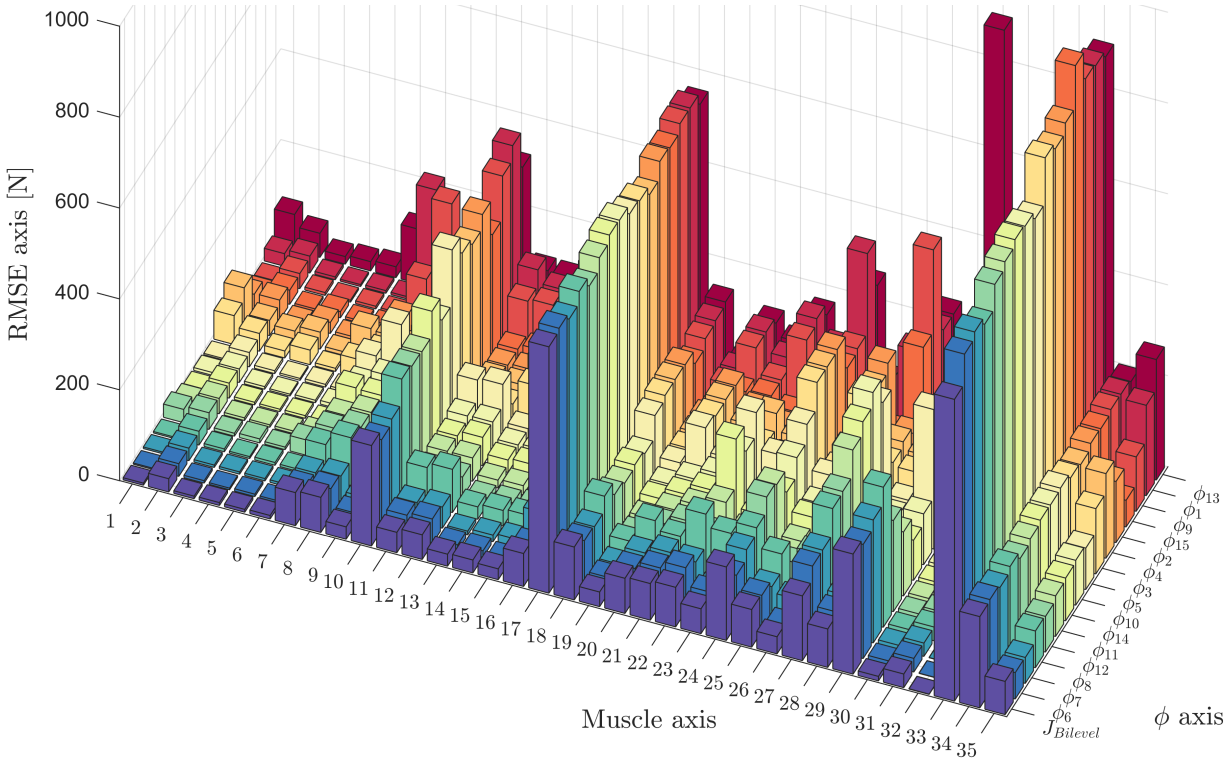

Figure 4.4: Bar graph of individual muscle force average RMSE across the 10 gait cycles depending on the objective function used for prediction.

forces and their prediction obtained from the DOC with the bilevel hybrid objective functions for a selected gait cycle. The RMSE was 159N, and the CC was 0.77 for this particular cycle. The forces developed by the most important muscles, such as the rectus femoris, vastii, and gastronemi ($i = 23$ to 27), were well predicted, contrary to muscles that contribute less such as adductors ($i = 1$ to 6). The individual objective functions that provide the best results are ϕ_6 and ϕ_7 (sum of squares and cubes of muscle activations).

The hybrid objective functions identified for the stance and swing phases using the bilevel IOC process are given in Table 4.3. Note that the selected objective functions are those that include time-varying parameters such as instantaneous minimal and maximal muscle forces

Table 4.3: Identified objective function parameters using the bilevel approach

.

	ω_1	ω_2	ω_3	ω_4	ω_5	ω_6	ω_7	ω_8	ω_9	ω_{10}	ω_{11}	ω_{12}	ω_{13}	ω_{14}	ω_{15}
$\boldsymbol{\omega}_{\text{Stance}}$	0	0	0	0	0.22	0.18	0	0	0	0.05	0	0	0.33	0.22	0
$\boldsymbol{\omega}_{\text{Swing}}$	0	0	0	0	0	0	0.61	0	0	0	0	0.25	0.15	0	0

($\boldsymbol{f}_{\text{min}t}$ and $\boldsymbol{f}_{\text{max}t}$), instantaneous maximal muscle torques ($\boldsymbol{\tau}_{\text{max}t}$), or instantaneous muscle velocity (vmt_t) as opposed to constant parameters such as muscle cross-sectional area (pcsa) or maximal isometric force ($\boldsymbol{f}_0$). The objective function with the highest weight ($\boldsymbol{\omega} = 0.61$) is the sum of cubes of muscle activations (ϕ_7) during the swing, which was one of the objective functions with the lowest RMSE when using the DOC.

Figure 4.4 shows the RMSE for all muscle forces and objective functions. Objectives function are ranked by average RMSE (on the whole gait cycle) and reveal that the worst results typically correspond to the highest RMSE on the forces of $i = 10$ gluteus medius anterior, $i = 17$ psoas, and $i = 33$ soleus. These are the muscles with the highest forces during gait. This is interesting to see that with the objective functions ϕ_{13} (sum of squares of muscle powers), ϕ_1 (sum of muscle forces), and ϕ_9 (sum of muscle stresses), other hip and ankle muscles forces are deteriorated such as $i = 29$ tibialis posterior, $i = 27$ medial gastronemius, or $i = 8$ gluteus maximus middle.

Figure 4.5 depicts the mean and standard deviation of JS produced by the subject across 10 gait cycles, alongside a comparison of the reference and predicted stiffness computed by the identified model of force distribution for a given gait cycle. JS was computed from muscle forces and other Hill-type muscle-model parameters using equation (4.8) derived from the usual $K_{tj} = -\frac{\partial \tau_{tj}}{\partial \theta_{tj}}$ [144] where τ_{tj} is the torque produced by the muscle forces around the j-th joint axis and θ_{tj} is angular displacement at time t.

$$K_{tj} = -\sum_{i=1}^{n} \left(\frac{\partial r_{tji}}{\partial \theta_{tj}} f_{ti} - r_{tji}^2 \frac{\partial f_{ti}}{\partial \text{lmt}_{ti}} \right) \tag{4.8}$$

The terms r_{tji} and lmt_{ti} represent, at time t, the instantaneous moment arm of the i-th muscle about the j-th joint and the instantaneous muscle-tendon length of the i-th muscle.

Computations of JS show that an RMSE of about 170N in the muscle forces obtained with the bilevel approach turns into relatively low differences of 43 Nm.rad^{-1} in the JS. The global patterns of the JS at the hip, knee, and ankle are preserved, but the amplitudes are almost systematically underestimated.

4.3.2 Numerical Example

When the data is exactly optimal with respect to the underlying basis objective functions, we say it is consistent with the basis, and the solutions of the bilevel (4.5) and IKKT (4.7) should coincide. In practice, the data is rarely consistent with the basis for the reasons mentioned in Section 4.2.4. This subsection presents a toy counterexample to the IKKT method when the data is not consistent, proving it may yield maximal distance between measurements and model predictions.

In particular cases, such as this example, the cost function retrieved by IKKT may provide the largest possible RMSE with respect to the data out of all retrievable cost functions, which will be shown using the "max-bilevel" method maximizing error between model predictions and data, *i.e.* the same as the bilevel method (4.5) but with a minus in the outer-loop cost function. In contrast, the bilevel method always provides locally minimal distance estimates. Omitting index t, suppose that at a particular instant, the constraints of our model are described by equations 4.9a-4.9b,

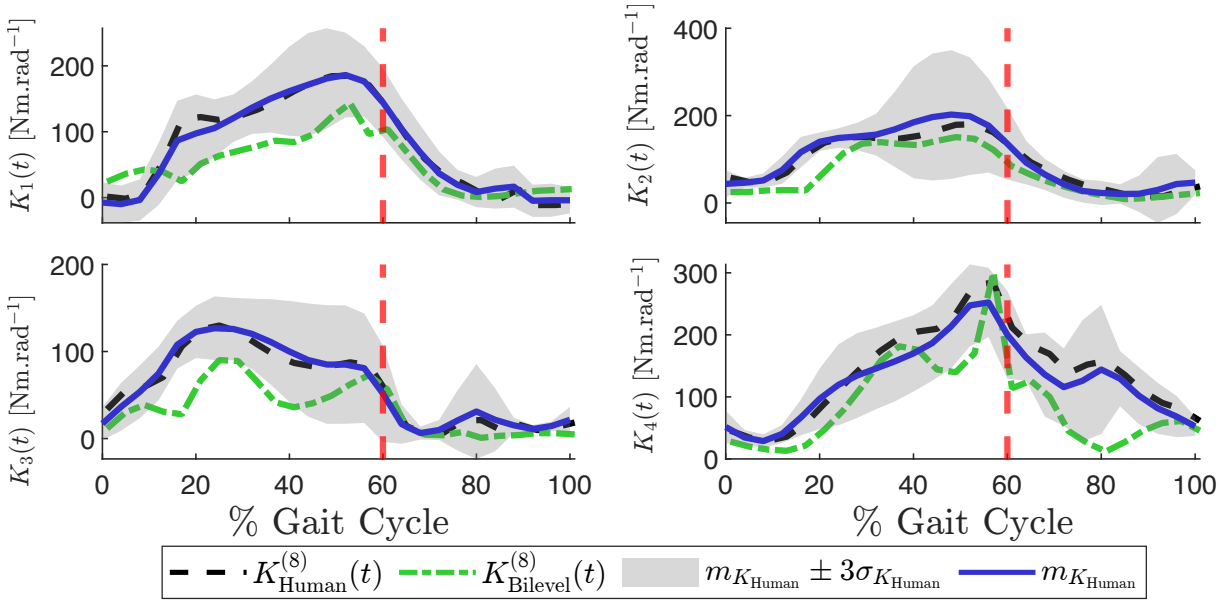

Figure 4.5: Mean (solid blue lines) and standard deviation (gray areas) of the JS estimated during all gait cycles. Reference (dashed black lines) and predicted (dashed-dotted green lines) JS. Joints are: $j = 1$ hip flexion-extension; $j = 2$ hip abduction-adduction; $j = 3$ knee flexion-extension; $j = 4$ ankle plantar-dorsal flexion.

$$\boldsymbol{A} = [1 \quad 1 \quad 1], \qquad \boldsymbol{\tau} = 1 \tag{4.9a}$$

$$\boldsymbol{f}_{\min} = [0 \quad 0 \quad 0]^T, \qquad \boldsymbol{f}_{\max} = [1 \quad 1 \quad 1]^T \tag{4.9b}$$

and that the features are given in equations (4.10a) and (4.10b).

$$\phi_1 = \frac{1}{2}\boldsymbol{f}^T \begin{bmatrix} 5 & 0 & 0 \\ 0 & 1.25 & 0 \\ 0 & 0 & 1 \end{bmatrix} \boldsymbol{f} \tag{4.10a}$$

$$\phi_2 = \frac{1}{2}\boldsymbol{f}^T \begin{bmatrix} 1.25 & 0 & 0 \\ 0 & 5 & 0 \\ 0 & 0 & 1 \end{bmatrix} \boldsymbol{f} \tag{4.10b}$$

The feasible set of instantaneous forces $\boldsymbol{f}$ is the unit simplex and is shown in Figure 4.6. The constrained minima of ϕ_1 and ϕ_2 ((4.10a) and (4.10b)) are shown as a blue and green dot, respectively. The black line represents the Pareto efficient solutions of the multi-objective optimization with objectives ϕ_1 and ϕ_2. In other words, it represents the set of all minima obtained by letting $\boldsymbol{\omega}$ take all values from Δ^2.

IOC was performed using the IKKT (4.7), the bilevel (4.5), and the max-bilevel methods with the given measurement (test point) $\boldsymbol{f}^* = \frac{1}{3}(1, 1, 1)$ which is shown in yellow on the figure. IKKT (silver square), bilevel (pink diamond), and max-bilevel (red triangle) predictions are shown, with their projection lines being displayed for easier visualization.

Numerically, the bilevel method returned $\boldsymbol{\omega}_{\text{Bilevel}} = (0.0124, 0.9876)$, which after solving the DOC (4.2) with given $\boldsymbol{\omega}_{\text{Bilevel}}$ returned the point $\boldsymbol{f}_{\text{Bilevel}} = (0.3909, 0.1023, 0.5068)$ which is a distance of $d_{\text{Bilevel}} = 0.2946$ away from the test point $\boldsymbol{f}^*$. The IKKT method returned $\boldsymbol{\omega}_{\text{IKKT}} = (0.5, 0.5)$ with a KKT-residual of $r = 0.0830$, which after solving the DOC (4.2) returned the point $\boldsymbol{f}_{\text{IKKT}} = (0.1951, 0.1951, 0.6098)$ which is a distance of $d_{\text{IKKT}} = 0.3385$ away from the test point $\boldsymbol{f}^*$. The max-bilevel method returned the same $\boldsymbol{\omega}_{\text{MaxBilevel}}$ and

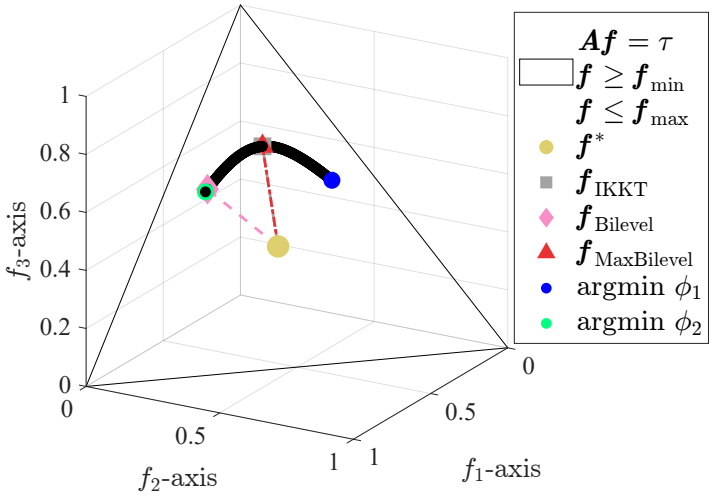

Figure 4.6: Three muscles forces $f_1, f_2, f_3 \in [0, 1]$ generate joint torque $\tau = 1$. Two features ϕ_1, ϕ_2, and a single measurement $\boldsymbol{f}^*$ are considered. The bilevel, max-bilevel, and IKKT predictions $\boldsymbol{f}_{\text{Bilevel}}, \boldsymbol{f}_{\text{MaxBilevel}}, \boldsymbol{f}_{\text{IKKT}}$ are shown.

$\boldsymbol{f}_{\text{MaxBilevel}}$ as IKKT

$$\|\boldsymbol{\omega}_{\text{MaxBilevel}} - \boldsymbol{\omega}_{\text{IKKT}}\|_\infty = 9.28e-06$$
$$\|\boldsymbol{f}_{\text{MaxBilevel}} - \boldsymbol{f}_{\text{IKKT}}\|_\infty = 2.33e-06$$

which practically means IKKT produced the largest prediction error with respect to the L_2-norm.

Therefore, minimizing the residual of the KKT constraints is not a reliable heuristic to minimize when we want to achieve a small distance between data and model predictions.

4.4 Limitations and Perspectives

Because of sparsely available open-source EMG data, this study was based on multiple trials of a single subject. Obviously, the generalization potential of the findings is limited. However, some preliminary conclusions can be drawn, as done in Section 4.5. Analysis of intra-subject and inter-subject objective function variability should be subject to future studies with more subjects, so as to examine generalization capabilities.

Table 4.1 presented the most commonly investigated objective functions in the biomechanics literature. An extended basis may be investigated, with objectives sampled from an even larger body of literature. Research on a feature selection tool for IOC may prove useful in dealing with larger bases of objectives.

The bilevel method described in equation (4.5) and further implemented to generate results in Section 4.3 is based on the outer-loop minimization of the sum of squares of L_2-norms between muscle forces generated by the optimization model, and the data. Minimizing (*resp.* maximizing) other measures of difference (*resp.* similarity) ought to be attempted, and mathematically analyzed.

The counterexample in Section 4.3.2 shows that one should not expect to obtain model predictions close to the data in terms of the L_2-norm, using the IKKT method [139]. This method's more formal treatment and analysis are in order, as it may have other virtuous properties.

4.5 Conclusion

This chapter systematically compared standard objective functions used for solving the force-sharing problem during gait via an optimization approach in the biomechanical literature. Two IOC techniques were used to identify a hybrid objective function for the force-sharing problem, one of them outperforming the existing individual objective functions. The bilevel method outperformed IKKT by 16% in the average RMSE metric, which was also outperformed even by some individual objective functions. This result was explained through a counterexample, showing that minimizing the KKT residual may result in maximization of the distance between model predictions and observations. This effectively invalidates the unverified claim some authors make that IKKT will provide a model whose predictions are "at least close" to the data. Future applicative studies should avoid the IKKT technique and resort to more robust formulations like the bilevel technique.

The bilevel hybrid objective function achieved the best RMSE, with 176N for the stance and 162N for the swing phase. The corresponding CCs were 0.76 and 0.68 showing that this objective function was not fully efficient in reproducing some of the muscle patterns. For instance, for some muscles ($i = 5$ adductor magnus middle and $i = 30$ peroneus brevis), the estimated forces are virtually null for the whole gait cycle which negatively affects the CC but not the RMSE (see Figure 4.4) as the force amplitude was very low. Therefore, as for the objective function used to solve the force-sharing problem, the choice of the error function (model predictions *vs.* data) in the outer loop of the IOC is an open question. The sum of squares of L_2-norms, as classically used in the present study, tends to minimize errors on the peaks of the maximal forces among muscles (*e.g.* $i = 10$ gluteus medius anterior or $i = 33$ soleus) as shown in Figure 4.4. This error function also resulted in some quite sparse solutions in the present case where the different objective functions are not independent. The hybrid objective function revealed that minimization of the sum of activations is an appropriate choice, but a simultaneous selection of the sum of activations at powers 1, 2, and 3 was not observed. It seems from the DOC that the results of objective functions ϕ_6 and ϕ_7 were very close and that a sparse solution for the minimum of the sum of squares of L_2-norms included one or the other depending on the gait cycle phase. Another choice for the error function could have somewhat changed the selection or the objective function weights ω but it is very unlikely that the objective functions with the worst results from the DOC would have been selected. The hybrid objective function revealed that minimization of the sum of muscle forces or stress (at power 1, 2, 3, or taking the maximum) is not an appropriate choice. Conversely, minimizing the sum of muscle activations provided lower RMSE, especially at power 3, as confirmed by the DOC results. In the literature, using forward dynamics optimal control with the minimization of the sum of cubes of muscle activations yielded the best correlations with EMG measurements and knee contact forces measured by an instrumented prosthesis [128]. This study confirms that minimizing the sum of muscle forces or stress is less accurate [128]. Minimizing the sum of squares of muscle powers or muscle forces normalized by maximal muscle moments is rarely studied in the literature, but the results of both DOC and IOC suggest these objective functions can provide reliable results. Generally, all the objective functions that introduce instantaneous variation of parameters such as muscle velocities or moment-arms provide better results. This supports the claim that control made by the central nervous system is likely based on the knowledge of the current body state rather than constant values of the physiological cross-sectional area or maximal isometric force. JS is also controlled by the central nervous system and demonstrates typical patterns during gait [144]. As represented in Figure 4.5, the two classical peaks of JS occurring during the stance phase of gait, at loading response and pre-swing, and the progressive decreases during the swing phase were observed and reproduced. However, when using our estimated

muscle forces, the JS was under-estimated, showing a lack of co-contraction. During the swing phase, the JS seems to better match with the reference, except for the ankle. It is well known that many objective functions, such as the sum of forces, activations, or stresses at power 1, do not allow the prediction of co-contraction. Future studies with IOC can discard objective functions based on muscle force or stress, especially at power 1, while maximization of JS can be an interesting objective function to test for the force-sharing problem. In the future, the JS prediction should be used to develop a human-in-the-loop control strategy when using an assistive device.

Chapter 5

Box Lifting

This chapter studies the box-lifting task, an important human movement that is well-studied both in the "human" fields of biomechanics and ergonomics, as well as in (humanoid) robotics. In particular, this chapter analyzes human motion generation for the box-lifting task, through the lens of constrained multi-objective optimization. Data-driven inverse optimization is used to identify, from collected motion data, the trade-offs between the different objective functions hypothesized to give rise to human-like box-lifting motion in the literature.

The motion planning for the box-lifting task was modeled as a constrained OCP using a planar 6 DoF model for the human body. The kinematic and dynamic parameters of the human body model were identified from the data before proceeding with the investigation. After establishing a biomechanically-inspired constrained optimal control model for motion generation, a collection of various bio-mechanical objective functions from the literature were investigated as possible generators of the motion, whose plausibility has been measured by the RMSE between the predicted motion and the measured data.

From a single sample of the lifting motion, data-driven IOC was used to infer the best trade-off between these different objective functions *i.e.* to identify one compound objective function that is most consistent with the measured data in terms of RMSE. The objective retrieved by the data-driven inverse optimization approach has been evaluated on the whole data set with an RMSE of 21° in the joint angle trajectory space.

5.1 Introduction

5.1.1 Significance of Lifting

Manual handling of heavy objects is a basic but crucial task for any job performed in manufacturing, supermarkets, and warehouses. Lifting is also important in the construction and shipping industries. It is well known that the repetitive exertion of demanding tasks can lead to musculoskeletal disorders. In particular, lifting heavy objects and dropping them with accuracy put a lot of strain on the operator. Such tasks can increase ergonomics risks such as low back problems [47]. Thus, there is a need to propose robotic assistance for physically demanding tasks. Assistive robots can be exoskeletons or collaborative robots but both should provide personalized, subject-specific, assistance to the operator. Due to anthropometry changes between the subjects it is not possible to use directly averaged joint trajectories [97, 111]. Moreover, even when performing a simple task such as lifting and dropping an object the human central nervous system, as the controller of the body, can choose from an unlimited number of joint trajectories thanks to the high redundancy of the human musculoskeletal system. In addition, humans can handle constraints, eventually, ones that can vary with time, and plan ahead a series of tasks to be performed [44].

Over 40% of the workforce in Europe experience musculoskeletal disorders related to their jobs, including pain in the lower back, neck, or shoulder, even with continual endeavors to enhance workplace conditions. Work-related Musculoskeletal Disorders (WMSDs) arise primarily due to strenuous physical activities involving repetitive motions (61%), improper postures (44%), and handling of heavy materials (31%). These disorders account for 3%–6% of time off from work, imposing an average economic burden amounting to 2.5% of the Gross Domestic Product throughout Europe. Amongst all the WMSDs, 52% are attributed to strain during lifting activities, with 65% impacting the back [126].

In comparison, in the United States, such disorders are frequently the origin of occupational injuries, leading to substantial lost workforce hours due to sick leaves, and resultant disability insurance payouts, reflecting notable economic repercussions [134]. Specifically, manual lifting is intricately linked with low-back discomfort; in the US, its occurrence is presumed to surpass 60%, generating an annual expense exceeding $100 billion [50].

Elevated stress on the lumbar spine is recognized as the primary contributor to lower back pain [104, 126]. Various lifting strategies can be adopted, contingent upon individual anthropometry and the weight, shape, and position of the item to be lifted. Prevalent strategies explored in studies encompass squat and stoop (back) lifts. While squat lifting is generally deemed safer regarding the stress it puts on the lumbar spine compared to stoop lifting, some research contradicts this, finding higher peak spinal loads in squat lifting [126].

Simulation of human lifting can produce postures and movements under diverse task conditions and is thus a valuable tool in deepening our understanding of the mechanisms of lower back pain injuries. It assists in enhancing the design of lifting tasks and holds the potential to decrease the occurrence of work-related lower back pain [70, 104, 134].

High loads in the lumbar spine have been identified as the main cause of lower back pain. Many strategies for lifting can be chosen depending on human anthropometry, as well as on the weight, shape, and position of the object to lift. Major strategies discussed in the literature include the squat and back (stoop) lift [126]. Human lifting simulation is capable of generating postures and motions under varied task scenarios and thus may help better understand lower back pain injury mechanisms, improve lifting task designs, and eventually reduce occupational lower back pain incidence [104].

Human motion simulation is important, but challenging, as it provides a way to obtain unmeasurable quantities such as torques, forces, and stresses. Chumacero-Polanco and Yang [107] distinguish between (i) optimization-based approaches to human motion simulation where the goal is to use an optimization procedure to generate a path between initial and target positions, and (ii) control-based approaches where the goal is to find the required input (joint torques) such that the output (joint angle trajectories) tracks a given reference. Numerous studies are based on the idea that the CNS resolves the motor-control redundancy problem by using optimization [38, 44, 104]. Human motion simulation is regarded as an effective ergonomic tool to predict major risk factors associated with occupational injuries. More accurate simulations can help improve the assessment of the risk of occupation injuries [70, 104, 134].

Consequently, the development of accurate and robust human motion simulations, *i.e.*, establishing universal representations of human motion that are effective across diverse body morphologies and task situations, is invaluable. This approach not only facilitates a deeper understanding of the critical factors contributing to occupational injuries and aids in reducing the incidence of such injuries but is also pivotal in advancing the quality of robotic aid and rehabilitation systems [34].

Table 5.1: Segments and actuating DoFs of the most common planar sagittal 5 DoF human body model for the box lifting task.

Segment	foot	shanks	thighs	torso	arms	forearms
Actuating DoF	-	ankle plantar flexion/ dorsiflexion	knee flexion/ extension	hip flexion/ extension	shoulder flexion/ extension	elbow flexion/ extension
DoF on Figure 5.1	-	q_1	q_2	q_3	q_4	q_5

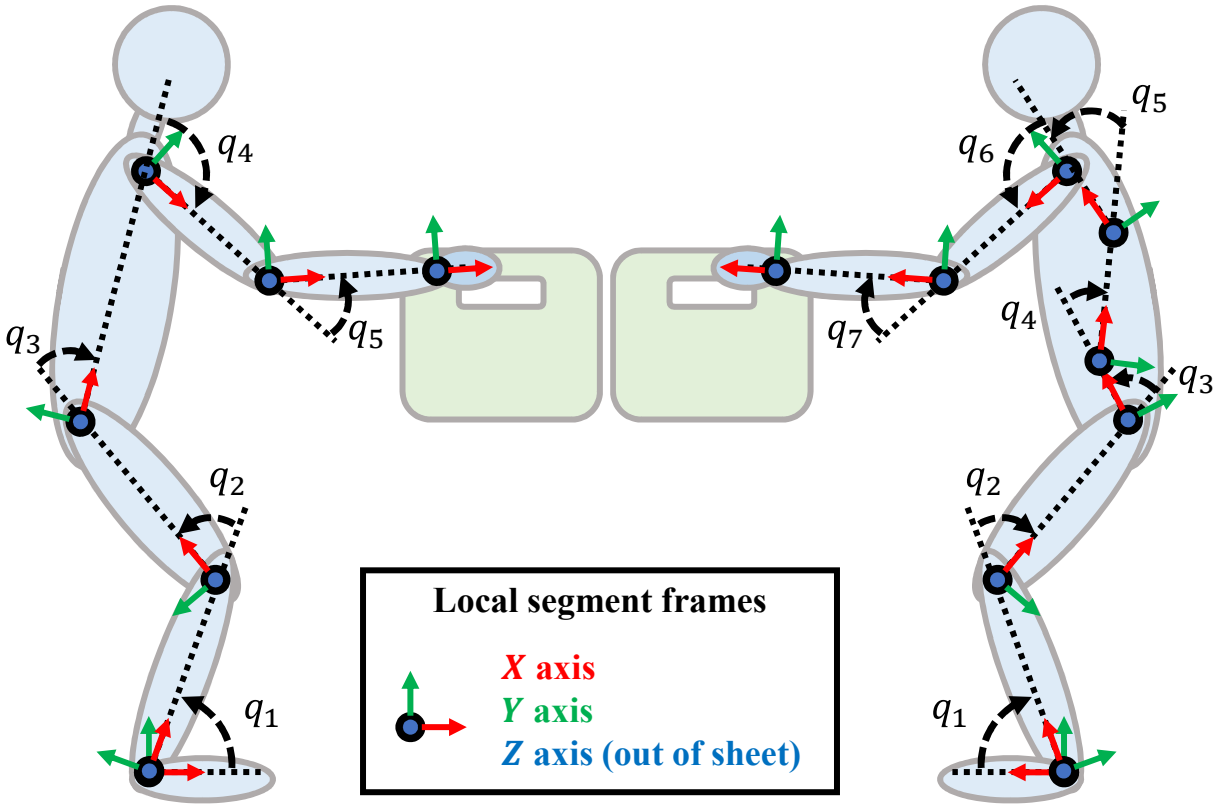

Figure 5.1: Representative sagittal plane models of the human body with 5 DoF (on the left) and 7 DoF (on the right).

5.1.2 Optimization-Based Approaches

A review of the approaches used for human motion simulation and prediction in lifting tasks has been given in [107]. The authors observe that the most common human skeletal models across the reviewed literature have been two-dimensional in the sagittal plane, but that some three-dimensional models have been used.

The most extensively used model is the sagittal plane model with five planar DoFs. Because of its widespread use, Table 5.1 has been dedicated to describing its links and corresponding actuating DoFs, and the left part of Figure 5.1 has been dedicated to representing it graphically. This model has been the most extensively used throughout lifting motion generation studies [9, 23, 24, 35, 46, 90, 104, 113] because of its relatively low complexity, in comparison to full-body 3D models, and its high degree of fidelity in capturing the essence of the lifting motion.

The most widely used model is the 5 DoF sagittal plane model, however, the use of sagittal plane models with some extra DoFs is pretty common. One example would be the seven DoF sagittal plane model from [75] shown on the right side of Figure 5.1. Compared to the 5

DoF, the torso has been split up into the pelvis, the thoracic spine, and the cervical spine, and two additional DoFs are added corresponding to the lumbar spine flexion/extension and the thoracic spine flexion/extension [75], *i.e.* to q_4 and q_5 on Figure 5.1. Another example would be the robot model from Arisumi et al. [55] and Arisumi et al. [58], who use a seven DoF sagittal plane model which has an additional DoF in the back, like the 6 DoF model presented in Figure 5.2, and another DoF in the wrist joint. On the other hand, Rakshit, Xiang, and Yang [134] endow the model with three global DoFs, allowing for the translation and rotation of the whole Figure in the sagittal plane, and moreover add an additional DoF in the spine, and an additional DoF in the metatarsophalangeal joint in the foot, allowing for a more precise study of the Ground Reaction Wrench (GRW). Meanwhile, the use of 3D models in lifting simulations has been pioneered by Xiang et al. [61, 70, 85, 86], who have conducted multiple studies of lifting motion generation using a 55 DoF 3D full-body human model. The main advantage of 3D models is their more apparent similarity to a real human body and the possibility of capturing small details and eventual asymmetries that may exist in real human motion. However, Xiang et al. used criteria that were side-neutral and produced symmetrical motion, and moreover, Xiang et al. analyze the lifting motion joint space kinematics through 6 main joints: the ankle, knee, hip, spine, shoulder, and elbow, *i.e.* the ones most commonly found in sagittal plane models.

So as to maintain a reasonable level of complexity in the lifting motion generation algorithm, the study conducted in this chapter rests upon a 6 DoF sagittal plane model, as presented in Figure 5.2. The simplification of the motion to the sagittal plane brings the advantage of simpler equations of motion with far fewer variables to consider, allowing for more reasonable computation times, in light of the computational requirements of IOC.

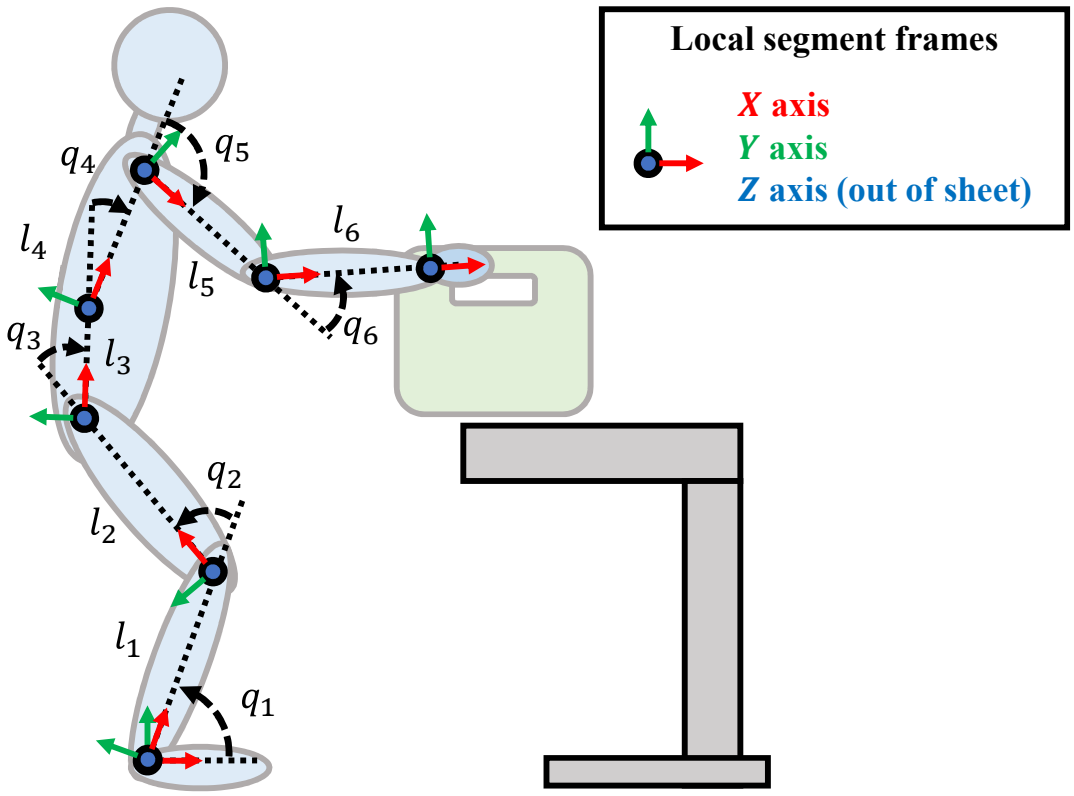

Figure 5.2: Two-dimensional 6DoF human biomechanical model for lifting with annotated segment axes and joint angles. Segments are the shanks, thighs, pelvis-abdomen, thorax-neck-head, upper arm, and forearm whose lengths are denoted by l_1 through l_6. These segments are connected by the ankle, knee, hip, back, shoulder, and elbow joints whose angles are denoted by q_1 through q_6.

Compared to the standard 5 DoF model, the spine/back joint was introduced as spine load is a frequently studied parameter in the traditional ergonomic and biomedical literature on box-lifting motion [73, 126, 133]. Moreover, the spine joint is the most frequent addition to the standard 5 DoF model, alongside the wrist joint, and is present in Arisumi et al. [55, 58], Rakshit, Xiang, and Yang [134], and Xiang et al. [61, 70, 85, 86]. On the other hand, the wrist joint was omitted for simplicity, which implied that the hand and the box were assumed to be rigidly linked to the forearm.

For optimization-based lifting motion prediction and simulation, the authors of [107] identify a multitude of minimization criteria used in the literature. These criteria have been gathered alongside their symbolic representation and description within Table 5.2. Every criterion listed in the cost function table expresses a preference for either energy-efficient motion, smooth motion, posturally stable motion, or load minimizing (*i.e.* pain, effort minimizing) motion.

Total muscular effort was one of the earliest objective functions optimized for predictive dynamic simulations of the lifting motion in studies such as [9, 18, 23], but remains in use in modern studies as well [104, 113]. While Hsiang and McGorry [18] analyze the differences in predictions provided by the minimization of total muscular effort, of total hand jerk, and of total center of mass jerk on a 5 DoF sagittal plane model, the work of Song, Qu, and Chen [113] generates trajectories by minimizing a mixture of total muscular effort and total hand jerk. The total torque and the static balance minimization were investigated in [16]. Xiang et al. [70] use a three-dimensional model with 24 segments and 55 DoF to generate trajectories using multi-objective minimization of two criteria *viz.* the dynamic effort and the dynamic balance criterion, while in [61] the maximum later shear force is investigated. The minimization objectives are normalized to eliminate the dependence on units. Within [90] the authors use a two-dimensional sagittal plane 5 DoF model to generate trajectories by minimizing ankle torque, which acts as a measure of instability. Arisumi et al. [58], who worked with a 7 DoF robot model and minimized a total energy criterion to generate the motion. As an interesting alternative, in [134] the authors study maximum weight-lifting simulation, where the motion is generated by selecting a motion pattern that maximizes the weight of the box the subject can lift by using that pattern. The majority of these objective functions, which are task-independent, have been studied for different tasks within the IOC literature [72, 77, 97].

As a compromise between maintaining consistency with the literature on box lifting and the literature on IOC, and the computational complexity of the IOC procedure, only a subset of the objective functions in Table 5.2 have been chosen and implemented in the study described in this Chapter. This subset has been augmented with a few related but simpler objective functions and is described in detail within Subsection 5.3.3.

Constraints are a very important part of optimization-based motion generation and simulation, as they ensure the physical consistency of the generated motion *i.e.* physical limits of the system are respected. Authors of [107] review some of the most commonly employed constraints in use in optimization-based motion prediction and simulation. Based on this review, a majority of the encountered constraints in the literature have been consolidated in Table 5.3, with a description of their purpose, a symbolic representation when applicable, and a classification of their commonality.

Xiang et al. [61] impose boundary conditions on the hand position in ambient space and on the joint velocities in joint space, as well as joint angle limits and joint torque limits. Collision avoidance constraints between the box and the body are also imposed. At the same time, hand orientation is constrained to match the perpendicular to the box edge and the

[1]S is the support polygon, and ∂S is its boundary. This notation has been borrowed from mathematical analysis.

Table 5.2: Most common objective functions from the literature on the biomechanics and motion generation of human box-lifting motions.

Name	Symbolic	Description
Total muscular effort or muscle utilization ratio.	$\int_0^T \boldsymbol{\tau}^T \boldsymbol{S}^{-2}(\boldsymbol{q})\boldsymbol{\tau}\ dt$	Minimization of the total time integral of the sum of squared ratios of joint torques divided by the joint position-dependent joint torque capacity.
Dynamic effort or minimum effort.	$\int_0^T \lVert\boldsymbol{\tau}\rVert_2^2\ dt$	Minimization of the total time integral of the sum of squared joint torques.
Ankle torque.	$\int_0^T \tau_{\text{ankle}}^2\ dt$	Minimization of the total time integral of the squared ankle torque.
Dynamic balance or stability.	$\int_0^T \text{d}(\mathbf{ZMP}, \partial\text{S})\ dt$ [1]	Minimization of the total time integral of the sum of squared distances from the ZMP to the foot support boundaries.
Maximum shear force and maximum pressure force at spine joint(s).	$\int_0^T \lVert\boldsymbol{f}_{x,y,\text{ spine}}\rVert_2^2\ dt$ $\int_0^T f_{z,\text{ spine}}^2\ dt$	Minimization of the total time integral of the sum of squared forces felt at one or multiple spine joints.
Minimal hand, load, or center-of-mass jerk.	$\int_0^T \dddot{\boldsymbol{p}}^T \dddot{\boldsymbol{p}}\ dt$	Minimization of the total time integral of the squared Cartesian jerk of the corresponding object; is supposed to produce smooth trajectories.
Total torque.	$\int_0^T \lVert\boldsymbol{\tau}\rVert_1\ dt$	Minimization of the total time integral of the sum of absolute torques; is supposed to produce trajectories where a small number of joints are loaded.
Static balance.	$\int_0^T \lVert\boldsymbol{\tau}_{\text{ball}} - \boldsymbol{\tau}_{\text{heel}}\rVert_1\ dt$	Minimization of the maximum difference in torque applied at the ball of the foot and at the heel; is supposed to prevent falling over.
Energy consumption	$\int_0^T \lVert\dot{\boldsymbol{q}} \odot \boldsymbol{\tau}\rVert_1\ dt$	Minimization of the total time integral of the sum of joint powers.

vision vector (perpendicular to the forehead) has been constrained to point toward the center of the box. Within [70], Xiang et al. impose the same constraints as in [61], with the physical workspace layout and ground penetration constraints imposed explicitly in both studies [61, 70], but are implicit in almost all other literature.

In [23, 24], the authors impose joint angle limits, joint torque limits, collision constraints, and static postural stability constraints. Arisumi et al. [58] impose torque limits and dynamic postural stability constraints, while they also impose an interesting constraint preventing the joint torque and joint velocity from aggregating more than a 100% their maximum values simultaneously *i.e.* $|\frac{\dot{\boldsymbol{q}}}{\dot{\boldsymbol{q}}_{\max}} + \frac{\boldsymbol{\tau}}{\boldsymbol{\tau}_{\max}}| \leq 1$. This constraint is interesting as it is known that the maximum joint torque is dependent on the position and on the velocity of the joint, and decreases as the velocity increases [89], but this concrete formulation is fairly restrictive. Shoushtari [90] assume that the box is rigidly attached to the wrist with a horizontal orientation. They enforce boundary conditions in terms of the box's initial and final position in Cartesian space, joint angles and torques are lower and upper bounded, the dynamics are implemented as a constraint while the joint torques are treated as a variable. Collision avoidance constraints are present as well. Another constraint dubbed wrist elevation is implemented, enforcing a non-decrease in wrist height during the movement. Song, Qu, and Chen impose standard joint angle, joint torque, and collision avoidance constraints are imposed within [104], as well as [113]. Static postural stability is imposed by forcing the

projection of the center of mass of the body-load system to be within the foot support area. Data-driven joint velocity limits were also included because they have been previously shown to be dependent upon the load weight, destination height, and subject age [96]. The dependence is identified from the data by using quadratic regression. Biological joints are different from robotic ones, their torque capacity is dependent on the muscles that actuate it, whose own force-producing capabilities depend on moment-arms, force-length, and force-velocity properties of the muscle itself. To capture that relationship, Rakshit, Xiang, and Yang [134] propose to identify joint-angle and joint-velocity dependent model of joint-torque production capacity, and use it to estimate safe maximal load weight.

So as to respect the baseline of physical and biomechanical consistency, the joint angle limits, the joint torques, and the collision avoidance constraints have been implemented in the study this chapter describes. The most physically accurate postural stability condition, *i.e.* the dynamic postural stability constraint, has been implemented as it is a necessary condition for postural stability [43, 45]. With the goal of allowing greater freedom in the choice of trajectories, the final boundary condition was concerned with the wrist position, while the initial condition was concerned with the joint angle configuration so as to provide a consistent comparison with the collected data *i.e.* as it is desirable that the simulated trajectories start from the exact same configurations as the real trajectories. The physical layout and ground penetration are taken into account implicitly.

Xiang et al. Xiang et al., Xiang et al., Xiang, Arora, and Abdel-Malek, Xiang, Arora, and Abdel-Malek formulate the OCP in joint space using B-splines and is solved using sequential quadratic programming. The authors monitored the error between the simulated trajectories and the experimental data across 6 DoFs which determine the lifting motion the most *i.e.* hip flexion/extension, knee flexion/extension, ankle plantar/dorsiflexion, trunk flexion/extension, shoulder flexion/ extension, and elbow flexion/extension and found that the simulated trajectories best fitted experimental data when the weights placed on normalized dynamic effort and normalized stability are in a ratio of 0.1 to 0.9 [70]. The accuracy of the joint angle trajectory prediction yielded by the model in [70] with respect to the data is not quantified numerically, but is shown to be within the 95 % confidence interval of the data collected on 5 subjects. Formulations of the OCP in [23, 24] are in the joint space using polynomial trajectories, and are solved using a general-purpose nonlinear optimization software written in FORTRAN called GRG2. Within [90], in which the authors use B-splines to formulate the OCP, it is shown that the movement obtained by minimizing the ankle torque is stable in the sense that the ZMP remains within the polygon of support. The authors provide a graphical comparison of predicted and experimental joint angle trajectories. Multiple innovations are provided by [104] by including data-driven joint velocity constraints, recruiting subjects from different age groups, measuring maximum lifting capacity by using a dynamometer, and varying task parameters like box weight and table height. The OCP is formulated using B-splines. A comparison of the simulated trajectories with respect to the experimental measurements yielded an approximately constant RMSE in the vicinity of 11° independently of load weight or destination height. The model yielded more accurate predictions for younger subjects than for older ones.

This chapter opts for a spline representation of trajectories, because of multiple advantages compared to polynomials *i.e.* they are less prone to oscillations, allow local control (modifying one part of the spline doesn't affect the whole trajectory), tend to preserve curvature better thus allowing for smoother trajectories, and avoid the problem of raising floating-point numbers to high powers. This is not only advantageous numerically but naturally fits the nature of the human's very smooth box-lifting motion. Modern software solutions were used for implementation, with automatic differentiation software CasADi [124] used for the computation of derivatives and Hessians in the OCP formulation, while the nonlinear optimization

Table 5.3: Most common constraint functions from the literature on the biomechanics and motion generation of human box-lifting motions.

-	Name	Symbolic	Description
Common	Joint angle limits.	$\boldsymbol{q}_{\min} \leq \boldsymbol{q} \leq \boldsymbol{q}_{\max}$	Ensures that the joint angles remain within limits consistent with a human's biological range of motion.
	Joint torque limits.	$\boldsymbol{\tau}_{\min} \leq \boldsymbol{\tau} \leq \boldsymbol{\tau}_{\max}$	Ensures that the joint torques remain within limits consistent with a human's biological muscle force capacity production range.
	Boundary conditions.	$\boldsymbol{q}(0) = \boldsymbol{q}_i,\ \boldsymbol{q}(T) = \boldsymbol{q}_f$ $\dot{\boldsymbol{q}}(0) = 0,\ \dot{\boldsymbol{q}}(T) = 0$ $[\boldsymbol{p}^{\text{wrist}}(0) = \boldsymbol{p}_i,$ $\boldsymbol{p}^{\text{wrist}}(T) = \boldsymbol{p}_f]$	Ensures that the starting and ending configurations are consistent with the experimental parameters. Ensures the motion starts and ends with a static position. [Sometimes, only the wrist position is imposed.]
	Collision avoidance constraints.	$\mathbf{d}_{i,j} \geq 0, \forall i, j$	Ensures that no pair of collidable objects are in collision.
Uncommon or Unique	Static postural stability.	$\text{Proj}_{\text{floor}}\mathbf{COM} \in \text{S}$	Ensures that the projection of the center of mass stays within the polygon of support; guarantees postural stability in the static case.
	Dynamic postural stability.	$\mathbf{ZMP} \in \text{S}$	Ensures that the ZMP stays within the polygon of support; guarantees postural stability in the dynamic case.
	Joint velocity limits.	$\dot{\boldsymbol{q}}_{\min} \leq \dot{\boldsymbol{q}} \leq \dot{\boldsymbol{q}}_{\max}$	Ensures that the joint velocities remain within bounds extracted from the data.
	Wrist elevation constraint.	$h_{\text{wrist}}(t_{i+1}) \geq h_{\text{wrist}}(t_i)$	Ensures that the wrist height is non-decreasing during the movement.
	Vision constraint.	$\alpha \leq \angle(\vec{\boldsymbol{n}}_{\text{eye}}, \vec{\boldsymbol{r}}_{\text{eye,box}}) \leq \beta$	Ensures that the "vision" vector (perpendicular to the eye) is within a cone around the vector connecting the eye to the box center of mass.
	Hand distance and orientation.	$\vec{\boldsymbol{n}}_{\text{hand}} \times \vec{\boldsymbol{v}}_{\text{box,edge}} = 0$ $\vec{\boldsymbol{T}}_{\text{hand}} \times \vec{\boldsymbol{v}}_{\text{box,handle}} = 0$	Ensures that the hand's normal vector is along the box's edge and that the hand's tangential vector is along the box's handle. The distance is enforced to the box width.
Implicit	Physical workspace layout.	-	Enforces the geometry of the load and the table, and where they will be placed.
	Ground penetration.	-	Ensures that all the links are above the ground.

software IPOPT [53] is used to solve the OCP.

Some studies [86, 104, 134] also opt for a hybrid approach where they use information from the motion capture data directly in the motion simulation procedure in order to guide the simulation trajectories to be more human-like. Multiple hybrid approaches can be found in the literature that are consolidated in [86] and can be classified under the following categories:

(a) minimizing the tracking error with respect to the data,

(b) minimizing a multi-objective criterion, where one criterion is the tracking error with respect to the data, while the other criterion is related to the biomechanics of the task,

(c) constraining the tracking error with respect to the data, while minimizing a biomechan-

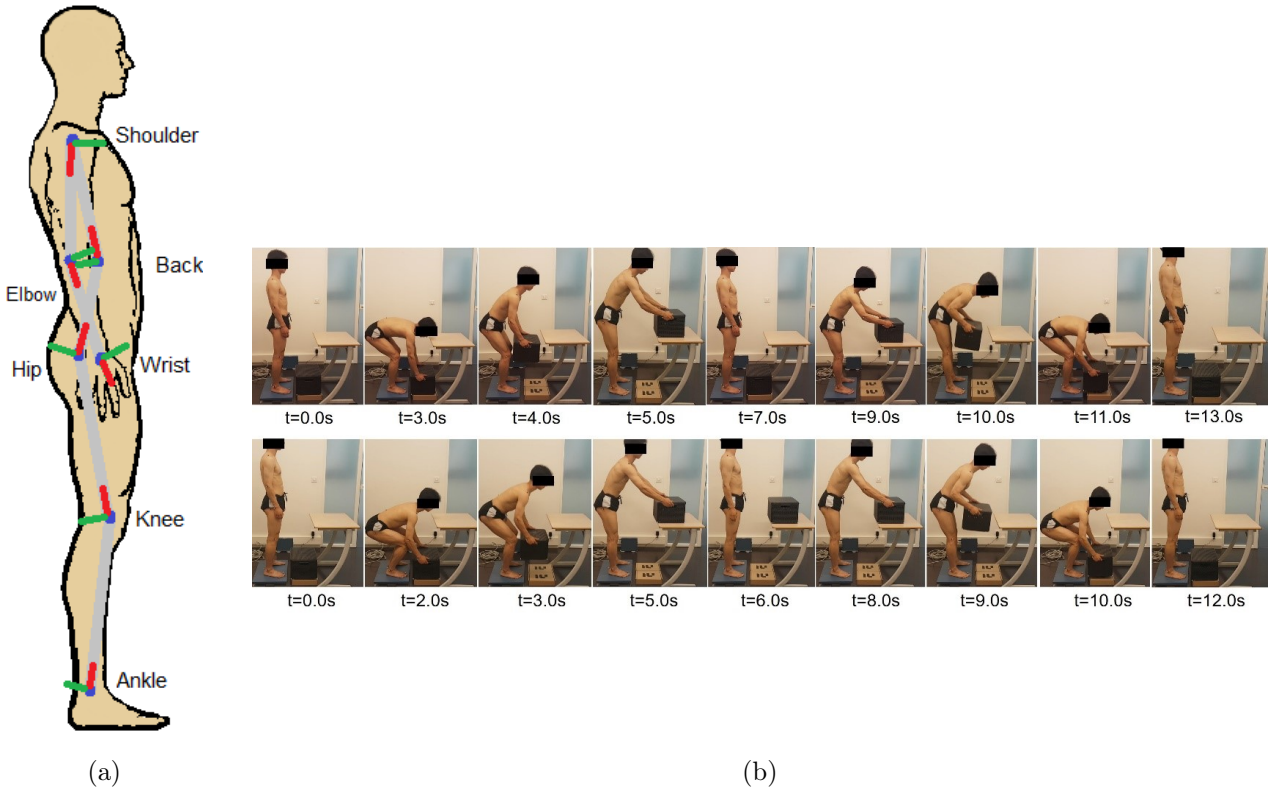

(a) (b)

Figure 5.3: (a) The 6DoF planar biomechanical model of the human. (b) A randomly selected participant while performing one repetition of standard and squat box lifting. Note that one repetition includes both upward (floor-to-table) and downward (table-to-floor) lifting movements.

ical task criterion,

(d) constraining the tracking error with respect to the data, while minimizing a multi-objective criterion composed of the tracking error and some biomechanical task criterion.

Using these approaches, the predictions may attain and surpass the threshold of 15° of RMSE, which is considered an accurate prediction.

While these results are very interesting from the point of view of accuracy, they require subject-specific and task-specific data collection in order to implement the tracking error costs or constraints. On the other hand, there is evidence of the existence of a general biomechanical task criterion [38, 44, 52] which is minimized by a human moving. The study in this chapter uses only biomechanical task criteria and biomechanical constraints, described previously and further in Section 5.3.3 and Section 5.3.2, to formulate the OCP of human box-lifting motion generation. The motion capture data is however used to infer the optimal weighting of the various biomechanical task criteria, by optimizing the RMSE of the predictions. The result of this process is an optimal control model that contains only biomechanical task criteria and biomechanical task constraints and is independent of the data at the time of the motion generation but is inferred from data so as to be optimal in terms of accuracy.

5.2 Model and Data

5.2.1 Biomechanical Model

The human body is modeled as a linkage of rigid bodies connected by joints. The symmetry of the task has been leveraged to simplify the model, as the motion is happening uniquely in the sagittal plane of the human body, leading to a planar model which is illustrated in Figure 5.3a, and whose diagram is given in Figure 5.2. Symmetric parts of the body have been fused, and will hereafter be referred to with singular nouns. Moreover, the pelvis-abdomen pair is treated as rigidly linked, as are the forearm-hand pair and the thorax-neck-head triple. The base of the human model is the foot, while its segments are the shank, the thigh, the pelvis-abdomen pair, the thorax-neck-head triple, the upper arm, and the forearm-hand pair. The base and segments, in the same order, are connected by joints at the ankle, the knee, the hip, the back, the shoulder, and the elbow. These joints together provide six planar DoFs to the model, meaning the configuration of the model at a particular time is described by six joint angles.

Within the model-based trajectory generation algorithm, many kinematic and dynamic quantities are computed from the trajectory and taken into account. Dependance on time is dropped for compactness. The kinematics and the dynamics are calculated numerically via symbolically generated functions using the software package SYMORO+ [19]. Joint and torque limits have been assumed fixed and determined from previous studies [89].

End-effector and Box Kinematics

The end-effector (wrist) position ${}^0\boldsymbol{p}^W = {}^0\,\mathrm{FKM}^W(\boldsymbol{q})$ is calculated using the forward-kinematic model of the mechanism representing the human, while the end-effector velocity ${}^0\boldsymbol{v}^W = {}^0\boldsymbol{J}^W(\boldsymbol{q})\dot{\boldsymbol{q}}$ can be calculated using the Jacobian of the forward-kinematic model.

For brevity of exposition, authors [49] usually introduce shortened notation. A variant of this notation is introduced in equation (5.1).

$$\mathrm{S}_{1:i} = \sin\left(\sum_{j=1}^{i} q_j\right) \tag{5.1a}$$

$$\mathrm{C}_{1:i} = \cos\left(\sum_{j=1}^{i} q_j\right) \tag{5.1b}$$

The forward kinematic equations of a planar manipulator are fairly simple and are given in equation (5.2) for the 6 DoF planar manipulator model of a human that has been adopted within this study.

$${}^0\boldsymbol{p}^W = \begin{bmatrix} {}^0p_x^W \\ {}^0p_y^W \end{bmatrix} = {}^0\,\mathrm{FKM}^W(\boldsymbol{q}) = \sum_{i=1}^{6} L_i \cdot \begin{bmatrix} \cos\left(\sum_{j=1}^{i} q_j\right) \\ \sin\left(\sum_{j=1}^{i} q_j\right) \end{bmatrix} = \sum_{i=1}^{6} L_i \cdot \begin{bmatrix} \mathrm{S}_{1:i} \\ \mathrm{C}_{i:i} \end{bmatrix} \tag{5.2}$$

The Jacobian of the forward kinematic model is computed by deriving the forward kinematic model equations with respect to time and then factoring out the joint velocities in order to be left with the matrix representing the Jacobian. For completeness, the Jacobian of the forward kinematic model is given within equation (5.3).

$$ {}^{0}J^{W}(\boldsymbol{q}) = \begin{bmatrix} -\sum_{i=1}^{6} L_i \cdot \mathrm{S}_{1:i} & -\sum_{i=2}^{6} L_i \cdot \mathrm{S}_{1:i} & \dots & -\sum_{i=5}^{6} L_i \cdot \mathrm{S}_{1:i} & -L_6 \cdot \mathrm{S}_{1:6} \\ \sum_{i=1}^{6} L_i \cdot \mathrm{C}_{1:i} & \sum_{i=2}^{6} L_i \cdot \mathrm{C}_{1:i} & \dots & \sum_{i=5}^{6} L_i \cdot \mathrm{C}_{1:i} & L_6 \cdot \mathrm{C}_{1:6} \end{bmatrix} \tag{5.3} $$

The box is assumed to be rigidly linked to the wrist with a constant position vector ${}^{0}\boldsymbol{r}^{W,B}$ as no angular wrist motions greater than $\pm 5°$ have been observed in the data. As such the box position is calculated as ${}^{0}\boldsymbol{p}^{B} = {}^{0}\boldsymbol{p}^{W} + {}^{0}\boldsymbol{r}^{W,B}$.

Torques and Ground Reaction Wrenches

The joint torques are related to the trajectory by the equations of motion of an actuated mechanism

$$ \boldsymbol{\tau} = \mathrm{M}(\boldsymbol{q})\ \ddot{\boldsymbol{q}} + \mathrm{C}(\boldsymbol{q}, \dot{\boldsymbol{q}})\ \dot{q} + \mathrm{G}(\boldsymbol{q}) + J(\boldsymbol{q})^{T}\ \boldsymbol{w}^{\mathrm{ext}} \tag{5.4} $$

and are influenced by the box's weight $m_B \boldsymbol{g}$[2] which requires an external wrench

$$ \boldsymbol{w}^{\mathrm{ext}} = -(m_B \boldsymbol{g}, {}^{0}\boldsymbol{r}^{W,B} \times m_B \boldsymbol{g}) $$

to be exerted by the human, at the wrist.

The joint torques are computed using an automatically generated [95] Recursive Newton-Euler Algorithm (RNEA) implementation of the equations of motion

$$ (\boldsymbol{\tau}, \boldsymbol{w}^{\mathrm{grw}}) = \mathrm{RNEA}(\boldsymbol{q}, \dot{\boldsymbol{q}}, \ddot{\boldsymbol{q}}, \boldsymbol{w}^{\mathrm{ext}}) \tag{5.5} $$

which also outputs the GRWs $\boldsymbol{w}^{\mathrm{grw}}$.

The Zero-Moment Point

The ZMP can be computed from the GRWs. If we separate the GRWs into force and moment components $\boldsymbol{w}^{\mathrm{grw}} = (\boldsymbol{f}^{\mathrm{grw}}, \boldsymbol{m}^{\mathrm{grw}})$, we can obtain the position of the ZMP in the sagittal plane.

$$ \mathrm{ZMP} = m_Z^{\mathrm{grw}} \ / \ f_Y^{\mathrm{grw}} \tag{5.6} $$

Collisions

The collisions are treated using collision spheres [70] in order to obtain a differentiable representation of collisions. A collision sphere $\mathcal{S} = (r, {}^{C}\mathrm{FKM})$ is characterized by its radius r and the forward-kinematic model of its center ${}^{C}\mathrm{FKM}$. At a given configuration $\boldsymbol{q}$, the distance $\mathrm{d}(\mathcal{S}_1, \mathcal{S}_2)$ between two spheres $\mathcal{S}_1$ and $\mathcal{S}_2$ can be computed as

$$ \mathrm{d}(\mathcal{S}_1, \mathcal{S}_2) = \| {}^{C_1}\boldsymbol{p} - {}^{C_2}\boldsymbol{p} \|_2 - (r_1 + r_2) \tag{5.7} $$

where ${}^{C_i}\boldsymbol{p} = {}^{C_i}\mathrm{FKM}(\boldsymbol{q})$ $(i = 1, 2)$ are the positions of the centers of the spheres. The no-collision constraint between the two spheres is readily imposed by requiring $\mathrm{d}(\mathcal{S}_1, \mathcal{S}_2) \geq 0$, and is differentiable with respect to the joint configurations by virtue of the differentiability of the norm $\|.\|_2$ and of the forward-kinematic model FKM.

Each segment of the human's body is assigned a sphere $\mathcal{S}_{\mathrm{seg}}$, which is centered at the segment's estimated center of mass $C_{\mathrm{seg}} = \mathrm{COM}_{\mathrm{seg}}$, with a radius $r_{\mathrm{seg}} = \varphi L_{\mathrm{seg}}$ equal to a factor $\varphi \in (0, \frac{1}{2}]$ times the segment length L_{seg}. The box is assigned a sphere $\mathcal{S}_B$ which is centered at the box $C_B = B$ with a radius $r_B = \frac{1}{2}\max(B_W, B_L)$ equal to half the maximum

[2] m_B is the box's mass and $\boldsymbol{g} = (0, -9.81, 0)$ is the gravity vector.

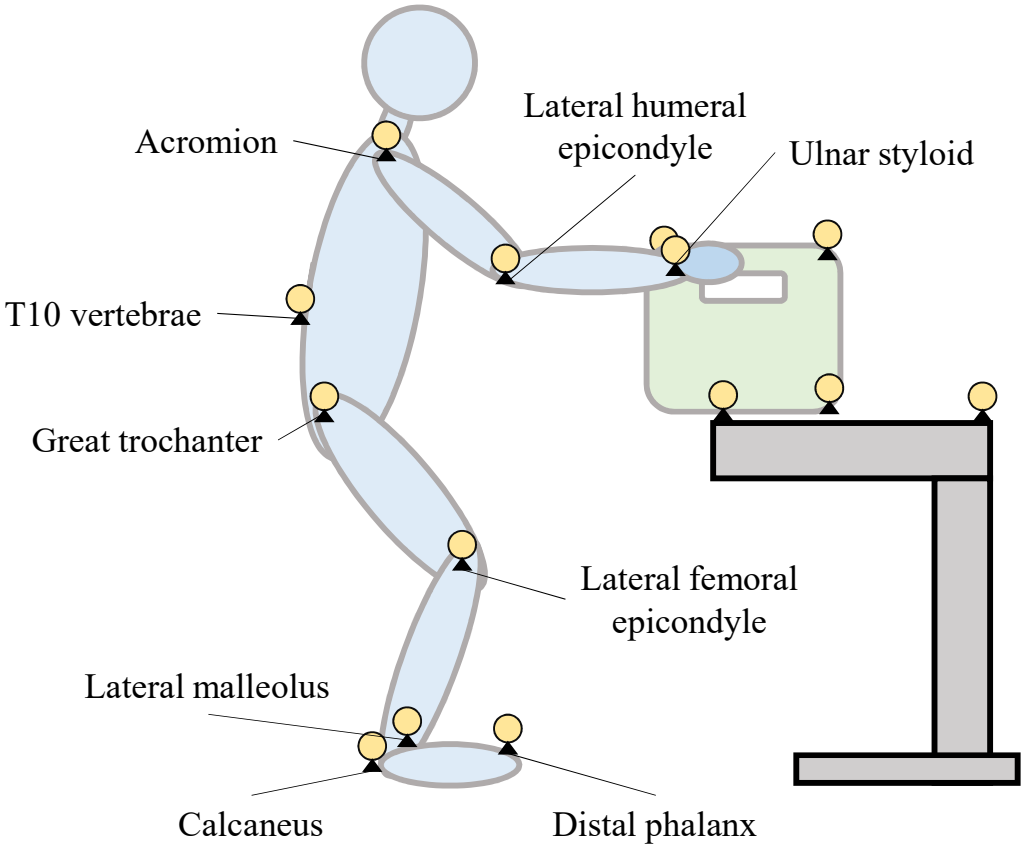

Figure 5.4: Diagrammatic representation of marker placement.

between the width and length of the box. The table is assigned multiple spheres[3] $\mathcal{S}_{\text{tab}}$ whose centers C_{tab} and radii r_{tab} are chosen such that the union of the spheres approximates the surface of the table. The position of the table spheres is independent of the joint angles $\boldsymbol{q}$, so their center does not have a Forward Kinematic Model (FKM) but a constant instead.

5.2.2 Experiments

Experimental Setup

Experimental data were collected from six healthy young adult males who performed four sets of five box lifting-lowering motions at their self-selected speed and at their self-selected distance from the box using a motion capture system and a force plate, yielding a set of 120 total captured motions.

The objective of the experiments was to study repetitive load lifting from the floor to support located at 0.75m and vice-versa. Participants stood vertically at a comfortable self-selected distance from the table. They manually lifted a 10 kg box (42.7x28.4x21.9cm), located at the center between the force plate and the table. A stereophotogrammetric system (six Flex 13 cameras, 100 Hz, Optitrack) and a force plate (100Hz, AMTI) recorded synchronously 3D positions of nine retro-reflective markers and GRWs, respectively. Markers were located at the following right anatomical landmarks: distal phalanx, calcaneus, lateral malleolus, lateral femoral epicondyle, great trochanter, t10 vertebrae, acromion, lateral humeral epicondyle, and ulnar styloid. The marker placement is diagrammatically represented in Figure 5.4.

[3] In the implementation there are 5 spheres, so tab $\in \{1, \ldots, 5\}$.

Experimental Procedure

Seven healthy male volunteers (age: 26.9 ± 4.7 years, height: 179.4 ± 7.6cm, weight: 77 ± 44.9Kg) with no history of musculoskeletal disorders, neurological injuries, or back pain, participated in the study after giving informed consent. Before data recording, each participant underwent a familiarization session with the whole experiment. Thereafter, three main trials were recorded for each participant. First, in order to identify the Body Segment Inertial Parameterss (BSIPs), participants were asked to perform upper and lower limbs excitation motions in the sagittal plane [105]: squat-like and pendulum-like motions, shoulder flexion/extension, and elbow flexion/extension motions. For each type of motion, fifteen repetitions were performed by increasing the execution speed each time. Figure 5.5 displays snapshots of a subject performing the said identification movements.

After a self-selected rest time, the box lifting task started by asking the participants to stand in a neutral posture on the force plate and lift the plastic box with both hands holding the handles. Two lifting motions were conducted: standard lifting and squat lifting. In the first case, participants performed four sets of five repetitions each, separated by 2min of rest. Whereas squat lifting consisted of only one set of five repetitions. Note that a repetition consists of picking up the box from the floor to the table, and then lifting it back to the floor (see Figure 5.3b).

Kinematic and Dynamic Identification

Finally, both kinematic and dynamometric data were introduced into the dynamic identification pipeline for BSIPs estimation [25]. Within the model-based trajectory generation framework founded upon the optimization of dynamic quantities, like effort or torque, it is important to perform the dynamic identification of the model *i.e.* to identify the BSIPs as the torque estimates can deviate up to 50% with respect to real values [105].

The raw motion capture data (*i.e.* X, Y, Z coordinates of all markers) was captured at 100 Hz and has been filtered using a 5$^{\text{th}}$ order zero-phase filter with a bandpass frequency of 3 Hz. The raw force plate data (*i.e.* $F_X, F_Y, F_Z, M_X, M_Y, M_Z$ all components of force and moment) was captured at 100 Hz and has been filtered using a 5$^{\text{th}}$ order zero-phase filter with a bandpass frequency of 1.5 Hz.

By solving the problem from Equation (5.8), the segment lengths $\boldsymbol{L}$ and joint trajectories $\boldsymbol{q}_i$ $(i = 0, \ldots, N)$ were extracted from marker data. The measured marker positions are denoted with ${}^0\boldsymbol{p}_i^m$, where m represents indices of markers and i the indices of time, while the predicted positions of the markers are denoted ${}^0\hat{\boldsymbol{p}}_i^m$ and are computed using the forward-kinematic model ${}^0\hat{\boldsymbol{p}}_i^m = {}^0\,\text{FKM}^m(\boldsymbol{q}_i)$.

$$\underset{\boldsymbol{L},\boldsymbol{q}}{\text{minimize}} \quad \sum_{i,m} \|{}^0\boldsymbol{p}_i^m - {}^0\hat{\boldsymbol{p}}_i^m\|_2^2 + \lambda\|\Delta\boldsymbol{q}_i\|_2^2 \tag{5.8a}$$

$$\text{subject to} \quad \boldsymbol{L}^- \leq \boldsymbol{L} \leq \boldsymbol{L}^+ \tag{5.8b}$$

$$\boldsymbol{q}^- \leq \boldsymbol{q}_i \leq \boldsymbol{q}^+, \qquad i = 0, \ldots, N \tag{5.8c}$$

The regularization term $\lambda\|\Delta\boldsymbol{q}_i\|_2^2$ serves to mitigate discontinuities and noise in joint trajectories.

By solving the problem from Equation (5.9), the segment masses $\boldsymbol{M}$, the segment center of mass position vectors COM, and the segment inertias $\boldsymbol{I}$ were extracted from the AMTI force plate data. Problem (5.9) also identifies the offset vector $\boldsymbol{r}$ between the local frame of the model base and the local frame of the force plate. The measured GRWs are denoted with ${}^{\text{FP}}\boldsymbol{F}_i^{\text{grw}} = ({}^{\text{FP}}\boldsymbol{f}_i^{\text{grw}}, {}^{\text{FP}}\boldsymbol{m}_i^{\text{grw}})$, while the predicted GRWs are denoted with ${}^0\hat{\boldsymbol{F}}_i^{\text{grw}} = ({}^0\hat{\boldsymbol{f}}_i^{\text{grw}}, {}^0\hat{\boldsymbol{m}}_i^{\text{grw}})$, both being composed of three forces and three moments. The mea-

(a) Squatting.

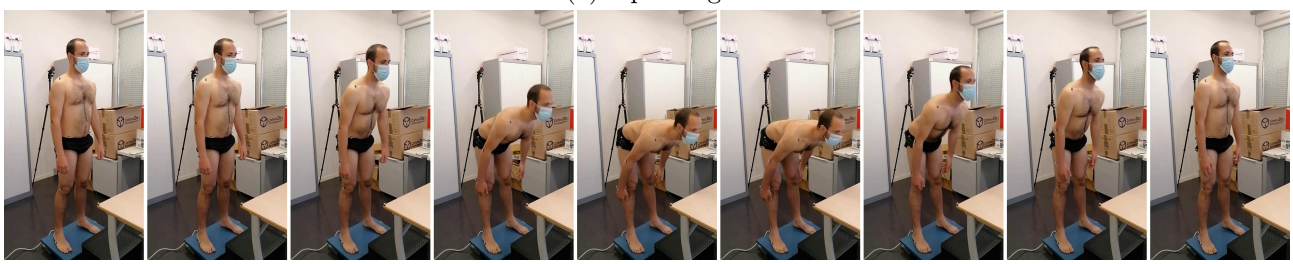

(b) Trunk bending.

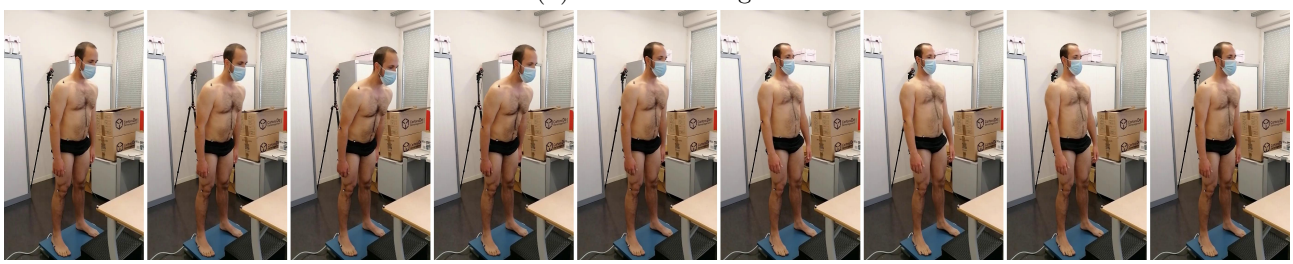

(c) Pendulum-like body swinging.

(d) Arm raises.

(e) Forearm swings.

Figure 5.5: Dynamically exciting movements performed for the dynamic identification of the model.

sured GRWs are natively expressed in the local frame of the force plate but are readily transformed to the local frame of the model base[4], hence the dependence on $\boldsymbol{r}$.

[4] ${}^{40}\boldsymbol{F}_i^{\text{grw}} = ({}^{0}\text{R}_{\text{FP}}{}^{\text{FP}}\boldsymbol{f}_i^{\text{grw}}, {}^{0}\text{R}_{\text{FP}}{}^{\text{FP}}\boldsymbol{m}_i^{\text{grw}} + {}^{0}\boldsymbol{r}_{0,\text{FP}} \times {}^{0}\text{R}_{\text{FP}}{}^{\text{FP}}\boldsymbol{f}_i^{\text{grw}})$ where ${}^{0}\text{R}_{\text{FP}}$ is the matrix describing the rotation of the local frame of the force plate in the local frame of the model base

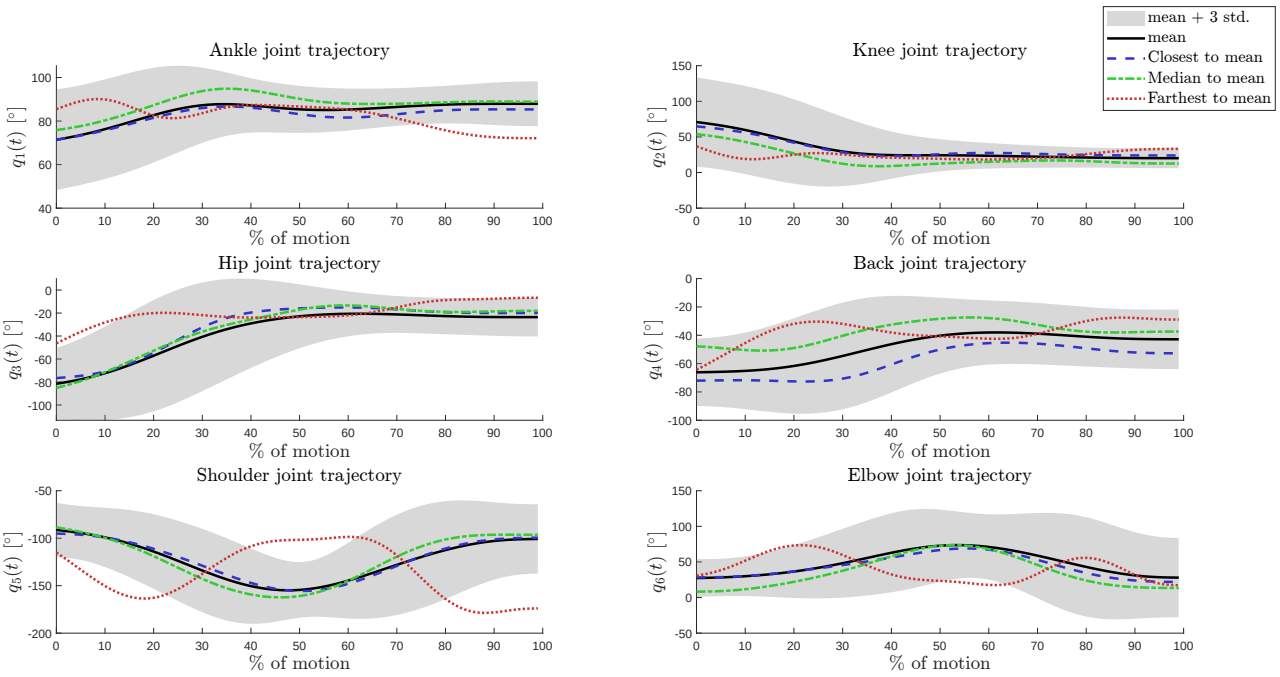

Figure 5.6: Statistics of the joint angle trajectories extracted from the data of all subjects. The mean of all joint angle trajectories is shown as a full black line, while the three standard deviations are depicted as the gray-shaded area. Three individual joint angle trajectories are shown, representing the trajectories that are the closest (dashed blue line), the median (dotted-dashed green line), and the farthest (dotted red line) from the mean joint angle trajectory in terms of the mean squared error.

$$\underset{\boldsymbol{M},\mathrm{COM},\boldsymbol{I},\boldsymbol{r}}{\text{minimize}} \quad \sum_i \| {}^0\boldsymbol{F}_i^{\mathrm{grw}} - {}^0\hat{\boldsymbol{F}}_i^{\mathrm{grw}} \|_U^2 \tag{5.9a}$$

$$\text{subject to} \quad \boldsymbol{M}^- \leq \boldsymbol{M} \leq \boldsymbol{M}^+ \tag{5.9b}$$

$$\mathrm{COM}^- \leq \mathrm{COM} \leq \mathrm{COM}^+ \tag{5.9c}$$

$$\boldsymbol{I}^- \leq \boldsymbol{I} \leq \boldsymbol{I}^+ \tag{5.9d}$$

$$\boldsymbol{r}^- \leq \boldsymbol{r} \leq \boldsymbol{r}^+ \tag{5.9e}$$

$$\boldsymbol{\tau}^- \leq \boldsymbol{\tau}_i \leq \boldsymbol{\tau}^+, \qquad i = 0, \ldots, N \tag{5.9f}$$

In order to accommodate the difference in units between forces and moments, the norm in (5.9a) is computed with respect to $U = \mathrm{diag}(1, 1, 0, 0, 100)$.

The predicted GRWs are computed alongside joint torques $\boldsymbol{\tau}_i$ using a RNEA [49], where the joint trajectories and their derivatives $\boldsymbol{q}_i, \dot{\boldsymbol{q}}_i, \ddot{\boldsymbol{q}}_i$ are the output of problem from Equation (5.8).

$$(\boldsymbol{\tau}_i, {}^0\hat{\boldsymbol{F}}_i^{\mathrm{grw}}) = \mathrm{RNEA}(\boldsymbol{q}_i, \dot{\boldsymbol{q}}_i, \ddot{\boldsymbol{q}}_i, \boldsymbol{w}^{\mathrm{ext}} = \boldsymbol{0} \mid \boldsymbol{M}, \mathrm{COM}, \boldsymbol{I})$$

In the problems from Equations (5.8) and (5.9), the bounds $\boldsymbol{L}^{\pm}$ (5.8b), $\boldsymbol{M}^{\pm}$ (5.9b), $\mathrm{COM}^{\pm}$ (5.9c), and $\boldsymbol{I}^{\pm}$ (5.9d) represent $\pm 20\%$ the values drawn from the anthropometric tables [121]. The bounds $\boldsymbol{q}^{\pm}$ (5.8c) have been chosen in accordance with literature [131]. The bounds $\boldsymbol{r}^{\pm}$ (5.9e) have been chosen as ± 5cm with respect to the expected offset given the experiment setup (OptiTrack global frame and AMTI force plate placement). The bounds $\boldsymbol{\tau}^{\pm}$ (5.9f) have been drawn from studies on the maximum joint torque capacities [89].

5.3 Methods

This section describes the optimization-based trajectory generation procedure in three steps, ending with describing the IOC based objective function identification. Section 5.3.1 the spline representation of the trajectories is described. Section 5.3.2 describes the exact formulation of the trajectory generation problem, using the kinematic and dynamic quantities that were previously described in Section 5.2. Finally, Section 5.3.3 describes the objective function identification via IOC.

5.3.1 Spline Trajectory Representation

For a general model with n DoFs enacted as joints, motion can be thought of as a trajectory within the n-dimensional configuration space of joints. Trajectories, being continuous functions of time, are inherently infinite-dimensional. A finite-dimensional spline representation is adopted here.

A spline is a continuous and smooth piece-wise polynomial. It is characterized by the degree d of the polynomials and by the $\mathcal{C}+1$ control points consisting of time-configuration pairs

$$(t^{\sigma_0}, \boldsymbol{q}^{\sigma_0}), (t^{\sigma_1}, \boldsymbol{q}^{\sigma_1}), \ldots, (t^{\sigma_\mathcal{C}}, \boldsymbol{q}^{\sigma_\mathcal{C}}) \tag{5.10}$$

which are used to compute the polynomial coefficients and interpolate the configurations in between. The spline trajectory $\boldsymbol{q}(t \mid \boldsymbol{t}^\sigma, \boldsymbol{q}^\sigma)$ is defined as the concatenation of $\mathcal{C}$ polynomials,

$$\begin{aligned}
&\forall k = 0, \ldots, \mathcal{C}-1: \\
&\boldsymbol{q}(t \mid \boldsymbol{t}^\sigma, \boldsymbol{q}^\sigma) = \boldsymbol{q}_k(t \mid \boldsymbol{t}^\sigma, \boldsymbol{q}^\sigma), && \text{for } t^{\sigma_k} \leq t \leq t^{\sigma_{k+1}} && \text{(5.11a)} \\
&\boldsymbol{q}_k(t \mid \boldsymbol{t}^\sigma, \boldsymbol{q}^\sigma) = \sum_{i=0}^{d} \boldsymbol{c}_i^{(k)} t^i, && \text{for } t^{\sigma_k} \leq t \leq t^{\sigma_{k+1}} && \text{(5.11b)}
\end{aligned}$$

where each polynomial $\boldsymbol{q}_k(t \mid \boldsymbol{t}^\sigma, \boldsymbol{q}^\sigma)$ is determined by its coefficients $\boldsymbol{c}_i^{(k)} = \boldsymbol{c}_i^{(k)}(\boldsymbol{t}^\sigma, \boldsymbol{q}^\sigma)$ which depend on the control point times $\boldsymbol{t}^\sigma = (t^{\sigma_0}, \ldots, t^{\sigma_\mathcal{C}})$ and depend *linearly* on the control point configurations $\boldsymbol{q}^\sigma = (\boldsymbol{q}^{\sigma_0}, \ldots, \boldsymbol{q}^{\sigma_\mathcal{C}})$.

By fixing the control point times $\boldsymbol{t}^\sigma \in \mathbb{R}^{\mathcal{C}+1}$, the trajectory $\boldsymbol{q}(t \mid \boldsymbol{q}^\sigma)$ becomes uniquely defined by the concatenated vector of control point configurations $\boldsymbol{q}^\sigma \in \mathbb{R}^{(\mathcal{C}+1)n}$. With a choice of degree $d = 5$ and because of its piece-wise polynomial structure, the time-derivatives of the trajectory $\dot{\boldsymbol{q}}(t), \ddot{\boldsymbol{q}}(t), \dddot{\boldsymbol{q}}(t)$ are smooth and easily computed.

5.3.2 Optimization

The trajectory generation problem is formulated as a constrained optimization problem. The decision variables of the trajectory generation problem are control point configurations $\boldsymbol{q}^\sigma \in \mathbb{R}^{(\mathcal{C}+1)n}$, since trajectories are represented as splines. The constraint functions guarantee adherence to the task description and the physical consistency of the motion. They are:

- initial configuration constraints (eq. (5.12b)),
- final wrist position in Cartesian space (eq. (5.12c)),
- joint angle limits (eq. (5.12d)),
- torque limit constraints (eq. (5.12e)),
- ZMP constraints (eq. (5.12f)),

- collision constraints (eq. (5.12g) and eq. (5.12h)).

The objective function encodes a preference for certain types of trajectories. In this work, it is supposed that the objective function is unknown and that it will be retrieved from data. However, it is supposed that the function has a parametric form $f(\boldsymbol{q}^\sigma, \boldsymbol{\omega})$, and it is the parameters $\boldsymbol{\omega}$ that will be identified. The parametric form and the identification procedure will be described in Section 5.3.3.

The trajectory generation is encoded as the following parametric optimization problem.

$$
\begin{aligned}
\underset{\boldsymbol{q}^\sigma \in \mathbb{R}^{(\mathcal{C}+1)n}}{\text{minimize}} \quad & f(\boldsymbol{q}^\sigma, \boldsymbol{\omega}) && && \text{(5.12a)}\\
\text{subject to} \quad & \boldsymbol{q}(0) = \boldsymbol{q}_i && && \text{(5.12b)}\\
& {}^W\boldsymbol{p}(T) = {}^W\boldsymbol{p}_f && && \text{(5.12c)}\\
& \boldsymbol{q}^- \leq \boldsymbol{q}(t) \leq \boldsymbol{q}^+ && \forall t \in [0, T] && \text{(5.12d)}\\
& \boldsymbol{\tau}^- \leq \boldsymbol{\tau}(t) \leq \boldsymbol{\tau}^+ && \forall t \in [0, T] && \text{(5.12e)}\\
& \text{ZMP}^- \leq \text{ZMP}(t) \leq \text{ZMP}^+ && \forall t \in [0, T] && \text{(5.12f)}\\
& \text{d}(\mathcal{S}_{\text{seg}}(t), \mathcal{S}_B(t)) \geq 0, \ \forall \text{seg} && \forall t \in [0, T] && \text{(5.12g)}\\
& \text{d}(\mathcal{S}_{\text{tab}}(t), \mathcal{S}_B(t)) \geq 0, \ \forall \text{tab} && \forall t \in [0, T] && \text{(5.12h)}
\end{aligned}
$$

The dependence of the quantities upon control points $\boldsymbol{q}^\sigma$ has been left out for clarity. The requirement that the constraints hold $\forall t \in [0, T]$ is very difficult to handle, and as such, they will be relaxed and required to hold at a finite number of times $t_i = \frac{i}{N} T$ $(i = 0, \ldots, N)$. For future reference, let the subscript i denote that a quantity is evaluated at time t_i, *i.e.* $\boldsymbol{q}_i = \boldsymbol{q}(t_i)$.

5.3.3 Inverse Optimal Control

Using knowledge from the literature, in Equation (5.13) we propose a set of features[5], *a.k.a.* basis functions, that encode preferences for certain types of trajectories. The minimization of the time-integrals $\sum_i \phi_i^m(\boldsymbol{q}^\sigma)$ of some of these features has been shown to produce human-like motion trajectories [23, 24, 61, 70].

$$
\begin{aligned}
\phi_i^1(\boldsymbol{q}^\sigma) &= \dot{\boldsymbol{q}}_i^T \dot{\boldsymbol{q}}_i && \text{(5.13a)}\\
\phi_i^2(\boldsymbol{q}^\sigma) &= \ddot{\boldsymbol{q}}_i^T \ddot{\boldsymbol{q}}_i && \text{(5.13b)}\\
\phi_i^3(\boldsymbol{q}^\sigma) &= \dddot{\boldsymbol{q}}_i^T \dddot{\boldsymbol{q}}_i && \text{(5.13c)}\\
\phi_i^4(\boldsymbol{q}^\sigma) &= {}^W\boldsymbol{v}_i^T {}^W\boldsymbol{v}_i && \text{(5.13d)}\\
\phi_i^5(\boldsymbol{q}^\sigma) &= {}^W\boldsymbol{a}_i^T {}^W\boldsymbol{a}_i && \text{(5.13e)}\\
\phi_i^6(\boldsymbol{q}^\sigma) &= \boldsymbol{\tau}_i^T \boldsymbol{\tau}_i && \text{(5.13f)}\\
\phi_i^7(\boldsymbol{q}^\sigma) &= (\boldsymbol{\tau} \odot \dot{\boldsymbol{q}}_i)^T (\boldsymbol{\tau} \odot \dot{\boldsymbol{q}}_i) && \text{(5.13g)}
\end{aligned}
$$

When each feature sum $\sum_i \phi_i^m = \phi^m$ is treated as a single feature and is assigned a single weight, the dimensionality of the parameter space $\dim \boldsymbol{\omega} = \dim \boldsymbol{\phi}$ is equal to the dimensionality of the feature vector. The objective function of the problem from Equation (5.12) has

[5] $\odot$ is the vector component-wise product.

the parametric form given in Equation (5.14).

$$f(\boldsymbol{q}^\sigma, \boldsymbol{\omega}) = \sum_m \omega^m \sum_i \phi_i^m(\boldsymbol{q}^\sigma) \tag{5.14}$$

IOC as a Bilevel Program

The measured human trajectory denoted with $\boldsymbol{q}^\chi(t)$ will be the data from which we will learn *i.e.* identify the parameters $\boldsymbol{\omega}$ by solving the problem from Equation (5.15). The loss function is the mean-squared-error[6] between the measured trajectory and the predicted trajectory $\boldsymbol{q}(\boldsymbol{\omega})$. The cost function identification, *i.e.* the IOC problem, is a bilevel optimization problem [99] as the constraint (5.15c) includes the result of an optimization process. The feasible weight set is $\Omega = \mathbb{R}_{++}^{\dim \boldsymbol{\phi}}$ when the parametric function form is chosen as (5.14) .

$$\begin{aligned}
\underset{\boldsymbol{\omega}\in\Omega}{\text{minimize}} \quad & \text{MSE}(\boldsymbol{q}^\chi, \boldsymbol{q}(\boldsymbol{\omega})) && \text{(5.15a)}\\
\text{subject to} \quad & \boldsymbol{q}(\boldsymbol{\omega}) = \text{from eq. (5.11) using } \boldsymbol{q}^\sigma(\boldsymbol{\omega}) && \text{(5.15b)}\\
& \boldsymbol{q}^\sigma(\boldsymbol{\omega}) = \text{solution of (5.12)} && \text{(5.15c)}
\end{aligned}$$

Bilevel problems are particularly hard to solve as they are generically non-convex [99], and contain computationally intensive constraints.

5.3.4 Software Implementation

This section presents and quantifies the results and solutions of the different optimization problems described in Sections 5.2 and 5.3. These problems are the model kinematic identification (5.8c), the model dynamic identification (5.9f), the DOC problem of motion generation (5.12), as well as the problem of motion generation parameter identification (5.15) *i.e.* the IOC problem. The IOC problem (5.15) also requires solving multiple DOC motion generation problems (5.15c).

All of these optimization problems fall under the category of continuous nonlinear programming problems [17, 29] and have continuously differentiable objective functions and constraints. Except for the IOC problem (5.15) which is a bilevel problem, these problems are solved numerically using the open-source IPOPT software [54] for nonlinear programming, based on a primal-dual interior point method which is a highly robust optimization approach for solving large-scale nonlinear optimization problems.

The primal-dual interior point method can be interpreted as solving a sequence of (logarithmic) barrier problems, *i.e.* problems where the inequality constraints are integrated into the cost function through a scaled logarithmic barrier function, with a decreasing sequence of barrier scaling parameters converging to 0. Alternatively, one can think of it as solving the primal-dual equations via a homotopy method [54]. All barrier problems are solved using essentially Newton's method. Various heuristics and safeguards are implemented, such as optimality error scaling, adaptive update of the primal-dual step sizes and the barrier parameter, a line-search filter, and second-order corrections, rendering the method very robust for a wide range of problems [54].

The DOC and IOC models were built using the software package CasADi [124], which is built upon symbolic-like data structures that act as model variables and parameters. These data structures, referred to as SX (scalar) and MX (matrix) variables in the CasADi paper [124], are propagated through the model functions to construct a computational graph of

[6] $\text{MSE}(\boldsymbol{q}^\chi, \boldsymbol{q}) = \frac{1}{N+1}\sum_{i=0}^{N} \|\boldsymbol{q}_i^\chi - \boldsymbol{q}_i\|_2^2$

the different cost and constraints functions involved in the DOC and IOC models. From the computational graph, CasADi uses algorithmic differentiation [60] to infer first and second-order derivatives of the cost and constraints of the DOC model, which are the main building blocks of local-search-based nonlinear programming solvers [29]. The functions and their derivatives are provided to the IPOPT [54] nonlinear programming solver, which is used to compute the solution to the DOC problem (5.12) to generate predictions.

The IOC problem instances were solved using combined grid-search and local search. The grid search is initialized by constructing a point-grid G_r^m, over the m-simplex Δ^m containing parameter $\boldsymbol{\omega}$, which partitions each simplex edge into $r-1$ parts. The grid search proceeds by computing the DOC solution $\boldsymbol{q}^{\sigma,(\ell)}$ for each parameter value $\boldsymbol{\omega}^{(\ell)}$ from the set of grid points $G_r^m = \left\{\boldsymbol{\omega}^{(\ell)} \mid \ell = 1, \ldots, \binom{m+r-2}{m-1}\right\}$, and then checking which one has the smallest error with respect to the data. More details about grid search over the m-simplex, along with some examples, can be found within Appendix A.

5.4 Results

5.4.1 Model Identification

Across various subjects and trials, the results of the kinematic identification, depicted by Equation (5.8), have been tabulated in Table 5.4, representing the mean and standard deviation of the distance between the model-predicted marker positions and those measured by the motion capture system, involving markers corresponding to the knee, hip, back, shoulder, elbow, and wrist. These markers correspond respectively to the markers depicted in Figure 5.4 as the lateral femoral epicondyle, great trochanter, T10 vertebrae, acromion, Lateral humeral epicondyle, and the ulnar styloid markers. As mentioned in Section 5.2.2, the sample comprises 6 subjects.

Similarly, the outcomes of the dynamic identification as expressed by Equation (5.9) are summarized in Table 5.5. This table illustrates the mean and the standard deviation of the RMSE between the GRWs anticipated by the model and the GRWs ascertained by the force plate, focusing on the ground reaction forces in the **X** and **Y** directions, and the ground reaction moment in the **Z** direction, with the same sample size of 6 subjects.

Table 5.4: The mean and standard deviation of the distance between the marker positions predicted by the model and the marker positions measured by the motion capture system. The sample size is 6 subjects.

Marker	Knee	Hip	Back	Shoulder	Elbow	Wrist
RMSE [cm]	1.11 ± 0.17	1.00 ± 0.16	1.67 ± 0.31	1.91 ± 0.42	1.67 ± 0.36	1.63 ± 0.34

Table 5.5: The mean and standard deviation of the RMSE between the GRWs predicted by the model and the GRWs measured by the force place. The sample size is 6 subjects.

Force/Torque	Force X	Force Y	Torque Z
RMSE [N/N.m]	10.87 ± 4.47	27.1420 ± 14.19	16.79 ± 5.70

The results of the kinematic and the dynamic identification procedures in terms of identified parameters have been presented in Figures 5.7, 5.8, 5.9, and 5.10 for a randomly selected

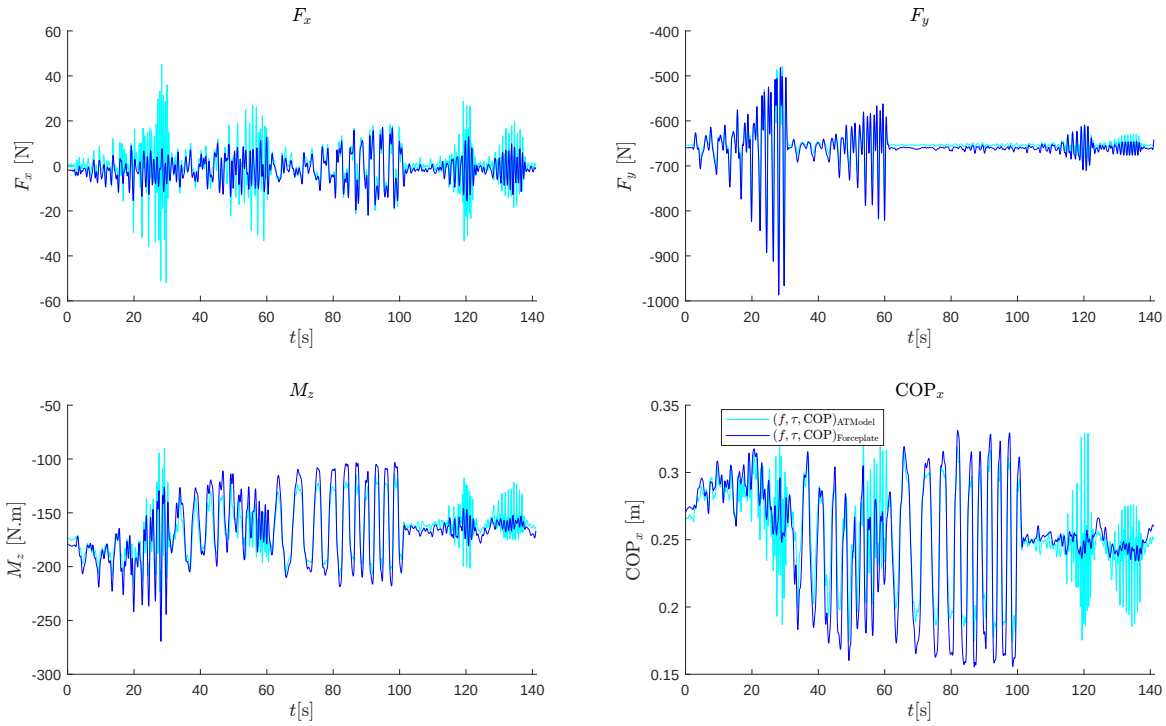

Figure 5.7: Fitting of the force plate measurements with the identified BSIPs.

subject, *i.e.* subject 2. In Figure 5.7, the fitting of the force plate measurements with the identified BSIPs is depicted, providing visual insights into the accuracy and reliability of the measurement approach and the identification process. Figure 5.8 presents a comparative analysis of the identified body segment masses against the values anticipated by anthropometric tables [121]. Similarly, Figure 5.9 contrasts the identified body segment inertias in the link frame against the predictions made by anthropometric tables [121]. Lastly, Figure 5.10 provides a comparative overview between the identified body segment center of mass positions and those forecast by anthropometric tables [121]. This comparison is crucial to validate the identified values and to ensure they conform to established anthropometric data. For a description of the segment frames, recall Figure 5.2.

5.4.2 Motion Generation

Using a single box-lifting trial and IOC, weights for the box-lifting objective function were identified, and were sparse, with only $\omega_3 = 0.96$ and $\omega_6 = 0.04$. The DOC problem instances were initialized using the measured trajectories $\boldsymbol{q}^{\chi}$, which were feasible with respect to the constraints of the problem (5.12). The IPOPT solver was run with default tolerance parameters, with options for numerical derivative and regularity checking turned on. The average computation time of the DOC would be around 30s, on a Dell Inspiron 15 [7] with an Intel®Core™i5-10400H CPU @ 2.60GHz [8].

A series of regularly timed snapshots of the model configuration in Cartesian space throughout the trajectory is given in Figure 5.11. The figure contains two characters, of which one animates the measured trajectory of the human subject while the other animates the trajectory predicted for that human. Each snapshot contains the entire path of the wrist, displayed as a dashed line for both characters. During the first third of the movement, the difference between the predicted and measured postures is negligible. During the second

[7] Dell's site link for specifications.
[8] Intel's site link for specifications.

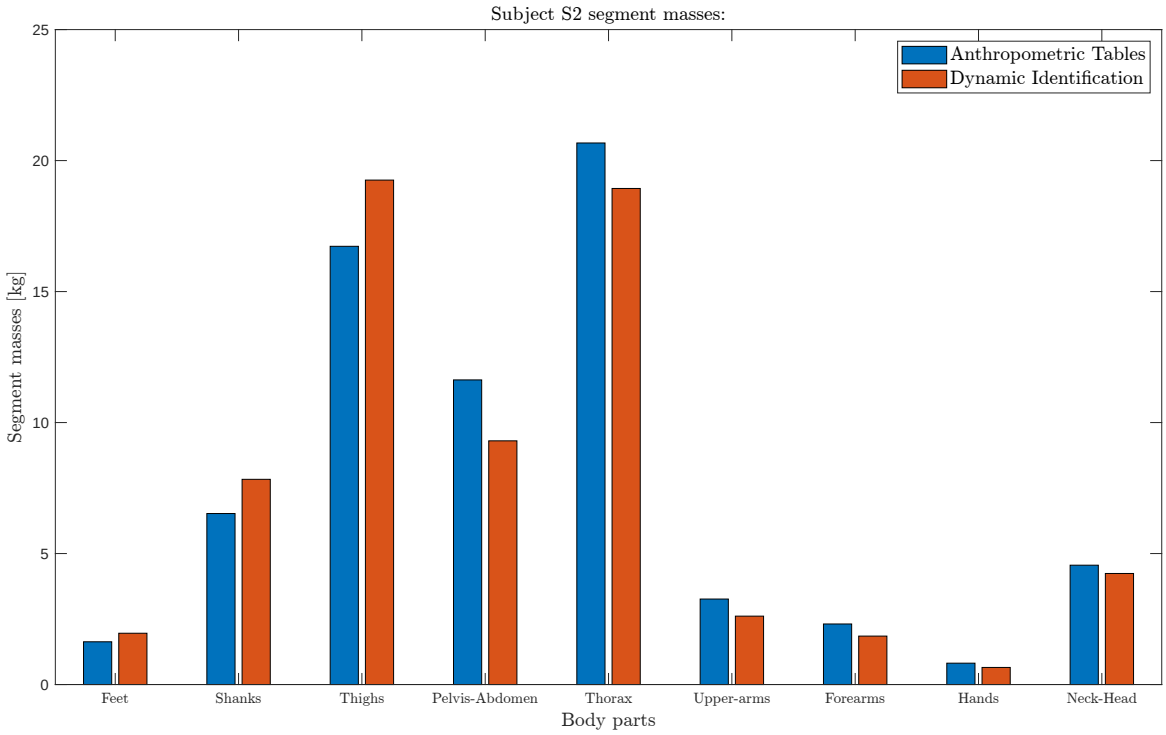

Figure 5.8: Comparison of identified body segment masses compared to values predicted by anthropometric tables [121].

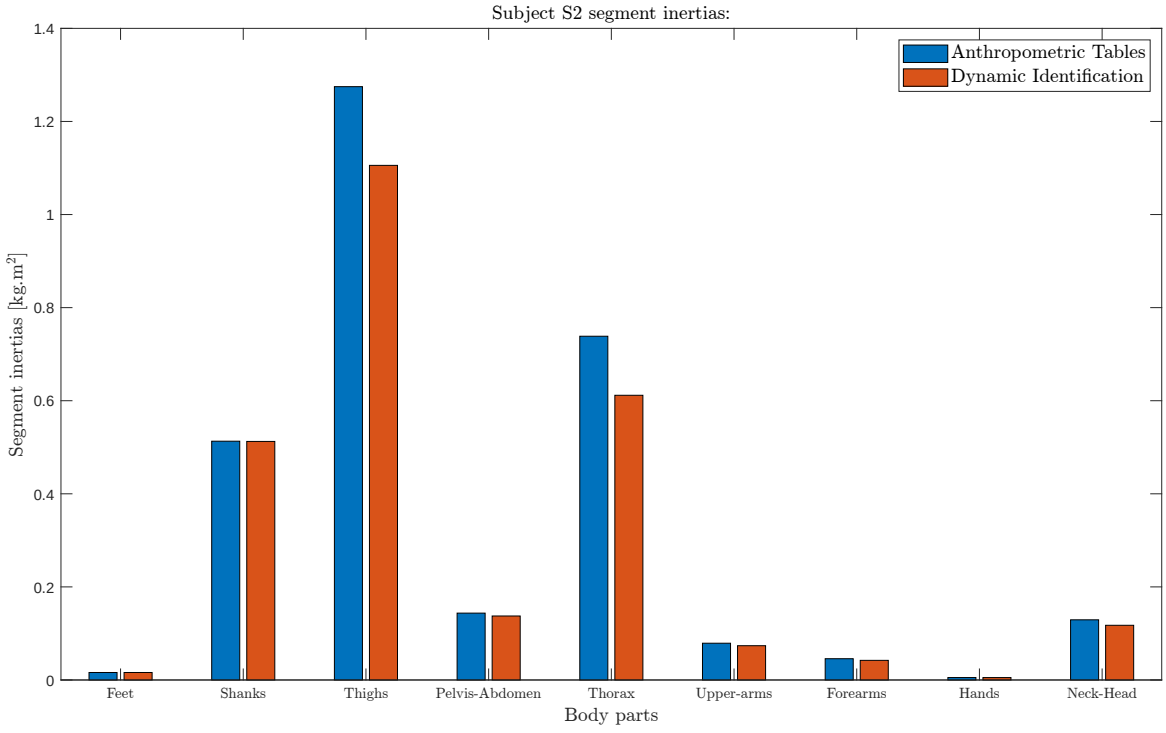

Figure 5.9: Comparison of identified body segment inertias (w.r.t link frame) compared to values predicted by anthropometric tables [121].

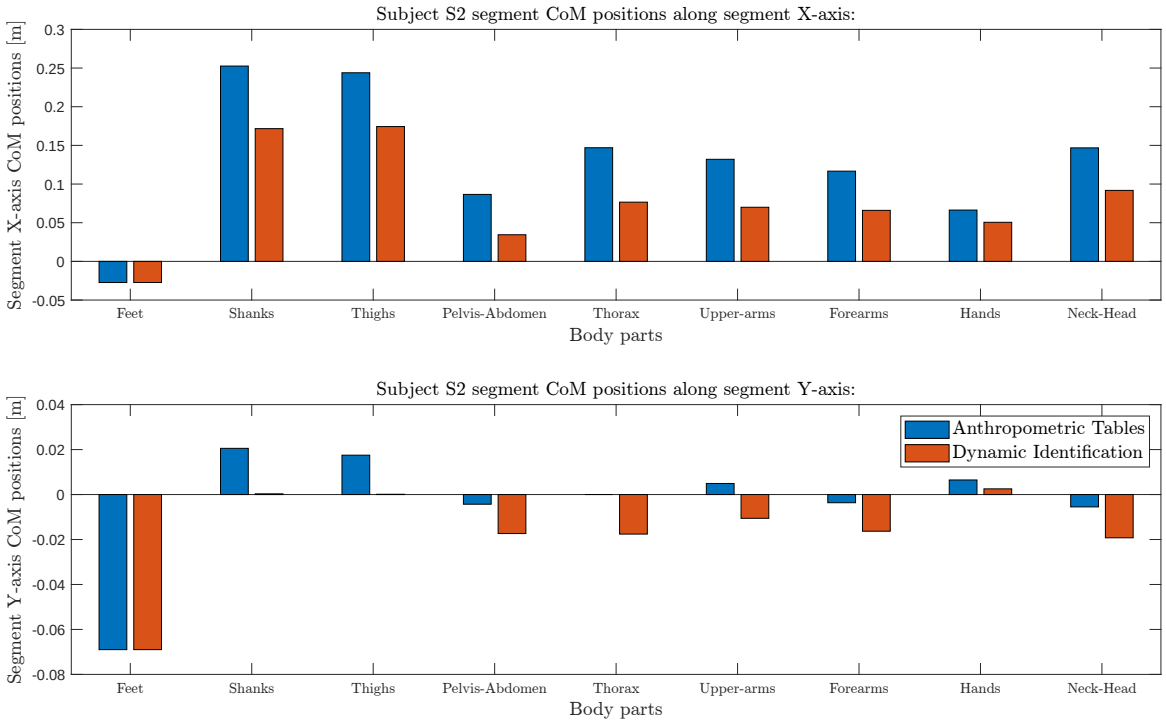

Figure 5.10: Comparison of identified body segment center of mass positions compared to values predicted by anthropometric tables [121].

third of the movement, the postures start to diverge most visibly, which can be explained by a difference in the strategy retrieved by the IOC and the one used by the human. We hypothesize that the actual human chooses to maintain a higher margin of safety when avoiding collision with the table. At about 65% of the movement, the postures regain their similarity and maintain an approximately constant error during the last third of the movement. Overall, the postures within the snapshots differ visibly but remain visually similar across the majority of the movement.

Figure 5.12 provides a comparison of the joint angle trajectories separately for each joint. One can notice the magnitude of the errors for the ankle, knee, and hip joints remains relatively small in comparison to the magnitude of the errors for the shoulder and elbow joints. The magnitude of the errors in the back joint is also relatively large towards the last part of the trajectory.

RMSE [°]	Subject_1	Subject_2	Subject_3	Subject_4	Subject_5	Subject_6
Ankle	5 ± 2	6 ± 3	7 ± 3	4 ± 1	11 ± 4	5 ± 2
Knee	18 ± 11	18 ± 10	33 ± 18	16 ± 6	24 ± 3	16 ± 6
Hip	21 ± 10	19 ± 8	29 ± 10	16 ± 6	23 ± 4	16 ± 6
Back	11 ± 8	7 ± 3	11 ± 5	10 ± 4	21 ± 6	16 ± 3
Shoulder	33 ± 14	25 ± 9	48 ± 14	27 ± 6	32 ± 12	38 ± 12
Elbow	32 ± 11	27 ± 9	43 ± 9	28 ± 7	22 ± 7	38 ± 11
Mean	20 ± 6	17 ± 5	28 ± 7	17 ± 3	22 ± 3	22 ± 4

Table 5.6: Rounded mean RMSEs ($\pm$ standard deviations of RMSEs) of the joint angle trajectories of the predicted motions compared to the joint angle trajectories of the measured motions for all subjects. The sample size for each subject is 20 trials.

Table 5.6 gives us further insight into the distribution of RMSEs of the predictions across joints and across subjects. The RMSE increases as we progress in the kinematic chain from

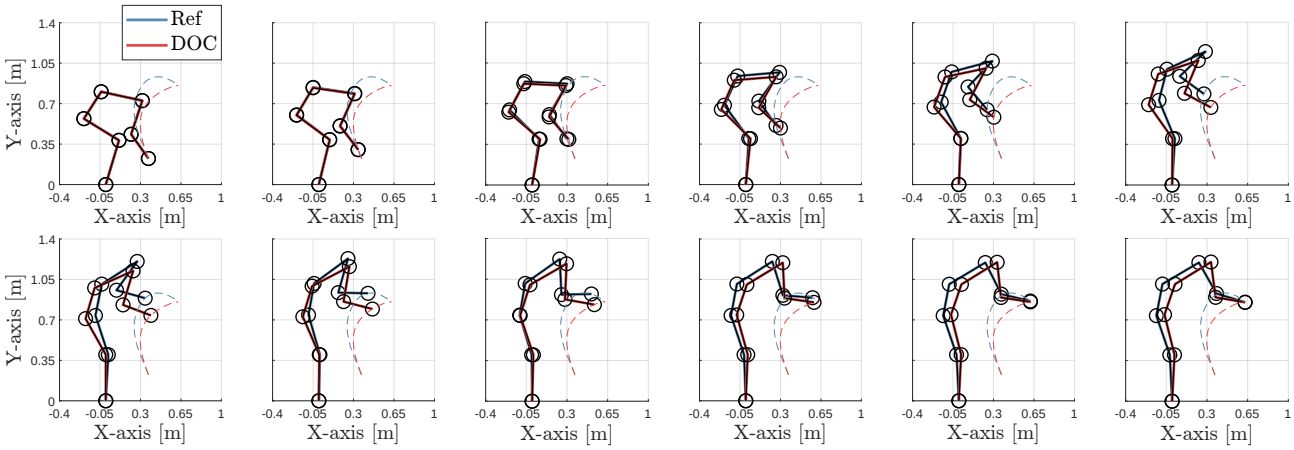

Figure 5.11: Twelve isochronous snapshots of the human's configuration during the lifting motion, at $0\%, 9.09\%, \ldots, 90.91\%,$ and 100% of the lifting motion (left-to-right, up-to-down). Both the measured motion (in blue) and the predicted motion (in red) for a single representative trial of a single subject are showcased. Dashed lines represent the trajectory of the human wrist, which is treated as the end-effector in this study.

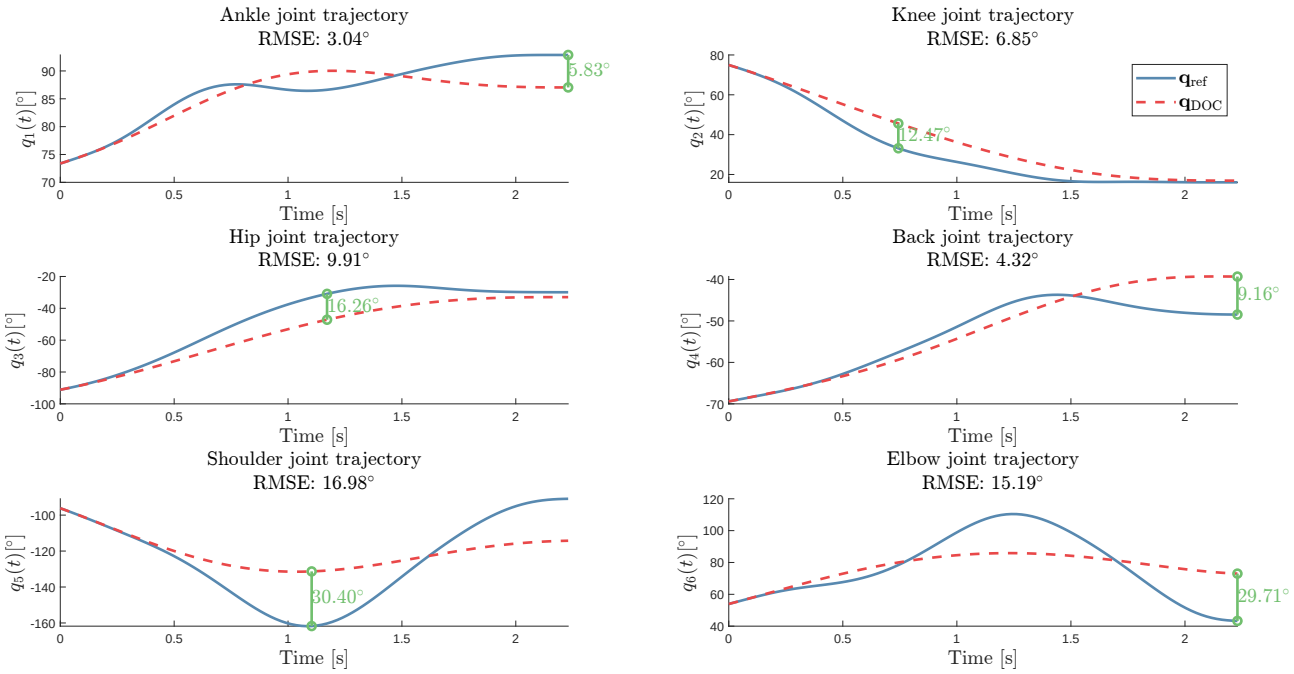

Figure 5.12: Individual joint angle trajectories during the lifting motion. Both the joint angles of the measured motion (blue full lines) and the joint angles of the predicted motion (red dashed lines) for a single trial of a single subject are showcased. The RMSEs for each joint angle trajectory is given above the corresponding plot. The maximum differences between measured and predicted joint angle trajectories are highlighted with green vertical lines and their numerical values are given.

the ankle to the elbow joint. The average RMSE is relatively similar across subjects, except for subject number 3, which has been identified as an outlier in terms of height/weight ratio. Table 5.7 exhibits the mean correlation coefficients of the predictions across joints and subjects. The CC decreases throughout the kinematic chain. Similar to the RMSE, the CC remains similar for all subjects, bar subject 3. The RMSE of the predictions is higher than state-of-the-art approaches using data-driven modeling [104, 134], indicating that the chosen objective function basis does not do a good enough job of explaining the motion of the subjects.

CC [1]	Subject_1	Subject_2	Subject_3	Subject_4	Subject_5	Subject_6
Ankle	$.47 \pm .54$	$.51 \pm .28$	$.91 \pm .07$	$.73 \pm .12$	$.54 \pm .25$	$.82 \pm .14$
Knee	$.86 \pm .37$	$.52 \pm .62$	$.76 \pm .34$	$.70 \pm .16$	$.84 \pm .13$	$.90 \pm .03$
Hip	$.97 \pm .03$	$.88 \pm .02$	$.92 \pm .05$	$.91 \pm .06$	$.85 \pm .23$	$.87 \pm .05$
Back	$.85 \pm .15$	$.86 \pm .07$	$.71 \pm .47$	$.71 \pm .17$	$.76 \pm .11$	$.84 \pm .11$
Shoulder	$.38 \pm .43$	$.56 \pm .28$	$-.22 \pm .38$	$.58 \pm .22$	$.44 \pm .38$	$.40 \pm .41$
Elbow	$.15 \pm .59$	$.08 \pm .37$	$-.44 \pm .28$	$.35 \pm .35$	$-.01 \pm .33$	$-.00 \pm .47$
Mean	$.61 \pm .15$	$.57 \pm .21$	$.44 \pm .14$	$.66 \pm .12$	$.57 \pm .17$	$.64 \pm .14$

Table 5.7: Mean correlation coefficients ($\pm$ standard deviations of correlation coefficients) of the joint angle trajectories of the predicted motions compared to the joint angle trajectories of the measured motions for all subjects. The sample size for each subject is 20 trials.

This distribution of errors can be partially explained by the inadequate modeling of the back joint. The entirety of the spine is modeled using only 1 DoF which is not enough to capture all of the variability of the spine-induced motion. The human spine is a complex structure consisting of 24 articulating vertebrae each containing nominally 3 DoFs (*i.e.* flexion-extension, lateral bending, axial rotation) but which are simultaneously constrained by the intervertebral discs and ligaments, and certain vertebraes connection to the ribs. When considering the whole spine as a singular unit, the entire motion of the spine is most often modeled using a 6 DoFs model with 3 translational and 3 rotational DoFs [114]. Even though the lifting motion we are studying is constrained to the plane, 1 DoF is not enough to encompass all motion details, which subsequent joints must compensate.

Even though the task is planar within the sagittal plane, the upper arm tends to move in the frontal and transversal planes due to the shoulder joint's multiple-DoFs nature. For this reason, previous research has outlined a need for modeling all the DoFs of the shoulder joint to account for all possible variations in the measured and predicted motions [105].

Some errors are also incurred in the elbow joint angle and elbow joint torque because of the simplified modeling of contact between the box and the human. The contact is assumed to be rigid and non-actuated at the wrist, which implies that the elbow joint angle (alongside other joint angles) must compensate for the motion introduced by the wrist joint. Moreover, the external wrench applied by the box is assumed constant in Cartesian space thus its variations are not taken into account during the motion, which implies that there is a discrepancy between the required external wrench in the model and the one in reality, inducing errors in the applied joint torques.

Because the body is modeled as a chain of rigid bodies, errors in the joint angles of joints closer to the chain's base tend to propagate to the joints closer to the chain's end. As such, the errors previously described and incurred in the earlier joint angles of the ankle, knee, hip, and back tend to propagate to the shoulder and elbow joints. To a certain extent, this justifies the large errors we observe in the shoulder and elbow joints. Moreover, joint torque errors incurred near the chain's end tend to propagate backward to joint torques of joints closer to the chain's base. This yields errors in the torque which is enforced in the dynamic equation of the model (5.4) implemented via the RNEA (5.5).

On the other hand, Figure 5.13 illustrates the extremes of box-lifting predictions. It provides an overlay of the best (Figure 5.13a), median (Figure 5.13b), and worst predictions (Figure 5.13c) in terms of RMSE on data of joint angle trajectories gathered from all subjects. In each sub-, the mean of all the joint angle trajectories is delineated by a solid black line, and the area shaded in gray is the 99.7% confidence interval, the dashed colored lines represent the joint trajectory prediction for that particular trial, while the full colored lines represent the reference joint trajectory. Figure 5.13a highlights that the best prediction lies entirely in

the confidence interval, while Figure 5.13b highlights that the median prediction lies mostly in the confidence interval. Even the worst predicted trajectory on Figure 5.13c stays in the confidence interval for the ankle, back, and elbow joints, but is far outside of it for the knee, hip, and shoulder joints. While the current model does not achieve high accuracy, the fact that the median prediction remains within the confidence intervals indicates that it still makes relatively sensible predictions of the lifting motion in more than half the cases.

5.5 Conclusion

This chapter presented an approach to biomechanical lifting simulation based on data. The importance of biomechanical simulations for lifting has been highlighted and optimization-based simulation approaches for biomechanical lifting have been reviewed. A 6 DoF model, consistent with the literature, was used in order to biomechanically model the human body. The methodology and results of kinematic and dynamic identification of BSIP have been presented. Trajectories were represented as B-splines, while the optimization-based motion generation model was supplied with standard constraints from the literature. When applicable, less constraining versions of the constraints have been imposed (*i.e.* constraining the final end-effector position instead of the final joint configuration, dynamic stability instead of static stability, ...). A set of basis objective functions has been established, in accordance with the trends from the literature, but restricted and curated by complexity. These objective functions were investigated as instigators of human motion using data-driven IOC. The optimal weighting of these objectives in terms of RMSE between the motion prediction they generated and the data that was input. The training set consisted of one sample. The prediction results were presented and analyzed on all samples.

The final accuracy obtained on the data set was not on par with other data-based approaches from the literature. An argument could be made, however, that the approach is much less restrictive in terms of the way the data is integrated within the model. Data-based approaches from the literature use the collected data in a direct manner within the optimization-based motion generation procedure, by constraining or tracking the error between the prediction and the data, whereas the approach presented in this chapter uses the data to identify the inversely optimal objective function which is then used independently of the data for later predictions.

Improvements are warranted in the domain of accuracy. From the perspective of IOC, this would require training on larger sets of training data and more objective functions within the basis. Current approaches are not fast enough to be able to handle that amount of computation. A necessary condition for this is the improvement of the IOC solution method, which would require a thorough inquiry into the bilevel optimization methods state-of-the-art and the use of efficient and robust bilevel solvers capable of handling general nonlinear bilevel problems, which to the best of the author's knowledge, do not currently exist.

From the perspective of human modeling and experiment design, it would seem that a different model of the spine would induce less error in the distal joints of the 6 DoF model, while more detailed modeling of the wrist joint may account for less error in the elbow joint trajectory predictions, due to inaccuracies in the box's position and thus in the perceived collision constraints. Moreover, designing the experiment or the model in a way that takes into account the drift of the elbow joints from the sagittal plane could decrease the large prediction errors that are seen in the distal joints of the model.

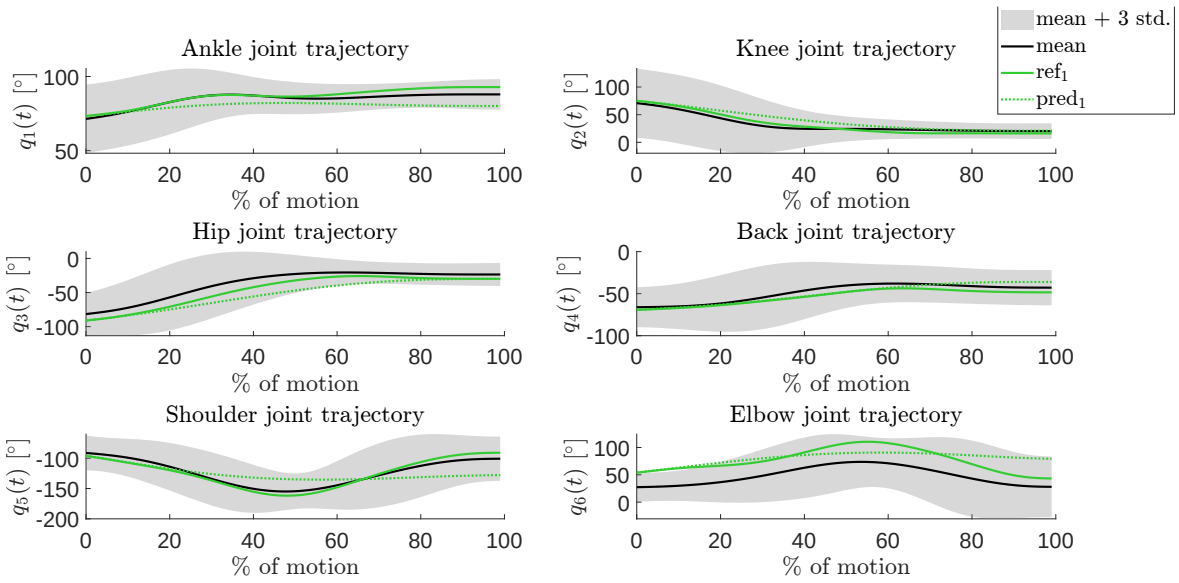

(a) Best prediction.

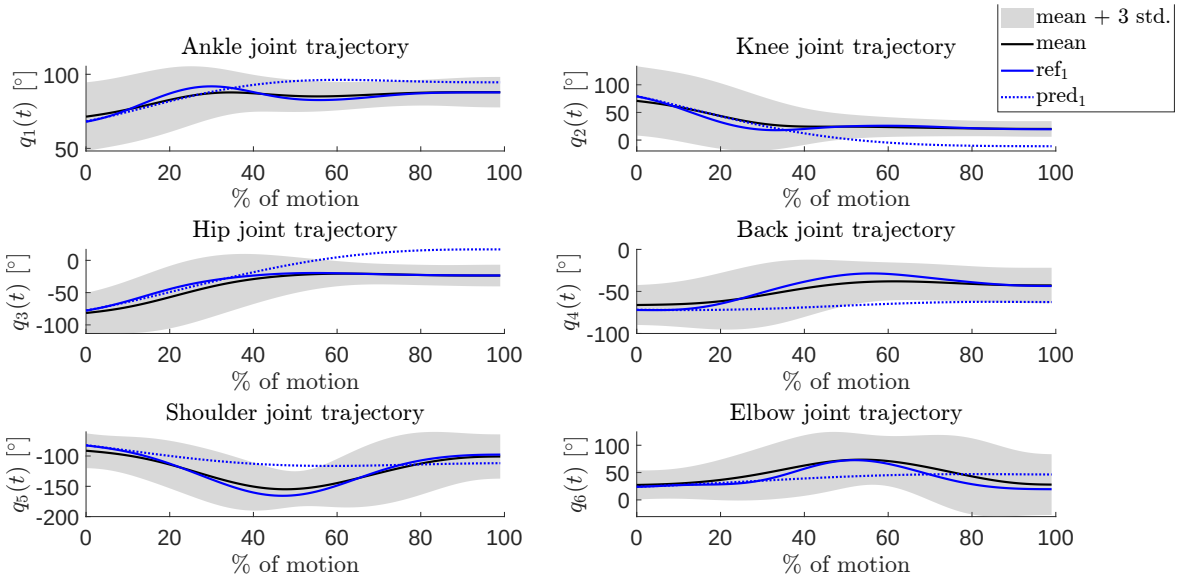

(b) Median prediction.

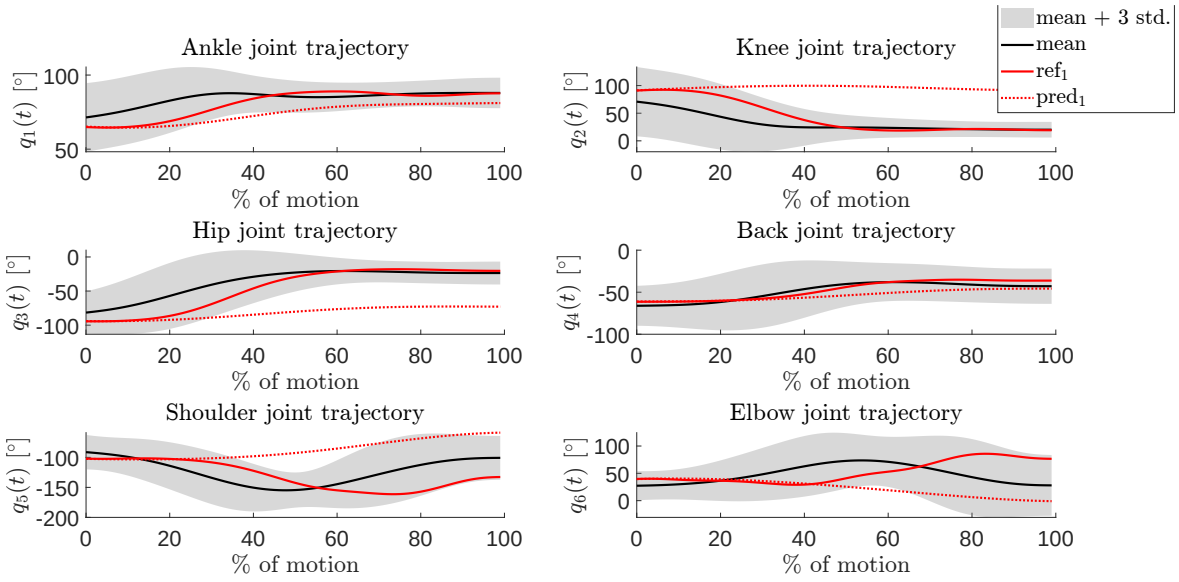

(c) Worst prediction.

Figure 5.13: Extremes of box lifting predictions: best, median, and worst predictions of joint angle trajectories overlaid with statistics extracted from all subjects' data. The overall mean is the solid black line and the gray-shaded area represents three standard deviations.

Chapter 6

Conclusion and Future Works

6.1 Summary

This thesis is a study in optimization-based human motion simulation and IOC. The goal has been to advance data-driven IOC theory and to apply data-driven IOC to further the accuracy of human motion simulations which are applicable in rehabilitation, ergonomics and workplace design, and humanoid robotics.

Chapter 2 is dedicated to the IOC problem, which naturally arises as a method to increase optimization-based human motion simulation accuracy by using data. This chapter delves into the broad literature on the subject, focusing predominantly on applications of IOC in human motion analysis, lending itself to a formalization of the IOC problem and elucidating different approaches.

The introduction provides a recollection of the emergence of IOC in the field of human motion analysis, tracing the development of two fairly popular methods, referred to in this manuscript as the bilevel method and the IKKT method. Surveying the applications of IOC, the section summarizes the main findings of each article and sorts the literature into two opposing stances *i.e.* in favor of, or not in favor of IKKT. The general formalization of IOC required setting up a framework where the DOC is thought of as a constrained parametric optimization problem, and the argmin operator is thought of as a set mapping. The general DOC formalization was done in the section on the general direct problem. The general inverse problem section proceeds to formalize general IOC as a type of complex, set-valued, non-linear regression problem. Perfect fitting of the data by the model is described by a property named consistency and is defined as a property of the model itself when the data set is fixed, and is very important later in the chapter. By exposing the issues one would encounter by attempting to do general IOC in a non-parametric way, the section on direct and inverse optimal control introduces the predominant and specific variety of IOC models that are used throughout the rest of the manuscript and much of the literature. What we refer to IOC relies on representing the DOC objective function as a weighted combination of basis objective functions. IOC then uses data to infer the optimal weighting of these objective functions, such that the optimization-based prediction is the most accurate. The section on the verification of inverse optimality unveils how KKT conditions may be used for determining when a DOC model is consistent with the data, for both convex and non-convex DOC models, in both the unconstrained and constrained case. Checking if a model is consistent with the data requires solving a linear or a conic programming problem, in the case of an unconstrained or a constrained DOC model respectively. The chapter culminates with the presentation of the two most popular "approximate" IOC methods as regression problems with different loss functions in the final section approximate optimality, where the bilevel method regresses with the mean-squared-error loss and the IKKT method regresses with the

KKT residual loss. This presentation included common analytic and algebraic manipulations used to reformulate these regression problems in literature.

Therefore, Chapter 2 contributes a novel formalization of the general DOC and general IOC problems. It introduces general IOC as a complex set-valued regression problem with different loss functions, introducing key concepts such as the KKT conditions, the parametric direct optimal mapping, and model-to-data consistency. Though it provides an introduction to both the bilevel and the IKKT methods, the chapter positions itself in favor of the bilevel method which sets the tone for the rest of the chapters as well.

Chapter 3 was dedicated to developing a method for computing lower bounds on the error of IOC for QP models of the DOC. The developed method can be used in the process of feature selection.

The first section delves into how the optimality conditions may be used to characterize the set of global optima of a parametrized optimization problem and presents Algorithm 1 for feature selection. The spotlight is focused on QP models in the following two sections. Global optima sets of unconstrained QP models are precisely characterized, and their compactness and path-connectedness properties are proven under strict convexity assumptions. This result is very important to theoretically justify using local-search algorithms to solve the bilevel IOC problem arising from unconstrained QP models of DOC. For global optima sets of constrained QP models the strict convexity assumption is lifted, and only their characterization is provided as the aforementioned properties require additional assumptions to prove. The heart of the chapter lies in the numerical methods section. After introducing gradients and Hessians needed to solve the bilevel IOC problem in the QP model case, the section focuses on LMI methods to compute lower bounds on the optimal value of the IOC objective function, *i.e.* the error between data and predictions. The main algorithms of this chapter are Algorithm 2 and Algorithm 3 for lower-bounding the IOC error, in the unconstrained and the constrained QP case respectively. A section is dedicated to numerical examples showcasing the results of the local search algorithm and the lower-bounding algorithms for both unconstrained and constrained cases. Important extensions are also discussed in the last section of the chapter.

The chapter formalizes the global optima sets for QP models of DOC and explores its analytical properties, of which compactness and path-connectedness are particularly important for justifying the use of local-search procedures to solve bilevel IOC problems. Using LMI relaxations of bilevel IOC problems to compute lower bounds and perform feature selection is a novel idea in the IOC literature. Therefore, the chapter opens the door to future methods for feature selection in IOC, and in particular ones based on relaxations of the bilevel IOC problem.

Chapters 4 and 5 are oriented towards practical applications and present analyses of two tasks related to human biomechanics and motor control. The tasks were chosen to have industrial and rehabilitation connotations so that the thesis results would have the potential for the development of future real-world solutions.

Chapter 4 studied the task of muscle force sharing during gait, which is widely studied in the literature on biomechanics and rehabilitation. IOC is applied to learn a DOC model of muscle force prediction during gait, which also allows for the prediction of joint stiffness.

The methods section formalizes the muscle force sharing problem as a DOC problem. Basis objective functions are sampled from the literature on optimal control-based muscle force sharing studies and are introduced in Table 4.1. The corresponding IOC problem is formalized using both the bilevel and the IKKT formalism. By using open-source muscle force data, optimization models of the muscle force sharing are identified with both IOC methods. Figure 4.3 showcases the central result: a comparison of the bilevel IOC muscle force predictions and muscle force data, contextualized by the overlaid data statistics. Table

4.2 showcases that using bilevel IOC significantly improves predictions compared to any individual objective function, which is not the case for the IKKT method of IOC. The JS is also well predicted as shown in Figure 4.5. A reduced numerical example of force-sharing shows that the IKKT method can produce pessimal results, supporting the overall preference for the bilevel method throughout the thesis. One of the limitations of the study is the need for validation on large data sets, which is hindered by the difficulty of collecting EMG data.

Besides contributing an identified optimal control model for muscle force sharing, which provides the best muscle force predictions during gait as measured by RMSE, the chapter contributes predictions and comparisons of joint stiffness. The stiffness prediction shows a lack of co-contractions, as it is systematically underestimated. This points to the lack of objective functions in the function basis that would favor co-contraction since the only way muscle agonist-antagonist pairs are linked is through the model constraints on torque. One key takeaway is that the CNS seems to favor minimizing muscle activations (L_1 and L_2 norms during stance, and L_3 norm during swing) and muscle power. Both of these quantities are dependent upon the state of the muscle, implying that there is a proprioceptive component to the contraction commands of the CNS. In the context of IOC, this chapter demonstrated the failure of the IKKT method and provided an example where it gave pessimal results when considering the bilevel IOC objective.

Chapter 5 studied the human box-lifting motion, a widely studied task in the literature on ergonomics and workplace design. A thorough examination of the literature on optimization-based approaches for lifting motion simulation has been presented at the beginning of the chapter, culminating in Table 5.3 and Table 5.2, respectively grouping constraints and objective functions most frequently encountered. The tables present a contribution in their own right. Subsequently, a 6 DoF biomechanical model in the sagittal plane has been adopted. Data collection was carried out with 6 healthy male subjects, using a motion capture system and single force plate. The data was processed using standard kinematic and dynamic identification procedures, yielding a marker tracking RMSE of 1.5 cm, a force GRW force-tracking RMSE of 19 N and moment-tracking 16.79 N. The fairly large error in moment tracking is attributed to frequent deviation of the identification movements from the sagittal plane. Using spline representations for trajectories, the motion generation algorithm has been formalized as a DOC containing joint, torque, and zero-moment-point limits, as well as boundary constraints and collision constraints. A small and computationally simple basis of objective functions was sampled from a large body of objective functions from the literature. Using bilevel IOC and a single sample of the experimentally collected data, the optimal weights of the objective functions were identified, and tested on the collected box-lifting data set. The resulting angular RMSE between the predicted and the measured joint trajectories across the whole data set was about 21°, but going as low as 9° for the best predictions. The best, median, and worst predictions are showcased in Figure 5.13. The median prediction falls within three standard deviations of the dataset. While the best of predictions would be considered at the state-of-the-art level, the median and average accuracy does not match the state-of-the-art in data-driven box-lifting motion simulation.

This chapter provided an initial inquiry into the capabilities of IOC when dealing with complex optimization-based models of DOC. The results indicated that the basis objective functions presented in Equation 5.13 are not expressive enough to generate human-like motions on average, but may attain state-of-the-art performance in the best cases. Including more biomechanically and physiologically realistic objective functions in the basis may help alleviate this problem, like for instance total muscular effort or dynamic balance. However, out of the considered optimization-based models the minimum-jerk model seems to work the best, as is commonly shown for arm motions in the literature. Body proportions may have a definitive influence on strategies used during lifting. This is indicated by the average

prediction RMSE and CC being similar across all subjects except subject 3, which is the only subject with significantly different body proportions.

A systematic overview and analysis of the literature and methods related to human motion modeling, IOC, muscle force sharing, and box-lifting were provided throughout all of the main chapters. Throughout the dissertation, the use of bilevel IOC and rejection of the much more popular IKKT method, because of its lack of robustness, was advocated. Although the bilevel method is much less computationally efficient, its results can be trusted in situations with much measurement noise and uncertain models, which is not the case for IKKT, which was demonstrated through examples in Chapters 3 and 4.

The general research hypotheses have been validated. On the one hand, the data analysis of the human box-lifting motion in joint space and the muscle force sharing during gait in muscle space has provided conclusive evidence of invariant aspects in the motions. The similarity of the trends in box-lifting joint angle trajectories across all subjects has been convincing, considering the different body proportions between the subjects. The muscle force sharing has shown a more striking similarity between different trials, but only one subject was considered. On the other hand, some invariant aspects of the motion produced by the motor control system have been captured in the optimization model, both in the muscle force-sharing problem and the box-lifting problem. A subset of muscles in the muscle force problem was extremely well-tracked by the simulation. As for the box-lifting, it was showcased that the median prediction in terms of RMSE did lay within the confidence intervals. The obtained results have shown the capability of the proposed models and methods to capture the inherent complexity of human movements and decisions using optimization with a compound objective function.

6.2 Future Works

The identified gaps and limitations in this thesis and in existing approaches accentuate the potential of further explorations in IOC, bilevel optimization, and the applications of IOC in biomechanics. The gaps include the establishment of analytic properties of the global or local optima sets of our biomechanical DOC models and reliable and efficient feature selection methods in the general case. Though local-search was applied to the IOC problem in the box lifting chapter, its path-connectedness and compactness were not guaranteed, and the algorithm could, and did easily encounter difficulties. Moreover, the features for the lifting motion were not optimally selected as manifested by the average accuracy of the model.

The most prominent limitation is the computational complexity of bilevel IOC. The box lifting IOC training procedure took over a day in computation time. Improvements in the accuracy and computational efficiency of bilevel program solution methods, as well as the existence and availability of reliable open-source software for solving bilevel programs, are essential and would be the most beneficial to current developments in IOC.

As IOC is still a relatively young field of research, and although valiant efforts have been made to collect and classify terminology [129, 138], the field could benefit from more papers that identify the most important research directions, standardize terminology, and connect the field to the related field of Inverse Reinforcement Learning which has benefited from more widespread interest.

The differences in the loss function used in IOC have been only rarely explored, though a multitude of different ones have been suggested. As such, understanding the properties of these different loss functions and designing new but useful ones in the future is an open challenge. Similarly, IOC is rarely combined with probability and statistics, in the sense that no probability distributions are placed upon the input data, the static task environment

parameters, or the model parameters. One way to arrive at more useful loss functions for IOC could be by fusing these two theories. However, being able to grapple with these ideas will require a very high degree of mathematical sophistication.

Another difficulty with IOC is the enormous complexity it requires to be trained on a data set. As presented in Equation (2.9), training IOC on a whole data set requires solving a bilevel problem with as many inner loop optimization problems as there are data points. As such, current IOC methods are usually required to limit themselves to only one training example in the case of complex models. Being able to simplify such training procedures using a decomposition of some sort would be a huge step forward for the field.

A natural continuation to the work developed in this thesis is the extension of the IOC-error lower-bounding methods to include max-representable and polynomial objective functions, by using the theory of polynomial optimization. It is the case that if the DOC model is a polynomial optimization problem, then the single-level IOC problem resulting from the application of the KKT conditions to the inner loop of the bilevel IOC problem will also be a polynomial optimization problem. Therefore, one can use the first step of the Lasserre hierarchy [100] to get an LMI providing an easy lower bound on the IOC error of the polynomial IOC problem. The extension of the IOC-error lower-bounding method to non-convex objective functions appears particularly difficult and may not submit to the application of LMIs for the lower-bounds. It will probably require case-specific relaxations of the DOC optimality requirement.

On the other hand, the field of IOC could benefit from the development of more feature selection methods that have mathematical guarantees. At the moment, there exist feature selection algorithms with no guarantees, based on the IKKT method. To the best of the author's knowledge, the feature selection algorithm for QP models is one of the few with some sort of mathematical guarantee.

Future endeavors should aim to refine the choice of error and objective functions in muscle force problems, enhancing the models' ability to reflect human physiology and biomechanics accurately by including objective functions that reflect the current muscle state, or the current body state. The use of higher-order temporal characteristics of the muscle forces within the basis of objective functions could be of interest. In a similar vein, objective functions based on joint stiffness, or agonist-antagonist muscle pairs, could be worth studying.

Concerning the box lifting motion, as well as general whole-body human movements, cornering the most important individual features before running the lengthy IOC procedure seems to be of great importance. Extending the box lifting study of this thesis could be done by including more biomechanically realistic functions like total muscle effort or dynamic balance. Higher-level, task-oriented features like distance to the goal, maximum collision margin, or completion time, could provide a much richer DOC representation of the box-lifting motion. However, including these features in the study would be more interesting if simultaneously modeling the human perception system, and will certainly require access to powerful computers.

On the other hand, consideration of time-varying features is another possibility for future research. The way human subjects bring the box close to their body during the first part of the box-lifting motion is indicative of the minimization of joint torques. Moreover, the changing nature of the important features is supported in the muscle force sharing study where different weights were found for the objective functions in the stance and the swing phase. Literature in this direction already exists, but is focused on the IKKT method, which has played an antagonistic role in this manuscript.

Finally, traditional research in the biomechanics field has been focusing on optimization-based approaches to motion prediction, leaving a legacy on today's research in human motion. Eventually, a paradigm shift to reinforcement learning and its corresponding IRL for modeling

human motion in biomechanical studies may bring about some interesting insights.

Acronyms

BSIP Body Segment Inertial Parameters. 74, 81, 86, 97

CC Correlation Coefficient. 55, 56, 60, 84, 91, 98

DOC Direct Optimal Control. 10, 11, 24, 26–29, 33, 47, 48, 50, 52, 55–58, 60, 79–81, 88–92, 98

DoF Degree of Freedom. 4, 5, 9, 62, 64–66, 68, 71, 77, 85, 86, 90, 96, 98

DP Dynamic Programming. 11

EMG Electromyography. 2, 54, 59, 60, 90

FKM Forward Kinematic Model. 73

GRW Ground Reaction Wrench. 65, 72–76, 80, 90, 98

IKKT Inverse Karush-Kuhn-Tucker. 10, 11, 25, 26, 46–48, 54, 55, 57–60, 88–92, 96

IOC Inverse Optimal Control. 1–3, 6, 8–11, 13, 15, 16, 18, 19, 24–28, 30, 43, 45–48, 50, 52, 53, 56, 58–62, 65, 66, 77, 79–81, 83, 86, 88–92, 96, 99

JS Joint Stiffness. 46, 48, 49, 57, 58, 60, 61, 90, 96

KKT Karush-Kuhn-Tucker. 10, 20–22, 24, 25, 32, 39–41, 44, 47, 54, 55, 58–60, 88, 89, 92

LICQ Linear Independence Constraint Qualification. 20–22

LMI Linear Matrix Inequality. 30, 38–40, 43–45, 89, 92, 99

LP Linear Programming. 19–21, 30–32

MD Musculoskeletal Disorder. 1, 3

OCP Optimal Control Problem. 5, 11, 13, 14, 62, 68–70

PD Positive Definite. 34, 44

PGM Projection onto Global Minimizers. 29–32, 37, 43–45

PMP Pontryagin Maximum Principle. 9

PSD Positive Semidefinite. 30, 38, 41

QCQP Quadratically Constrained Quadratic Program. 27, 38

QP Quadratic Programming. 25, 27, 32, 33, 36, 39, 40, 45, 89, 92

RMSE Root Mean-Squared Error. 46, 47, 55–57, 60, 62, 68, 70, 80, 83–86, 90, 91, 96–98

RNEA Recursive Newton-Euler Algorithm. 72, 76, 85

SDP Semidefinite Programming. 27, 38, 39

SOS Sum of squares. 38, 44

ZMP Zero-Moment Point. 67–69, 72, 77

List of Figures

List of Tables

List of Algorithms

Bibliography

[1] John A Nelder and Roger Mead. "A simplex method for function minimization". In: *The computer journal* 7.4 (1965), pp. 308–313.

[2] Winston L Nelson. "Physical principles for economies of skilled movements". In: *Biological cybernetics* 46 (1983), pp. 135–147.

[3] Neville Hogan. "An organizing principle for a class of voluntary movements". In: *Journal of neuroscience* 4 (1984), pp. 2745–2754.

[4] Tamar Flash and Neville Hogan. "The coordination of arm movements: an experimentally confirmed mathematical model". In: *Journal of neuroscience* 5 (1985), pp. 1688–1703.

[5] Neville Hogan. "The mechanics of multi-joint posture and movement control". In: *Biological cybernetics* 52 (1985), pp. 315–331.

[6] Yoji Uno, Mitsuo Kawato, and Rika Suzuki. "Formation and control of optimal trajectory in human multijoint arm movement". In: *Biological cybernetics* 61 (1989), pp. 89–101.

[7] Mihalis Yannakakis. "Expressing combinatorial optimization problems by Linear Programs". In: *Journal of Computer and System Sciences* 43.3 (1991), pp. 441–466.

[8] W Herzog and P Binding. "Effects of replacing 2-joint muscles with energetically equivalent 1-joint muscles on cost-function values of non-linear optimization approaches". In: *Human movement science* 13 (1994), pp. 569–586.

[9] Simon M Hsiang and MM Ayoub. "Development of methodology in biomechanical simulation of manual lifting". In: *International Journal of Industrial Ergonomics* 13.4 (1994), pp. 271–288.

[10] Scott D Chasalow and Richard J Brand. "Algorithm AS 299: Generation of simplex lattice points". In: *Journal of the Royal Statistical Society. Series C (Applied Statistics)* 44.4 (1995), pp. 534–545.

[11] JJ Collins. "The redundant nature of locomotor optimization laws". In: *Journal of biomechanics* 28.3 (1995), pp. 251–267.

[12] Arthur D Kuo. "An optimal control model for analyzing human postural balance". In: *IEEE transactions on biomedical engineering* 42.1 (1995), pp. 87–101.

[13] MG Pandy, BA Garner, and FC Anderson. "Optimal control of non-ballistic muscular movements: a constraint-based performance criterion for rising from a chair". In: (1995).

[14] John F Soechting et al. "Moving effortlessly in three dimensions: does Donders' law apply to arm movement?" In: *Journal of Neuroscience* 15.9 (1995), pp. 6271–6280.

[15] Menashe Dornay et al. "Minimum muscle-tension change trajectories predicted by using a 17-muscle model of the monkey's arm". In: *Journal of motor behavior* 28.2 (1996), pp. 83–100.

[16] Marc J Dysart and Jeffrey C Woldstad. "Posture prediction for static sagittal-plane lifting". In: *Journal of Biomechanics* 29.10 (1996), pp. 1393–1397.

[17] Dimitri P Bertsekas. "Nonlinear programming". In: *Journal of the Operational Research Society* 48.3 (1997), pp. 334–334.

[18] Simon M Hsiang and Raymond W McGorry. "Three different lifting strategies for controlling the motion patterns of the external load". In: *Ergonomics* 40.9 (1997), pp. 928–939.

[19] Wisama Khalil and Denis Creusot. "SYMORO+: a system for the symbolic modeling of robots". In: *Robotica* 15 (1997), pp. 153–161.

[20] Dimitrios Tsirakos, Vasilios Baltzopoulos, and Roger Bartlett. "Inverse optimization: functional and physiological considerations related to the force-sharing problem". In: *Critical Reviews™ in Biomedical Engineering* 25 (1997).

[21] Christopher M Harris and Daniel M Wolpert. "Signal-dependent noise determines motor planning". In: *Nature* 394 (1998), pp. 780–784.

[22] Emanuel Todorov and Michael I Jordan. "Smoothness maximization along a predefined path accurately predicts the speed profiles of complex arm movements". In: *Journal of Neurophysiology* 80.2 (1998), pp. 696–714.

[23] TM Bernard, MM Ayoub, and CJ Lin. "Evaluation of a biomechanical simulation model for sagittal plane lifting". In: *International Journal of Industrial Ergonomics* 24.2 (1999), pp. 157–171.

[24] CJ Lin, MM Ayoub, and TM Bernard. "Computer motion simulation for sagittal plane lifting activities". In: *International Journal of Industrial Ergonomics* 24.2 (1999), pp. 141–155.

[25] T-W Lu and JJ O'connor. "Bone position estimation from skin marker co-ordinates using global optimisation with joint constraints". In: *Journal of biomechanics* 32.2 (1999), pp. 129–134.

[26] Kaisa Miettinen. *Nonlinear multiobjective optimization*. Vol. 12. Springer Science & Business Media, 1999.

[27] Eri Nakano et al. "Quantitative examinations of internal representations for arm trajectory planning: minimum commanded torque change model". In: *Journal of Neurophysiology* 81.5 (1999), pp. 2140–2155.

[28] Jorge Nocedal and Stephen Wright. "Numerical Optimization". In: *Springer Science* 35 (1999), pp. 67–68.

[29] Jorge Nocedal and Stephen J Wright. *Numerical optimization*. Springer, 1999.

[30] Nguyen Nang Tam. "On continuity properties of the solution map in quadratic programming". In: *Acta Mathematica Vietnamica* 24 (1999), pp. 47–61.

[31] Richard H Byrd, Jean Charles Gilbert, and Jorge Nocedal. "A trust region method based on interior point techniques for nonlinear programming". In: *Mathematical programming* 89.1 (2000), pp. 149–185.

[32] James R Munkres. *Topology*. 2000.

[33] Andrew Y Ng, Stuart J Russell, et al. "Algorithms for inverse reinforcement learning." In: *Icml*. Vol. 1. 2000, p. 2.

[34] Dejan B Popovic and Thomas Sinkjaer. *Control of movement for the physically disabled: control for rehabilitation technology*. Springer, 2000.

[35] Chien-Chi Chang et al. “Biomechanical simulation of manual lifting using spacetime optimization”. In: *Journal of Biomechanics* 34.4 (2001), pp. 527–532.

[36] John Rasmussen, Michael Damsgaard, and Michael Voigt. “Muscle recruitment by the min/max criterion—a comparative numerical study”. In: *Journal of biomechanics* 34 (2001), pp. 409–415.

[37] Don B Chaffin. “On simulating human reach motions for ergonomics analyses”. In: *Human Factors and Ergonomics in Manufacturing & Service Industries* 12.3 (2002), pp. 235–247.

[38] Emanuel Todorov and Michael I Jordan. “Optimal feedback control as a theory of motor coordination”. In: *Nature neuroscience* 5.11 (2002), pp. 1226–1235.

[39] Farid Alizadeh and Donald Goldfarb. “Second-order cone programming”. In: *Mathematical programming* 95.1 (2003), pp. 3–51.

[40] Pieter Abbeel and Andrew Y Ng. “Apprenticeship learning via inverse reinforcement learning”. In: *Proceedings of the twenty-first international conference on Machine learning*. 2004, p. 1.

[41] Stephen Boyd, Stephen P Boyd, and Lieven Vandenberghe. *Convex optimization*. Cambridge university press, 2004.

[42] J. Lofberg. “YALMIP : a toolbox for modeling and optimization in MATLAB”. In: *ICRA (IEEE Cat. No.04CH37508)*. 2004, pp. 284–289.

[43] Philippe Sardain and Guy Bessonnet. “Forces acting on a biped robot. Center of pressure-zero moment point”. In: *IEEE Transactions on Systems, Man, and Cybernetics-Part A: Systems and Humans* 34.5 (2004), pp. 630–637.

[44] Emanuel Todorov. “Optimality principles in sensorimotor control”. In: *Nature neuroscience* 7.9 (2004), pp. 907–915.

[45] Miomir Vukobratović and Branislav Borovac. “Zero-moment point—thirty five years of its life”. In: *International journal of humanoid robotics* 1.01 (2004), pp. 157–173.

[46] Ömer Gündogdu, Kurt S Anderson, and Mohamad Parnianpour. “Simulation of manual materials handling: Biomechanial assessment under different lifting conditions”. In: *Technology and Health Care* 13.1 (2005), pp. 57–66.

[47] L. Lei et al. “Risk factors for the prevalence of musculoskeletal disorders among Chinese foundry workers.” In: *International Journal of Industrial Ergonomics.* 35.12 (2005), pp. 197–204.

[48] Carlo L Bottasso et al. “A numerical procedure for inferring from experimental data the optimization cost functions using a multibody model of the neuro-musculoskeletal system”. In: *Multibody System Dynamics* 16 (2006), pp. 123–154.

[49] John J Craig. *Introduction to robotics*. Pearson Educacion, 2006.

[50] Jeffrey N Katz. “Lumbar disc disorders and low-back pain: socioeconomic factors and consequences”. In: *JBJS* 88.suppl_2 (2006), pp. 21–24.

[51] M Praagman et al. “The relationship between two different mechanical cost functions and muscle oxygen consumption”. In: *Journal of biomechanics* 39 (2006), pp. 758–765.

[52] Emanuel Todorov et al. “Optimal control theory”. In: *Bayesian brain: probabilistic approaches to neural coding* (2006), pp. 268–298.

[53] Andreas Wächter and Lorenz T Biegler. “On the implementation of an interior-point filter line-search algorithm for large-scale nonlinear programming”. In: *Mathematical programming* 106.1 (2006), pp. 25–57.

[54] Andreas Wächter and Lorenz T Biegler. "On the implementation of an interior-point filter line-search algorithm for large-scale nonlinear programming". In: *Mathematical programming* 106 (2006), pp. 25–57.

[55] Hitoshi Arisumi et al. "Dynamic lifting motion of humanoid robots". In: *Proceedings 2007 IEEE International Conference on Robotics and Automation*. IEEE. 2007, pp. 2661–2667.

[56] Ahmet Erdemir et al. "Model-based estimation of muscle forces exerted during movements". In: *Clinical biomechanics* 22 (2007), pp. 131–154.

[57] J Spjøtvold, P Tøndel, and TA Johansen. "Continuous Selection and Unique Polyhedral Representation of Solutions to Convex Parametric Quadratic Programs". In: *Journal of Optimization Theory and Applications* 134.2 (2007), pp. 177–189.

[58] Hitoshi Arisumi et al. "Dynamic lifting by whole body motion of humanoid robots". In: *2008 IEEE/RSJ International Conference on Intelligent Robots and Systems*. IEEE. 2008, pp. 668–675.

[59] Andrea Bauer, Dirk Wollherr, and Martin Buss. "Human–robot collaboration: a survey". In: *International Journal of Humanoid Robotics* 5.01 (2008), pp. 47–66.

[60] Andreas Griewank and Andrea Walther. *Evaluating derivatives: principles and techniques of algorithmic differentiation*. SIAM, 2008.

[61] Yujiang Xiang et al. *Optimization-based dynamic human lifting prediction*. Tech. rep. SAE Technical Paper, 2008.

[62] Jean-Pierre Aubin and Hélène Frankowska. *Set-Valued Analysis*. Springer Science & Business Media, 2009.

[63] Jean Bernard. Lasserre. *Moments, Positive Polynomials And Their Applications*. Imperial College Press Optimization Series. World Scientific Publishing Company, 2009. ISBN: 9781908978271.

[64] Michael JD Powell et al. "The BOBYQA algorithm for bound constrained optimization without derivatives". In: *Cambridge NA Report NA2009/06, University of Cambridge, Cambridge* 26 (2009).

[65] David A Winter. *Biomechanics and motor control of human movement*. John wiley & sons, 2009.

[66] Edith M Arnold et al. "A model of the lower limb for analysis of human movement". In: *Annals of biomedical engineering* 38 (2010), pp. 269–279.

[67] Bruno R Da Costa and Edgar Ramos Vieira. "Risk factors for work-related musculoskeletal disorders: a systematic review of recent longitudinal studies". In: *American journal of industrial medicine* 53.3 (2010), pp. 285–323.

[68] R Timothy Marler and Jasbir S Arora. "The weighted sum method for multi-objective optimization: new insights". In: *Structural and multidisciplinary optimization* 41 (2010), pp. 853–862.

[69] Katja Mombaur, Anh Truong, and Jean-Paul Laumond. "From human to humanoid locomotion—an inverse optimal control approach". In: *Autonomous robots* 28.3 (2010), pp. 369–383.

[70] Yujiang Xiang et al. "Human lifting simulation using a multi-objective optimization approach". In: *Multibody System Dynamics* 23.4 (2010), pp. 431–451.

[71] Xiaowei Bao, Nikolaos V Sahinidis, and Mohit Tawarmalani. "Semidefinite relaxations for quadratically constrained quadratic programming: A review and comparisons". In: *Mathematical programming* 129 (2011), pp. 129–157.

[72] Bastien Berret et al. "Evidence for composite cost functions in arm movement planning: an inverse optimal control approach". In: *PLoS computational biology* 7.10 (2011), e1002183.

[73] Gert S Faber, Idsart Kingma, and Jaap H van Dieën. "Effect of initial horizontal object position on peak L5/S1 moments in manual lifting is dependent on task type and familiarity with alternative lifting strategies". In: *Ergonomics* 54.1 (2011), pp. 72–81.

[74] Arezou Keshavarz, Yang Wang, and Stephen Boyd. "Imputing a Convex Objective Function". In: *2011 IEEE international symposium on intelligent control*. IEEE. 2011, pp. 613–619.

[75] Parvin Abedi and Ali Leylavi Shoushtari. "Modelling and Simulation of Human-like Movements for Humanoid Robots." In: *ICINCO (1)*. 2012, pp. 342–346.

[76] Navid Aghasadeghi, Andrew Long, and Timothy Bretl. "Inverse optimal control for a hybrid dynamical system with impacts". In: *2012 IEEE International Conference on Robotics and Automation*. IEEE. 2012, pp. 4962–4967.

[77] Sebastian Albrecht, Marion Leibold, and Michael Ulbrich. "A bilevel optimization approach to obtain optimal cost functions for human arm movements". In: *Numerical Algebra, Control & Optimization* 2.1 (2012), p. 105.

[78] Sebastian Albrecht et al. "Modeling and analysis of human navigation with crossing interferer using inverse optimal control". In: *IFAC Proceedings Volumes* 45.2 (2012), pp. 475–480.

[79] Bob F Caviness and Jeremy R Johnson. *Quantifier Elimination and Cylindrical Algebraic Decomposition*. Springer Science & Business Media, 2012.

[80] Benjamin J Fregly et al. "Grand challenge competition to predict in vivo knee loads". In: *Journal of orthopaedic research* 30.4 (2012), pp. 503–513.

[81] Ross H Miller et al. "Evaluation of the minimum energy hypothesis and other potential optimality criteria for human running". In: *Proceedings of the Royal Society B: Biological Sciences* 279 (2012), pp. 1498–1505.

[82] Samer Mohammed, Yacine Amirat, and Hala Rifai. "Lower-limb movement assistance through wearable robots: State of the art and challenges". In: *Advanced Robotics* 26 (2012), pp. 1–22.

[83] Karthik Mohan and Maryam Fazel. "Iterative Reweighted Algorithms for Matrix Rank Minimization". In: *The Journal of Machine Learning Research* 13.1 (2012), pp. 3441–3473.

[84] Anne-Sophie Puydupin-Jamin, Miles Johnson, and Timothy Bretl. "A convex approach to inverse optimal control and its application to modeling human locomotion". In: *2012 IEEE ICRA*. 2012, pp. 531–536.

[85] Yujiang Xiang, Jasbir S Arora, and Karim Abdel-Malek. "3D human lifting motion prediction with different performance measures". In: *International Journal of Humanoid Robotics* 9.02 (2012), p. 1250012.

[86] Yujiang Xiang, Jasbir S Arora, and Karim Abdel-Malek. "Hybrid predictive dynamics: a new approach to simulate human motion". In: *Multibody System Dynamics* 28 (2012), pp. 199–224.

[87] Joao Gouveia, Pablo A Parrilo, and Rekha R Thomas. "Lifts of Convex Sets and Cone Factorizations". In: *Mathematics of Operations Research* 38.2 (2013), pp. 248–264.

[88] Miles Johnson, Navid Aghasadeghi, and Timothy Bretl. "Inverse optimal control for deterministic continuous-time nonlinear systems". In: *52nd IEEE Conference on Decision and Control*. IEEE. 2013, pp. 2906–2913.

[89] Thomas Robert, Julien Causse, and Gérard Monnier. "Estimation of external contact loads using an inverse dynamics and optimization approach: general method and application to sit-to-stand maneuvers". In: *Journal of biomechanics* 46.13 (2013), pp. 2220–2227.

[90] Ali Leylavi Shoushtari. "What strategy central nervous system uses to perform a movement balanced? Biomechatronical simulation of human lifting". In: *Appl Bionics Biomech* 10 (2013), pp. 113–124.

[91] Navid Aghasadeghi and Timothy Bretl. "Inverse optimal control for differentially flat systems with application to locomotion modeling". In: *2014 IEEE international conference on robotics and automation (ICRA)*. IEEE. 2014, pp. 6018–6025.

[92] Immanuel M Bomze, Stefan Gollowitzer, and E Alper Yıldırım. "Rounding on the standard simplex: Regular grids for global optimization". In: *Journal of Global Optimization* 59 (2014), pp. 243–258.

[93] N. Boumal et al. "Manopt, a Matlab Toolbox for Optimization on Manifolds". In: *Journal of Machine Learning Research* 15.42 (2014), pp. 1455–1459. URL: https://www.manopt.org.

[94] Weiguang Huo et al. "Lower limb wearable robots for assistance and rehabilitation: A state of the art". In: *IEEE systems Journal* 10.3 (2014), pp. 1068–1081.

[95] Wisama Khalil et al. "OpenSYMORO: An open-source software package for Symbolic Modelling of Robots". In: *2014 IEEE/ASME International Conference on Advanced Intelligent Mechatronics*. IEEE. 2014, pp. 1206–1211.

[96] Jiahong Song and Xingda Qu. "Effects of age and its interaction with task parameters on lifting biomechanics". In: *Ergonomics* 57.5 (2014), pp. 653–668.

[97] Nahema Sylla et al. "Human arm optimal motion analysis in industrial screwing task". In: *5th IEEE RAS/EMBS international conference on biomedical robotics and biomechatronics*. IEEE. 2014, pp. 964–969.

[98] Aharon Ben-Tal, Dick Den Hertog, and Jean-Philippe Vial. "Deriving robust counterparts of nonlinear uncertain inequalities". In: *Mathematical programming* 149.1-2 (2015), pp. 265–299.

[99] Stephan Dempe et al. "Bilevel programming problems". In: *Energy Systems. Springer, Berlin* 10 (2015), pp. 978–3.

[100] Jean Bernard Lasserre. *An introduction to polynomial and semi-algebraic optimization*. Vol. 52. Cambridge University Press, 2015.

[101] Mark L Latash and Vladimir Zatsiorsky. *Biomechanics and motor control: defining central concepts*. Academic Press, 2015.

[102] Adina M Panchea and Nacim Ramdani. "Towards solving inverse optimal control in a bounded-error framework". In: *2015 American Control Conference (ACC)*. IEEE. 2015, pp. 4910–4915.

[103] Claudio Pizzolato et al. "CEINMS: A toolbox to investigate the influence of different neural control solutions on the prediction of muscle excitation and joint moments during dynamic motor tasks". In: *Journal of biomechanics* 48 (2015), pp. 3929–3936.

[104] Jiahong Song, Xingda Qu, and Chun-Hsien Chen. "Lifting motion simulation using a hybrid approach". In: *Ergonomics* 58.9 (2015), pp. 1557–1570.

[105] Vincent Bonnet et al. "Optimal exciting dance for identifying inertial parameters of an anthropomorphic structure". In: *IEEE Transactions on Robotics* 32.4 (2016), pp. 823–836.

[106] Edo de Bruijn, FCT Van der Helm, and Riender Happee. "Analysis of isometric cervical strength with a nonlinear musculoskeletal model with 48 degrees of freedom". In: *Multibody System Dynamics* 36 (2016), pp. 339–362.

[107] Erik A Chumacero-Polanco and James Yang. "A review on human motion prediction in sit to stand and lifting tasks". In: *International Design Engineering Technical Conferences and Computers and Information in Engineering Conference*. Vol. 50077. American Society of Mechanical Engineers. 2016, V01AT02A066.

[108] Debora Clever and Katja D Mombaur. "An Inverse Optimal Control Approach for the Transfer of Human Walking Motions in Constrained Environment to Humanoid Robots." In: *Robotics: Science and systems*. 2016.

[109] Friedl De Groote et al. "Evaluation of direct collocation optimal control problem formulations for solving the muscle redundancy problem". In: *Annals of biomedical engineering* 44 (2016), pp. 2922–2936.

[110] Vaithilingam Jeyakumar et al. "Convergent Semidefinite Programming Relaxations for Global Bilevel Polynomial Optimization Problems". In: *SIAM Journal on Optimization* 26.1 (2016), pp. 753–780.

[111] Jonathan Feng-Shun Lin et al. "Human motion segmentation using cost weights recovered from inverse optimal control". In: *2016 IEEE-RAS 16th International Conference on Humanoid Robots (Humanoids)*. IEEE. 2016, pp. 1107–1113.

[112] Jim Mainprice, Rafi Hayne, and Dmitry Berenson. "Goal set inverse optimal control and iterative replanning for predicting human reaching motions in shared workspaces". In: *IEEE Transactions on Robotics* 32.4 (2016), pp. 897–908.

[113] Jiahong Song, Xingda Qu, and Chun-Hsien Chen. "Simulation of lifting motions using a novel multi-objective optimization approach". In: *International Journal of Industrial Ergonomics* 53 (2016), pp. 37–47.

[114] Hans-Joachim Wilke et al. "A new dynamic six degrees of freedom disc-loading simulator allows to provoke disc damage and herniation". In: *European Spine Journal* 25 (2016), pp. 1363–1372.

[115] Peter Englert, Ngo Anh Vien, and Marc Toussaint. "Inverse KKT: Learning cost functions of manipulation tasks from demonstrations". In: *The International Journal of Robotics Research* 36.13-14 (2017), pp. 1474–1488.

[116] Marta Gomez-Galan et al. "Musculoskeletal disorders: OWAS review". In: *Industrial health* 55.4 (2017), pp. 314–337.

[117] Andrew J Meyer, Carolynn Patten, and Benjamin J Fregly. "Lower extremity EMG-driven modeling of walking with automated adjustment of musculoskeletal geometry". In: *PloS one* 12.7 (2017), e0179698.

[118] Adina M Panchea and Nacim Ramdani. "Inverse Parametric Optimization in a Set-Membership Error-in-Variables Framework". In: *IEEE Transactions on Automatic Control* 62.12 (2017), pp. 6536–6543.

[119] Arash Ajoudani et al. "Progress and prospects of the human–robot collaboration". In: *Autonomous Robots* 42 (2018), pp. 957–975.

[120] Anil Aswani, Zuo-Jun Shen, and Auyon Siddiq. "Inverse optimization with noisy data". In: *Operations Research* 66.3 (2018), pp. 870–892.

[121] Raphaël Dumas and Janis Wojtusch. *Estimation of the Body Segment Inertial Parameters for the Rigid Body Biomechanical Models Used in Motion Analysis. In: Müller B., Wolf S.(eds) Handbook of Human Motion.* 2018.

[122] Adina M Panchea et al. "Human Arm Motion Analysis Based on the Inverse Optimization Approach". In: *2018 7th IEEE International Conference on Biomedical Robotics and Biomechatronics (Biorob)*. IEEE. 2018, pp. 1005–1010.

[123] Georg Still. "Lectures on parametric optimization: An introduction". In: *Optimization Online* (2018), p. 2.

[124] Joel A E Andersson et al. "CasADi – A software framework for nonlinear optimization and optimal control". In: *Mathematical Programming Computation* 11.1 (2019), pp. 1–36. DOI: 10.1007/s12532-018-0139-4.

[125] Wilian M. dos Santos and Adriano A.G. Siqueira. "Optimal impedance via model predictive control for robot-aided rehabilitation". In: *Control Engineering Practice* 93 (2019), p. 104177. ISSN: 0967-0661.

[126] Arthur van der Have, Sam Van Rossom, and Ilse Jonkers. "Squat lifting imposes higher peak joint and muscle loading compared to stoop lifting". In: *Applied Sciences* 9.18 (2019), p. 3794.

[127] Wanxin Jin et al. "Inverse optimal control for multiphase cost functions". In: *IEEE Transactions on Robotics* 35.6 (2019), pp. 1387–1398.

[128] Azin Zargham et al. "Inverse dynamic estimates of muscle recruitment and joint contact forces are more realistic when minimizing muscle activity rather than metabolic energy or contact forces". In: *Gait & Posture* 74 (2019), pp. 223–230.

[129] Nematollah Ab Azar, Aref Shahmansoorian, and Mohsen Davoudi. "From inverse optimal control to inverse reinforcement learning: A historical review". In: *Annual Reviews in Control* 50 (2020), pp. 119–138.

[130] MOSEK ApS. *The MOSEK optimization toolbox for MATLAB manual. Version 9.2.* 2020. URL: https://docs.mosek.com/9.2/toolbox/index.html.

[131] Saikat Chakraborty et al. "Accuracy of image data stream of a markerless motion capture system in determining the local dynamic stability and joint kinematics of human gait". In: *Journal of biomechanics* 104 (2020), p. 109718.

[132] Wanxin Jin, Zihao Liang, and Shaoshuai Mou. "Inverse Optimal Control from Demonstration Segments". In: *arXiv preprint arXiv:2010.15034* (2020).

[133] Frederik Greve Larsen et al. "Estimation of spinal loading during manual materials handling using inertial motion capture". In: *Annals of Biomedical Engineering* 48 (2020), pp. 805–821.

[134] Ritwik Rakshit, Yujiang Xiang, and James Yang. "Dynamic-joint-strength-based two-dimensional symmetric maximum weight-lifting simulation: Model development and validation". In: *Proceedings of the Institution of Mechanical Engineers, Part H: Journal of Engineering in Medicine* 234.7 (2020), pp. 660–673.

[135] Kevin Westermann, Jonathan Feng-Shun Lin, and Dana Kulić. "Inverse optimal control with time-varying objectives: application to human jumping movement analysis". In: *Scientific reports* 10.1 (2020), p. 11174.

[136] Amir Ali Ahmadi and Jeffrey Zhang. "Semidefinite Programming and Nash Equilibria in Bimatrix Games". In: *INFORMS Journal on Computing* 33.2 (2021), pp. 607–628.

[137] Filip Bečanović et al. *Pronalazak Optimizacione Funkcije Kretanja iz Simulirane Demonstracije Pokreta Čučnja*. 2021.

[138] Timothy CY Chan, Rafid Mahmood, and Ian Yihang Zhu. "Inverse optimization: Theory and applications". In: *arXiv preprint arXiv:2109.03920* (2021).

[139] Jessica Colombel, David Daney, and François Charpillet. "On the Reliability of Inverse Optimal Control". In: (2021).

[140] Bennet Gebken and Sebastian Peitz. "Inverse multiobjective optimization: Inferring decision criteria from data". In: *Journal of Global Optimization* 80.1 (2021), pp. 3–29.

[141] Luca Gualtieri, Erwin Rauch, and Renato Vidoni. "Emerging research fields in safety and ergonomics in industrial collaborative robotics: A systematic literature review". In: *Robotics and Computer-Integrated Manufacturing* 67 (2021), p. 101998.

[142] Ines Jammeli et al. "An assistive explicit model predictive control framework for a knee rehabilitation exoskeleton". In: *IEEE/ASME Transactions on Mechatronics* 27.5 (2021), pp. 3636–3647.

[143] Wanxin Jin et al. "Inverse Optimal Control from Incomplete Trajectory Observations". In: *The International Journal of Robotics Research* 40.6-7 (2021), pp. 848–865.

[144] Geng Li et al. "How well do commonly used co-contraction indices approximate lower limb joint stiffness trends during gait for individuals post-stroke?" In: *Frontiers in Bioengineering and Biotechnology* 8 (2021), p. 588908.

[145] Qiuwei Li, Daniel McKenzie, and Wotao Yin. *From the simplex to the sphere: Faster constrained optimization using the Hadamard parametrization*. 2021. DOI: 10.48550/ARXIV.2112.05273. URL: https://arxiv.org/abs/2112.05273.

[146] Marija Radmilović et al. *Influence of muscle co-contraction indicators for different task conditions*. 2021.

[147] Filip Bečanović et al. "Assessing the Quality of a Set of Basis Functions for Inverse Optimal Control via Projection onto Global Minimizers". In: *2022 IEEE 61st Conference on Decision and Control (CDC)*. IEEE. 2022, pp. 7598–7605.

[148] Jessica Colombel, David Daney, and François Charpillet. "On the Reliability of Inverse Optimal Control". In: *2022 International Conference on Robotics and Automation (ICRA)*. IEEE. 2022, pp. 8504–8510.

[149] Filip Becanovic et al. "Force Sharing Problem During Gait Using Inverse Optimal Control". In: *IEEE Robotics and Automation Letters* 8.2 (2023), pp–872.

[150] Jessica Colombel, David Daney, and François Charpillet. "Holistic view of Inverse Optimal Control by introducing projections on singularity curves". In: *2023 IEEE International Conference on Robotics and Automation (ICRA)*. IEEE. 2023, pp. 12240–12246.

Appendix A

Grid Search on the Simplex

Challenging optimization problems, often characterized by cost or constraint functions that are difficult to compute, and even more challenging to compute derivatives of, are often solved using derivative-free optimization methods. Examples of derivative-free methods are the grid search method and the Nelder-Mead simplex [1]. Randomized search algorithms like Simulated Annealing and Evolutionary Algorithms are often used. Another example includes the many derivative-free algorithms devised by Powell [64] which often rely on approximations and interpolations of the function being optimized.

Standard Grid Search

Equation (A.1) gives a placeholder constrained optimization problem that contains bound constraints $\boldsymbol{\omega}^- \leq \boldsymbol{\omega}' \leq \boldsymbol{\omega}^+$ on the optimization variable $\boldsymbol{\omega}'$.

$$\begin{aligned} \boldsymbol{\omega} = \underset{\boldsymbol{\omega}' \in \mathbb{R}^m}{\operatorname{argmin}} \quad & f(\boldsymbol{\omega}') \\ \text{subject to} \quad & \boldsymbol{h}(\boldsymbol{\omega}') = 0 \\ & \boldsymbol{g}(\boldsymbol{\omega}') \leq 0 \\ & \boldsymbol{\omega}^- \leq \boldsymbol{\omega}' \leq \boldsymbol{\omega}^+ \end{aligned} \tag{A.1}$$

The most simple and direct method to solve such optimization problems is the grid-search method. To satisfy the bound constraints, each of the coordinates $\omega_i,\ i = 1, \ldots, m$ of the optimization variable should be contained within a finite-length interval $[\omega_i^-,\ \omega_i^+] \subset \mathbb{R}$. Grid search is based on the idea of discretization of each of those intervals into a finite amount of points.

In standard grid-search, the interval is subdivided into $r - 1$ $(r > 1)$ subintervals of equal length, obtaining points

$$\omega_i^{(j)} = \omega_i^- + \frac{j}{r}(\omega_i^+ - \omega_i^-),\ j = 0, \ldots, r,$$

as the subinterval endpoints. Combining the subinterval endpoints once they are computed, a regular grid

$$G = \{(\omega_1^{(j_1)}, \ldots, \omega_m^{(j_m)}) \mid j_i = 0, \ldots, r\ (i = 1, \ldots, m)\}$$

over the finite coordinate box $\{\boldsymbol{\omega} \mid \boldsymbol{\omega}^- \leq \boldsymbol{\omega} \leq \boldsymbol{\omega}^+\} \subset \mathbb{R}^m$ is formed and contains r^m points, which we will denote with $\boldsymbol{\omega}^{(\ell)}$ with $\ell = 1, \ldots, r^m$. One then computes the value of the cost f and of the constraints $\boldsymbol{h},\ \boldsymbol{g}$ for each value of $\boldsymbol{\omega}^{(\ell)}$, yielding $f^{(\ell)},\ \boldsymbol{h}^{(\ell)},\ \boldsymbol{g}^{(\ell)}$. Subsequently, one simply chooses the grid point ℓ with the smallest $f^{(\ell)}$ where the constraints $\boldsymbol{h}^{(\ell)} = 0,\ \boldsymbol{g}^{(\ell)} \leq 0$

are satisfied *i.e.*

$$\ell^* = \underset{\ell=1,\ldots,r^m}{\operatorname{argmin}} \{ f^{(\ell)} \mid \boldsymbol{h}^{(\ell)} = 0,\ \boldsymbol{g}^{(\ell)} \leq 0 \}.$$

Simplex Grid Search

There are certain cases under which the constraints impose a special structure upon the decision variable, which allows the construction of a more efficient grid. When the special simplex constraint $\boldsymbol{\omega} \in \Delta^m$ occurs, where

$$\Delta^m = \{ \boldsymbol{\omega} \mid \omega_i \geq 0 \ (i = 1, \ldots, m),\ \sum_{i=1}^{m} \omega_i = 1 \}$$

is the m-simplex (or probability simplex), one can construct a slightly more efficient grid than the standard one. Equation (A.2) gives a placeholder constrained optimization problem that contains the simplex constraint on the optimization variable $\boldsymbol{\omega}'$.

$$\begin{aligned} \boldsymbol{\omega} = \underset{\boldsymbol{\omega}' \in \Delta^m}{\operatorname{argmin}} \quad & f(\boldsymbol{\omega}') \\ \text{subject to} \quad & \boldsymbol{h}(\boldsymbol{\omega}') = 0 \\ & \boldsymbol{g}(\boldsymbol{\omega}') \leq 0 \end{aligned} \tag{A.2}$$

Constructing a grid G_r^m on the m-simplex Δ^m with $r-1$ partitions of each simplex edge can be reformulated as a combinatorial problem. First, let us describe the grid points using integer variables. The set of grid points is equivalent to the set of all m-tuples of non-negative integers whose components sum to $r-1$,

$$(\omega_1, \ldots, \omega_m) = \frac{(j_1, \ldots, j_m)}{r-1}, \qquad j_i \in \mathbb{N},\ j_i \geq 0 \ (i = 1, \ldots, m),\ \sum_{i=1}^{m} j_i = r - 1,$$

and finding them can be reformulated as the problem of finding all the ways $r-1$ items may be distributed amongst m categories, which is colloquially referred to as the "Stars and Bars" problem. Such a grid contains $|G_r^m| = \binom{m+r-2}{m-1}$ grid points [10].

Once the grid points are generated, the search for the optimal point proceeds as per usual, by checking the value of the cost function and of the constraints at each grid point and choosing the one where the function value is the least, while the constraints are satisfied.

Figure A.1 presents two examples of regular grids G_4^3 and G_7^3 on the 3-simplex Δ^3 with $r-1=3$ and $r-1=6$ partitions along each edge, respectively. Grid G_4^3 contains $\binom{5}{2} = 10$ points, while the grid G_7^3 contains $\binom{8}{2} = 28$ points. The G_7^3 grid contains the G_4^3 grid as a subset $G_4^3 \subset G_7^3$, even though it is in general not true that $G_r^m \subset G_s^m$ when $r < s$.

The individual grid points for G_4^3 and G_7^3 are given in equation (A.3), with $G_4^3 = \{\boldsymbol{\omega}^{(1)}, \ldots, \boldsymbol{\omega}^{(10)}\}$ while $G_7^3 = \{\boldsymbol{\omega}^{(1)}, \ldots, \boldsymbol{\omega}^{(10)}, \boldsymbol{\omega}^{(11)}, \ldots, \boldsymbol{\omega}^{(28)}\}$. The grid points from the figure have been generated using Algorithm 4.

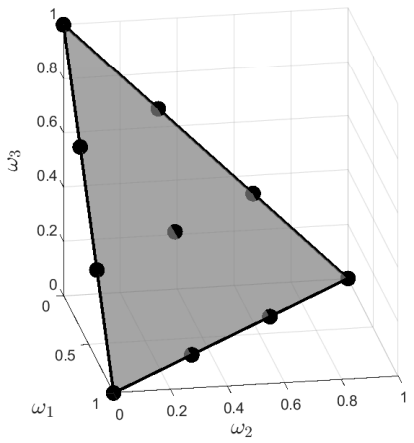

(a) A regular grid on the 3-simplex Δ^3 with 3 partitions along each edge ($m = 3,\ r = 4$), yielding $\binom{3+4-2}{3-1} = \binom{5}{2} = 10$ grid points.

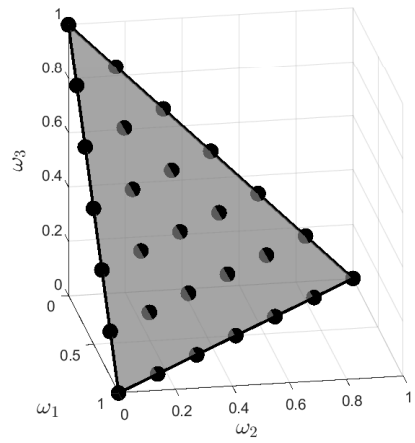

(b) A regular grid on the 3-simplex Δ^3 with 6 partitions along each edge ($m = 3,\ r = 7$), yielding $\binom{3+7-2}{3-1} = \binom{8}{2} = 28$ grid points.

Figure A.1: Examples of grids with different partitions ((a) $r = 4$, (b) $r = 7$) on a 3-simplex Δ^3.

$$
\begin{aligned}
\boldsymbol{\omega}^{(1)} &= \begin{bmatrix}0.000 & 0.000 & 1.000\end{bmatrix}^T & \boldsymbol{\omega}^{(15)} &= \begin{bmatrix}0.167 & 0.167 & 0.667\end{bmatrix}^T \\
\boldsymbol{\omega}^{(2)} &= \begin{bmatrix}0.000 & 0.333 & 0.667\end{bmatrix}^T & \boldsymbol{\omega}^{(16)} &= \begin{bmatrix}0.167 & 0.333 & 0.500\end{bmatrix}^T \\
\boldsymbol{\omega}^{(3)} &= \begin{bmatrix}0.000 & 0.667 & 0.333\end{bmatrix}^T & \boldsymbol{\omega}^{(17)} &= \begin{bmatrix}0.167 & 0.500 & 0.333\end{bmatrix}^T \\
\boldsymbol{\omega}^{(4)} &= \begin{bmatrix}0.000 & 1.000 & 0.000\end{bmatrix}^T & \boldsymbol{\omega}^{(18)} &= \begin{bmatrix}0.167 & 0.667 & 0.167\end{bmatrix}^T \\
\boldsymbol{\omega}^{(5)} &= \begin{bmatrix}0.333 & 0.000 & 0.667\end{bmatrix}^T & \boldsymbol{\omega}^{(19)} &= \begin{bmatrix}0.167 & 0.833 & 0.000\end{bmatrix}^T \\
\boldsymbol{\omega}^{(6)} &= \begin{bmatrix}0.333 & 0.333 & 0.333\end{bmatrix}^T & \boldsymbol{\omega}^{(20)} &= \begin{bmatrix}0.333 & 0.167 & 0.500\end{bmatrix}^T \\
\boldsymbol{\omega}^{(7)} &= \begin{bmatrix}0.333 & 0.667 & 0.000\end{bmatrix}^T & \boldsymbol{\omega}^{(21)} &= \begin{bmatrix}0.333 & 0.500 & 0.167\end{bmatrix}^T \\
\boldsymbol{\omega}^{(8)} &= \begin{bmatrix}0.667 & 0.000 & 0.333\end{bmatrix}^T & \boldsymbol{\omega}^{(22)} &= \begin{bmatrix}0.500 & 0.000 & 0.500\end{bmatrix}^T \\
\boldsymbol{\omega}^{(9)} &= \begin{bmatrix}0.667 & 0.333 & 0.000\end{bmatrix}^T & \boldsymbol{\omega}^{(23)} &= \begin{bmatrix}0.500 & 0.167 & 0.333\end{bmatrix}^T \\
\boldsymbol{\omega}^{(10)} &= \begin{bmatrix}1.000 & 0.000 & 0.000\end{bmatrix}^T & \boldsymbol{\omega}^{(24)} &= \begin{bmatrix}0.500 & 0.333 & 0.167\end{bmatrix}^T \\
\boldsymbol{\omega}^{(11)} &= \begin{bmatrix}0.000 & 0.167 & 0.833\end{bmatrix}^T & \boldsymbol{\omega}^{(25)} &= \begin{bmatrix}0.500 & 0.500 & 0.000\end{bmatrix}^T \\
\boldsymbol{\omega}^{(12)} &= \begin{bmatrix}0.000 & 0.500 & 0.500\end{bmatrix}^T & \boldsymbol{\omega}^{(26)} &= \begin{bmatrix}0.667 & 0.167 & 0.167\end{bmatrix}^T \\
\boldsymbol{\omega}^{(13)} &= \begin{bmatrix}0.000 & 0.833 & 0.167\end{bmatrix}^T & \boldsymbol{\omega}^{(27)} &= \begin{bmatrix}0.833 & 0.000 & 0.167\end{bmatrix}^T \\
\boldsymbol{\omega}^{(14)} &= \begin{bmatrix}0.167 & 0.000 & 0.833\end{bmatrix}^T & \boldsymbol{\omega}^{(28)} &= \begin{bmatrix}0.833 & 0.167 & 0.000\end{bmatrix}^T
\end{aligned}
\tag{A.3}
$$

Algorithm 4 describes a procedure for generating a list containing all the grid points of an m-simplex with r partitions. The procedure is recursive, with the function `SimplexGrid` being the base case which initializes the required variables, and the function `SimplexGridRecursion` being the recursive function. The algorithm generates points of the grid G_r^m inside a list in a programming language, by calling `SimplexGrid` with the desired parameters m and r.

Algorithm 4 assumes the existence of a method `add` for lists, which appends an element to the end of the list, as well as a language capacity for vector algebra with the existence of the method `zeros` which creates a vector of zeros of a given dimension, and scalar-vector multiplication with expressions such as $\boldsymbol{j}/(r-1)$ within `SimplexGridRecursion`.

Algorithm 4: Simplex Grid Generation by Recursion

Input: m, r
Output: G_r^m

Function `SimplexGrid`(m, r)**:**
    // Initialize recursion inputs
    $d = 0$ // Current component index
    $\boldsymbol{j} =$ `zeros`(m, 1) // Integer component vector
    $\Sigma = 0$ // Component sum
    $G_r^m =$ `list()` // Grid point list
    // Start recursion
    $G_r^m =$ `SimplexGridRecursion`(d, m, r, $\boldsymbol{j}$, Σ, G_r^m)
    return G_r^m

Function `SimplexGridRecursion`(d, m, r, $\boldsymbol{j}$, Σ, G_r^m)**:**
    // If the last component is reached
    if $d \geq m - 1$ **then**
        $\boldsymbol{j}[d] = (r - 1) - \Sigma$ // Last component completes integer sum
        G_r^m.`add`($\boldsymbol{j}/(r - 1)$) // Normalized vector added to list
        return G_r^m

    // Traverse all possible values for current component
    for $i = 0, \ldots, (r - 1) - \Sigma$ **do**
        $\boldsymbol{j}[d] = i$ // Set current component value
        $\Sigma_i = \Sigma + i$ // Update current sum value
        $G_r^m =$ `SimplexGridRecursion`($d + 1$, m, r, $\boldsymbol{j}$, Σ_i, G_r^m) // Call recursion for next component with updated sum

    return G_r^m

образац изјаве о ауторству

Изјава о ауторству

Име и презиме аутора Филип Бечановић

Број индекса 2020/5019

Изјављујем

да је докторска дисертација под насловом

Откривање оптималних стратегија у људском кретању путем инверзног оптималног управљања

- резултат сопственог истраживачког рада;
- да дисертација у целини ни у деловима није била предложена за стицање друге дипломе према студијским програмима других високошколских установа;
- да су резултати коректно наведени и
- да нисам кршио/ла ауторска права и користио/ла интелектуалну својину других лица.

Потпис аутора

У Београду, 24.11.2023.

Ф. Бечановић

Изјава о истоветности штампане и електронске верзије докторског рада

Име и презиме аутора Филип Бечановић

Број индекса 2020/5019

Студијски програм Електротехника и рачунарство

Наслов рада Откривање оптималних стратегија у људском кретању путем инверзног оптималног управљања

Ментор Коста Јовановић и Самер Мохамед

Изјављујем да је штампана верзија мог докторског рада истоветна електронској верзији коју сам предао/ла ради похрањивања у **Дигиталном репозиторијуму Универзитета у Београду.**

Дозвољавам да се објаве моји лични подаци везани за добијање академског назива доктора наука, као што су име и презиме, година и место рођења и датум одбране рада.

Ови лични подаци могу се објавити на мрежним страницама дигиталне библиотеке, у електронском каталогу и у публикацијама Универзитета у Београду.

Потпис аутора

У Београду, 24.11.2023.

Ф. Бечановић

образац изјаве о коришћењу

Изјава о коришћењу

Овлашћујем Универзитетску библиотеку „Светозар Марковић“ да у Дигитални репозиторијум Универзитета у Београду унесе моју докторску дисертацију под насловом:

Откривање оптималних стратегија у људском кретању путем инверзног оптималног управљања

која је моје ауторско дело.

Дисертацију са свим прилозима предао/ла сам у електронском формату погодном за трајно архивирање.

Моју докторску дисертацију похрањену у Дигиталном репозиторијуму Универзитета у Београду и доступну у отвореном приступу могу да користе сви који поштују одредбе садржане у одабраном типу лиценце Креативне заједнице (Creative Commons) за коју сам се одлучио/ла.

1. Ауторство (CC BY)

2. Ауторство – некомерцијално (CC BY-NC)

3. Ауторство – некомерцијално – без прерада (CC BY-NC-ND)

4. Ауторство – некомерцијално – делити под истим условима (CC BY-NC-SA)

5. Ауторство – без прерада (CC BY-ND)

6. Ауторство – делити под истим условима (CC BY-SA)

(Молимо да заокружите само једну од шест понуђених лиценци.
Кратак опис лиценци је саставни део ове изјаве).

Потпис аутора

У Београду, 24.11.2023.

Ф. Бешановић